Measurement of the total W- and Z-boson production cross sections in pp collisions at $\sqrt{s} = 2.76$ TeV with the ATLAS detector

Dissertation

zur Erlangung des akademischen Grades

doctor rerum naturalium (Dr. rer. nat.)

im Fach Physik

eingereicht an der

Mathematisch-Naturwissenschaftlichen Fakultät

der Humboldt Universität zu Berlin

von

Ksenia Gasnikova

Präsident der Humboldt-Universität zu Berlin

Prof. Dr. Jan-Hendrik Olbertz

Dekan der Mathematisch-Naturwissenschaftlichen Fakultät

Prof. Dr. Elmar Kulke

Gutachter:

1. Prof. Dr. Klaus Mönig
2. Prof. Dr. Thomas Lohse
3. Prof. Dr. Ulrich Husemann

Datum der Disputation:
2.11.2017

Abstract

Measurements of the total $pp \to W/Z \to ll'$ cross sections in the electron and muon channels are presented. Data collected at a center-of-mass energy $\sqrt{s} = 2.76$ TeV with the ATLAS detector at the LHC (in 2013), corresponding to a total integrated luminosity of 4 pb^{-1}, are used for this analysis.

In this measurement, several sources of systematic uncertainties are estimated. The background contribution is estimated using simulation (for electroweak and $t\bar{t}$ backgrounds) as well as data-driven methods (for the multijet background). The combined results for electron and muon channels provide the following cross sections:

$$\sigma_W^{fid}(W \to l\nu) = 2206.3 \pm 20.2(stat.) \pm 10.6(sys.) \pm 68.4(lumi.)\ [pb],$$
$$\sigma_Z^{fid}(Z \to ll) = 200.4 \pm 6.1(stat.) \pm 0.3(sys.) \pm 6.2(lumi.)\ [pb].$$

The combined cross sections are used for the calculation of the W/Z and W^+/W^- cross section ratios.

These results are compared with different orders of QCD calculations. The effect of the addition of the measured cross sections to the parton density functions (PDF) is estimated. The total uncertainty of the measurements is comparable to the current global PDF uncertainties, which makes them applicable for future PDF determination.

Additionally, studies of the Frozen Showers method for fast simulation have been performed. A new method of Frozen Showers library generation, allowing to reduce time spend on this stage, is developed.

Kurzfassung

Es werden Messungen der totalen Wirkungsquerschnitte der Prozesse $pp \to W/Z \to ll'$ in Endzuständen mit Elektronen und Myonen präsentiert. Für diese Analyse werden Daten, die im Jahr 2013 mit dem ATLAS-Detekor am LHC bei einer Schwerpunktsenergie von $\sqrt{s}$= 2.76 TeV aufgezeichnet wurden und einer integrierten Luminosität von pb^{-1} entsprechen, verwendet.

In dieser Analyse werden mehrere Quellen systematischer Unsicherheiten berücksichtigt. Die Untergründe werden sowohl mittels Simulationen (für elektroschwache und $t\bar{t}$ Untergründe) als auch mithilfe datengetriebener Methoden (für den Multi-Jet Untergrund) abgeschätzt. Die Resultate der Elektron- und Myon-Kanäle werden kombiniert und ergeben die folgenden Wirkungsquerschnitte:

$$\sigma_W^{fid}(W \to l\nu) = 2206.3 \pm 20.2(stat.) \pm 10.6(sys.) \pm 68.4(lumi.)\,[pb],$$
$$\sigma_Z^{fid}(Z \to ll) = 200.4 \pm 6.1(stat.) \pm 0.3(sys.) \pm 6.2(lumi.)\,[pb].$$

Die kombinierten Wirkungsquerschnitte werden zur Berechnung der Wirkungsquerschnitts-Verhältnisse W/Z und W^+/W^- benutzt.

Die Ergebnisse werden mit QCD-Berechnungen unterschiedlicher Ordnungen verglichen. Der Einfluss dieser Messung auf Partonverteilungsfunktionen (parton distribution functions, PDFs) wird abgeschätzt. Die gesamte Unsicherheit dieser Messungen ist vergleichbar mit den Unsicherheiten aktueller PDFs, weshalb diese Analyse zur Einbeziehung in zukünftige PDF-Bestimmungen geeignet ist.

Außerdem wurden Studien zur Frozen Showers Methode zur schnelleren Simulation von Ereignissen im ATLAS-Detektor durchgeführt. Es wurde eine neue Methode zur Generierung einer Frozen Showers Bibliothek entwickelt, die eine Reduzierung der für diesen Abschnitt benötigten Zeit erlaubt.

Declaration of Independent work

I declare that I have completed the thesis independently using only the aids and tools specified. I have not applied for a doctor's degree in the doctoral subject elsewhere and do not hold a corresponding doctor's degree. I have taken due note of the Faculty of Mathematics and Natural Sciences PhD Regulations, published in the Official Gazette of Humboldt-Universität zu Berlin no. 126/2014 on 18/11/2014.

_____ _____

Datum Unterschrift Doktorandin

Contents

Chapter 1

Thesis organization

This thesis presents the measurement of W and Z-boson production cross sections in the electron and muon channels using 2.76 TeV p-p data collected by the ATLAS experiment in 2013.

The thesis is organized into three main parts. The theoretical basis is described in part 1. The experimental input and software organization is explained in part 2. The measurements performed by the author are described in part 3. The results and its interpretation in the context of parton density functions are presented in a part 3.

The presented work was performed within the ATLAS collaboration. All plots in this thesis were produced by the author unless it is referenced otherwise.

The theoretical input as presented in part one consist of the following chapters:

Chapter 2 (Theoretical introduction) contains a brief overview of the current status of the Standard Model, the proton structure and the theory of the W and Z bosons in pp collisions. The production cross sections predictions are presented;

Chapter 3 (Methodology) describes the procedures of the cross section measurement and the calculation of their ratios and also methods of extractions of parton density functions (PDF).

The experimental setup is described in part two in the following chapters:

Chapter 4 (The LHC and the ATLAS experiment) gives an overview of the Large Hadron Collider (LHC) accelerator complex and its experiments. The ATLAS detector, used to collect data for this analysis, is shortly discussed;

Chapter 5 (Event reconstruction) contains the detailed description of the physics objects reconstruction. The study of missing transverse energy reconstruction algorithm, performed by author, is presented;

Chapter 6 (Monte Carlo) describes the Monte Carlo (MC) production steps and contains a short description of generators used in this analysis;

Chapter 7 (Frozen Showers) gives a description of so-called Frozen Showers method used for fast MC simulation at the ATLAS experiment. The machine learning procedure for optimization of this method, developed by author, is presented;

Chapter 8 (Data and Monte Carlo samples) describes experimental data and simulated samples, used in the analysis.

The following chapters present work, done by the author, unless stated otherwise:

Chapter 9 (Event selection) gives a set of selection criteria used to derive W and Z boson candidate events in collected data samples;

Chapter 10 (Monte Carlo corrections) presents the corrections applied to the simulated events, which are required to improve data to MC agreement. The correction factors have been derived by the ATLAS performance group, except for the muon trigger scale factors, which are determined by the author;

Chapter 11 (Hadronic recoil calibration) describes a method of missing transverse energy calibration in the data and methods for the corresponding uncertainty determination;

Chapter 12 (Background estimation) provides a description of the main background processes and the techniques to estimate their contributions;

Chapter 13 (Uncertainties in the cross section measurements) presents the sources of experimental and theoretical uncertainties and shows the methods of their propagation to the final results;

Chapter 14 (Control distributions) shows the comparison of different distributions between data and MC simulation;

Chapter 15 (Results) presents the results of the measurements of production cross section for W and Z-bosons in electron and muon channels. The results have been used to test the lepton universality. Moreover, the combined cross sections and their ratios are shown. The impact of these measurements on the PDF distributions is estimated. The NNLO predictions used in this chapter have been provided to author by the ATLAS W/Z group.

Part I

Theoretical basis

Chapter 2

Theoretical introduction

This thesis presents the measurement of a Standard Model (SM) process. Therefore the first section of this chapter gives a small overview of this model. The proton structure (Sec. 2.2) and physics of W and Z bosons in proton collisions (Sec. 2.3) are also discussed. Additionally, the predictions for $W \to l\nu$ and $Z \to ll$ cross sections are presented in Sec. 2.3.

Several references were used for a preparation of this chapter, including [1,2].

2.1 The Standard Model

The Standard Model is the model that explains the interactions between the elementary particles. It provides our current best understanding of the particle physics and unifies the quantum mechanics, special relativity, and a field theory. It was postulated by Weinberg and Salam in mid-1970 [3–5] and is successfully tested for the last 40 years. Despite the fact that there are some unexplained phenomena in SM such as dark matter [6], the SM describes almost all laboratory data. The summary of all SM production cross section measurements at ATLAS experiment is given in Fig. 2.1. The results agree with SM prediction over several orders of magnitude, and no significant deviation from SM has been found yet.

The SM postulates two types of fundamental particles: fermions and boson. Graphical representation of particles in SM with their masses and quantum numbers is shown in Fig. 2.2. The bosons are the carriers of the fundamental forces with the integer spin. Strong interactions are mediated by 8 massless gluons. The massless photons are carrying the electromagnetic interactions, while the W and Z-bosons are responsible for the weak forces. The last SM boson, observed in experimental data is the Higgs boson [8,9]. It is associated with Yukawa interactions, which are responsible for the fermion masses.

The fermions are the spin 1/2 particles that form the ordinary atomic matter. They can be further divided to leptons and quarks. Leptons can interact just electromagnetically and weakly, while quarks also undergo strong interactions. Both groups are divided into three separate generations.

The SM is a *non-abelian gauge theory*, meaning, that this theory is based on Lagrangian that is invariant under local and global transformations (called *symmetries*). From the Noether the-

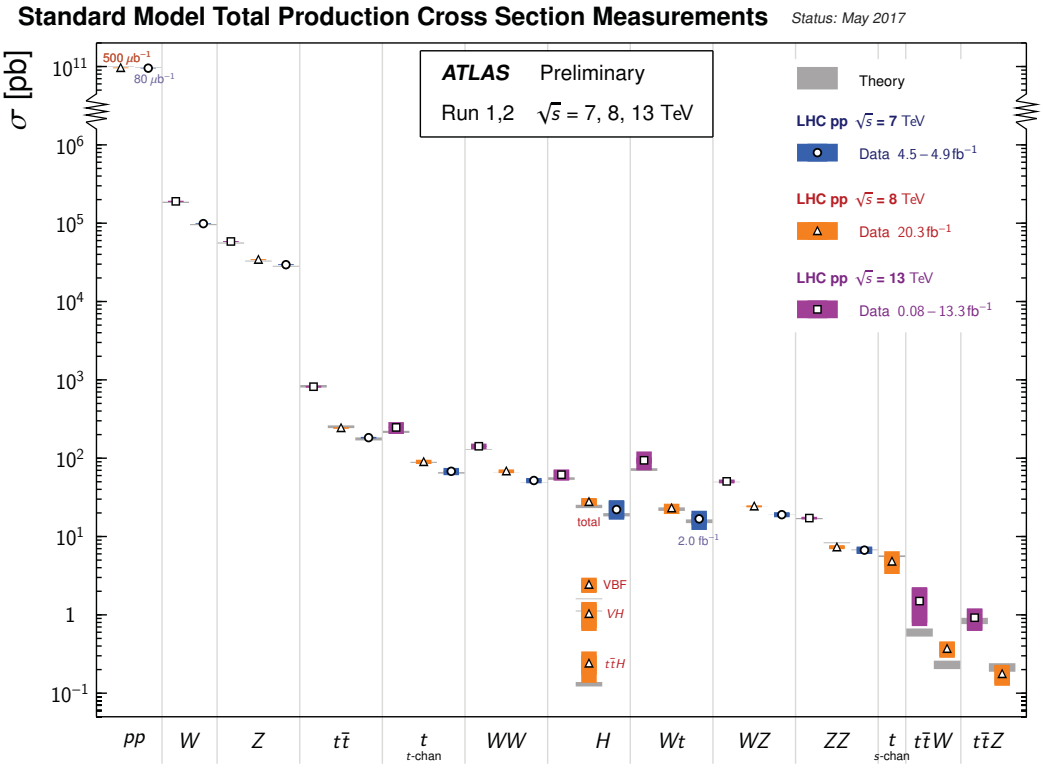

Fig. 2.1: Summary of SM production cross section measurements in the ATLAS experiment, corrected for leptonic branching fractions, compared to the corresponding theoretical expectations. The amount of data used for each measurement is indicated close to the data point [7].

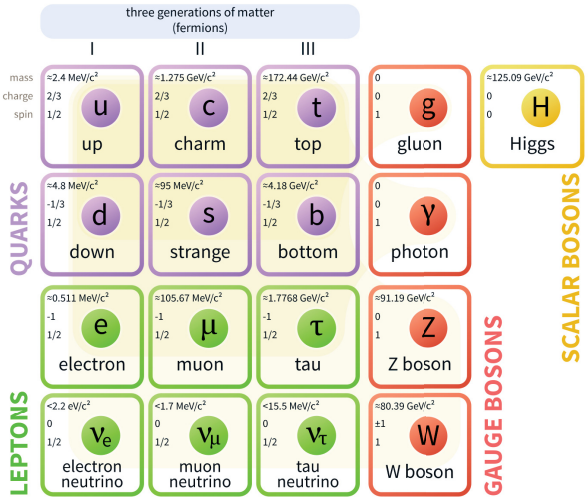

Fig. 2.2: Fundamental particles of the Standard Model: three generations of fermions, the gauge bosons and Higgs boson [10].

orem [11, 12] it is known that each symmetry is connected to at least one conserved quantity. The symmetry group of SM is:

$$SU(3)_C \times SU(2)_L \times U(1)_Y, \tag{2.1}$$

where hypercharge Y, a left-handed helicity L and a color charge C are the quantum numbers of the corresponding symmetry group. The $SU(2)_L \times U(1)_Y$ symmetry describes the electroweak (EW) theory, while the $SU(3)_C$ corresponds to the theory of strong interactions - Quantum Chromodynamics (QCD) [13–15].

The EW part of SM postulates three massless vector fields in $SU(2)_L$ - the isospin triplet of vector fields W^1_μ, W^2_μ, W^3_μ with the coupling constant g and a single gauge field B_μ in $U(1)_L$ group with coupling strength g'. The massless γ and the massive Z and W bosons are produced due to the spontaneous breaking of the electroweak gauge symmetry:

$$\begin{pmatrix} \gamma \\ Z^0 \end{pmatrix} = \begin{pmatrix} \cos\theta_W & \sin\theta_W \\ -\sin\theta_W & \cos\theta_W \end{pmatrix} \begin{pmatrix} B \\ W^3 \end{pmatrix}, \tag{2.2}$$

$$W^\pm = \frac{W^1 \pm iW^2}{\sqrt{2}}, \tag{2.3}$$

where θ_W is the electroweak mixing angle whose value is not predicted in the SM. The masses of Z and W bosons are connected by the relation:

$$M_W^2 = cos\theta_W^2 M_Z^2. \tag{2.4}$$

The QCD Lagrangian has only one free parameter - the *strong coupling constant* α_s. The QCD does not predict the value of α_s, however it predicts its evolution with renormalization scale μ_R using the renormalization group equation (RGE):

$$\beta(\alpha_s) = \mu^2 \frac{d\alpha_s(\mu^2)}{d\mu^2} = -b_0\alpha_s^2(\mu) - b_1\alpha_s^3(\mu) - O(\alpha_s, n \geqslant 4), \tag{2.5}$$

where the first coefficient is:

$$b_0 = \frac{33 - 2f}{12\pi}, \tag{2.6}$$

and $f = 3$ is the number of quark flavors. A typical scale of μ_R for a physics process corresponds to the momentum transferred Q^2 between the interacting objects. The energy dependence of the strong coupling constant is showed in Fig. 2.3. The α_s value increases towards smaller scales, and it becomes small for higher Q^2. As a consequence, the quarks have a property of *asymptotic freedom* and *confinement*, meaning that they cannot be observed as free particles, but there are bound in QCD states, for example, a proton.

The physical quantities like cross sections, do not depend on renormalization scale. However, the calculation on any perturbative order in α_s is a function of μ_R. The cross section for the partonic interactions (or the *partonic cross section*) $\sigma_{ab\to X}$ can be expressed perturbatively in α_s as:

$$\sigma_{ab\to X} = \hat{\sigma_0} + \alpha_s(\mu_R)\hat{\sigma_0} + \alpha_s^2(\mu_R)\hat{\sigma_2} + ..., \tag{2.7}$$

where σ_i is the i-th order contribution to the final cross section. The cross section, calculated at the lowest-order of the expansion is called the *leading order* (LO) cross section. The calcu-

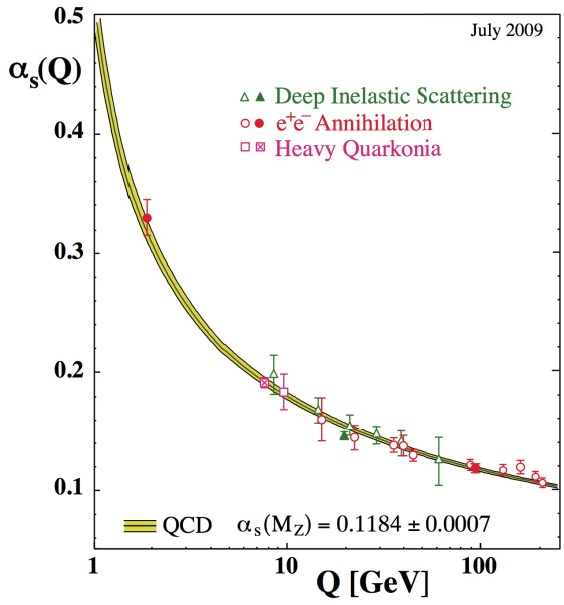

Fig. 2.3: The coupling of the strong interaction, α_s, as a function of energy scale [17].

lation using the expansion of α_s up to the i-th order is called (next-to)^i order (N^{i}LO) cross section. The inclusion of higher order corrections in the calculations allows the reduction of the dependency on the renormalization scale.

2.2 Proton structure

QCD predicts the cross section for the individual quark–quark interactions at different orders in α_s. However, since quarks have not been observed in a free state, the tests of QCD are possible using the experiments with hadrons (e.g. proton beams), so the internal quark composition in the hadron should be taken into account.

In 1969 Feynman proposed a model of the proton structure called a parton model of the hadrons [18]. In this model he assumed that any hadron can be treated as a composition of point-like constituents called partons. In the high-energy scattering, the soft interaction between partons can be neglected, and therefore they can be treated as quasi-free in the collision. In this approximation, a total cross section for the process in hadron–hadron interaction can be written as a sum of all partonic cross sections:

$$\sigma = \sum_{i,j} \int dx_i dx_j f_i^{(P_1)}(x_i) f_j^{(P_2)}(x_j) \hat{\sigma}(x_i x_j s), \tag{2.8}$$

where:

- $f_i^{(P_k)}(x_i)$ are the parton distribution functions (PDF) for both colliding hadrons. They describe the probability to find parton i in hadron k with a fraction of longitudinal momentum x_i;
- $s = (P_1 + P_2)^2$ is the center-of-mass energy of colliding hadrons;

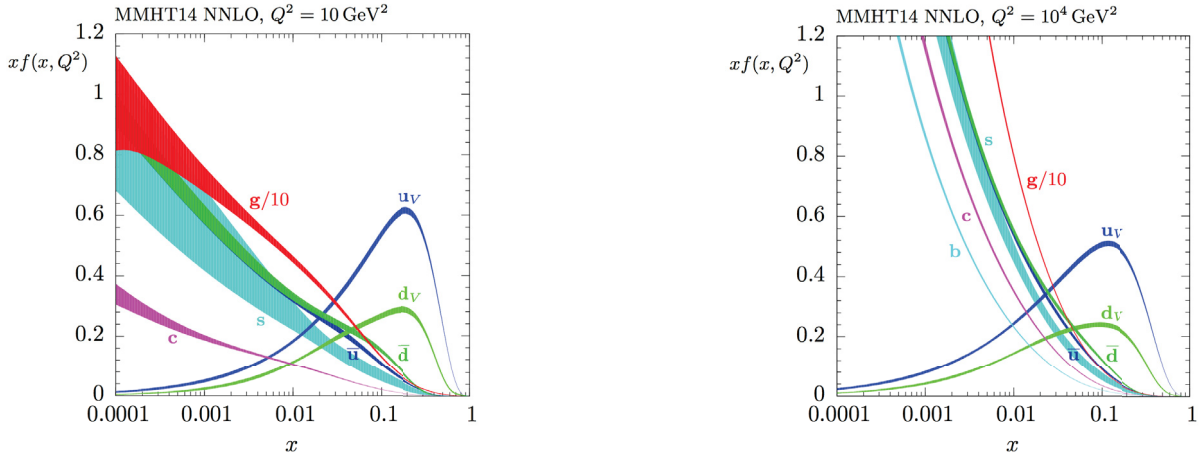

Fig. 2.4: The MMHT2014 NNLO PDFs predictions at a) $Q^2 = 10GeV^2$ and b) $Q^2 = 10^4GeV^2$ with associated 68% confidence-level uncertainty bands [20].

- $\hat{\sigma}(x_1 x_2 s)$ is the partonic cross section for a given scattering process, calculated in QCD.

The partons, which determine the quantum numbers of hadrons, are called *valence quarks* (u and d quarks in case of the proton). However, due to the quantum fluctuations, some number of quark pairs (of $u\bar{u}$, $d\bar{d}$, $c\bar{c}$ etc) with low momentum can be created. These quarks are called *sea-quarks*. Due to the conservation of the total momentum and the quark flavor of a proton, the following sum rules are applicable for proton PDFs:

$$\begin{gathered}\int_0^1 dx \sum_i x f_i^{(p)}(x) = 1; \\ \int_0^1 dx (f_u^{(p)}(x) - f_{\bar{u}}^{(p)}(x)) = 2; \\ \int_0^1 dx (f_d^{(p)}(x) - f_{\bar{d}}^{(p)}(x)) = 1; \\ \int_0^1 dx (f_s^{(p)}(x) - f_{\bar{s}}^{(p)}(x)) = 0,\end{gathered}$$

where index i runs over the quark flavors.

For the partonic cross sections, the soft emission of real and virtual gluons causes collinear singularities. However, it is possible to include initial state emissions below a given scale into non-perturbative parton distribution functions. The cutoff parameter in this procedure is called a *factorization scale* μ_F [19]. This definition of PDFs is universal, i.e. they do not depend on the physics process. Similarly, the factorization scale μ_F is not a physical quantity, and the total partonic cross section should be independent of μ_f. The typical choice of the scale is $\mu_F \approx \mu_R \approx Q^2$.

The parton density distributions cannot be calculated perturbatively in QCD and therefore need to be extracted from the experimental data. However, it is possible to predict the evolution of PDFs with factorization scale using the Dokshitzer-Gribov-Lipatov-Altarelli-Parisi (DLGAP) evolution equations [21–24]. An example of quark and gluon PDFs in the proton predicted by MMHT2015 NNLO [20] for different energy scales is shown in Fig. 2.4. The PDFs of valence (u and d) quarks are reaching maximum at x=1/3, while the sea quark and gluon densities are rising at low-x. The contribution of the sea quarks and gluons becomes larger with increasing Q^2.

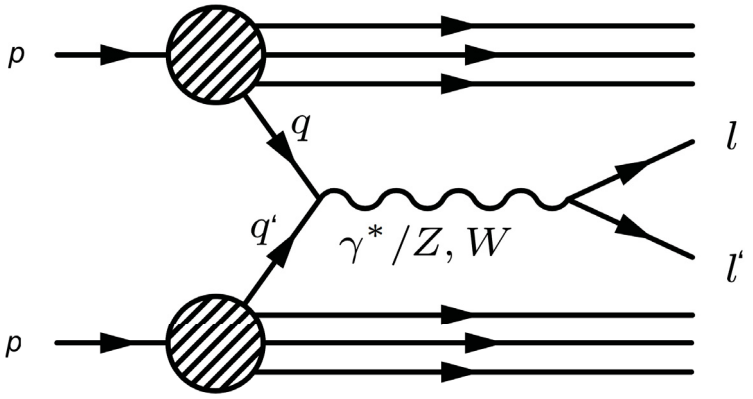

Fig. 2.5: A schematic representation of the W/Z production via Drell-Yan process in a hadron collider.

2.3 Physics of W and Z bosons in pp collisions

The W and Z bosons are the massive vector bosons in the Standard Model. They have been predicted by the Glasgow, Weinberg, Salam in 1960's [3–5] and discovered in 1983 by UA1 and UA2 at CERN $p\bar{p}$ collider [25–28]. These particles are mediating weak interactions and decaying almost immediately ($t \approx 10^{-25}$ s).

The leading order production mechanism of W/Z boson in pp collisions is the Drell-Yan mechanism, shown schematically in Fig. 2.5. It is defined as an annihilation of the quark–antiquark pair through the exchange of a gauge boson, which then decays into a fermion pair. A simplest example of this process is the production of the virtual photon $q\bar{q} \rightarrow \gamma^* \rightarrow l^+l^-$. The corresponding cross section can be calculated using QED:

$$\hat{\sigma}(q\bar{q} \rightarrow \gamma^* \rightarrow e^+e^-) = \frac{4\pi\alpha}{3\hat{s}} \frac{1}{N} Q_q^2, \tag{2.9}$$

where Q_q is the quark charge, $\hat{s}$ is the center-of-mass energy of the quark–antiquark system, and $1/N = 1/3$ is the color factor, coming from the fact that quark and antiquark colors should match to create a color-singlet final state.

In analogy to this process, the on-shell production of W and Z bosons using Drell-Yan reaction can be calculated as:

$$\hat{\sigma}^{q\bar{q}' \rightarrow W} = \frac{\pi}{3}\sqrt{2} G_F M_W^2 |V_{q\bar{q}'}|^2 \delta(\hat{s} - M_W^2), \tag{2.10}$$

$$\hat{\sigma}^{q\bar{q} \rightarrow Z} = \frac{\pi}{3}\sqrt{2} G_F M_Z^2 (v_q^2 + a_q^2) \delta(\hat{s} - M_Z^2), \tag{2.11}$$

where the q and q' are the different quarks. The $V_{q\bar{q}'}$ is the appropriate Cabibbo-Kobayashi-Maskawa matrix element (describes a strength of flavor changing weak decays), and v_q (a_q) the vector (axial vector) coupling of the Z-boson to the quarks. For the full production cross section, the partonic spectrum of colliding hadrons has to be considered. For two quarks, carrying fractions x_1 and x_2 of the colliding protons momenta, the momentum transfer Q^2 can be written as:

$$Q^2 = (x_1 P_1 + x_2 P_2)^2 \approx x_1 x_2 s = M_{Z,W,\gamma^*}^2, \tag{2.12}$$

where the parton masses have been neglected in the calculation, the $\sqrt{s}$ in the Eq. 2.12 is the center-of-mass energy of 2 hadrons:

$$s = (P_1 + P_2)^2. \tag{2.13}$$

Another variable used to describe the parton–parton scattering is the rapidity of the boson, defined as:

$$y = \frac{1}{2} log \frac{E + P_z}{E - P_z}, \tag{2.14}$$

where E is the energy of the boson and P_z is its z component of the momentum. This quantity can be connected to the momentum fraction carried by initial partons in a leading order approximation as:

$$x_{1,2} = \frac{M_{Z,W,\gamma^*} e^{\pm y}}{\sqrt{s}}. \tag{2.15}$$

The maximum accessible rapidity range for the production of the bosons can be determined from the $\sqrt{s}$ and the mass of the boson as:

$$|y_{bos}^{max}| = ln \frac{\sqrt{s}}{M_{Z,W,\gamma^*}}. \tag{2.16}$$

The kinematic phase space of the proton, accessible at ATLAS for different center-of-mass energies is shown in Fig. 2.6. The W and Z cross sections at 2.76 TeV correspond to $Q^2 \approx 10^4\, GeV^2$ and therefore can probe the ranges of momentum fractions $x^W > 8 \cdot 10^{-4}$ and $x^Z > 1 \cdot 10^{-3}$ for W and Z bosons respectively. The W^+ production depends mainly on the u and $\bar{d}$-quark distributions (the leading process is $u\bar{d} \to W^+$) and the W^- to $\bar{u}$ and d-quark distributions. The Z boson production cross section is most sensitive to the valence quark distributions.

The Drell–Yan process contributes to around 65% of cross section [30], with both valence–sea and sea–sea quarks interactions included. The dominant higher order corrections are determined by the interaction of quarks with gluon (occurs in approximately 20% of the events).

Due to the very small lifetime of W and Z-bosons, this production is instantly followed by decay. The probability of a certain decay mode is described by the *branching ratio*, $\mathbf{BR}(X \to a + b)$, that is a fraction of a partial decay rate (of the decay mode of interest) and the total decay rate of the boson. The W and Z-boson decay modes are summarized in Tab. 2.1. The W and Z bosons can decay hadronically with the production of a quark–antiquark pair for all quark flavors, except for top quark since its mass exceeds the mass of the bosons. This mode of the decay is the dominant one because of the three possible color states for each quark. In a leptonic decay mode of the W-boson, the lepton plus corresponding same flavor neutrino/antineutrino pair are produced. The leptonic decays of Z-boson create a lepton-antilepton pair. The visible fraction of Z-bosons decaying into leptons is smaller (compared to W) because of the invisible mode of Z-bosons decay, where a neutrino-antineutrino pair is produced. Because of the *lepton universality* in the SM and large masses of W and Z-bosons compared to lepton ($M_Z > M_W \gg M_l$), the branching ratios of the leptonic decays are almost identical.

Due to experimental difficulty to measure the hadronic decays, the W/Z cross sections are usually measured through their leptonic decay modes. The expected NNLO production cross sections times their branching ratios to one of the leptons is estimated using FEWZ program

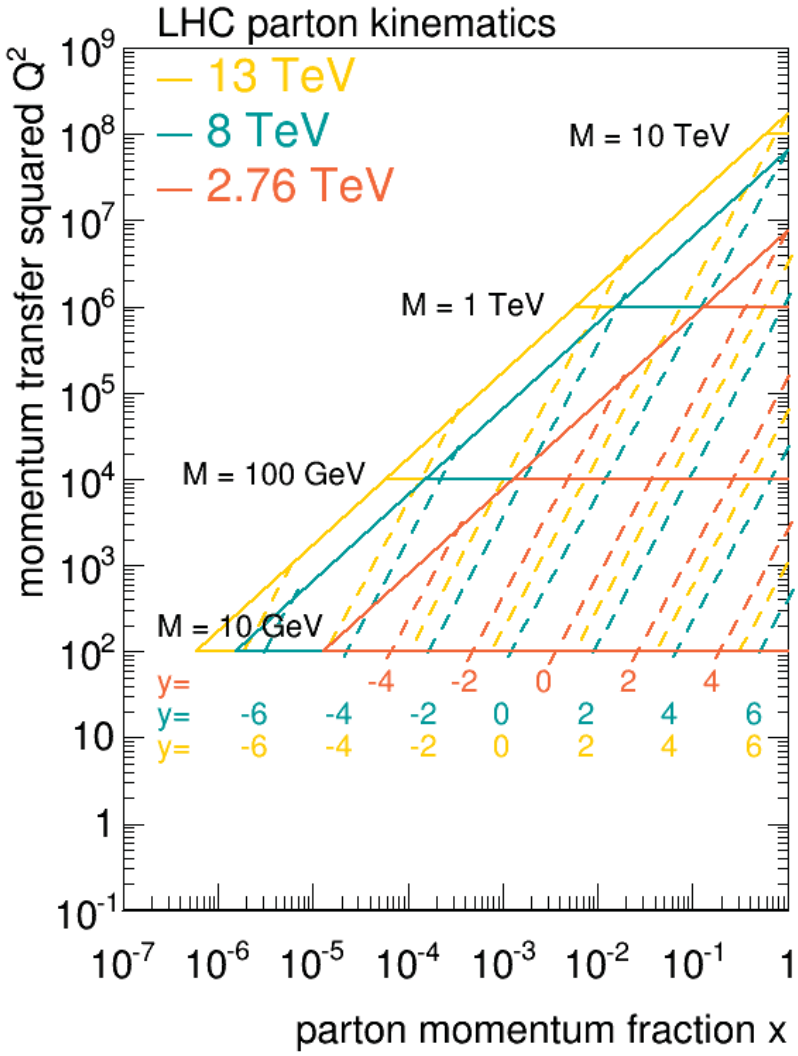

Fig. 2.6: The parton kinematics accessible in the ATLAS experiment in Q^2–x plane. The limits are shown for $\sqrt{s}$ = 13 TeV, $\sqrt{s}$ = 8 TeV and $\sqrt{s}$ = 2.76 TeV [29].

[32] and CT14nnlo [33] at $\sqrt{s}$=2.76 TeV are:

$$\sigma^{NNLO}_{W^+\to l\nu} = 2114^{+8}_{-11}(scale)\,{}^{+57}_{-59}(PDF)\,[pb], \tag{2.17}$$

$$\sigma^{NNLO}_{W^-\to l\nu} = 1265^{+5}_{-6}(scale)\,{}^{+32}_{-38}(PDF)\,[pb] \tag{2.18}$$

and

$$\sigma^{NNLO}_{Z^-\to ll} = 304^{+1}_{-1}(scale)\,{}^{+7}_{-7}(PDF)\,[pb], \tag{2.19}$$

where the the first uncertainty comes from the uncertainty of the scale choice. The second uncertainty arises from the imperfect knowledge of proton PDFs. The difference between W^+ and W^- cross sections (called charge asymmetry) is due to the higher probability of finding a u–quark rather than d–quark in the proton.

The NNLO QCD predictions of W and Z-boson cross sections in pp and $p\bar{p}$ collisions to-

Table 2.1: Branching ratios of the different W and Z decay modes [31]. Invisible denotes the Z decays with a neutrino-antineutrino pair as a final state. The predicted values are estimated with $\sin^2\theta_W = 0.23$.

Boson	Decay mode	Measured branching ratio	SM prediction
W	$e\nu_e$	$(10.71 \pm 0.16)\%$	
	$\mu\nu_\mu$	$(10.63 \pm 0.15)\%$	11.1%
	$\tau\nu_\tau$	$(11.38 \pm 0.21)\%$	
	hadrons	$(67.41 \pm 0.27)\%$	66.7%
Z	e^+e^-	$(3.363 \pm 0.004)\%$	
	$\mu^+\mu^-$	$(3.366 \pm 0.007)\%$	3.4 %
	$\tau^+\tau^-$	$(3.3658 \pm 0.008)\%$	
	invisible	$(20.00 \pm 0.06)\%$	20.5%
	hadrons	$(69.91 \pm 0.06)\%$	69.2%

gether with the results obtained using different experiments are shown in Fig. 2.7. It can be observed that the W and Z-boson cross sections have not been measured so far in the region around 1 TeV < $\sqrt{s}$ < 7 TeV in pp collisions.

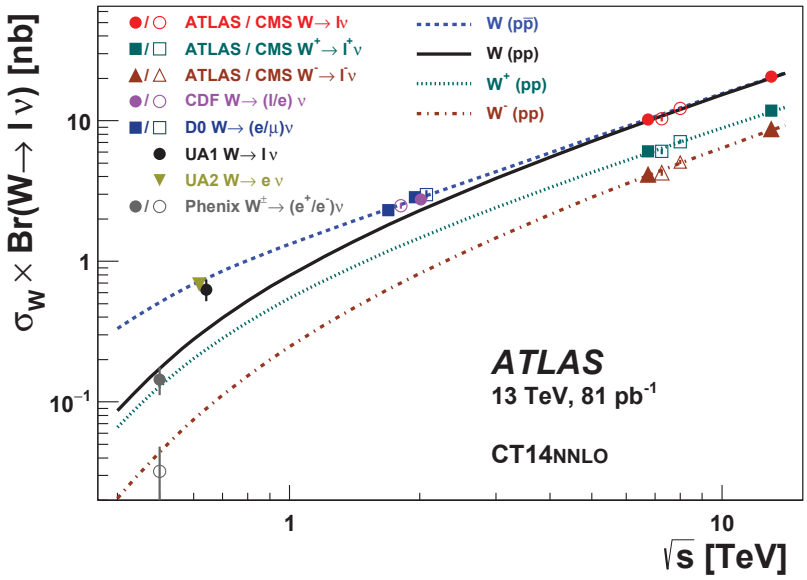

a)

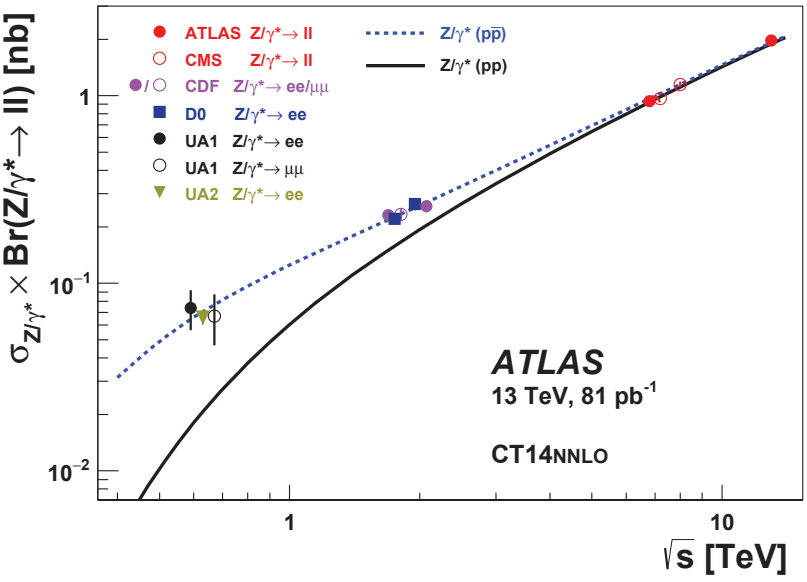

b)

Fig. 2.7: The measured values of a) $\sigma_{W\to l\nu}$ and b) $\sigma_{Z\to ll}$ compared to the theoretical predictions based on NNLO QCD calculations. The predictions and previous measurements are shown for both proton-proton and proton-antiproton colliders as a function of $\sqrt{s}$. All data points are displayed with their total uncertainty. The calculations were performed with the program FEWZ using the CT14nnlo parton density function parameterization. The theoretical uncertainties on the cross section predictions are not shown. Figure taken from [34].

Chapter 3

Measurement methodology

In this chapter, the methodology of the measurements is given. The first section gives a description of cross section measurement in the different phase space regions. The second section presents the method of linear averaging of the results, used for the combination of electron and muon channel analyses. In the last section, the PDF fit procedure used to put constraints on PDFs is described.

3.1 Cross section calculation

Due to the limited geometrical detector acceptance and reconstruction efficiency of the ATLAS detector (Sec. 4.2) the W and Z-boson cross sections cannot be measured in the full phase space. The fiducial cross section, i.e. the cross section limited to a given selection region, is measured, using the formula:

$$\sigma^{fid}_{W/Z} = \frac{N^{W/Z} - B^{W/Z}}{C_{W/Z} L_{int}} = \frac{N^{W/Z}_{sig}}{C_{W/Z} L_{int}}, \tag{3.1}$$

where:

- N is the number of events measured in the data;
- B is the estimated number of background events;
- $N^{W/Z}_{sig} = N^{W/Z} - B^{W/Z}$ is the number of the signal events;
- L_{int} is the integrated luminosity of a dataset;
- $C_{W/Z}$ is a correction factor that accounts for event selection and detector resolution effects.

For each process, the correction factor $C_{W/Z}$ is calculated from the simulation (Chap. 6) as :

$$C_{W/Z} = \frac{N_{MC,rec}}{N_{MC,gen,selection}}, \tag{3.2}$$

where $N_{MC,rec}$ is the total number of simulated events which pass the final selection requirements after reconstruction, and $N_{MC,gen,selection}$ is the total number of simulated events after fiducial selection on the generator level.

The measurements can be then extrapolated to the full phase space using simulated events:

$$\sigma^{tot}_{W/Z} = \frac{\sigma^{fid}_{W/Z}}{A_{W/Z}}, \tag{3.3}$$

where $\sigma^{tot}_{W/Z}$ is the total inclusive production cross section for the W or Z-bosons, and $A_{W/Z}$ is the acceptance factor.

The $A_{W/Z}$ factor is determined from the simulation using:

$$A_{W/Z} = \frac{N_{MC,gen,selection}}{N_{MC,gen,all}}, \tag{3.4}$$

where $N_{MC,gen,all}$ is the total number of simulated events. Both $A_{W/Z}$ and $C_{W/Z}$ are defined at the "born level", i.e. before the decay leptons emit photons via QED final state radiation.

3.1.1 Fiducial phase space definition

The fiducial region definition corresponds to the analysis selection described in Chap. 9. For W boson measurement, it is depicted as:

- $P^l_T > 20$ GeV;
- $|\eta^l| < 2.5$;
- $P^\nu_T > 25$ GeV;
- $M^W_T > 40$ GeV,

where P^l_T (P^ν_T) is the charged lepton (neutrino) transverse momentum, η^l is the lepton pseudorapidity, and M^W_T is the transverse mass, defined as:

$$M^W_T = \sqrt{2P^l_T \cdot P^\nu_T[1 - cos(\phi_l - \phi_\nu)]}, \tag{3.5}$$

where $\phi_l - \phi_\nu$ is the azimuthal angle between charged lepton and neutrino.

For the Z-boson production measurement the fiducial phase space is defined as:

- $P^l_T > 20$ GeV;
- $|\eta^l| < 2.5$;
- 66 GeV $< M_Z <$ 116 GeV,

where M_Z is the di-lepton invariant mass.

The differences between analysis selection for the electron and muon channels are neglected in this definition.

3.1.2 Extrapolation to the 13 TeV fiducial phase space

The inclusive cross section measurements at $\sqrt{s}$=13 TeV use a stricter set of analysis criteria and therefore a stricter definition of the fiducial phase space. However, it is possible to extrapolate the relevant cross sections to a slightly different fiducial phase space using the relation:

$$\sigma_{W/Z}^{fid,13} = \frac{\sigma_{W/Z}^{fid}}{E_{W/Z}}, \tag{3.6}$$

where $E_{W/Z}$ is the extrapolation factor, defined as:

$$E_{W/Z} = \frac{N_{MC,gen,selection}}{N_{MC,gen,selection^{new}}}, \tag{3.7}$$

where $N_{MC,gen,selection^{new}}$ is the total number of simulated events after new fiducial selection on the generator level. The extrapolation procedure allows direct calculation of the cross section ratios for a different $\sqrt{s}$.

The 13 TeV fiducial phase space is defined as:

- $P_T^l > 25$ GeV;
- $|\eta^l| < 2.5$;
- $P_T^\nu > 25$ GeV;
- $M_T^W > 50$ GeV

for the W-boson production decays and as:

- $P_T^l > 25$ GeV;
- $|\eta^l| < 2.5$;
- 66 GeV $< m_Z <$ 116 GeV

for the Z-boson measurement.

3.1.3 The W boson cross section calculation

In this analysis, the cross section for the production of the W-boson is calculated by combining the W^+ and W^--bosons production cross sections in the following way:

$$\sigma_W = \sigma_{W^+} + \sigma_{W^-} = \frac{1}{L_{int}} \cdot \Big(\frac{N_{sig}^{W^+}}{A_{W^+} C_{W^+}} + \frac{N_{sig}^{W^-}}{A_{W^-} C_{W^-}} \Big). \tag{3.8}$$

The absolute systematic uncertainty of this measurement is calculated from uncertainties of W^+ and W^- cross sections as:

$$(\delta X_W)^2 = (\delta X_{W^+})^2 + (\delta X_{W^-})^2 + 2 \cdot \rho_{W^+W^-}^X \delta X_{W^+} \delta X_{W^-}, \tag{3.9}$$

where δX is a systematic component on the cross section and $\rho_{W^+W^-}^X$ is a correlation between W^+ and W^--bosons production for this component, which is estimated in Chap. 13.

3.2 Averaging of the results

The SM predicts the same branching ratios for the leptonic decays of W and Z bosons. Therefore, it is possible to combine the measurements in the electron and muon channels into a single cross section. This analysis uses the standard tool for averaging of the measurements (called Havereger), which was originally developed for the HERA experiment [35]. The tool uses a method of linear averaging, which is described below.

For a given observable, the probability density function for a "true" value m to get a value μ with uncertainty Δ in the measurement is:

$$P(m) = \frac{1}{\sqrt{2\pi}\Delta} exp\Big(- \frac{(m-\mu)^2}{2\Delta^2}\Big). \tag{3.10}$$

The corresponding χ^2 function, that describes the goodness of fit of observed values to a "true" value, calculated as:

$$\chi^2(m) = \frac{(m-\mu)^2}{\Delta^2}. \tag{3.11}$$

In the case of N statistically-independent measurements, one has:

$$P(m) \propto \prod_{i=0}^{N} exp\Big(- \frac{(m-\mu_i)^2}{2\Delta_i^2}\Big), \tag{3.12}$$

which corresponds to the:

$$\chi^2_{sum}(m) = \sum_i \chi^2_i = \sum_i \frac{(m-\mu_i)^2}{\Delta_i^2}, \tag{3.13}$$

that can be rewritten in the form of the Eq. 3.11:

$$\chi^2_{sum}(m) = \frac{(m-\mu_{ave})^2}{\Delta^2_{ave}} + \chi^2_0, \tag{3.14}$$

where μ_{ave} and Δ_{ave} are the average value and its uncertainty respectively. These values are found by minimizing χ^2_{sum} with respect to m. The value χ^2_0 indicates a consistency in the measurements and should be $\chi^2_0/N \approx 1$.

Systematic uncertainties are a consequence of imperfections in the experiment (e.g. due to its calibration) and are added to the χ^2 function:

$$\chi^2_{syst}(\alpha) = \frac{(\alpha-\alpha_0)^2}{\Delta^2_\alpha} \equiv b^2, \tag{3.15}$$

where α is the "true" value of the parameter and α_0 is measured at the experiment with uncertainty Δ_α. The nuisance parameter b corresponds to a coherent change of the measurements due to systematic effects $\mu_i \rightarrow \mu_i + \mathbf{bF_i}$.

Using this nuisance parameters representation, Eq. 3.14 can be rewritten in a more general way:

$$\chi^2_{sum}(\mathbf{m}, \mathbf{b}) = \sum_i \frac{(m - \mu_i - \sum_j \Gamma^j_i b_j)^2}{\Delta^2_i} + \sum_j b^2_j, \tag{3.16}$$

where:

- i runs over all measured values used in averaging;
- $\mathbf{b}$ is the vector of nuisance parameters, b_j, corresponding to each source of systematic uncertainties;
- Γ_i^j is the absolute correlated systematic uncertainty;
- Δ_i^2 is the uncorrelated (statistical) uncertainty.

3.3 Calculation of the cross section ratios

The calculation of the cross section ratios is a powerful tool for testing theory predictions, due to the cancellation of the correlated uncertainties. The ratio for two cross section measurements (σ_i and σ_j) is calculated as:

$$R_{i,j} = \frac{\sigma_i}{\sigma_j} = \frac{\frac{N^i_{sig}}{A^i_{W/Z} C^i_{W/Z} L_{int}}}{\frac{N^j_{sig}}{A^j_{W/Z} C^j_{W/Z} L_{int}}} = \frac{N^i_{sig}}{N^j_{sig}} \cdot \frac{A^j_{W/Z}}{A^i_{W/Z}} \cdot \frac{C^j_{W/Z}}{C^i_{W/Z}} = \frac{N^i_{sig}}{N^j_{sig}} \cdot A_{i/j} C_{i/j}. \tag{3.17}$$

This means that $R_{i,j}$ does not depend e.g. on the integrated luminosity and its uncertainty.

The relative uncertainty on $R_{i,j}$ can therefore be obtained by taking into account the correlations between two measurements:

$$\left(\frac{\delta R_{i,j}}{R_{i,j}}\right)^2 = \left(\frac{\delta N^i_{sig}}{N^i_{sig}}\right)^2 + \left(\frac{\delta N^j_{sig}}{N^j_{sig}}\right)^2 + \left(\frac{\delta A_{i/j}}{A_{i/j}}\right)^2 + \left(\frac{\delta C_{i/j}}{C_{i/j}}\right)^2. \tag{3.18}$$

Uncertainties on the first two terms are considered to be uncorrelated, while the uncertainties on $A_{i,j}$ and $C_{i,j}$ are derived using the following error propagation formula:

$$\left(\frac{\delta X_{i/j}}{X_{i/j}}\right)^2 = \left(\frac{\delta X_i}{X_i}\right)^2 + \left(\frac{\delta X_j}{X_j}\right)^2 - 2\rho_{ij} \frac{\delta X_i}{X_i} \frac{\delta X_j}{X_j}, \tag{3.19}$$

where X is the relevant systematic component and ρ_{ij} is the correlation between two measurements. The estimation of correlation parameters is discussed in details in Chap. 13.

3.4 Estimation of the parton density functions

As already mentioned in Chap. 2, the parton density functions (PDFs) cannot be calculated perturbatively in QCD. However, they can be calculated from the global fit to the experimental data. In this thesis the xFitter program [36] is used to determine the proton PDFs.

The PDFs are defined at a given starting scale Q_0^2 and then evoluted to a needed scale using the DLGAP equations. There are different parameterizations used for the PDFs at the starting scale. A very standard form uses a simple polynomial for interpolation between low- and high-x regions:

$$x f(x; Q_0^2) = A x^B (1-x)^C P_i(x), \tag{3.20}$$

where P_i is a polynomial of a given order. In the analysis presented in Chap. 15 a standard HERA parameterization is used, implementation is discussed in details below.

There are 11 different partons to consider, however heavy quark (c and b-quarks) distributions can be determined perturbatively. This leaves at least 7 independent combinations. The parameterized PDFs are the valence distributions (xu_v and xd_v), the gluon distribution (xg), and the u-type ($x\bar{U}$) and d-type ($x\bar{D}$) sea, where:

$$xu_v = xu - x\bar{u}\,;\, xd_v = xd - x\bar{d}\,;\, x\bar{U} = x\bar{u}\,;\, x\bar{D} = x\bar{d} + x\bar{s}\,.$$

For the strange quark distributions, it is assumed that at a given starting scale Q_0^2:

$$xs = x\bar{s} = f_s x\bar{D}, \tag{3.21}$$

where $f_s = 0.31$ - is a strange quark fraction which is chosen to match the experimental data.

The following functional form is used for PDFs parameterization:

$$xf(x;Q_0^2) = Ax^B(1-x)^C(1+Dx+Ex^2), \tag{3.22}$$

where A_{uv}, A_{dv} and A_g are constrained by the number sum-rules and the momentum sum-rule, and the parameters $B_{\bar{U}}$ and $B_{\bar{D}}$ are set to be equal, so there is a single parameter for the sea distributions [37].

Similar to the averaging procedure from Sec. 3.2, the nuisance parameters representation of the experimental systematic uncertainties is used in the PDF fiting procedure:

$$\mu_i = m_i(\mathbf{p}) + r_i\sigma_i + \sum_{\alpha=1}^{N_{syst}} \Gamma_\alpha^i b_\alpha, \tag{3.23}$$

where:

- $m_i(\mathbf{p})$ is the true value of a given observable, that depends on set of parameters $\mathbf{p} = (p_1, p_2, ...)$;
- μ_i is the value observed in the experiment;
- σ_i are the statistical and systematic uncertainties;
- Γ_α^i is the sensitivity of i-th measurement to the correlated systematic source α;
- r_i are the normally distributed random variables;
- b_α are the nuisance parameters associated with the corresponding experimental systematic uncertainty.

The simple parameterization form of χ^2 defined in Eq. 3.16 can be also used. This equation can be rewritten by introducing a Poisson distribution for the statistical uncertainty:

$$\chi^2_{sum}(\mathbf{m},\mathbf{b}) = \sum_i \frac{(m_i - \mu_i - \sum_j \Gamma_i^j b_j)^2}{\delta^2_{i,stat}\mu^i m^i \prod_\alpha exp(-\gamma_\alpha^i b_\alpha)} + \sum_\alpha b_\alpha^2, \tag{3.24}$$

where $\delta^2_{i,stat}$ is the statistical uncertainty.

The effect of adding new data to the PDF evaluation procedure can be obtained using the profiling procedure [38]. It is preformed using the following representation of the χ^2 function (with both theoretical and experimental uncertainties included):

$$\chi^2(\mathbf{m}, \mathbf{b_{exp}}, \mathbf{b_{th}}) = \sum_i \frac{(m - \mu_i - \sum_\alpha \Gamma^{exp}_\alpha b_{\alpha,exp} + \sum_\beta \Gamma^{th}_\beta b_{\beta,th})^2}{\delta^2_{i,stat} \mu^i m^i \prod_\alpha exp(-\gamma^i_\alpha b_\alpha)} + \sum_\alpha b^2_{\alpha,exp} + \sum_\beta b^2_{\beta,th}, \tag{3.25}$$

where $\mathbf{b_{exp}}$ and $\mathbf{b_{th}}$ are the vectors of correlated experimental and theoretical uncertainties respectively. The sensitivity of the measurements is split into two experimental and theoretical components: Γ^{exp}_α and Γ^{th}_β. This χ^2 function is represented as a system of linear equations, that can be minimized iteratively, allowing the shifted PDF parameters to be determined. Then, the value of χ^2 at its minimum provides a compatibility of the new measurement with a given PDF set.

Part II

Experimental setup

Chapter 4

The ATLAS experiment at the LHC

To probe QCD in its high-energy regime, large machines to accelerate particles have to be built. In this section an overview of the experimental setup used to collect data for this analysis will be given. The first section introduces the Large Hadron Collider (LHC). In the second section, the ATLAS detector will be described. In the last section, the procedure of luminosity measurement is given

4.1 The LHC accelerator complex

The LHC is currently the largest accelerator in the world. It is built near Geneva, Switzerland and started its operation with the first collisions in 2009. It is located in a tunnel 27 kilometers in circumference. It can be operated with proton and lead-ion beams. It was designed to make precise studies of the Standard Model (SM) predictions and to search for new physics beyond the SM. The heavy-ion program serves a purpose of studying nuclear matter properties and quark-gluon plasma [39].

Beams are accelerated in several stages [40], as it is shown in Fig. 4.1. The beam source is hydrogen gas or lead in the case of the heavy ion runs. An electrical current is used to remove the electrons from each atom, and then the ion begins its ride through the linear accelerator. For example, proton beams are accelerated in the linear accelerator LINAC2 up to energies of 50 MeV. Then, they are injected in the PS booster, where they are further accelerated to 1.4 GeV. The last steps before injecting beams into the LHC are the rings of the Proton Synchrotron (PS) and Super Proton Synchrotron (SPC) that accelerate protons to 25 GeV and 450 GeV respectively. The bunch structure of the beam is formed in the PS, and has a nominal pattern of 39 groups of 72 bunches with 25–50 ns time spacing. Because of a large number of protons in each bunch ($\sim 1 \cdot 10^{11}$), several separate events (called pileup event) in collisions can happen.

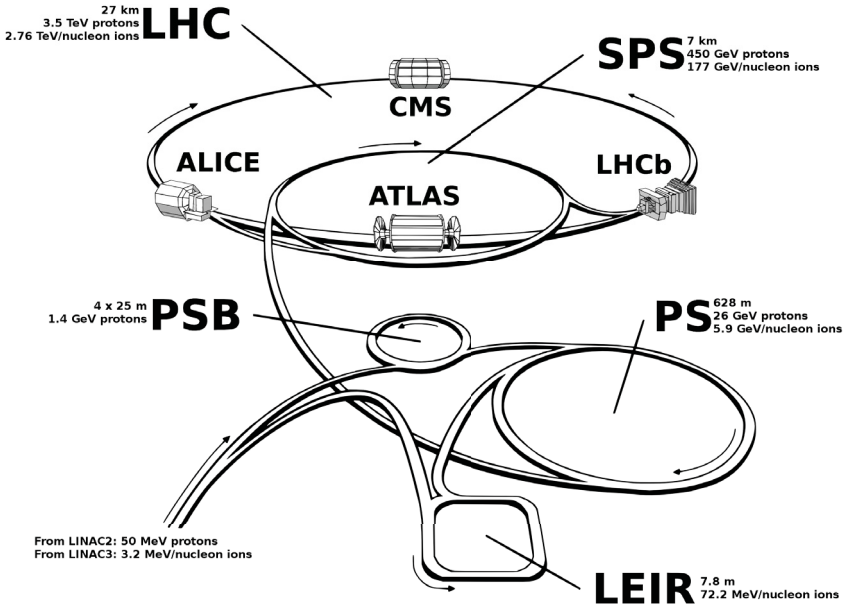

Fig. 4.1: The LHC acceleration complex [45].

In the LHC ring, proton beams are accelerated up to 7 TeV (currently 6.5 TeV achieved). The beams circulate in opposite directions inside 2 beam pipe. In order to bend the beam trajectory, the pipes are surrounded by 1232 superconducting dipole magnets. Superconducting cavities are used to accelerate the protons and maintain the beam at a constant energy during the operation time.

As with most of circular colliders, the LHC has several experiments installed in the regions, where beams are intersecting. The main experiments are:

ALICE A Large Ion Collider Experiment [41] - a dedicated detector to study heavy-ion physics, physics of strongly interacting matter, where a new phase of matter (quark-gluon plasma) is expected;

ATLAS A Toroidal LHC ApparatuS [42] is a largest particle detector at the LHC. It is a general purpose detector, that is used to study SM processes and searches for new physics. A detailed description of this detector is given in Sec. 4.2;

CMS the Compact Muon Solenoid [43] is an another multiple purpose detector at the LHC. It is built using slightly different technologies compared to ATLAS;

LHCb the Large Hadron Collider beauty [44] specializes in measurement of heavy (charm and bottom) quark properties, that allow the mechanism of CP violation to be studied.

4.2 The ATLAS experiment

The ATLAS detector is a multipurpose particle detector, designed to perform various types of analysis. The schematic representation of the ATLAS detector is shown in Fig. 4.2. The physics goals put a strict set of requirements on the ATLAS detector. Heavy particles, produced in pp

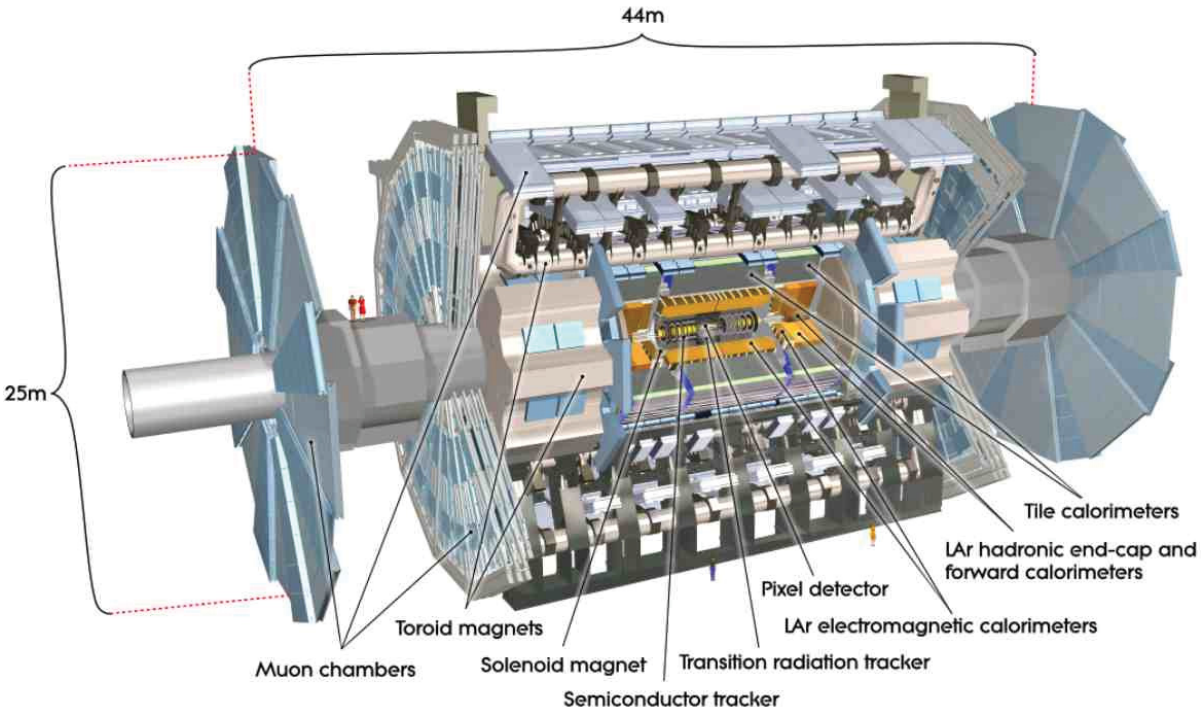

Fig. 4.2: The ATLAS detector [42].

collisions are expected to decay almost immediately. Thus their properties are measured only indirectly through their decay products, which should be precisely detected and identified. Good identification efficiency of photons, electrons and hadrons is achieved thanks to the system of calorimeters. Muons penetrate beyond the calorimeter system, so in order to detect them, muon chambers are built. Neutrinos escape the detector without interaction and therefore can be detected only indirectly through the energy imbalance in the detector.

The ATLAS detector can be divided into 3 main subdetectors:

- The Inner Detector (ID), that is used for tracking and precise measurement of charged particle momentum;
- The Calorimetry system that is used to measure the properties of electrons, photons and hadrons;
- The muon system, designed to detect muons and measure their momenta.

Due to the symmetric LHC beams, the detector is built symmetrically around the beam pipe. The magnet system is used for tracking charged particles for measurements of momentum and charge. The ATLAS detector has 2 sets of superconducting magnets: the solenoid is built around the Inner Detector and the toroid is used together with the muon spectrometer. The strength of the magnetic field varies from 0.8 T up to 3.8 T.

4.2.1 Coordinates and kinematic variables

The detector shape motivates the choice of the coordinate system. It is natural to choose the z axis to be aligned with the beam, with origin at the interaction point, while leaving the x and y

axis to be perpendicular to it. Because of detector symmetry along the beam z axis, cylindrical coordinates are often used, with the radial distance $r = \sqrt{x^2 + y^2}$ and the polar θ and azimuth ϕ angles.

The polar direction of the particles can be quantified via rapidity:

$$y = ln\sqrt{\frac{E + P_z}{E - P_z}}, \tag{4.1}$$

where E is the energy of the particle and P_z is the z component of its momentum. In the limit of the vanishing mass, this quantity converges into another commonly used variable, called pseudorapidity:

$$\eta = -ln\Big[tan\Big(\frac{\theta}{2}\Big)\Big]. \tag{4.2}$$

It is preferred over the polar angle, because the difference in rapidity is Lorentz invariant under the boost in the beam direction.

The spacial distance between two Lorentz vectors is defined as:

$$\Delta R = \sqrt{(\Delta\eta)^2 + (\Delta\phi)^2}. \tag{4.3}$$

Finally, the transverse momentum is defined as:

$$P_T = \sqrt{P_x^2 + P_y^2}, \tag{4.4}$$

where P_x and P_y are the x and y components of a particle momentum respectively. Since the incoming protons are aligned along the z-axis and have the same energy, the total transverse momentum of all particles produced in the interaction is expected to be zero.

4.2.2 Inner Detector

The Inner Detector (ID) is the tracking detector system located closest to the interaction point. It is used for reconstruction of charged particles trajectories. In order to achieve a good position resolution, it is necessary to use a high granularity detector. The layout of the ID is shown in Fig. 4.3.

The ID consists of 3 sub-detectors:

- The pixel detector consists of approximately 80.4 million readout channels placed in 3 barrel and 3 disk layers at the end of each barrel region. Each pixel module is made of silicon as an active material and a layer of front-end electronics. A charged particle, passing through the module, creates electron-hole pairs, that cause a signal in the read-out electronics. The pixel detector is placed close to the interaction point, which allows achieving 10 μm resolution for vertices;

- The silicon strip detector (SCT) consists of 6.3 million readout channels. It gives a significant contribution to the measurement of charged particle momentum, because of a large number of hits the particle produces in this detector. It works in a similar way as the pixel detector, however with the reduced tracking precision. On average, each track crosses around 8 strip layers;

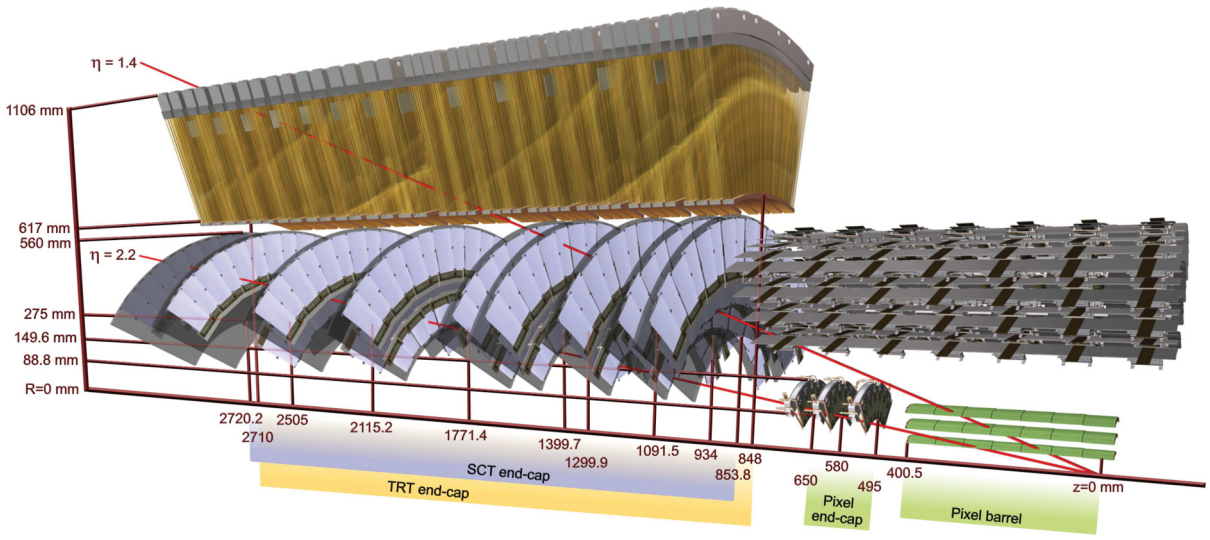

Fig. 4.3: Cut-away view of the ATLAS Inner Detector. Drawing is showing the sensors and structural elements traversed by two charged with P_T of 10GeV [46].

- The transition radiation tracker (TRT) consists of straw tubes and provides the largest number of hits ($\sim$ 36) per track. Each straw is a polyamide drift tube 4 mm in diameter.

The excellent precision of the coordinate measurements is achieved thanks to the combination of high precision measurements near the interaction point and plenty of hits at larger distances.

4.2.3 Calorimeter system

The general structure of the ATLAS calorimeter system is shown in Fig. 4.4. The calorimetric system consists of a barrel ($|\eta| < 1.7$) and two end-cap parts ($1.5 < |\eta| < 3.2$). The central part is used for the high-precision measurements, while the end-cap part with its coarser granularity is mostly used for the jet reconstruction and the E_T^{miss} measurements.

Particles, entering the calorimeter, produce a cascade of secondary particles called a particle shower. Each shower is registered by a set of small structures within the calorimeter (so-called cells). The distribution of cells energies differs for different types of particles and can be used for particle identification.

In order to measure the energy of the particle properly, calorimeters must provide good containment for showers. Since the depth of the shower, caused by the electromagnetic particle is significantly smaller than the depth of the hadronic shower, calorimeters are divided into two types: electromagnetic (EM) and hadronic. EM calorimeters are placed closer to the interaction point and have a smaller amount of the dead material, compared to the hadronic calorimeters.

In the central region, calorimeters are required to have high granularity for combination with ID information and a precision measurement of photons and electrons.

Electromagnetic calorimeter

The main purpose of the electromagnetic calorimeter is to measure energies of electrons and photons. The shower production in the EM calorimeter is mainly determined by electron-

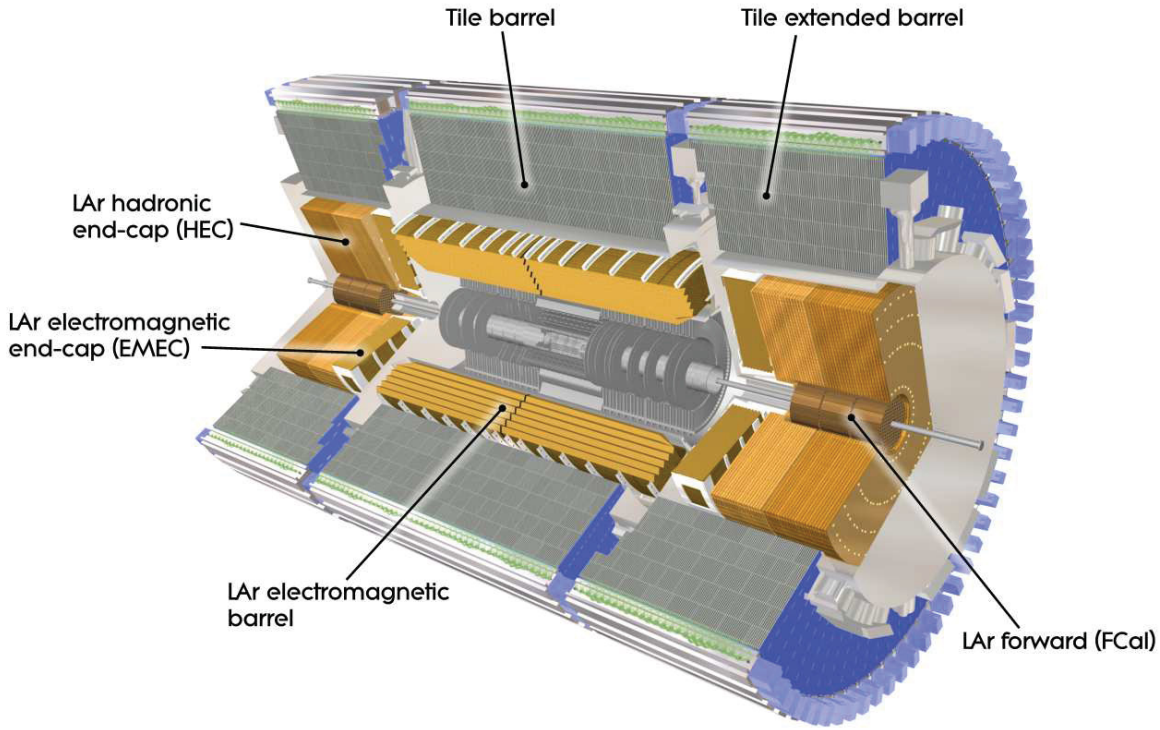

Fig. 4.4: Cut-away view of the ATLAS calorimeter system [46].

positron pairs production and photons emitted via bremsstrahlung. The EM shower starts from the initial high-energy electron or photon entering the calorimeter. The EM calorimeter consists of a barrel part (EMB) and two symmetric end-caps (EMEC), that cover a range of pseudorapidity of $|\eta| < 1.475$ and $1.5 < |\eta| < 3.2$ respectively. The EM calorimeters have an accordion structure, as shown in Fig. 4.5. This geometry allows for a full coverage in the ϕ coordinate. The calorimeters consist of layers of lead/steel, interplaced with liquid argon, that acts as a sensitive material.

The EMB calorimeter consist of four sampling layers:

- **presampler** A single layer of LAr without dead material. It allows to correct for the energy loss in front of the calorimeter. It covers the pseudorapidity range of $|\eta| < 1.8$;
- **1st sampling** The first layer has a fine segmentation in η with thin η strips with size $\Delta\eta \times \Delta\phi = 0.0031 \times 0.098$. Thanks to the fine granularity this layer provides an information for γ and π^0 separation;
- **2nd sampling** The majority of the energy is deposited in the second sampling layer. It consists of the square cells with size $\Delta\eta \times \Delta\phi = 0.0245 \times 0.0245$;
- **3rd sampling** Only the highest energy electrons are reaching the third layer. The size of the cells in this layer is $\Delta\eta \times \Delta\phi = 0.0245 \times 0.05$

All of the sampling layers, except for the presampler are shown in Fig. 4.5.

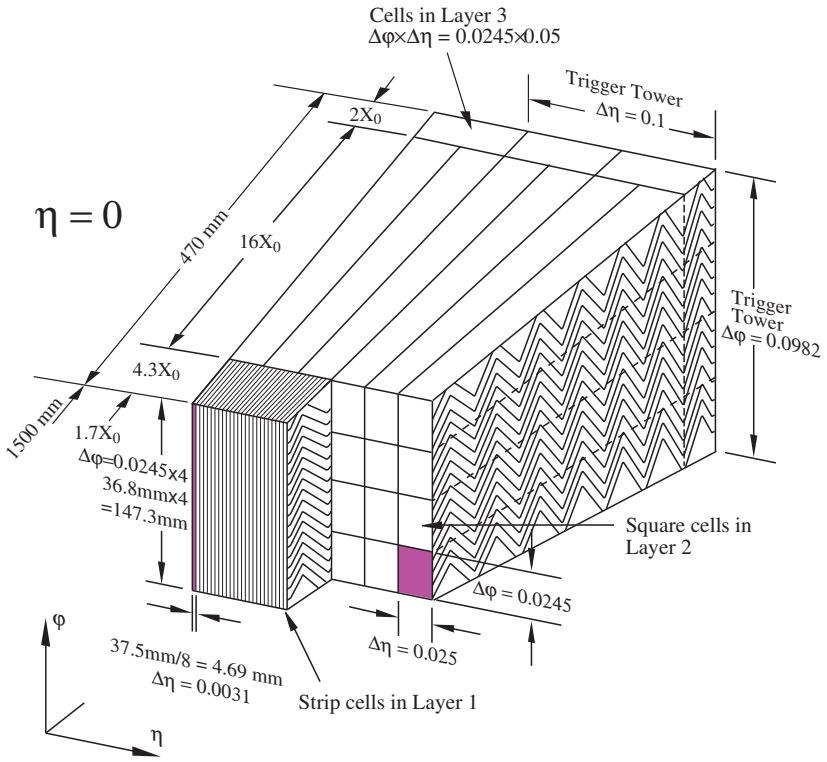

Fig. 4.5: The sketch of EMB module at $\eta \approx 0$. The granularity in η and ϕ of each of the three layers is also shown [46].

Each wheel of the EMEC calorimeter consists of 2 co-axial wheels: Inner Wheel (IW) and Outer Wheel (OW). Each endcap wheel is divided into 8 wedge-shaped modules. In the central region ($1.5 < |\eta| < 2.5$), the EMEC calorimeter consists of 3 layers with granularity $\Delta\eta \times \Delta\phi = 0.025 \times 0.025$.

Hadronic calorimeter

The mechanism of hadronic shower development differs from the relevant process in an EM shower. The main physical processes, determining the shower development are hadron production, nuclear deexcitation and pion decays. The ATLAS hadronic calorimeter consists of the central part (tile), the hadronic end-cap calorimeter (HEC) and the forward part of the hadronic calorimeter (discussed separately).

The tile calorimeter is placed right after the EMEC and covers a pseudorapidity range up to $|\eta|$=1.0 in the barrel region and $0.8 < |\eta| < 1.7$ in the two end-caps. It is a sampling calorimeter with steel acting as a dead material, and the scintillator tiles for a sensitive material. The signal readout from the scintillator is performed using wavelength shifting fibers. The readout cells are built by grouping several fibers into a single photomultiplier.

The HEC calorimeter uses a liquid argon as a sensitive material and shares the same LAr cryostat with the EMEC. The copper plates are acting as an absorbers. The size of the cell in HEC is $\Delta\eta \times \Delta\phi = 0.1 \times 0.1$ for $|\eta| < 2.5$ and $\Delta\eta \times \Delta\phi = 0.2 \times 0.2$ for forward region $2.5 < |\eta| < 3.2$.

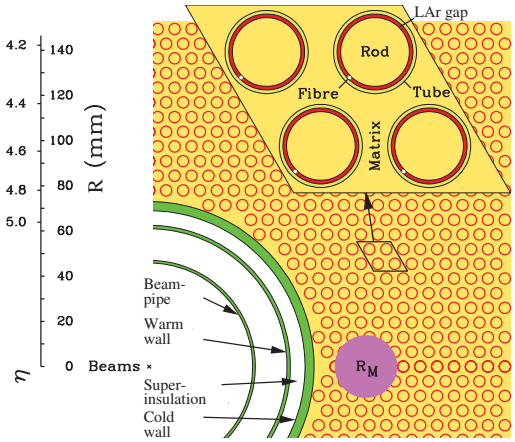

Fig. 4.6: Electrode structure of FCAL1 with the matrix of copper plates and copper tubes and rods with the LAr gap for electrodes [46].

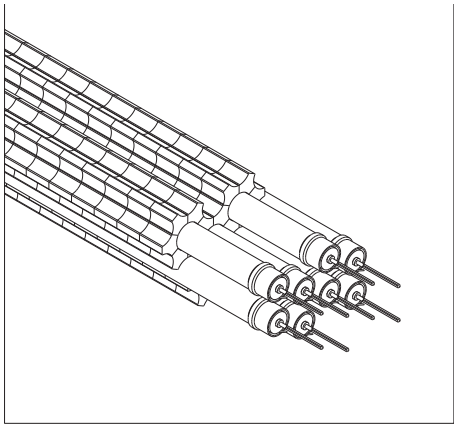

Fig. 4.7: View of the FCAL hadronic module absorber matrix, including a set of tungsten rods and copper tubes surrounded by 1 cm long tungsten slugs [46].

Table 4.1: Table of parameters for the three FCAL modules.

Module	Type	Absorber	Gap width (μm)	Number of electrodes	Number of readout channels
FCAL1	electromagnetic	copper	250	12 260	1008
FCAL2	hadronic	tungsten	375	10 200	500
FCAL2	hadronic	tungsten	500	8 224	254

Forward calorimeter

The forward calorimeter (FCAL) shares the same cryostat with the EMEC and covers the pseudorapidity range of $3.1 < |\eta| < 4.9$. It is placed 4.7 m away from the interaction point and exposed to very high particle fluxes. This motivates the choice of detector design, with a small amount of sensitive material. The FCAL module consists of co-axial copper rods and anode tubes, separated by wires around each rod. The LAr fills the gap between the rod and the anodes. The small size of the gaps produces a faster signal and helps to avoid signal degradation caused by distortion of the electric field in the gap. The structure of the FCAL calorimeter is shown in Fig. 4.6.

The FCAL is divided into 3 modules: one electromagnetic (FCAL1) and two hadronic (FCAL2 and FCAL3). Parameters of these modules are summarized in Tab. 4.1. In hadronic modules, tungsten is used instead of copper, in order to keep the large absorption length. These modules are similar to the FCAL1, except for the use of tungsten rods instead of copper rods. The space between the end-plates and tubes in FCAL2 and FCAL3 is filled with tungsten slugs, as shown in Fig. 4.7. The readout is formed from groups of four, six and nine electrodes for FCAL1, FCAL2 and FCAL3 respectively. The granularity of the FCAL is about $\Delta\eta \times \Delta\phi \approx 0.2 \times 0.2$.

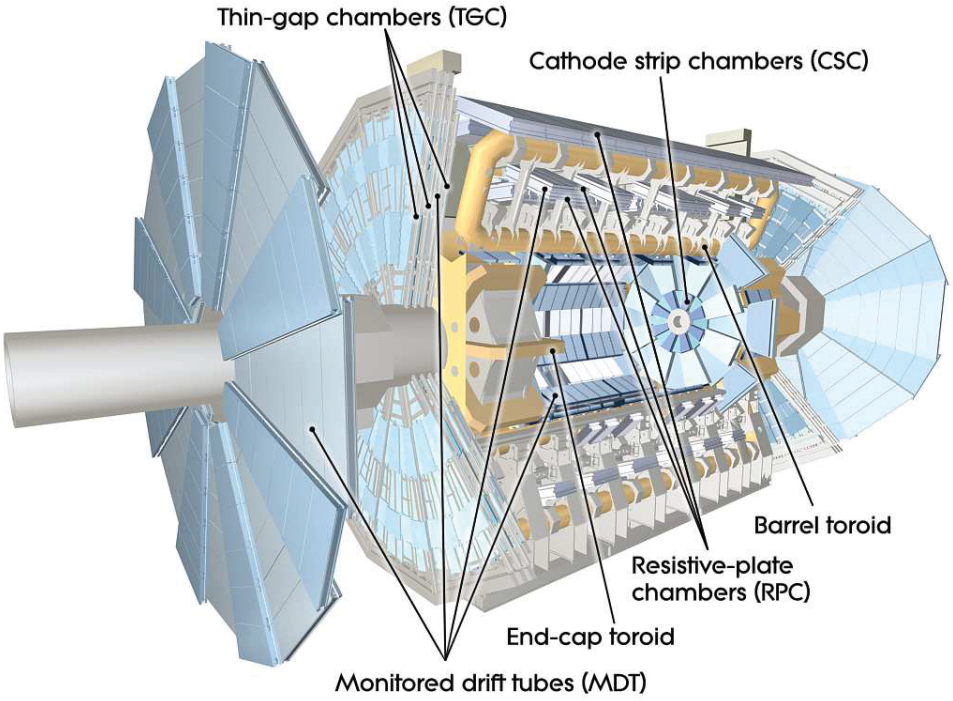

Fig. 4.8: Cut-away view of the ATLAS muon spectrometer [46].

4.2.4 Muon Spectrometer

The muon trajectories are measured in the ID, however, for a high-P_T muon, it could be difficult to make a precise determination of the charge and the momentum. The Muon Spectrometer (MS) measures more precisely the muon momentum and is also used for muon identification. The MS is placed in the outermost part of the ATLAS detector, close to the calorimeters. The cut-off view of the MS is shown in Fig. 4.8.

The Muon Spectrometer covers the area up to $|\eta| = 2.7$ and allows triggering on particles in the range $|\eta| < 2.4$. The precision muon tracking is performed by the Monitored Drift Tubes (MDT). The MDT consist of 8 layers of drift tubes and have a position resolution of 80 μm per tube (or 35 μm per chamber). In addition, in the forward region ($2.0 < |\eta| < 2.7$), Cathode-Strip Chambers (CSC) are used. The CSC are multiwire proportional chambers and give a spacial resolution of 40 μm in the bending plane and 5 mm in the transverse plane.

The trigger system in the Muon Spectrometer consists of fast Resistive Plate Chambers (RPC) and Thin Gap Chambers (TGC) which are located in the barrel ($|\eta| < 1.05$) and end-cap ($1.05 < |\eta| < 2.4$) regions respectively.

4.2.5 Trigger system

The trigger system is used for reducing the information stored while leaving "interesting" events untouched. The trigger system in ATLAS is divided into 3 steps:

Level-1 The first level trigger has a high operation speed and it uses reduced-granularity information from Resistive Plate Chambers (RPC) and Thin-Gap Chambers (TGC) and

calorimeter systems. It searches for leptonic and hadronic signatures (or large total transverse energy) in the detector. This trigger allows the rate to be reduced so that it can be handled by a readout electronics ($\sim$ 75 kHz);

Level-2 The second-level ATLAS trigger can analyze in more details Regions-of-Interest (RoI's) identified by the Level-1 trigger. It uses information on RoI's, such as energy and a position of clusters to further reduce the rate of events. The output Level-2 event rate is below 3.5 kHz;

High-Level Trigger (Event filter) The final level trigger selection is performed on a large scale computing farm. CPU cores analyze full information from detectors to refine the trigger selections. The additional information from tracking improves particle identification and can distinguish between electrons and photons. About 200 events per second are left after the HLT selection criteria and are transmitted further to the permanent storage.

4.3 Luminosity measurement

One of the main components characterizing the collider is its instantaneous luminosity $\mathcal{L}$, that is defined as a proportional factor between the cross section for a given process σ and the number of interactions per second $\frac{dR}{dt}$:

$$\frac{dR}{dt} = \mathcal{L} \times \sigma \tag{4.5}$$

At the LHC the instantaneous luminosity can be calculated as:

$$\mathcal{L} = \frac{N_p^2 N_b f_{\text{rev}}}{4\pi\sigma_x\sigma_y} F, \tag{4.6}$$

where N_p is the number of protons per beam, N_b - number of bunches, f_{rev} is the revolution frequency, σ_x and σ_y are the horizontal and vertical beam profile widths. The factor F comes from the beam crossing angle. In 2012, at $\sqrt{s}$ =8 TeV, the LHC reached an instantaneous luminosity of $7.7 \times 10^{33}\,[cm^{-2}s^{-1}]$.

Instantaneous luminosity can also be measured from the interaction rate μ_{vis} in a detector of some process as:

$$\mathcal{L} = \frac{\mu_{vis}}{\sigma_{vis}}, \tag{4.7}$$

where σ_{vis} is the visible interaction cross section and μ_{vis} is the visible in the detector interaction rate.

The ATLAS experiment uses several detectors to measure the instantaneous luminosity. The Beam Condition Monitors (BCM) are used to monitor beam parameters close to the interaction point and allows measurement of bunch intensities. In the forward region, a special detector for a luminosity measurements is placed: the LUCID (LUminosity measurement using Cerenkov Integrating Detector). The beam profile and the visible interaction cross section σ_{vis} are measured during so-called van-der-Meer scans [47].

Chapter 5

Event reconstruction

Raw detector information can not be used directly in the physics analysis. The reconstruction allows interpreting the electronic signals as parameters of physics objects. Event reconstruction is used to identify the particles, estimate their momenta and interaction vertices. In this chapter, the reconstruction and identification of the physics objects used in the ATLAS experiment is described.

Since this analysis presents the measurement of $W \to l\nu$ and $Z \to ll$ cross sections in both the electron and muon channels, the reconstruction and identification of electrons (Sec. 5.2) and muons (Sec. 5.3) are discussed in detail. The missing transverse energy (E_T^{miss}), which acts as an approximation for neutrino transverse momentum from W decays, is described in Sec. 5.4. It should be noted, that the standard E_T^{miss} reconstruction used in the ATLAS experiment was not applicable in the dataset used in the analysis and a different approach has been adapted.

5.1 Tracks and vertices

Tracks and vertices are reconstructed using the ID [48]. The reconstruction can be divided into 2 steps. On the first step, the inside-out algorithm is used based on the information from the pixel detector and SCT. Tracks are reconstructed from a set of three points called the seed and then the new hit positions are added while moving closer to the interaction point using the iterative algorithm called the Kalman filter [49].

Ambiguities in the track candidates are resolved in the final step and then the tracks are extended to the TRT position. In this step, the algorithm searches for track segments recon-

structed in the TRT and then extends them into the pixel detector and SCT. Tracks reconstructed in the TRT with no extension are referred to as TRT-standalone tracks.

Interaction vertices are reconstructed using the iterative vertex finding algorithm. The vertex finding starts from the z-position at the beam axis of a random track. The fit,d based on χ^2 minimisation, is performed on the initial track and nearby tracks. Tracks, that are displaced by more than 7σ from the vertex are used to form a separate vertex. The procedure is repeated until no new vertices are found. The vertices are required to contain at least two tracks. The vertex with the highest sum of outgoing track momenta is defined as the *primary vertex*.

5.2 Electron reconstruction and identification

The reconstructed electrons can be divided into two groups: central and forward. In the case of the central electrons ($|\eta| < 2.5$) there is ID tracking information available, which allows more precise reconstruction and identification. The forward electrons ($2.5 < |\eta| < 4.9$) are reconstructed using only the calorimeter information and a different electron reconstruction algorithm is used. In this section, the identification criteria of the central electrons and the reconstruction for both central and forward electrons, are discussed.

5.2.1 Central electrons reconstruction

Reconstruction of central electrons start from the EM cluster information. EM calorimeter clusters are formed from cells with size $\Delta\eta \times \Delta\phi = 0.25 \times 0.25$, with a total transverse energy in all calorimeter layers above 2.5 GeV, using the sliding window algorithm [50]. The position of the cluster is determined from the barycenter of the cluster.

In the second step, tracks with $P_T > 0.5$ GeV are extrapolated to the middle layer of the EM calorimeter. A track is considered matched with a cluster if the distance track impact point and cluster position is within $|\Delta\eta| < 0.05$. In order to take into account the effect of bremsstrahlung losses, the azimuthal distance between track and cluster position is required to be $\Delta\phi < 0.1$.

An electron is considered to be reconstructed if at least 1 track is matched to a given EM cluster. In case there are several tracks passing this requirement, the track with the smallest distance $\Delta R = \sqrt{\Delta\eta^2 + \Delta\phi^2}$ is selected as the match. In case there is no track matched, the EM cluster is treated as a photon candidate.

After track-matching the cluster size is enlarged. The total reconstructed electron energy is determined from the corrected cluster energy, energy deposits in the material in front of EM calorimeter and energy deposits outside of the cluster and calorimeter. The relevant energy scale determination is described in Sec. 10.2. The direction of the electron is determined from the corresponding track parameters.

5.2.2 Forward electrons reconstruction

Since there is no tracking information in the forward region ($2.5 < |\eta| < 4.9$), the electrons can be reconstructed using the information from EMEC and FCAL. Forward electron reconstruction uses the topological clustering algorithm [50] with a variable cell size. In this algorithm, cells with energy higher than the expected noise are merged together iteratively. The average noise in the cell is obtained in dedicated (calibration) runs. The cluster building procedure starts from the cell having a significantly large energy and then expands by neighborhood cells. If two clusters are sharing one neighboring cell, they are merged into a single cluster.

The energy of the electron is defined as the sum of the cell energies, taking into account the energy losses in the passive material in front of the calorimeter. The direction of a forward electron is defined from the barycentre of the associated cluster.

5.2.3 Electron identification

The application of additional selection criteria to reconstructed electrons allows rejection of objects, which can be misidentified as electrons, such as jets and photons.

The identification of central electrons is based on sequential selection criteria based on calorimeter and tracking information. There are three sets of electron identification criteria, used for physics analyses [51]. They are ordered by the increasing background rejection at the cost of decreasing identification efficiency:

Loose The loose identification criteria uses the shower shape variables in the first and the second layer of EM calorimeter and the fraction of cluster energy, deposited in the hadronic calorimeter. There are also additional requirements on electron track and track-cluster matching;

Medium The medium selection is based on loose identification incorporating additional information from the 3-rd layer of EM calorimeter, transverse impact parameter of the electron candidate and TRT information. Additionally, a hit in the innermost layer of the pixel detector is required to discriminate against the photon conversions.

Tight In addition to medium criteria, this selection puts stricter requirements on electron track quality, on the ratio of EM cluster energy to electron track momentum, and on the reconstructed photon conversion vertices associated with the cluster.

It should be noted that none of the electron identification criteria requires the presence of additional tracks near the identified electrons. The definition of these requirements (called isolation requirements) is specific to a given analysis.

5.3 Muon reconstruction and identification

To reconstruct muons in ATLAS the information from ID and MS is used. Energy measurements in the calorimeter can also be used for muon identification. The muons, based on the information, available for reconstruction, can be divided into different types:

Combined (CB) Muons with a track both in the ID and MS, that could be matched to each other.

Segment-tagged (ST) Muons with a track in the ID and at least one local track segment in the MDT or CSC chambers.

Stand-Alone (SA) These are the muons that are crossing at least 2 layers of MS chambers but have no reconstructed track in the ID. The parameters of the track are determined using the extrapolation to the primary vertex, taking into account the estimated energy loss in the detector in front of the MS.

Calorimeter-tagged (CaloTag) Muons, that have a track in the calorimeter, that can be associated with the minimum ionizing particle.

The ID track, used in the muon reconstruction, should satisfy additional requirements:

- at least 1 pixel hit;
- at least 2 SCT hits;
- at most 2 active pixel or SCT hits, that are traversed by the track, but have no hit;
- in the region of full TRT acceptance ($0.1 < |\eta| < 1.9$) at least 9 TRT hits.

The muons are reconstructed in MS in two steps: first, the local segments within one layer are combined and then the segments are combined in a full track. The reconstruction of the MS and combined ID-MS track can be done using one of the two independent reconstruction procedures, called Staco and Muid [52].

The Muid algorithm performs full track refit using the parameters from the ID and MS [53]. For the Staco algorithm, the reconstruction of the track in the MS starts from the segment from the outer station. The segments from the middle and inner layers are iteratively added until the full track is obtained. The matching between the ID and MS sub-detectors is performed via the statistical combination of the parameters in ID and MS using the corresponding covariance matrices [54].

5.4 Missing transverse energy reconstruction

The large angle coverage of the ATLAS detector allows calculation of the total energy imbalance inside the calorimeter. In this section, two methods of E_T^{miss} reconstruction and the reasons for use of non-standard method are discussed.

5.4.1 Standard reconstruction

Standard reconstruction of E_T^{miss} in the ATLAS experiment [55] uses contributions from the transverse energy deposits in the calorimeter ($E_{x(y)}^{miss,calo}$), measured muons ($E_{x(y)}^{miss,muon}$) and correction for the energy loss in the cryostat ($E_{x(y)}^{miss,cryo}$) as:

$$E_{x(y)}^{miss} = E_{x(y)}^{miss,calo} + E_{x(y)}^{miss,muon} + E_{x(y)}^{miss,cryo}. \tag{5.1}$$

The calorimeter-related $E_{x(y)}^{miss,calo}$ term is computed as follows:

$$E_{x(y)}^{miss,calo} = E_{x(y)}^{miss,e} + E_{x(y)}^{miss,\gamma} + E_{x(y)}^{miss,\tau} + E_{x(y)}^{miss,jets} + E_{x(y)}^{miss,SoftTerm} + E_{x(y)}^{miss,calo,\mu}, \tag{5.2}$$

where each term is calculated from the negative sum of calibrated cell energies inside the corresponding objects. Each jet with energy P_T>20 GeV is corrected for pile-up and a jet energy scale is applied. The soft $E_{x(y)}^{miss,SoftTerm}$ term is calculated from clusters and tracks, that are not associated with physics objects. The muon $E_{x(y)}^{miss,calo,\mu}$ term is the contribution to calorimeter part of E_T^{miss} from the muons energy loss in the calorimeter. Since pile-up has a significant effect on E_T^{miss}, several methods of pile-up suppression are used [56].

The $E_{x(y)}^{miss,cryo}$ term accounts for the energy lost in the cryostat between the LAr barrel electromagnetic calorimeter and the TileCal barrel hadronic calorimeter, which at the thickness

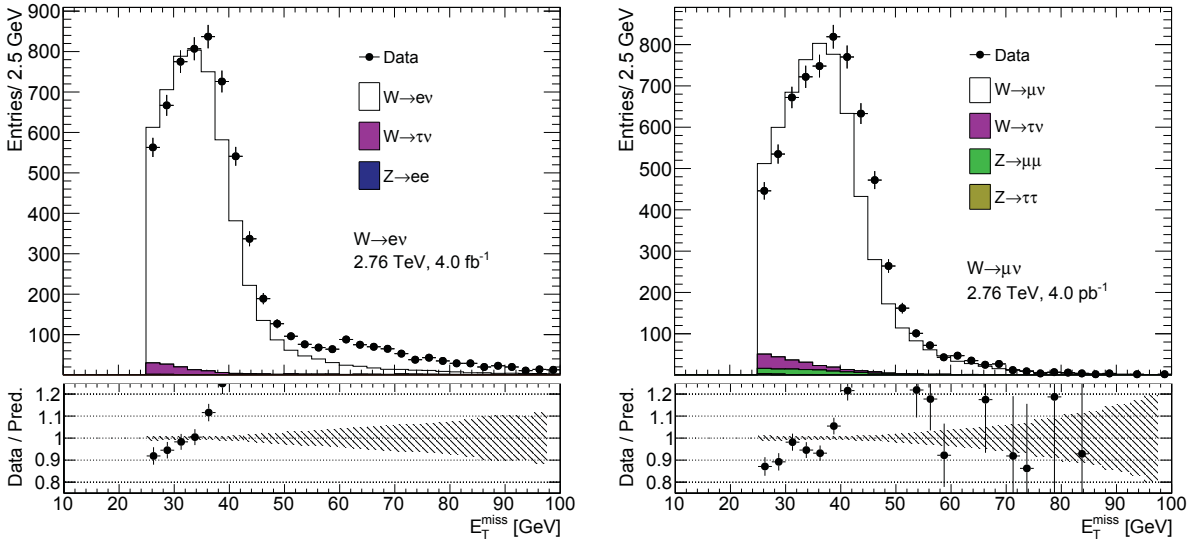

a) b)

Fig. 5.1: Missing transverse energy distribution for a) the $W \to e\nu$ selection and b) the $W \to \mu\nu$ selection (described in Chap. 9). E_T^{miss} is calculated using the standard ATLAS algorithm. The expected contributions from all backgrounds are estimated with Monte Carlo simulations, except for multijet background that is not included. All Monte Carlo corrections from Chap. 10 are applied. There are visible discrepancies between data and MC, that cannot be explained by the contribution of the multijet background, which is expected to contribute mostly in the low E_T^{miss} region (see Sec. 12.1).

of about half an interaction length can lead to significant energy losses in the shower. The $E_{x(y)}^{miss,muon}$ term in case of isolated muons is combined from the inner detector and MS and the $E^{miss,calo,\mu}$ is not added into the calorimetric term. For nonisolated muons measurement from MS is used and the parametrised energy loss in the calorimeter is subtracted. Outside the fiducial volume of ID the MS measurement is used alone.

The data used in the analysis are characterized by low pile-up (Chap. 8), so the usage of a standard ATLAS procedure (optimized for high pile-up 8 TeV runs) is not optimal. It was observed, that there are big discrepancies between the E_T^{miss} distributions for data and MC simulation, as shown in Fig. 5.1, where the missing transverse energy distribution for data is compared to signal and background MC predictions.

The differences are visible in both the electron and muon channels and cannot be explained by the contribution from the missing multijet background, which is expected mainly in the low E_T^{miss} region (see Sec. 12.1 for more details).

5.4.2 Hadronic recoil

An alternative method to calculate E_T^{miss} was developed in [57]. This procedure is based on a requirement of a balance in the transverse momentum of a W-boson and the initial (quark-gluon) state radiation:

$$\vec{P}_T^W = \vec{P}_T^l + \vec{P}_T^\nu = \sum \vec{P}_T^{ISRquarks,gluon} = \vec{HR}, \tag{5.3}$$

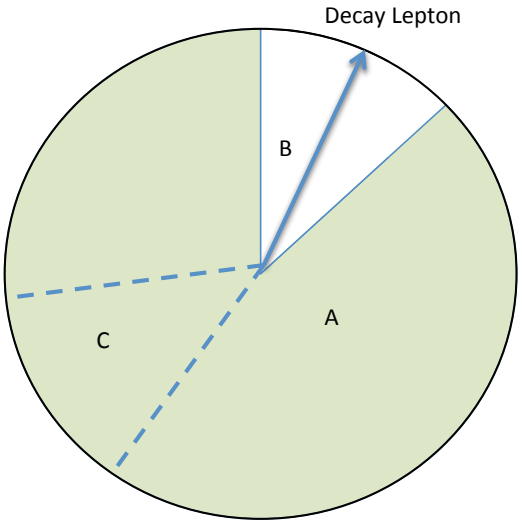

Fig. 5.2: Definition of different zones in the calculation of the cluster-based hadronic recoil. Zone B is excluded from hadronic recoil calculation because it contains decay lepton. To describe properly the overall activity it is replaced by the zone C, rotated in the direction of B. Zone A corresponds to the rest of the calorimeter [58].

where $\sum \vec{P}_T^{ISRquarks,gluon}$ is the transverse momentum of partons from the initial state radiation, also called hadronic recoil (HR) and $\vec{P}_T^{l}$, $\vec{P}_T^{\nu}$ are the transverse momenta of leptons and neutrinos respectively. Therefore, E_T^{miss} can be determined using the relation:

$$\vec{E}_T^{miss} = -\vec{P}_T^{\nu} = -\vec{HR} + \vec{P}_T^{l}. \tag{5.4}$$

This procedure assumes, that recoil arises from one single leading jet, and the rest is coming from soft hadronic activity. The hadronic recoil is computed as a vector sum of calorimeter clusters:

$$\vec{HR} = \sum_{i=0}^{N_{topo}} \vec{P}_T^{topo}, \tag{5.5}$$

while a scalar sum of cluster energies in the transverse plane corresponds to the hadronic activity in the event:

$$\sum E_T = \sum_{i=0}^{N_{topo}} E_T^{topo}. \tag{5.6}$$

To avoid double counting due to lepton energy loses in the calorimeter, the clusters energy inside a cone with a radius of dR = 0.2 around the lepton direction are excluded from the calculation. To compensate for the subtracted soft activity from a cone, a replacement cone is added (Fig. 5.2). This cone is defined as a cone at the same pseudorapidity but at a different ϕ and away from any other lepton and hadronic recoil direction. The cone is then rotated to the original lepton direction.

Fig. 5.3 shows the control plots for the distributions of missing transverse energy calculated

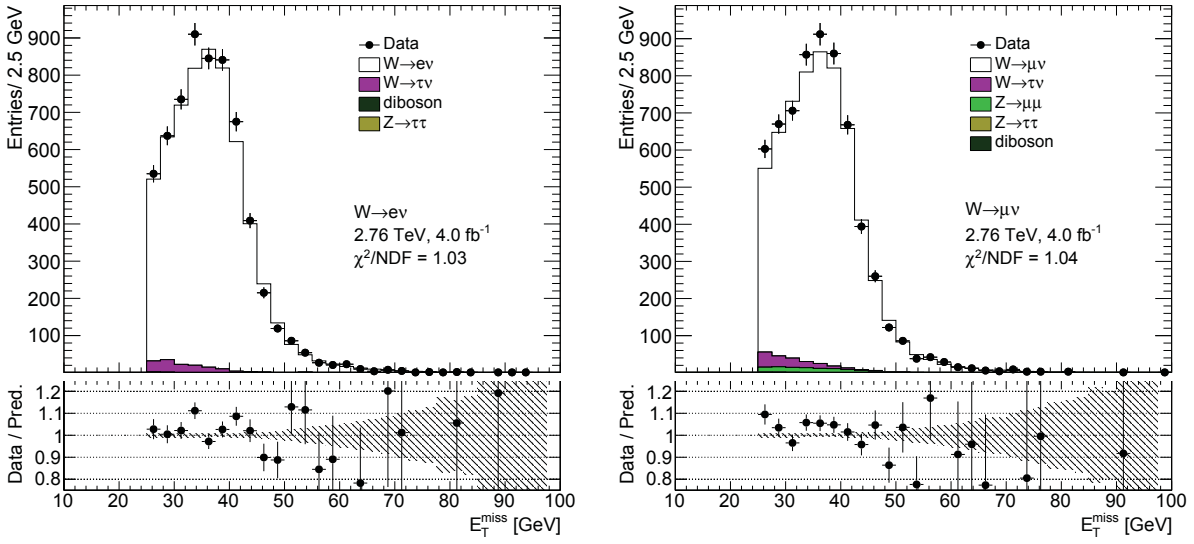

a) b)

Fig. 5.3: Missing transverse energy distribution for a) the $W \to e\nu$ selection and b) the $W \to \mu\nu$ selection (described in Chap. 9). E_T^{miss} calculated using the hadronic recoil algorithm. The expected contributions from all backgrounds are estimated with Monte Carlo simulations, except for multijet background that is not included. All Monte Carlo corrections from Chap. 10 are applied.

using the hadronic recoil procedure. In both the electron and muon channels the agreement between data and MC simulation is much better than in the case of the standard procedure (Fig. 5.1). Therefore it is decided to use hadronic recoil E_T^{miss} reconstruction method for the data sample used in the analysis.

Chapter 6

Monte Carlo simulation

The Monte Carlo (MC) method was invented by scientists working on the atomic bomb in the 1940s. Its core idea is to use random samples of parameters or inputs to explore the behavior of a complex system or process. Nowadays, MC simulation is the essential part of research in both theoretical and experimental particle physics. This chapter gives an overview of the ATLAS experiment simulation scheme, the simulation methods and the simulation software. Moreover, techniques for fast simulation are discussed.

6.1 Monte Carlo production in ATLAS

Monte Carlo method allows different types of analyses to be performed , such as generation of predictions for comparisons with data, to study the detector or the selection algorithms performance. The ATLAS simulation software is integrated into the Athena framework used at the ATLAS experiment [59]. The simulation chain is can be divided into four main steps (Fig. 6.1):

Event generation Simulation of hard interaction, parton evolution and hadronization. This step is independent of the ATLAS detector geometry;

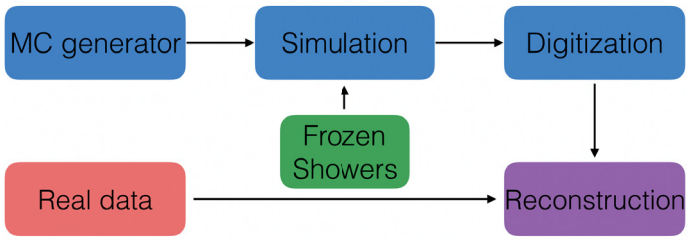

Fig. 6.1: Diagram of the ATLAS MC simulation chain.

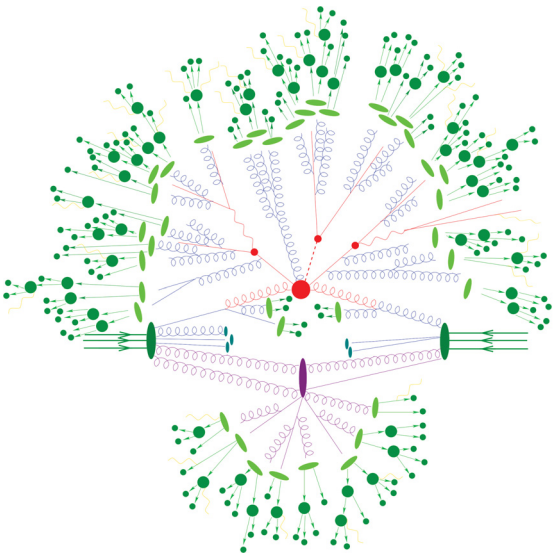

Fig. 6.2: Schematic view of top quark pair production associated with a Higgs boson event produced in a pp collision: the hard scattering is shown as a red blob with the solid and dashed lines as the resulting three particles. Multi-particle interactions are indicated by the violet blob. Parton showers are shown with curly lines. Hadronization is shown in light green, while the final state particles as dark green [60].

Detector simulation Simulation of energy deposits ("hits") which are produced by final state particles;

Digitalization Simulation of detector electronics response. This procedure can be divided into two steps: first the inputs to the read out drivers (ROD's) are simulated, in the second step the ROD functionality is emulated. Detector noise effects are also simulated in the second step;

Reconstruction Production of the Analysis Object Data (AOD) files, which contain the information needed for physics analysis. This stage is identical for both data and MC and discussed in details in Chap. 5.

Additionally, the pile-up effects are added to MC by overlaying the simulation of the hard interaction with the simulation of additional soft inelastic interactions. In the following sections, event generation and simulation will be described in more detail.

6.2 Event generation

The main goal of the event generator is to provide a complete picture of the final state: description of the particle types and momenta on an event-by-event basis. According to the factorization theorem [61], the event generation can be divided into four independent stages:

Modeling of hard subprocess The process of interest is simulated from its production channels using the corresponding matrix elements (ME) at a fixed order of the strong coupling constant. The momenta of the incoming protons in the matrix elements are ran-

domly chosen based on the parton distribution functions (PDF). Most of the generators make simulation at leading (LO) order or next to leading order (NLO) in α_s;

Parton showering Quarks and gluons from hard processes can radiate secondary partons, resulting in the production of additional hadrons in the event. This process is calculated as a step-by-step evolution of momentum transfer scales from highest (hard subprocess), to the lowest (around 1 GeV), where the perturbative calculations are not valid. There is a possible double counting between showering and hard process simulation which can be avoided by using different matching approaches.

Hadronization Final-state hadrons, which can be detected in an experiment, are formed during hadronization step. This process occurs at large scales, where perturbative calculations are not applicable and usually implemented using different phenomenological models [62];

underlying event In parallel to the main process, collisions of other partons can also occur. This effect is called underlying event.

The scheme of simulation of a top quark pair production associated with a Higgs boson event is shown in Fig. 6.2:

The current analysis uses samples generated with the following generators:

Powheg [63] is a Monte Carlo generator, which calculates the QCD process at the NLO level [64]. It can be interfaced to other generators (such as Pythia or Herwig) to get showering;

Pythia [65] is a general purpose generator for simulating hadron-hadron, hadron-lepton and lepton-lepton collisions. It can model initial and final state showers, hadronization, hadron decays and underlying event. Pythia contains around 240 QCD processes at LO. It uses the Lund String model [66] to simulate hadronization;

Herwig [67] is an LO general purpose event generator for simulation of lepton-lepton, hadron-lepton and hadron-hadron collisions. The main difference between Pythia and Herwig is that Herwig uses angular ordering in the parton showers [68] and models the hadronization using the cluster fragmentation [69];

Sherpa [70] is an event generator, that uses LO QCD predictions for a hard scattering and features its own implementation of parton shower and hadronization models;

Photos [71] is a program used to generate QED radiative corrections, that is additionally linked to multipurpose generators;

Tauola [72] is a generator, used to describe leptonic and semi-leptonic τ-decays, that is additionally linked to multipurpose generators.

6.3 Detector simulation

After the event generation step, a dedicated simulation software is used to provide detector response for final state particles. The main method used by ATLAS experiment, referred to as a *Full Simulation*, uses of the Geant4 [73] libraries. Geant4 is a C++ based toolkit for the simulation of the passage of particles through the matter. It is used in a wide range of experiments in the high energy and nuclear physics.

Geant4 can simulate complex detector structures with sensitive detector material and corresponding infrastructure. It can also calculate basic properties of composite materials, like radiation and interaction length. Geant4 stores "hits" information - snapshots of physical interactions. In Geant4, events and particles are simulated separately and each particle is moved in steps. The size of each step is chosen to preserve both CPU performance and required precision.

Interactions of particles with the detector are treated as a set of discrete processes. The Geant4 package provides different models for hadronic and electromagnetic interaction processes. It allows a set of the models (called physics list) depending on particular requirements to be chosen. There are several reference physics lists that are validated for each new release of Geant4 software. The ATLAS experiment uses one of these lists.

The simulation of detector response is the most CPU-time consuming part of the ATLAS simulation chain. Most of the CERN computing resources are used by a mass MC production, required for each data taking period. Uncertainties of some of the Run-I analyses are dominated by available MC statistics. It is possible to improve the CPU usage by tuning physics list or replacing complex magnetic field maps by a parameterization. Additionally, there are long-term developments for multi-threading and vectorization of the code. The fast and accurate simulation approach is essential. During the simulation the largest time is spent on simulation of calorimeters. This is motivation for the development of fast calorimetry simulation techniques.

There are two main methods currently used by ATLAS to reduce the time needed for the simulation of the calorimeter response [74]:

- Parameterization of the calorimeter cells response. The spacial energy response is simulated using longitudinal and lateral energy profiles;
- Frozen Showers. This technique is described in Chap. 7.

Chapter 7

Frozen Showers

Fast simulation techniques are an essential part of the Monte Carlo production in the ATLAS experiment. The typical time needed for simulating a top pair production event is around one minute. Most of this time is spent on the simulation of particle interaction in the calorimeters. This motivates the development of fast simulation techniques, allowing to describe calorimeter response.

In this chapter, a Frozen Showers method for the forward calorimeter simulation is described. The first section gives a small introduction to the method. In the second section properties of the electron shower in the FCAL are presented. In Sec. 7.3 the usage of this method is explained. Sec. 7.4 introduces a new procedure for finding initial parameters. Finally, in the last section, the validation of Frozen Showers accuracy is presented.

7.1 Introduction

Frozen Showers is currently the main fast calorimeter simulation algorithm used in the ATLAS experiment [75]. It is based on pre-simulated showers, used later in the simulation. This method allows reducing the time spent on a simulation of low energy sub showers of the main shower. It gives in comparison to the full simulation a 25% speedup. The method requires pre-generated libraries of showers for each detector and particle used.

For each pre-generated shower, its lateral and transverse size and a list of all energy depositions inside the sensitive material (hits) with information about their energy, position and time are stored. If the energy of a secondary electron in the simulation falls below the cut-off

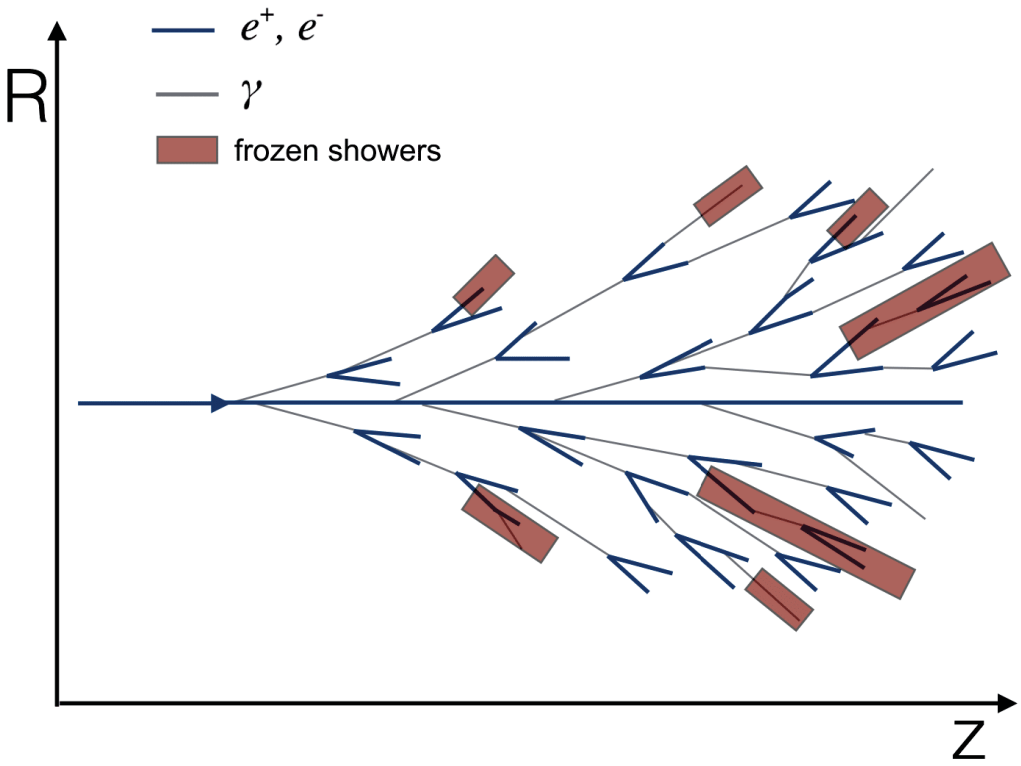

Fig. 7.1: Shower substitution of the low-energy electron, during the high energy electron simulation. Some of the showers from particles, substituted by Frozen Showers method marked by brown squares.

Table 7.1: Main parameters used for the frozen shower libraries. The FCAL1 and FCAL2 are the first two froward calorimeters (see Sec. 4.2.3) and E_γ, E_e, T_n are the maximum energies of photons, electrons and neutrons used in the method.

The general Frozen Showers parameters	
Detectors used	FCAL1, FCAL2
Type of the particle	photons, electrons, neutrons
Energy cut-off	$E_\gamma < 10$ MeV, $E_e < 1000$ MeV, $E_n < 100$ MeV

energy, it is replaced by a shower from a library, as presented in Fig. 7.1. The parameters used in the Frozen Showers method are summarized in Tab. 7.1.

7.2 Properties of electron showers in FCAL

The fast simulation of the ATLAS forward calorimeters is a complicated task, due to the complex structure. As it is mentioned in Sec. 4.2.3 FCAL consists of hexagonal absorber cells with the anode tube and cathode rod in the cell center and the liquid argon in the gap between the rod and tube. An efficient fast simulation technique should take into account this significant amount of non-uniformly distributed sensitive material to simulate electron resolution correctly.

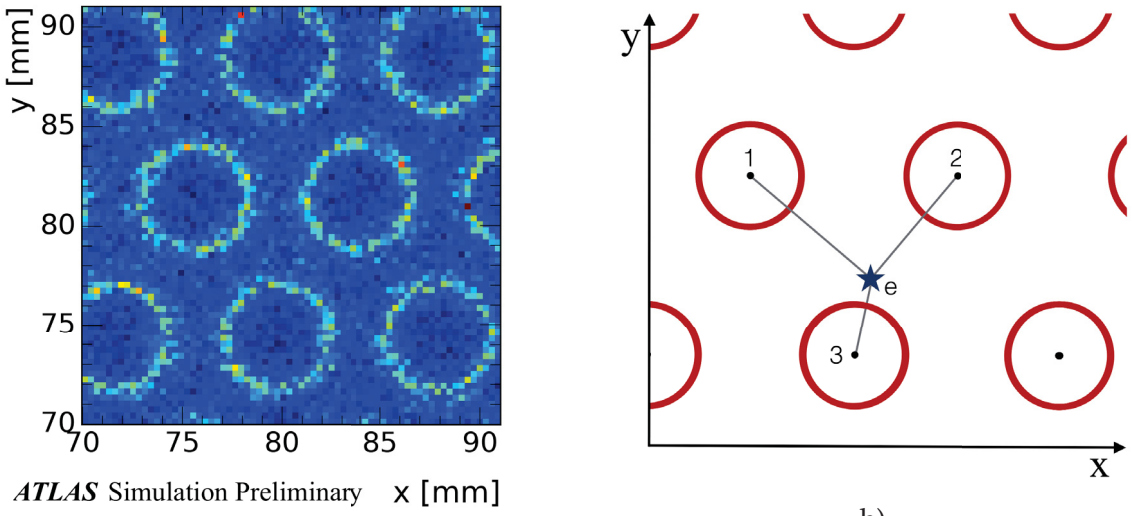

a) b)

Fig. 7.2: a) Electron shower energy response in the transverse FCAL plane. Light circles correspond to showers, developing inside the LAr gaps with on average higher energy response, while dark parts correspond to dead material with a smaller sum of the "hits" energy. b) Distance to the closest rod center scheme. The rod centers and liquid argon gaps are shown by black dots and red circles respectively.

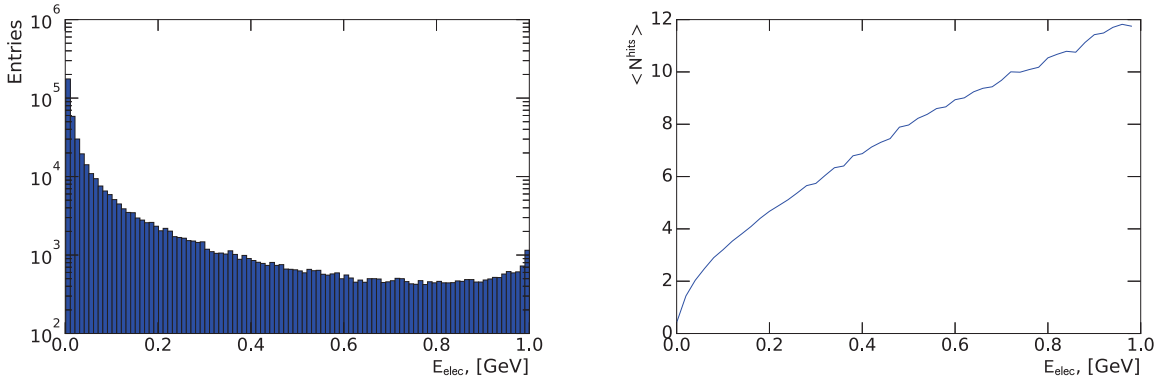

a) b)

Fig. 7.3: Distribution of the a) electron energies and b) a mean number of hits in the shower vs electron energy for electrons used in the generation of 1 TeV electron.

The electron energy resolution of a calorimeter can be written as [76]:

$$\frac{\sigma}{E} \approx \frac{a}{\sqrt{E}} \oplus \frac{b}{E} \oplus const, \tag{7.1}$$

where $\oplus$ indicates the quadratic sum. The first term is the 'stochastic term', which includes intrinsic shower fluctuations, the second one takes into account readout noise effects and pile-up fluctuations. The *const* term is connected to non-uniformities in the detector, causing significant fluctuations of the energy loss. The constant term dominates the typical energy resolution for high energy electrons.

Fluctuations due to the detector design can be observed in the simulation of low-energy electrons. The shower energy (E^{shower}) distribution in the transverse FCAL plane is shown in Fig. 7.2 (a). The shower energy is defined as:

$$E^{shower} = \sum E_i^{hits}, \tag{7.2}$$

where E_i^{hits} is the energy of the i-th hit in the shower inside the sensitive detector material. The periodic structure resembles the calorimeter design, where the light circles correspond to gaps in the liquid argon sensitive material. The distance to the closest rod center for the initial electron is calculated as (Fig. 7.2):

$$d_{rod} = min(d(1,e), d(2,e), d(3,e)), \tag{7.3}$$

where 1,2,3 are the positions of the rod centers and e is the position of the initial electron.

Most of the electrons, substituted by the Frozen Showers algorithm have a low energy (Fig. 7.3 a). The mean number of deposits in the sensitive material for the shower from the Frozen Showers algorithm is around 5 and this value rises with the electron energy (Fig. 7.3 b). Fig. 7.4 presents the distribution of the distance to the closest rod center and shower energies for Frozen Showers used in the simulation of 1 TeV electrons. There is a visible peak of shower energy for the region around liquid argon gap, marked by the red lines. A similar structure is also visible in a number of depositions in the sensitive material (Fig. 7.5 a) and the standard deviation of the hits energies in the shower (Fig. 7.5 b) distributions. The magnitude of the peak depending on the electron energy and is higher for the low energies (Fig. 7.6 a) and less significant for higher energies (Fig. 7.6 b). The proper simulation method should be able to reproduce these distributions in the simulation.

It should be noted, that this method is not used in the full electron energy range. For the high energy electrons, this method gives no significant speedup compared to the full simulation. The usage of the Frozen Showers in the low electron energy region can be suboptimal, due to limited energy depositions in the sensitive material. Most of the electrons with energy below 3 MeV have no hits in the sensitive material (Fig. 7.7 a) and only 0.5% produce more than one hit (Fig. 7.7 b). The studies of the Frozen Showers algorithm performance have shown, that introduction of the 3 MeV lower threshold for the algorithm allows to reduce time spent on the simulation of the high-energy electrons. The electrons with energy below 3 MeV are substituted with single hit in the detector.

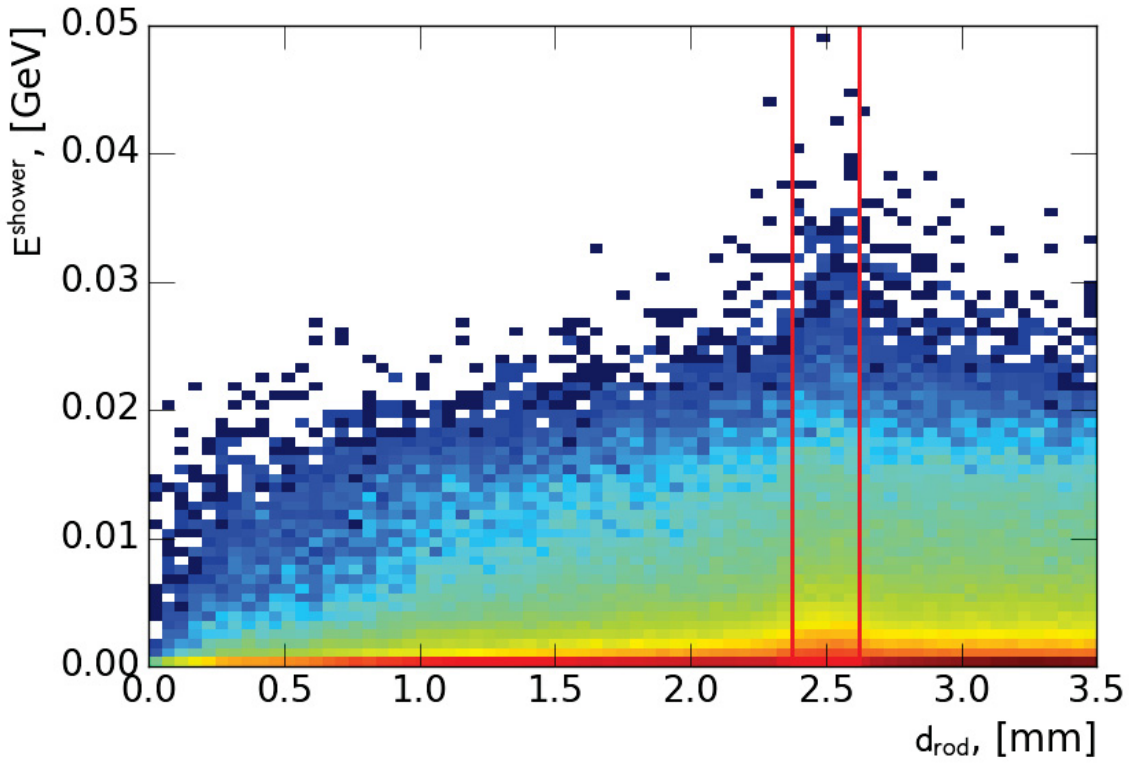

Fig. 7.4: Distribution of distance to the closest rod center vs shower energy for electron showers created by electrons used in the generation of 1 TeV electron in the distance to the closest rod center vs shower energy plane. Red lines note the position of the liquid argon gap.

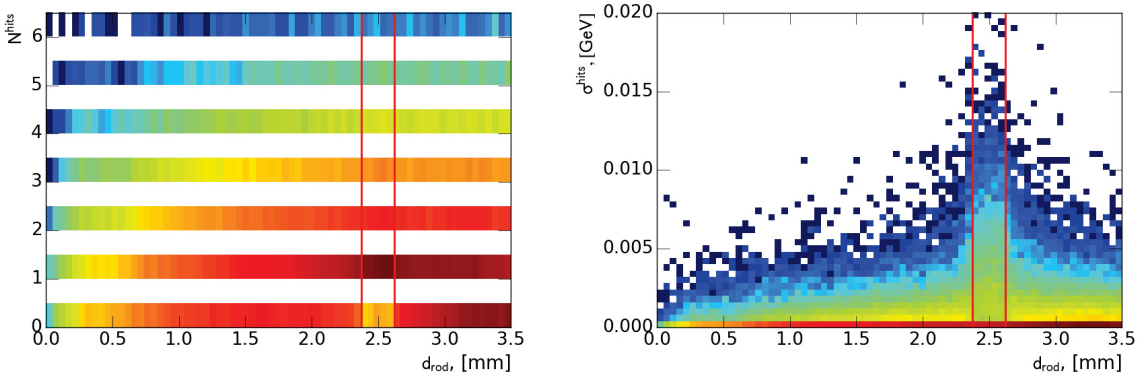

a) b)

Fig. 7.5: Distribution of distance to the closest rod center vs a) number of hits in a shower plane and b) standard deviation of hits energy in a shower from electrons used in the generation of 1 TeV electron. Red lines note the position of the liquid argon gap.

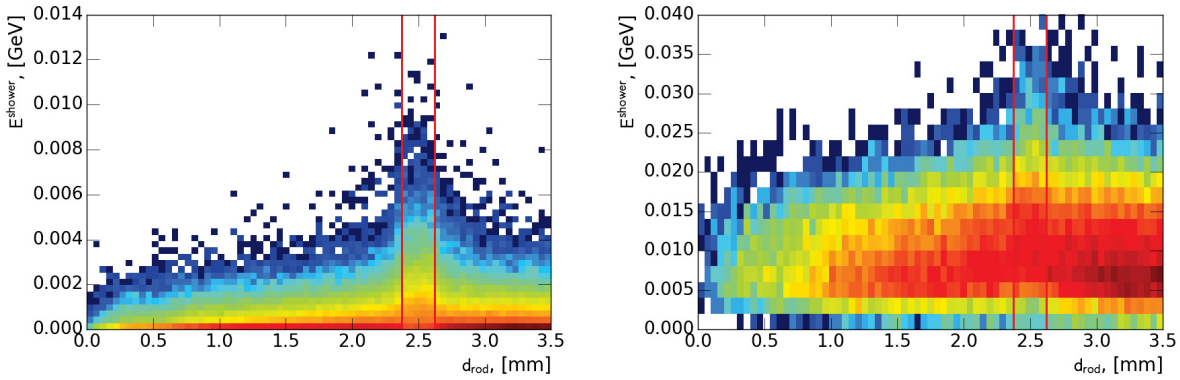

a) b)

Fig. 7.6: Distribution of distance to the closest rod center vs shower energy for electron showers created by electrons with energy a) less than 100 MeV and b) higher than 300 GeV coming from the initial electron with energy 1 TeV. Red lines note the position of the liquid argon gap.

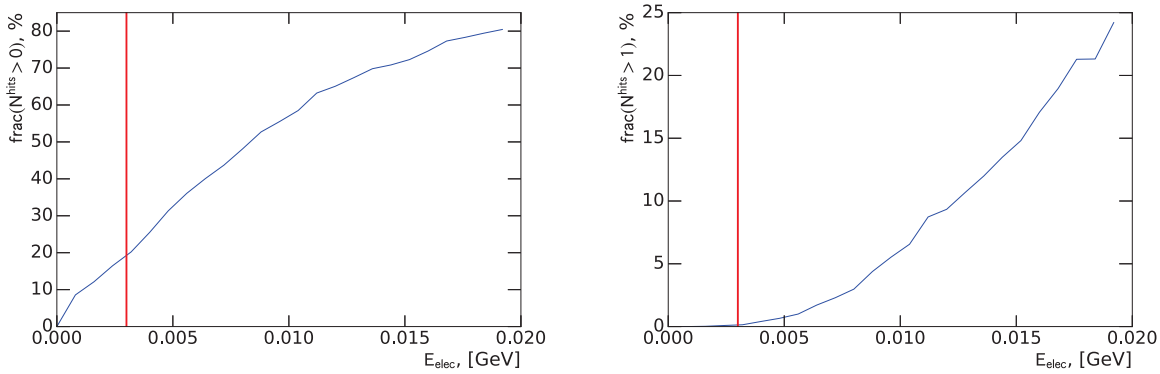

a) b)

Fig. 7.7: The fraction of showers with a) at least 1 b) at least two depositions inside the sensitive material as a function of the initial electron energy. The red line denotes the 3 MeV lower limit applied in the Frozen Showers method.

7.3 Generation and use in simulation

The Frozen Showers method consists of two stages: generation of libraries and the use in simulation. The generation process is repeated after each significant change in the simulation (e.g. detector or physics process description). Pre-simulated showers are parameterized in bins of pseudorapidity and distance to the closest rod center, while the energy of the initial electrons remains unbinned. The distance bin, which position corresponds to the position of the liquid argon gap is called *liquid argon bin*. This bin is introduced to simulate the peak in the distributions described in Sec. 7.2.

In simulation, particles originating from SM processes are used. The hit information is compressed in two steps:

Hit merging If the distance between two hits is smaller than a given parameter R_{min}, then the hits are merged into one deposit at the energy barycenter of the hits;

Truncation The hits with the energy below the cutoff energy are truncated. The energy of the remaining hits is rescaled to preserve the total deposited energy.

If during the simulation, the energy of a particle falls below a cut-off energy, the Frozen Showers algorithm examines the resulting shower. It checks that the shower energy is by 90% contained inside the calorimeter. This check depends on position and energy of the initial particle (since the shower size grows with the particle energy). Later, the algorithm matches the particle with a given entry in the Frozen Showers library. To correct for the differences in the energy between the initial particle and a matched library entry, each hit in the shower is scaled as:

$$E_{hit}^{new} = E_{hit} \cdot \frac{E_{part}}{E_{part,lib}}, \tag{7.4}$$

where E_{hit} is the energy of the hit, E_{part} is the energy of the particle and $E_{part,lib}$ is the energy of the particle stored in the library. In the final step, the particle is substituted with the shower and the rescaled shower hits are used in the reconstruction procedure.

7.3.1 Tuning procedure

The fast simulation method is required to be consistent with full simulation. In case of Frozen Showers in FCAL, there are problems with modeling the energy resolution, since the resolution of the reconstructed electrons coming from Frozen Showers simulation is found to be around two times smaller (Fig. 7.9), than in the full simulation. Using the Eq. 7.1, this behavior can be interpreted due to a too small size of fluctuations introduced in fast simulation and as a consequence a lack of the high-energy sub-showers. This problem can be solved by tuning the parameters of the library to match the full simulation.

The tuning procedure consists of two steps:

Bin width change At this stage the width of the liquid argon bin is enlarged. This procedure causes a higher number of showers with large energy response in simulation (and therefore higher fluctuations). This procedure causes an increase in the simulated energy scale and the resolution;

Shower energy scaling The shower energy is rescaled to correct for the shift in the mean reconstructed energies.

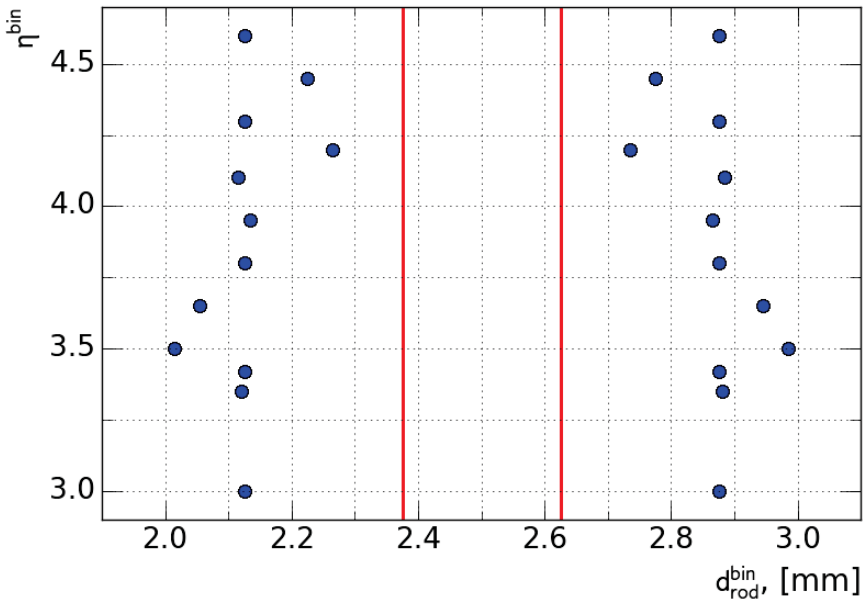

Fig. 7.8: The position of liquid argon gap bins for different η bins after the tuning procedure. Dots correspond to the each η and the distance to the closest rod center bin positions. The red lines are denoting the original position of the distance to the closest rod center bins and correspond to the position of the liquid argon gap in the calorimeter.

This procedure is repeated iteratively in each pseudorapidity bin separately until the desired agreement between the full and the fast simulation results is obtained. The resulting liquid argon bin positions for different pseudorapidity bins are shown in Fig. 7.8. This method yields a relatively good agreement with full simulation (black dots in Fig. 7.9). However, this method - as requiring a lot of human effort - has to be optimised before being used for the MC simulation.

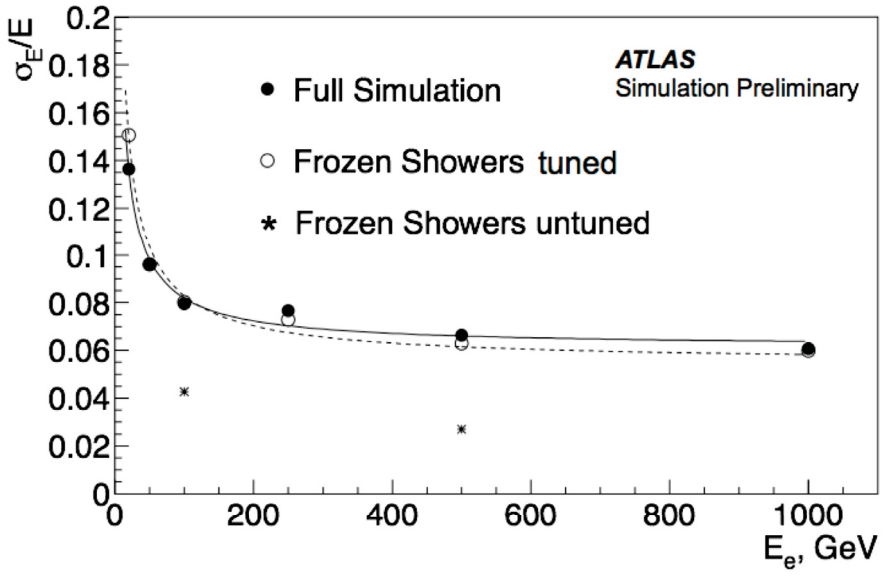

Fig. 7.9: Simulated electron resolutions for full simulation (black dots), tuned (white circles) and untuned (star points) Frozen Showers.

7.4 Machine learning based bin finding procedure

Since the Frozen Showers method is used in the ATLAS simulation, there was a need for a more automatic procedure of library contents generation with proper electron resolution. One of such automatizations is a procedure allowing to choose different positions of liquid argon bins using machine learning tools. In this section, a newly developed automatic bin finding procedure is explained.

7.4.1 Machine learning introduction

Machine learning is a set of algorithms for finding patterns in the data without being explicitly programmed. There are two main types of machine learning algorithms: *supervised*, where an example of the desired output is provided by the "supervisor" and *unsupervised* , where no labels are given to the algorithm [77]. The initial parameters of interest, which the algorithm uses in the learning process, are called *features*.

Machine learning algorithms can be used for solving a classification problem, where each event should be identified to one of the specified classes. In this analysis, decision trees and support vector machines from [78] are used.

Binary decision trees

Binary decision trees [79] (also called single decision trees) are one of the most commonly used machine learning algorithms for classification problems in particle physics. These algorithms can be represented as a set of sequential selections on input variables. The advantage of these

algorithms is simplicity of visualization and interpretation. An example scheme of this algorithm is shown in Fig. 7.10 a). Red circles indicate the nodes of the tree. Each node corresponds to one of the internal input variables and connects to two branches, which are split by the decision on the value of selected variable. The first node is called a root node. The depth of the tree is defined as the number of branches starting from the root node. A tree ends with squares, called leaf nodes, where all events are classified into a particular class. The tree, where each node has at most two branches is called binary decision tree.

A binary tree is build using the variable called Shannon entropy [80], which is defined similarly to entropy in physics:

$$S = -\sum_{i=1}^{N} p_i log_2 p_i. \tag{7.5}$$

Here p_i is the probability to find an event of class i. The information gain is defined as:

$$IG(Q) = S_0 - \sum_{i=1}^{2} S_i, \tag{7.6}$$

where S_0 is the initial entropy (without new node), S_i is the entropy of the one of the i-th branch of the node. From all the possible variants of splits, the one with the highest information gain is taken.

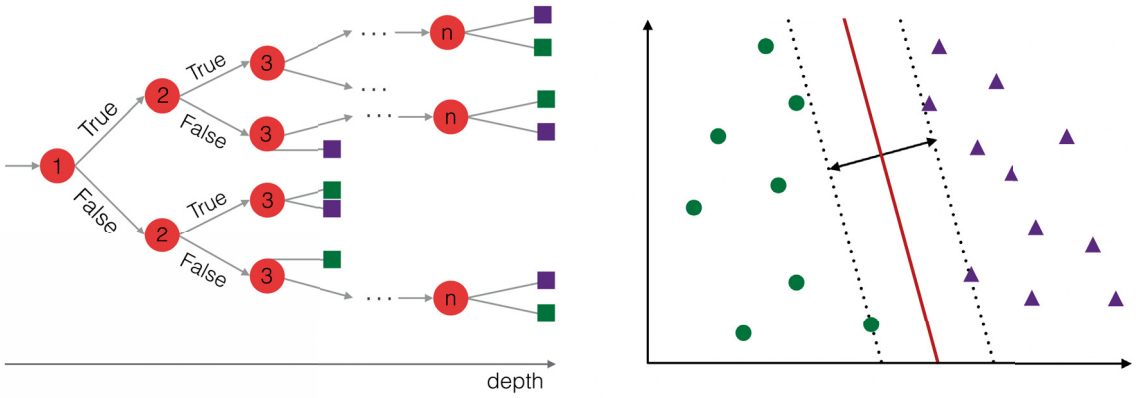

a) b)

Fig. 7.10: Schematic representation of machine learning algorithms, used in this analysis for the classification of showers. Green and violet figures represent the two classes of events. a) Representation of a binary decision tree structure: red circles correspond to nodes. Each node has two branches that are split by the decision on the value of selected variable. Squares represent "leafs", where events are classified into a particular class. b) Representation of the SVM algorithm. The solid line shows the dividing hyperplane. The dashed lines represent the maximum margin boundaries.

Support vector machines

Support vector machines (SVM) [81] is a machine learning algorithm which can be used for classification problems. In this algorithm, each event is represented in a p-dimensional parameter space. The classification is performed by finding a hyperplane that separates two given classes with the largest separation (Fig. 7.10 b). The hyperplane can be described using the set of points $\vec{x}$ in the parameter space satisfying the relation:

$$\vec{w} \cdot \vec{x} - b = 0, \tag{7.7}$$

where $\vec{w}$ is a vector normal to the hyperplane and the parameter $\frac{b}{\|\vec{w}\|}$ determines the offset of the hyperplane from the origin along the normal vector $\vec{w}$.

The maximum margin boundaries between two classes are described by equations:

$$\vec{w} \cdot \vec{x} - b = 1, \tag{7.8}$$
$$\vec{w} \cdot \vec{x} - b = -1, \tag{7.9}$$

where $\frac{2}{\|\vec{w}\|}$ is the distance between these 2 hyperplanes. The planes with the maximum margin between them correspond to the minimum $\|\vec{w}\|$.

In order to prevent each point from falling into the margin, the following constrain should be satisfied:

$$\vec{w} \cdot \vec{x} - b \geqslant 1(\text{ where } y_i = 1), \tag{7.10}$$
$$\vec{w} \cdot \vec{x} - b \leqslant -1(\text{ where } y_i = -1), \tag{7.11}$$

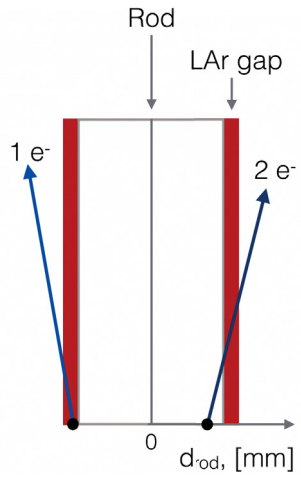

Fig. 7.11: Schematic representation of the model of shower creation in the FCAL. Electron 1 is created in a liquid argon gap. Electron 2 is created near a liquid argon gap and crosses the gap. This causes a smearing of shower distribution. Electrons created in the sensitive material tend to create more energetic showers than electrons produced in the dead material.

where y_i represents the class of the i-th event, classified as 1 or -1. These equations can be rewritten as:

$$y_i(\vec{w} \cdot \vec{x} - b) \geqslant 1. \tag{7.12}$$

It is also possible to construct a non-linear classifier by replacing the dot-product with a different kernel function. In this analysis, different kernel functions have been tested and the best performance was obtained using the radial basis function (RBF) kernel, defined as:

$$K_{rbf}(\vec{x}_i, \vec{x}_j) = e^{-\gamma|\vec{x}_i - \vec{x}_j|^2} \; \gamma > 0, \tag{7.13}$$

where the parameter γ adjusts the width of the kernel.

7.4.2 Electron shower categorization

The FCAL modules consist of different types of material and therefore showers produced inside the dead material are usually having lower energies than those created in sensitive material. However, the validation (summarized in Fig. 7.9) can be interpreted as an implication of high-energy showers production outside the liquid argon gap. This can be explained by the fact that electrons, created in a dead material, can cross a liquid argon gap (and give a hit) as shown in Fig. 7.11. These electrons would be indistinguishable from electrons created directly in the sensitive material (electron 1 in Fig. 7.11). Due to this similarity, electrons created outside the sensitive material can be combined in one class of the *sensitive material showers*. Showers that did not cross a liquid argon gap, are called *dead material showers*. The real gap position in this model is substituted by the *effective liquid argon gap*, which has a larger width.

The width of the effective liquid argon gap depends on the following parameters:

Electron energy From the data (Fig. 7.6) it is expected to have wider gap for the higher electron energies

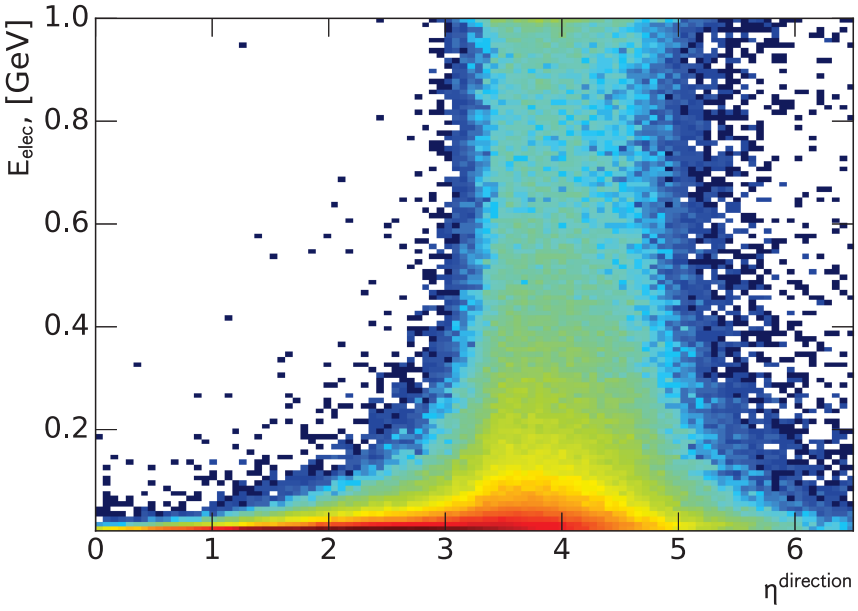

Fig. 7.12: Distribution of sub-shower energy vs direction of a shower (η) for showers used in the production of 1 TeV electrons.

Direction of the electron Electrons aligned collinearly with the liquid argon gap will have a smaller probability to cross it. This probability will grow with the angle (with reaching its maximum at 90°).

The procedure of finding the effective liquid argon gap is divided into two steps: in the first step the showers are classified using the simulated parameters of the showers, in the second step the dividing hyperplane in d_{rod} and E phase-space is produced. The training sample and classifiers used in these two steps are discussed in the following subsections.

Training sample

The parameters of electrons, substituted by the frozen showers, have a complicated structure and depend on the physics processes. Machine learning algorithms can identify these dependencies instead of identifying the true width of the effective liquid argon gap, so the simplified training sample is used. The training sample was produced by simulation of electrons produced in the FCAL.

Fig. 7.12 shows the distribution of the shower direction ($\eta^{direction}$) vs electron energy for electrons used in the simulation of 1 TeV electron. Most of the showers are produced in the η range between 3.0 and 5.0, which corresponds to the coordinates of the FCAL. The direction of the shower is highly correlated with the position of the electron. Therefore, electrons were generated uniformly in η between 3.0 and 5.0. In order to treat equally high and low energy electron initial showers, a uniform distribution of the electron energies is used.

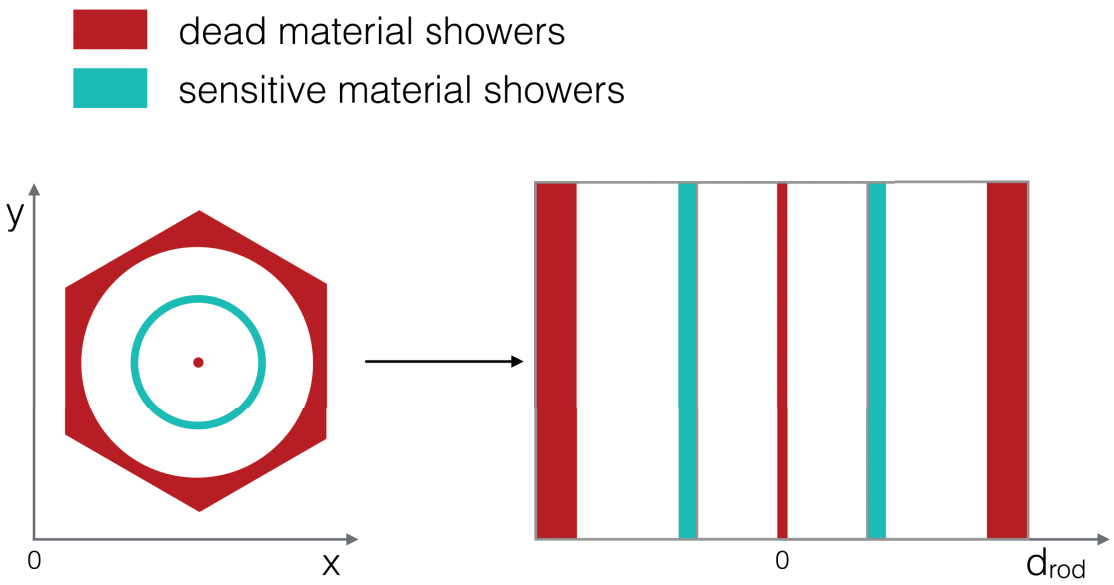

Fig. 7.13: Schematic representation of the preselected data for the first classifier in the x-y (left) and distance (right) plane. Electrons, created near the rod center and on the borders of the module have low probability to cross the sensitive material, while those created inside the liquid argon gap are considered as sensitive material showers.

First classifier

The first classifier aims to categorize all showers using the simulated parameters. A supervised learning algorithm is used on artificially reduced pre-labeled training sample. The results obtained can be expanded to the full sample afterwards.

The pre-labeling procedure uses the definitions of sensitive and dead material showers (Fig. 7.13). Showers, produced in the liquid argon gap are labeled as sensitive material showers. Showers, produced near the rod center and on the edges of the cell are labeled as dead material showers due to the small probability of the initial electrons to cross the liquid argon gap. For this classifier, simple decision trees have been chosen since it has shown an excellent classification efficiency on the reduced training sample. Different input parameters have been tested using variance. The best differentiating parameters are:

- Total shower energy, defined as the sum of all sensitive material hits energies in the shower;
- Maximum hit fraction, calculated as the energy of the most energetic hit divided by the total shower energy;
- RMS of the hits, calculated as the standard deviation of the hits energies in the shower.

The classification efficiency of the obtained binary search tree for the reduced sample is 97%. The results expanded to the full phase space are shown in Fig. 7.14 a).

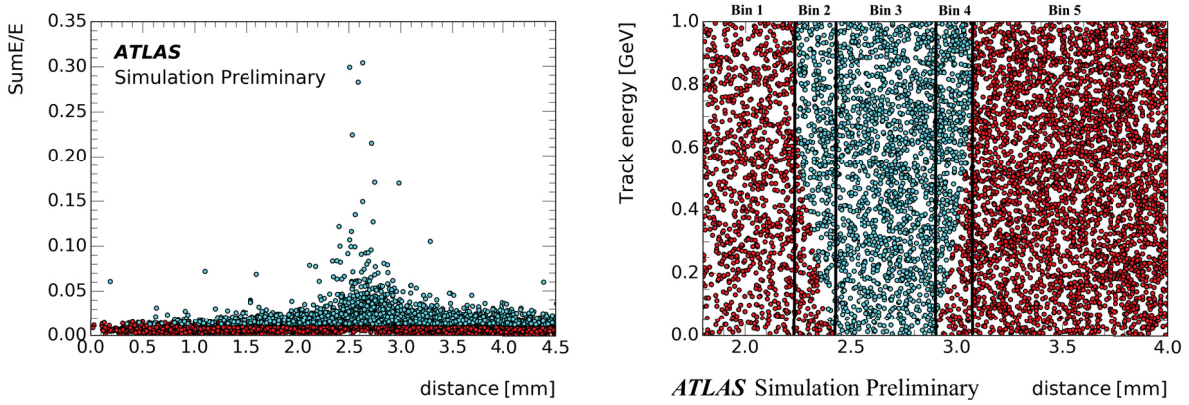

a) b)

Fig. 7.14: Results of machine learning algorithm classification for a) first classifier and b) second classifier. Cyan dots correspond to sensitive material showers, red to dead material showers. The black lines in Fig. b correspond to the resulting bin positions.

Second classifier

The second classifier uses predictions of the first classifier as an input. The algorithm reconstructs a hyperplane between two types of the shower using SVM. As an input it uses the truth parameters of the electron, e.g. energy of the initial electron and its distance to the closest rod center and RBF as a kernel function. A classification is performed separately in each η bin used in the library.

An example of the classifier output is shown in Fig. 7.14 b). The obtained gap positions are wider than the original ones, as expected from the model. The difference between obtained effective liquid gap widths for different η bin used in the library is considered to be small. The mean effective liquid argon gap width is used as an input for the bin finding procedure.

Interpretation of results

The resulting hyperplane from the second classifier can be translated to the bin positions in different ways. Therefore several interpretations of the bin positions have been tested. The different interpretations are compared using the toy MC method. The initial electron parameters generated using random generator and distributions of pseudorapidity $\eta^{position}$, the electron energy and distance to the closest rod center from the full simulation. This simulation allows comparing the shower energies and shower energies divided by the energy of the initial electron (SumE/E) distributions with the distributions coming from the full simulation, which is considered as a reference.

The best bin position is shown in Fig. 7.14 b) with black lines. The central bin, according to the classifier, contains only sensitive material showers events. Bins 2 and 4 include events from both classes. All events in bins 1 and 5 are treated as events with sensitive material showers. The effective liquid argon bin width (bin 3) is wider than a liquid argon gap width in the FCAL.

The comparison of the total shower energy divided by the initial electron energy distributions obtained from the toy MC using the old libraries (Fig. 7.15 a) and the toy MC using the

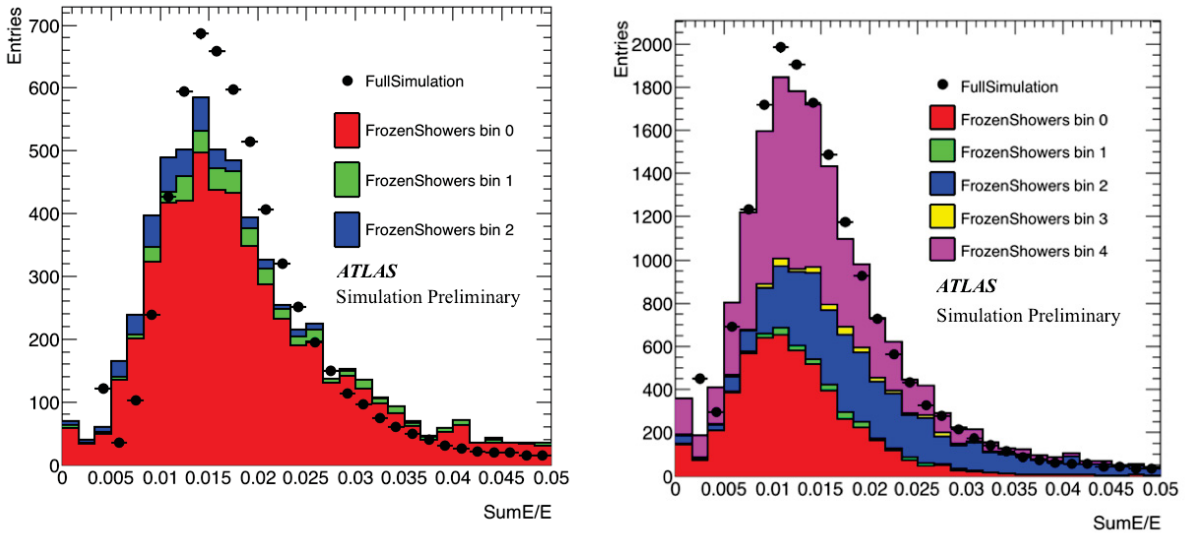

a) b)

Fig. 7.15: Comparison of the distributions of shower energy divided by the energy of the initial electron between full simulation and toy MC for a) old "tuned" libraries with 1 liquid argon gap bin and b) new libraries using 3 liquid argon gap bins. There are still remaining differences between full simulation and toy MC, but the new machine learning binning gives a better agreement with full simulation.

libraries with the new binning (Fig. 7.15 b) has shown, that we can expect a better performance of the reconstructed values for the new binning.

7.4.3 Validation of reconstructed electron energy

A validation is performed using single electrons of the following energies: 100 GeV, 200 GeV, 500 GeV and 1000 GeV and within the η directions that correspond to the 12 η bins of the library. The electron energy resolution is calculated as RMS of all reconstructed energies for each energy and η bin position. The validation plots are shown in Fig. 7.16- 7.17. The results obtained using the binning found by the machine learning procedure are compared to the full simulation results and to the results coming from the libraries using the old binning. The new method improves for many bins the agreement between full simulation and the Frozen Showers results. However there are some η bins, where the new algorithm performs significantly worse, than an old one ($\eta = 3.5$ and $\eta = 4.3$). The methods of the algorithm performance improvement are discussed in Sec. 7.4.4.

7.4.4 Outlook

The validation of the electron energy resolution simulation have shown a good agreement between the full and fast simulation results for most of the η-bins, however, this method still can be improved. The following ways of improvement have been investigated and planned to be implemented in the nearest future:

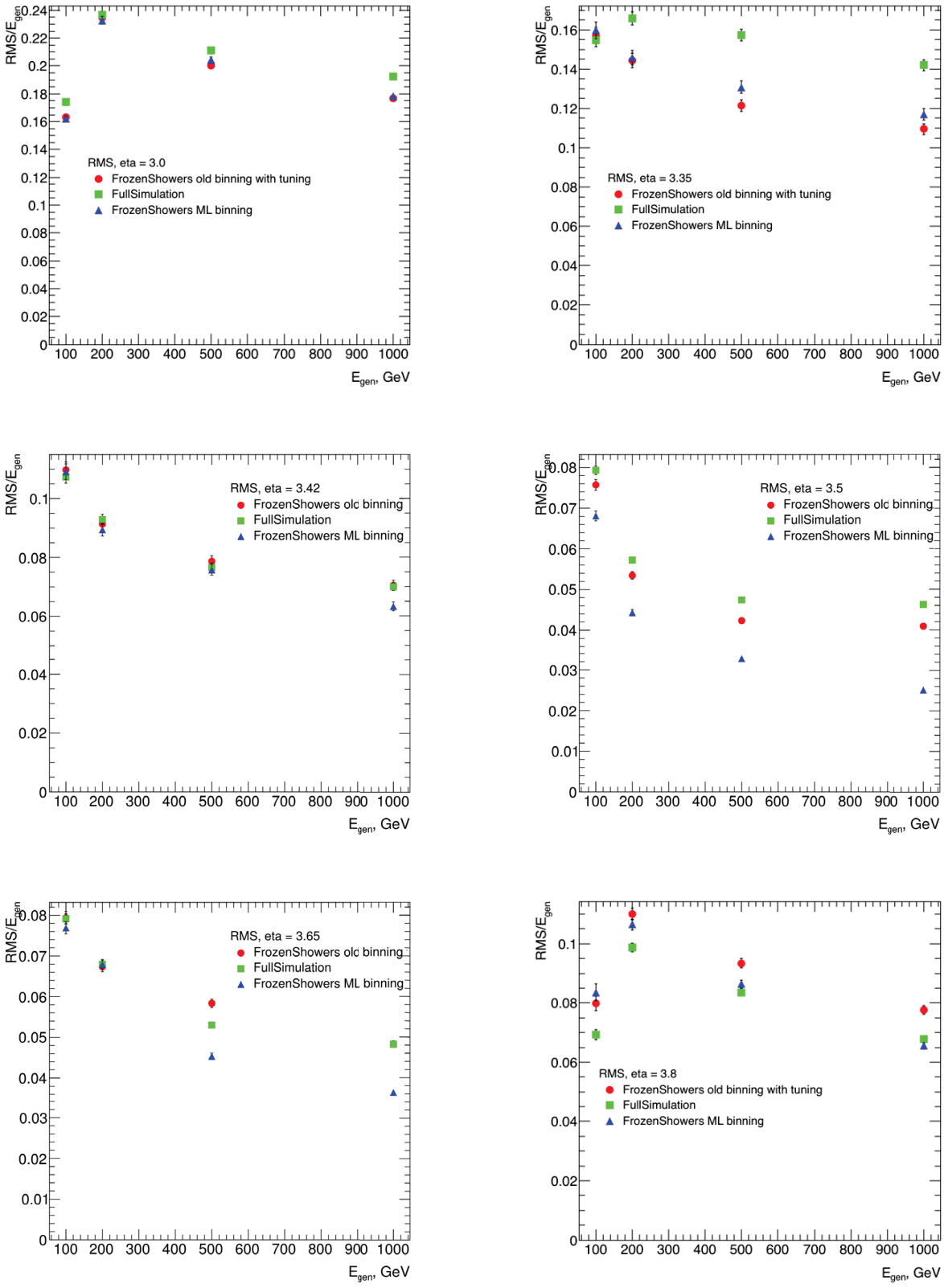

Fig. 7.16: The energy resolution of reconstructed electrons for full simulation, new libraries with machine learning binning and old libraries for different η ranges (η = 3.0, 3.35, 3.42, 3.5, 3.65, 3.8).

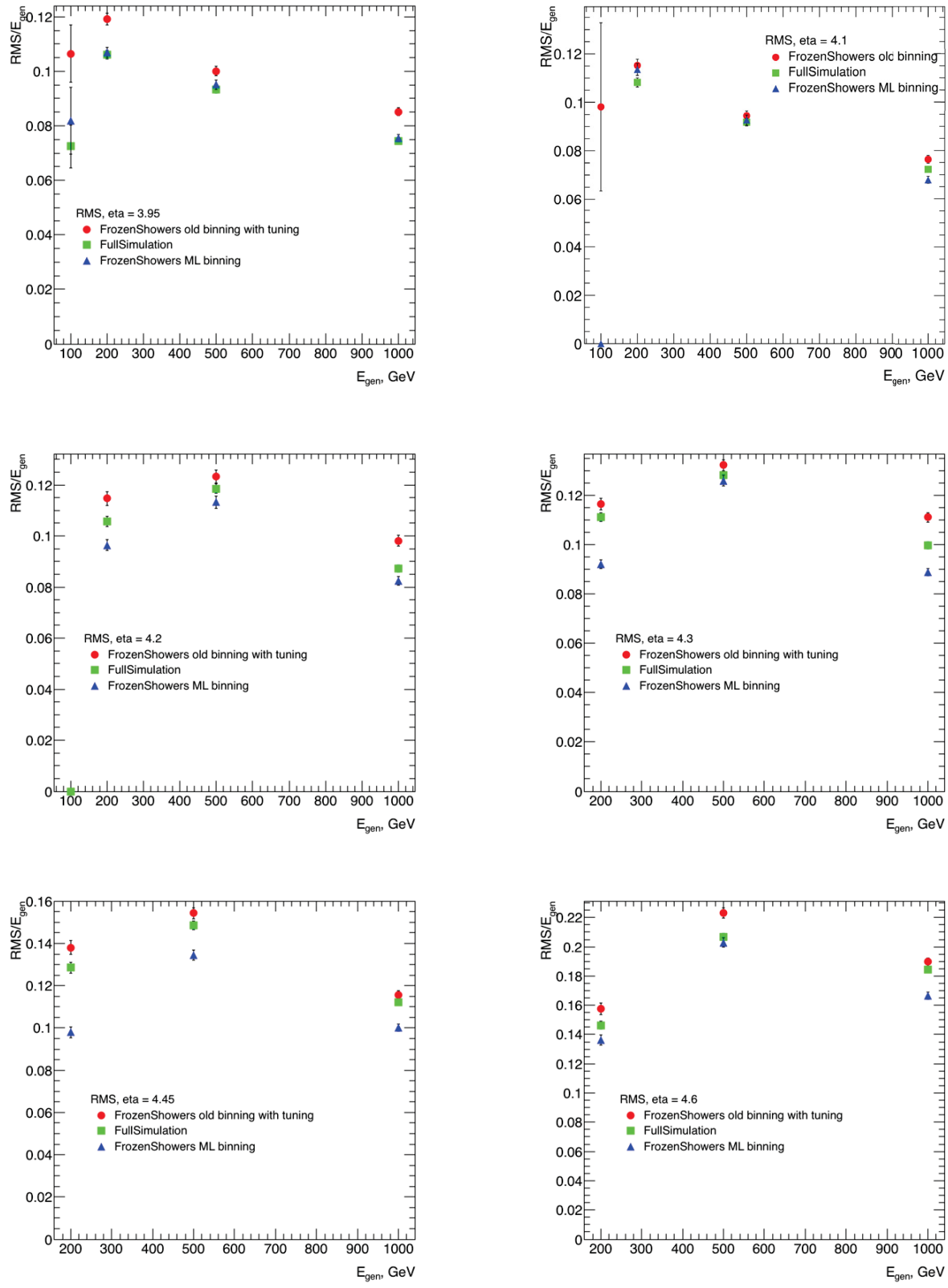

Fig. 7.17: The energy resolution of reconstructed electrons for full simulation, new libraries with machine learning binning and old libraries for different η ranges (η = 3.95, 4.1, 4.2, 4.3, 4.45, 4.6).

- η-dependent bin size. Currently, all of bins have the same width of the liquid argon bin. The procedure should be modified so that the effective width of the liquid argon gap is calculated separately for each η-bin;
- Improvement of the training sample. Too simplified training sample could also cause the problem of not perfectly described electron resolution. It is planned to repeat the training procedure using samples with distributions, closer to the nominal ones;
- Addition of a new variable, used in the library (e.g. direction of the shower). Since there is a complex dependency between the position of the electron and its direction (especially in the small energy region), an additional binning could solve the problems with the electron energy resolution modeling.

7.5 Validation

The fast simulation method should be in a good agreement with a full simulation results for all reconstructed objects. The Frozen Showers method is validated using the following physics objects:

- Z bosons decaying to one central and one forward electron (Fig. 7.19 a). The mass resolution of Z-boson is dominated by the resolution of the central electron. Therefore it is most sensitive to the mean energy of the forward electron. There is a visible shift observed in the mass distribution between the full and fast simulations (Fig. 7.18), however, is within the tolerable region;
- Jets from two jet events. This validation shows a good agreement with full simulation. The distribution of the jet response (Fig. 7.19 b) shows that the Frozen Showers method does not change the jet energy scale;
- Inclusive forward electron production. The forward electron validation, that usage of the Frozen Showers is not changing the η and E_T distributions of the forward electrons. Studies of the forward electrons resolution have been performed separately and are discussed in the previous section.

The total agreement between the full and the fast simulation results for different observables justifies the usage of the Frozen Showers method in an official ATLAS MC simulation production.

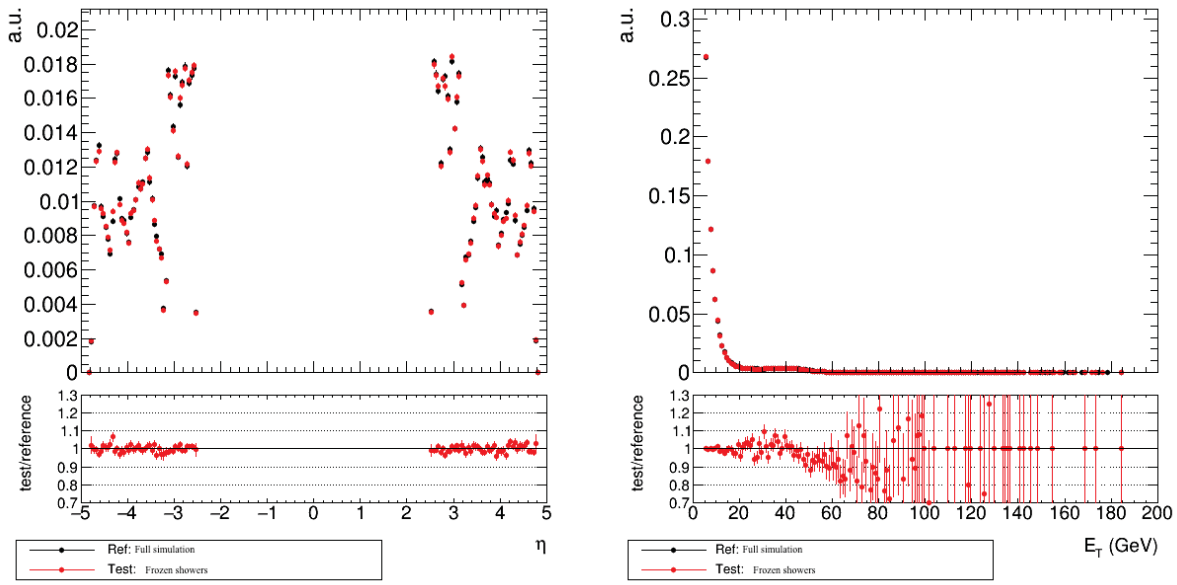

a) b)

Fig. 7.18: Results of validation of the Frozen Showers library on forward electrons. Comparison between full simulation and fast simulation using Frozen Showers in forward electron events a) electron pseudorapidity and b) electron transverse energy. Modified from [82].

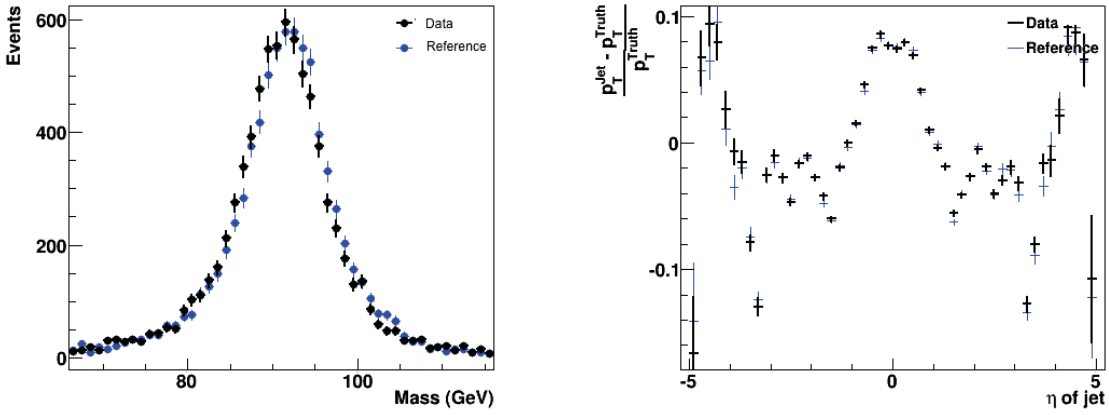

a) b)

Fig. 7.19: Results of validation of the Frozen Showers library on $Z \rightarrow ee$ and jets sample. Comparison between full simulation and fast simulation using Frozen Showers for and a) mass of the dilepton pair in $Z \rightarrow ee$ candidate events (modified from [83]) b) jets response vs pseudorapidity distribution (modified from [84]).

Chapter 8

Data and Monte Carlo samples

8.1 Collision data

The data used in this analysis was collected in proton–proton (pp) collision runs at a center-of-mass energy 2.76 TeV at the LHC operation using the ATLAS detector. The mean number of interactions per bunch crossing for this runs is shown in Fig. 8.1.

During these runs ATLAS collected 4.45 pb^{-1} of data (Fig. 8.1 b). However, not all of the data is applicable for a precise physics analysis, so a set of additional data quality (DQ) requirements is applied. Information about subdetectors that were disabled during data-taking is used. The information is stored in a Good Run List (GRL). The total luminosity of a data sample used in the analysis is 4.0 pb^{-1} with the uncertainty of 3.1% [85].

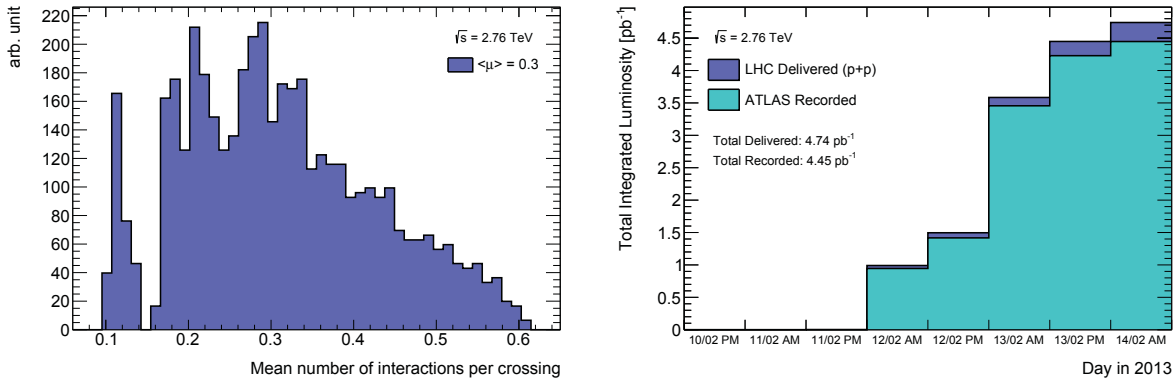

a) b)

Fig. 8.1: a) Mean number of interactions per bunch crossing and b) cumulative luminosity delivered by LHC (dark blue) versus day, and recorded by ATLAS (light blue) for pp collisions at the center-of-mass energy 2.76 TeV in 2013.

8.2 Monte Carlo samples

Simulated events are used to estimate both the signal and background processes contributions. A summary of the MC samples used in the analysis is given in Tab. 8.1. The primary signal samples are generated using Powheg generator with CT10 [86] PDFs and showered with Pythia8 using AU2 [87] tune. Alternative signal MC samples are produced for W-analyses. They are generated using Sherpa with CT10 PDFs. This sample is used for studies of systematic errors coming from the choice of the generator (see Chap. 13).

The Monte Carlo samples are also used to estimate the fraction of background events in data. More detailed description of the background sources can be found in Chap. 12. The $W \to \tau\nu$ and $Z \to \tau\tau$ processes are generated with Powheg+Pythia8 generator with CT10 PDF and AU2 tune. Events with diboson decays (WW, WZ, ZZ) are generated using Herwig with CTEQ6L1 [88] PDF set and AUET2 [89] tune. The top pair production ($t\bar{t}$) background is estimated using Powheg generator interfaced with Pythia6. The additional heavy quark pairs production ($b\bar{b}$ and $c\bar{c}$) samples needed for the multijet background determination (Sec. 12.1) are generated with Pythia8 with AU2 tune and CTEQ6L1 PDF set.

Table 8.1: Monte Carlo samples used to estimate signal and background processes.

Process	Generator	N_{events}
Signal MC		
$W^+ \to e\nu$	Powheg+Pythia8	$2.0 \cdot 10^5$
$W^+ \to \mu\nu$	Powheg+Pythia8	$2.0 \cdot 10^5$
$W^- \to e\nu$	Powheg+Pythia8	$1.2 \cdot 10^5$
$W^- \to \mu\nu$	Powheg+Pythia8	$1.2 \cdot 10^5$
$Z \to ee$	Powheg+Pythia8	$9.5 \cdot 10^4$
$Z \to \mu\mu$	Powheg+Pythia8	$7.0 \cdot 10^4$
$W \to e\nu$	Sherpa	$4.9 \cdot 10^5$
$W \to \mu\nu$	Sherpa	$4.8 \cdot 10^5$
Background MC		
$W^+ \to \tau\nu$	Powheg+Pythia8	$5.0 \cdot 10^4$
$W^- \to \tau\nu$	Powheg+Pythia8	$3.0 \cdot 10^4$
$Z \to \tau\tau$	Powheg+Pythia8	$2.0 \cdot 10^4$
$t\bar{t}$	Powheg+Pythia6	$5.0 \cdot 10^3$
WW	Herwig	$1.0 \cdot 10^3$
ZZ	Herwig	$5.0 \cdot 10^3$
WZ	Herwig	$1.0 \cdot 10^3$
$b\bar{b}$	Pythia8	$5.0 \cdot 10^5$
$c\bar{c}$	Pythia8	$4.8 \cdot 10^5$

Part III

The measurement

Chapter 9

Selection criteria

Selection criteria are defined as a set of requirements used to separate process of interest (signal) from other processes (background). For $pp \to W \to e\nu/\mu\nu$ and $pp \to Z/\gamma^* \to ee/\mu\mu$ the selection criteria can be divided into three main groups: data quality requirements, lepton selection criteria and boson selection criteria. The full set of selection requirements used in the analysis is summarized in Tab. 9.1 and are discussed in this chapter.

9.1 Event selection

Data-taking conditions are important in the analysis, so in order to preserve high data quality, selection criteria are applied. The events with unstable beam conditions, disabled parts of the

Table 9.1: Summary of analysis selection criteria.

Event selection	
Trigger	
Good Run List	
Reject events with LAr errors	
Number of tracks associated with primary vertex ≥ 3	
Lepton selection	
Electron selection	Muon selection
Trigger matching	Trigger matching
$P_T^l > 20$GeV	$P_T^l > 20$GeV
$\lvert\eta^l\rvert < 2.47$	$\lvert\eta^l\rvert < 2.5$
excluding $1.37 < \lvert\eta^l\rvert < 1.52$	
Object quality cut	Staco reconstruction chain
Medium electron identification	Combined muon
$P_T^{cone,20} < 0.1$	$P_T^{cone,20} < 0.1$
Boson selection	
W boson selection	Z boson selection
$E_T^{miss} > 25$ GeV	
$M_T^W > 40$ GeV	66 GeV $< M^Z < 116$ GeV

detector or events with high noise in calorimeter are rejected. Runs, that can be used in the analysis, are stored in the so-called Good Run List (GRL).

Events for which the LAr calorimeter was malfunctioning are excluded by LAr quality criteria. Furthermore, events are required to have at least one primary vertex formed with at least three tracks.

The online selection of events is based on single lepton triggers. For electrons EF_e15_loose1 trigger is used, which records electrons with E_T > 15 GeV. This trigger uses additional "loose" isolation requirements to exclude jets that are misidentified as electrons. In the muon channel, the lowest single lepton trigger is EF_mu10. It records events containing at least one muon with P_T >10 GeV.

9.2 Lepton selection

Both W and Z-boson analyses use similar offline lepton selection criteria. All leptons must satisfy a requirement, P_T^l > 20 GeV. The leptons are required to trigger the event and therefore to be within the distance $\Delta R = \sqrt{\Delta\eta^2 + \Delta\phi^2} = 0.2$ of the event trigger.

Electron candidates are required to be within pseudorapidity range of $|\eta^l|$< 2.47. Because the precise reconstruction of the electrons is not possible in the transition region between barrel and endcap, the electron candidates reconstructed within the pseudorapidity range 1.37 < $|\eta^l|$< 1.52 are not used. Additionally, for a better multijet background rejection medium identification criteria are applied. The object quality (OQ) criteria are also applied to electron candidates in order to remove events from runs where the EM calorimeter was malfunctioning.

Muons have to satisfy the following offline selection criteria: they should be reconstructed by a staco algorithm and fall within a range of $|\eta^l|$< 2.5. Additionally, for a better rejection of background, muons are required to be combined, i.e. having a matched track in both ID and MS.

In order to reach a better background rejection, the *isolation criteria* ($P_T^{cone,20}$< 0.1) is applied on both electron and muon candidates. These criteria use the information about ID tracks that fall within a distance of $\Delta R = \sqrt{\Delta\eta^2 + \Delta\phi^2} = 0.2$ around the lepton direction. Events with the sum of all tracks transverse momenta (except for the selected lepton) greater than $0.1 \times P_T^l$ are excluded from the analysis.

9.3 Boson selection

Events containing W-boson candidates are required to have exactly one reconstructed lepton. Missing transverse energy is required to be E_T^{miss} > 25 GeV. Transverse mass, calculated from the lepton and the missing transverse energy (Eq. 3.5) has to be bigger than 40 GeV.

Events for the Z-boson selection are required to contain exactly two, opposite sign, same flavor lepton candidates. The invariant mass of the reconstructed lepton pair is required to fall within the region 66 GeV < M^Z < 116 GeV.

The effect of each selection can be studied using the number of events passing each set of selections in a sequential order (Tab. 9.2). The events, fulfilling the all of the W and Z-boson selection requirements are called W and Z-boson candidate events, respectively.

Table 9.2: Number of W and Z-boson candidate events in data and signal simulation, remaining after each major requirement. The simulation is normalized to the NNLO cross section shown in Tab. 12.1.

Requirements	Number of candidates			
	Data	signal MC	Data	signal MC
	$W^+ \to e\nu$		$W^+ \to \mu\nu$	
No selection	27491394	8354	27491394	8354
Event selection	333054	6044	26475069	8226
Lepton selection	15075	4315	11466	4782
Boson selection	3914	3544	4365	3936
	$W^- \to e\nu$		$W^- \to \mu\nu$	
No selection	27491394	5002	27491394	5002
Event selection	333054	3139	26475069	4916
Lepton selection	15075	2306	11466	2595
Boson selection	2209	1941	2460	2164
	$Z \to ee$		$Z \to \mu\mu$	
No selection	27491394	1196	27491394	1196
Event selection	333054	1051	445817	1059
Lepton selection	459	430	698	621
Boson selection	430	418	646	603

Chapter 10

Monte Carlo simulation corrections

Monte Carlo simulation plays an important role in the cross section measurement. Therefore is is important to have the best possible agreement with the data. A subset of these corrections is described in Chap. 6. Some of the discrepancies between the data and the MC simulation are corrected using the reconstructed events. There are two possible methods for correcting the MC simulation: application of weights on the MC events (reweighing) and random changing of the reconstructed 4-vectors (smearing).

This chapter describes all additional corrections that are applied to MC simulation samples in this analysis.

10.1 Lepton efficiency corrections

The efficiency of the lepton selection at the ATLAS detector can be divided into three components:

- The reconstruction efficiency ϵ_{rec}. It is the probability to reconstruct a lepton as a lepton of the correct flavor;
- The identification efficiency $\epsilon_{id|rec}$. It is the probability that a reconstructed lepton survives the identification requirements;
- The trigger efficiency $\epsilon_{trig|rec,id}$. It is the probability that the lepton satisfies the trigger requirements.

The full selection efficiency for a single lepton can be written as:

$$\epsilon_{total} = \epsilon_{rec} \times \epsilon_{id|rec} \times \epsilon_{trig|rec,id}. \tag{10.1}$$

The efficiencies are measured using the tag-and-probe method with $Z \rightarrow ll$ decays. One of the leptons from the Z-boson, called "tag", is initially selected with the full set of selection requirements. Second lepton, "probe" candidate, is used for the efficiency measurements.

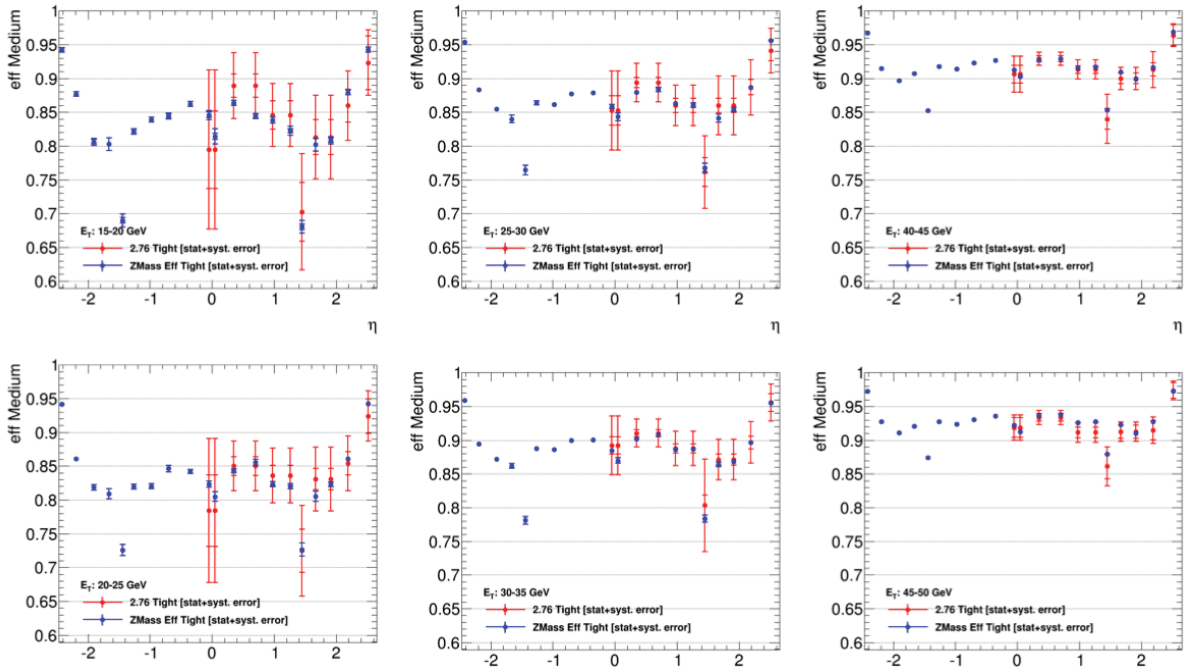

Fig. 10.1: Comparison of electron efficiencies as calculated for 8 TeV (blue points) and 2.76 TeV (red points) for MC simulation. Efficiencies are shown as a function of pseudorapidity (η) for different bins in electron E_T. Both statistical and systematic uncertainties are shown [90].

The single lepton efficiencies can be translated to the corresponding efficiency for the detection of a lepton in W and Z-boson decays :

$$\epsilon^{W}_{total} = \epsilon_{rec} \times \epsilon_{id|rec} \times \epsilon_{trig|rec,id}, \tag{10.2}$$

$$\epsilon^{Z}_{total} = \epsilon_{rec} \times \epsilon_{id|rec} \times (1 - (1 - \epsilon_{trig|rec,id})^2). \tag{10.3}$$

The reconstruction efficiency is associated with the algorithm used in the event reconstruction process. In the electron channels, the reconstruction efficiency is defined as the probability to reconstruct an electron given the presence of a cluster.

The muon reconstruction efficiency is estimated as:

$$\epsilon_{reco,muon} = \epsilon_{reco,muon|ID} \cdot \epsilon_{ID} \approx \epsilon_{reco,muon|ID} \cdot \epsilon_{ID|MS}, \tag{10.4}$$

where $\epsilon_{reco,muon|ID}$ is the probability that a muon which was reconstructed in ID is also reconstructed in the MS (combined muon), and ϵ_{ID} is the efficiency of the muon reconstruction given an ID track. The identification efficiency ϵ_{ID} cannot be measured directly in the data and can be approximated by the value of the $\epsilon_{ID|MS}$ efficiency to reconstruct a muon in the MS given an ID track.

The efficiency in MC simulation is corrected to match the lepton efficiencies in the data by

Table 10.1: Overall muon trigger scale factors and their statistical uncertainties.

	SF	SF stat.error
μ	0.988	0.011
μ^+	1.012	0.015
μ^-	0.964	0.015

introducing the relevant scale factor :

$$SF = \frac{\epsilon^{data}}{\epsilon^{MC}}, \tag{10.5}$$

where ϵ^{data} and ϵ^{MC} are the lepton efficiencies in the data and MC, respectively.

The scale factors are calculated as a function of P_T^l and η^l and have associated statistical and systematic uncertainty components. The statistical component is connected to the size of the $Z \to ll$ sample, which in our case is around 500 events for each lepton flavor. This makes the statistical error the dominant one and means that precise calculation of scaling factors based on this data is difficult.

It is possible, however, to use scale factors derived using $\sqrt{s}$ = 8 TeV 2012 data [90]. The main difference between $\sqrt{s}$ = 2.76 TeV and $\sqrt{s}$ = 8 TeV data samples are the center-of-mass energy and the pile-up conditions. The effects of these differences have been studied by the electron performance group at ATLAS using a $Z \to ee$ MC simulation sample. Fig. 10.1 shows the electron efficiencies for different E^e ranges as a function of η^e, for the MC simulation for $\sqrt{s}$ = 2.76TeV and $\sqrt{s}$ = 8 TeV. The obtained scale factors agree with each other within the uncertainties. This justifies the usage of the $\sqrt{s}$ = 8 TeV scaling factors with increased statistical uncertainty in the analysis at $\sqrt{s}$ = 2.76 TeV.

The muon trigger scale factors have to be derived from the $\sqrt{s}$ = 2.76 TeV data since the muon trigger used in the analysis had not been present in the 2012 data. The available statistics of the Z-boson candidates in data does not allow to measure the scale factors as a function of P_T^l and η^l. The selection criteria on the muon momenta are significantly higher than the trigger threshold. Therefore, the P_T dependence of the trigger scale factors can be neglected. Binning in η is motivated by the detector construction: $|\eta| < 1.05$ corresponds to the barrel part of the muon spectrometer, while $1.05 < |\eta| < 2.5$ is the end-cap of the MS (see Sec. 4.2.4). The bending of the muon trajectories in the magnetic field can cause differences in the trigger efficiencies for opposite muon charges. Additionally, a possible charge dependency of the scale factors is studied.

The obtained scale factors with neglected η dependency are shown in Tab. 10.1. The obtained scale factors for different muon charges are not in agreement with each other within the uncertainties, which can be interpreted as a non-negligible charge dependency. The comparison of trigger efficiencies for data and MC simulation as a function of η is shown in Fig. 10.2.

The effect of applying different scale factors on muons for the W analysis is shown in Fig. 10.3- 10.5. Good agreement between the data and simulation is achieved by applying non-η-dependent but charge-dependent scale factors. Therefore, for this analysis, the η dependency of the trigger scale factors is considered to be negligible.

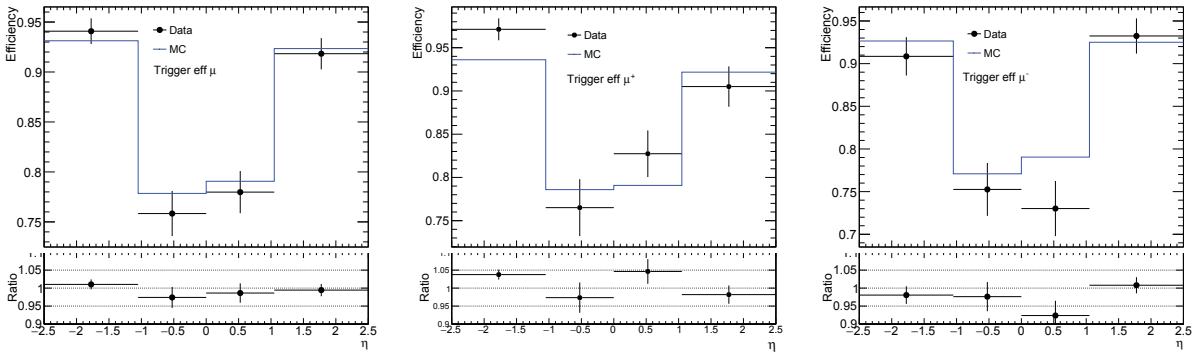

a) b) c)

Fig. 10.2: Trigger efficiencies for a) μ b) μ^+ c) μ^- as a function of muon pseudorapidity.

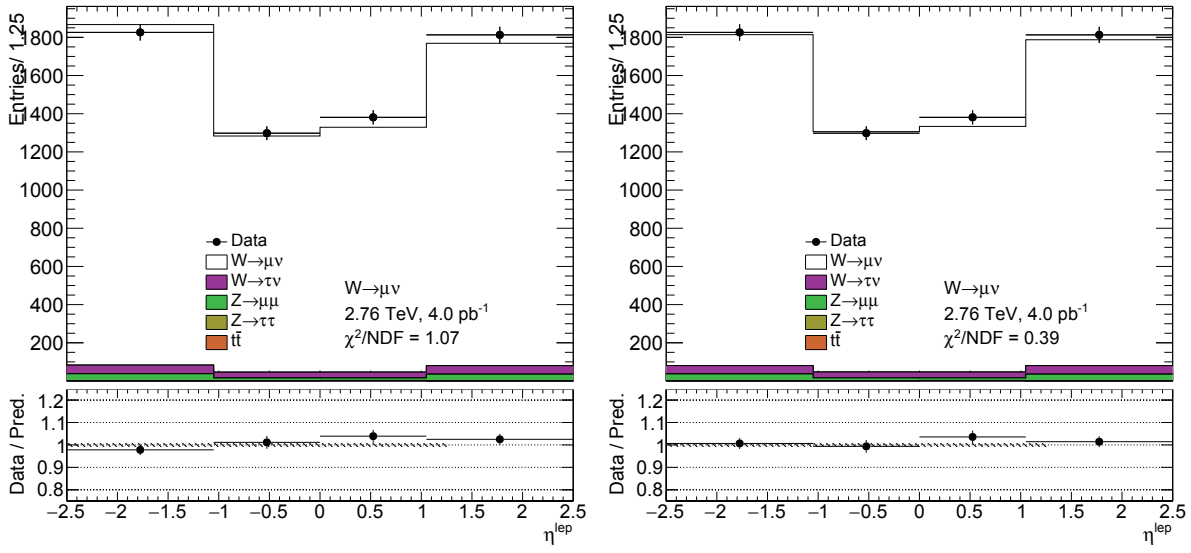

a) b)

Fig. 10.3: Muon pseudorapidity distributions for the $W \rightarrow \mu\nu$ event selection with a) binned b) un-binned charge-dependent trigger scale factors applied.

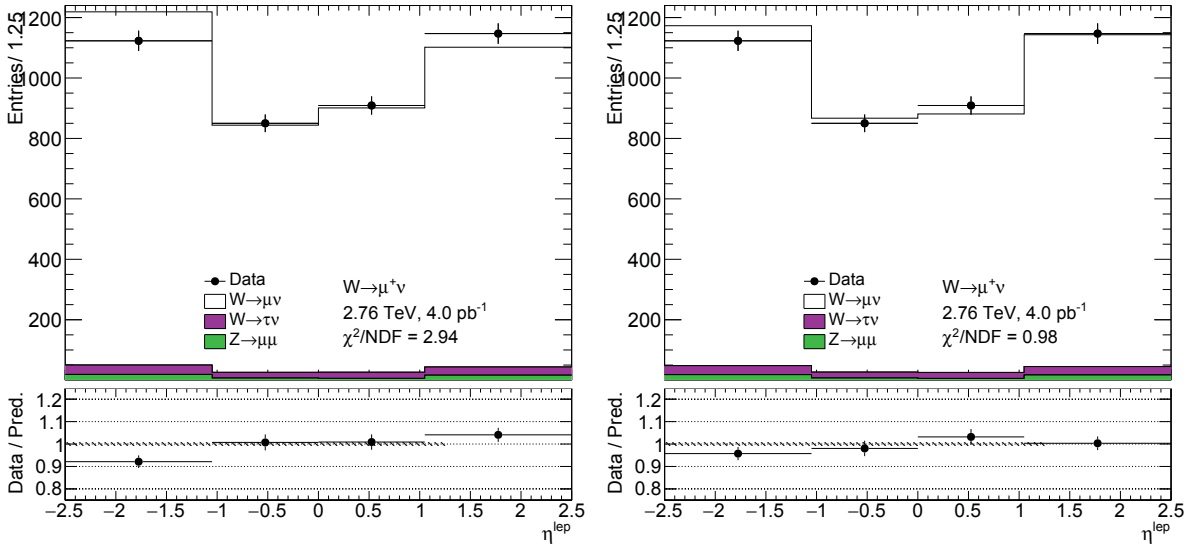

a) b)

Fig. 10.4: Muon pseudorapidity distributions for the $W \to \mu^{+}\nu$ event selection with a) binned b) un-binned charge-dependent trigger scale factors applied.

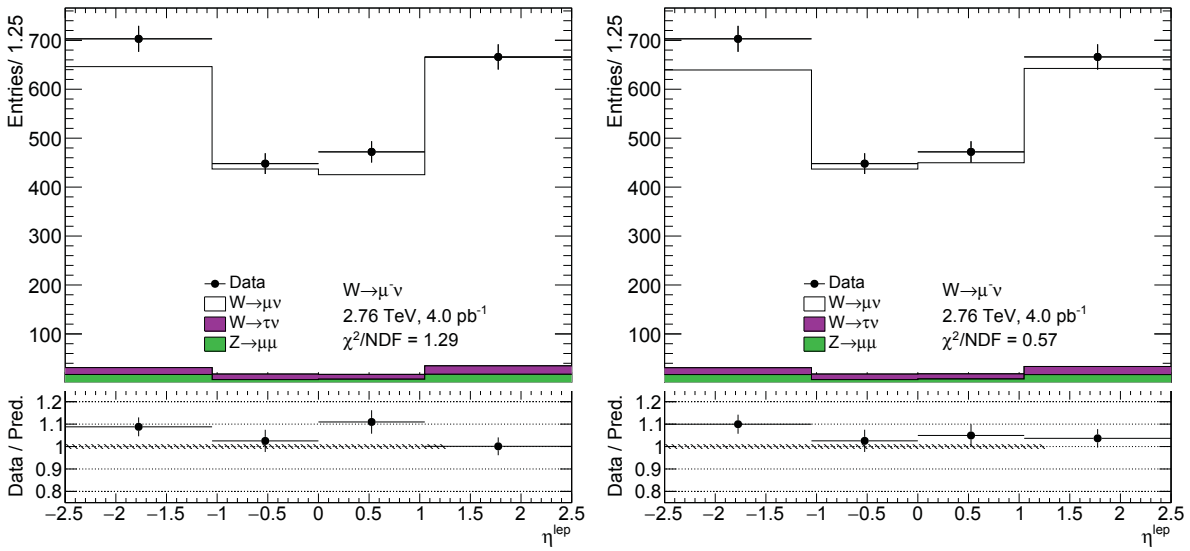

a) b)

Fig. 10.5: Muon pseudorapidity distributions for the $W \to \mu^{-}\nu$ event selection with a) binned b) un-binned charge-dependent trigger scale factors applied.

10.2 Electron energy scale and resolution correction

The possible shift in the reconstructed energy of the electron is corrected using a three-step procedure [91]:

- Calibration of the electronics, which matches a raw signal from the readout electronics to a cluster energy deposit.
- MC-based e/γ response calibration, that corrects effects of the energy loss in the material in front of the calorimeter and the leakage into the hadronic calorimeter. This calibration is applied on both data and MC.
- Correction of the calorimeter cell response in the data, which corrects the response variations in specific detector regions.

The overall energy shift is parameterized as:

$$E^{data} = E^{MC}(1+\alpha), \tag{10.6}$$

where E^{data} and E^{MC} are the energies in data and simulation, respectively and α is a mean shift. The effect of this miscalibration on a reconstructed mass of the Z boson, neglecting second order terms is:

$$M^{data} = M^{MC}(1+\alpha), \quad \alpha_{1,2} \sim \frac{\alpha_1+\alpha_2}{2}, \tag{10.7}$$

where M^{data} and M^{MC} are the reconstructed masses of the Z-boson for data and MC simulation, respectively, and α_i is the mean energy shift of the i-th electron from the Z-boson decay.

Additionally, the difference between data and MC simulation in the electron energy resolution is taken into account. The general dependency of the electron energy resolution on the electron energy is described by Eq. 7.1. It is assumed that the sampling and the noise terms are well-modeled by the MC simulation and the main difference comes from a constant term. Thus, the electron energy resolution correction can be written as:

$$\frac{\sigma_E}{E}^{Data} = \frac{\sigma_E}{E}^{MC} \oplus c, \tag{10.8}$$

where c is a resolution correction. Similar to the electron energy scale correction, it is possible to derive the electron energy resolution correction factor by comparing M^{data} and M^{MC} distributions.

The values α and c are obtained using the χ^2-based fit of an invariant mass of electron pairs in data and MC.

10.3 Muon momentum correction

Muon momentum resolution depends on η, ϕ and P_T of the muon [46]. There is an empirical formula to describe this dependence in the detector (ID or MS) [92]:

$$\frac{\sigma_{Det}(P_T)}{P_T} = \frac{r_0^{Det}(\eta,\phi)}{P_T} \oplus r_1^{Det}(\eta,\phi) \oplus r_2^{Det}(\eta,\phi)\cdot P_T. \tag{10.9}$$

The first term ($\frac{r_0^{Det}(\eta,\phi)}{P_T}$) originates from the fluctuations of the energy loss in the material. The second term (r_1^{Det}) comes from non-homogeneities in the magnetic field . The third term (r_2^{Det}) describes the intrinsic resolution effects.

Similarly to electrons, the overall muon momentum scale shift between data and MC is parameterized as:

$$P_T^{data} = P_T^{MC} + s_0^{Det}(\eta,\phi) + s_1^{Det}(\eta,\phi) \cdot P_T^{MC}, \tag{10.10}$$

where $s_0^{Det}(\eta,\phi)$ comes from the imperfect knowledge of energy losses for muons passing through the detector.

This leads to an overall correction formula:

$$P_T^{Cor,Det} = \frac{P_T^{MC,Det} + \sum_{n=0}^{1} s_n^{Det}(\eta,\phi)(P_T^{MC,Det})^n}{1 + \sum_{m=0}^{2} \Delta r_m^{Det}(\eta,\phi)(P_T^{MC,Det})^{m-1} g_m}, \tag{10.11}$$

where the g_m are normally distributed random variables (with a mean of 0 and a standard deviation of 1). Due to a small amount of material in the ID, $\Delta r_0^{ID}(\eta,\phi)$ and $s_0^{ID}(\eta,\phi)$ are set to zero. The misalignment effect of the MS is corrected in simulation by adding a random smearing to the MS alignment constants. This allows to set $\Delta r_2^{MS}(\eta,\phi)$ to zero during the fit procedure.

The relevant correction factors are extracted using events from $Z \to \mu\mu$ decays, where both muon candidates fulfill the combined muon criteria described in Sec.5.3. The correction extraction is performed first for the ID part and then for the MS part using the distributions of the mass of the lepton pair reconstructed in the ID and the MS. Additionally, the following fit variable is considered:

$$\rho = \frac{P_T^{MS} - P_T^{ID}}{P_T^{ID}}, \tag{10.12}$$

which represents the P_T imbalance (the difference between the ID and the MS).

The momentum correction factors are propagated to the combined muon momentum using a weighted average:

$$P_T^{Cor,CB} = f \cdot P_T^{Cor,ID} + (1-f) \cdot P_T^{Cor,MS}, \tag{10.13}$$

where the weight f is measured in MC simulation using the same equation.

Chapter 11

Hadronic recoil calibration

As mentioned in Sec. 5.4, due to discrepancies between the data and simulation, this analysis uses a hadronic recoil algorithm for the missing transverse energy reconstruction. The missing transverse energy (E_T^{miss}) significantly affects the W-boson measurement, so it is important to have a solid understanding of discrepancies in hadronic recoil. In Sec. 11.1 the hadronic recoil calibration procedure is described. Sec. 11.2 presents the procedure of the hadronic recoil resolution correction. In Sec. 11.3 the hadronic recoil bias determination is presented. The summary of the hadronic recoil calibration studies is given in Sec. 11.4.

11.1 Introduction

This analysis uses a standard hadronic recoil calibration procedure, described in details in [93], that was modified and adapted for the $\sqrt{s}$ = 2.76 TeV data sample. The procedure, described in [93] consists of three main steps.

In the first step, the differences in the pile-up modeling are corrected. Possible discrepancies are usually corrected by reweighting the average number of interactions per bunch crossing in MC to match the data. Due to the precision of the pile-up modeling at $\sqrt{s}$ = 2.76 TeV (Fig. 11.1) a precise reweighting is impossible. However, since the mean number of interactions per bunch crossing is below 1, the effect of pile-up mismodelling on E_T^{miss} distribution can be neglected.

In the second and the third steps, possible discrepancies in the resolution and the scale of the hadronic recoil are corrected. The performance of hadronic recoil algorithm can be studied in MC simulation using the projection of hadronic recoil vector $\vec{HR}$ on the direction of

the transverse momentum of the vector boson, as shown in Fig. 11.2. This projection can be divided into perpendicular $u_\perp$ and parallel $u_\parallel$ components as follows:

$$u_\parallel = \vec{v_{xy}} \cdot \vec{HR}, \tag{11.1}$$

$$u_\perp = v_x \cdot HR_y - v_y \cdot HR_x, \tag{11.2}$$

where $\vec{v_{xy}}$ is a unit vector along the transverse component of a vector boson momentum and v_x and v_y are its projections on the x and y axis respectively. In the case of the generator level kinematics $u_\parallel = -P_T^{bos}$ and $u_\perp = 0$. However, the limited calorimeter resolution causes relatively wide distributions for these projections. The parallel component $u_\parallel$ is sensitive to a possible bias in the hadronic recoil, while the perpendicular $u_\perp$ can be used for determination of the resolution discrepancies. The mean and the width of these distributions can depend on different variables, such as a mean number of interactions in an event per bunch crossing, hadronic activity and P_T^{bos}.

It is very convenient to use Z-boson decays for hadronic recoil calibration since their transverse momentum P_T^Z can be determined not only from the hadronic recoil but also from their decay products. It is observed that the P_T^Z resolution from a lepton reconstruction is 3-4 times more precise than the one extracted from a hadronic recoil. This allows leptonically reconstructed P_T^Z to be treated as a reference P_T of the boson and $u_\perp$ and $u_\parallel$ to be directly compared in the data and the simulation. However, the small size of the Z sample in the 2.76 TeV data leads to a high statistical error for this method.

The hadronic recoil calibration constants can also be derived from the W-boson decays. In order to exclude a possible bias from the P_T^W mismodelling in simulation, these calibration constants are derived through the data-MC comparison of the P_T^W independent distributions (such as M_T^W).

In this analysis, a combined procedure based on Z and W-bosons decays is used for a hadronic recoil calibration.

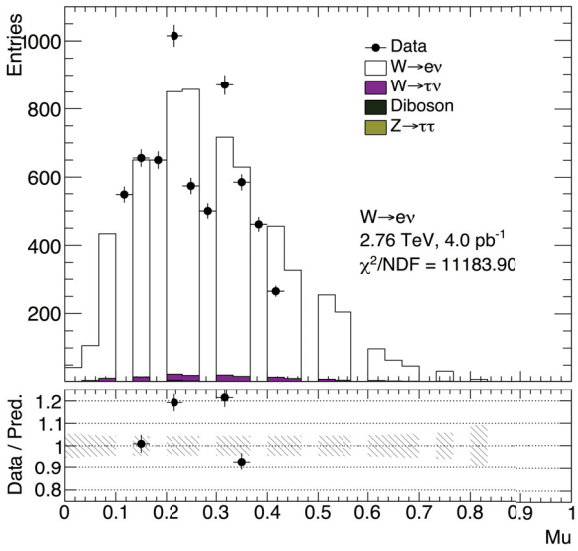

Fig. 11.1: Mean number of interactions per bunch crossing in $W \to e\nu$ analysis.

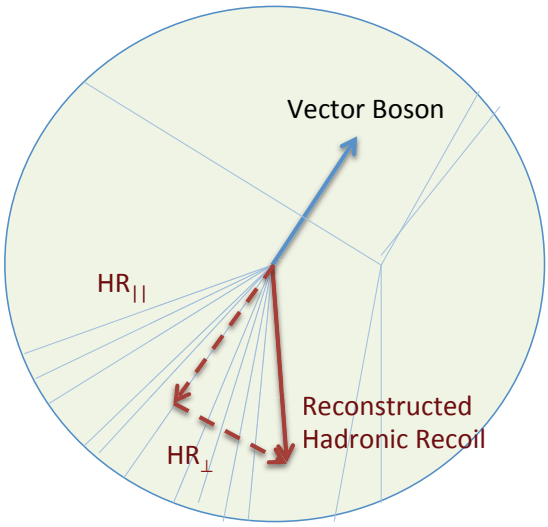

Fig. 11.2: Parallel and perpendicular projections of the hadronic recoil with respect to the transverse momentum of the vector boson [58].

11.2 Hadronic recoil resolution correction

The event activity plays an important role in the E_T^{miss} reconstruction. Since $\sum E_T$ and the hadronic recoil are correlated, the possible mismodelling of the event activity can lead to differences between the data and the Monte Carlo E_T^{miss} resolution. There are two ways to correct the resolution (Fig. 11.3):

- A two-step procedure, shown as path 1-2-3 in Fig. 11.3. In the first step, the $\sum E_T$ distribution in the simulation is corrected to match the data. In the second step, the remaining differences in hadronic recoil resolution between data and simulation are corrected.
- As a one-step procedure, where the second order effects on E_T^{miss} coming from $\sum E_T$ modeling are neglected and the resolution differences between data and MC corrected directly. This procedure is shown as the path 1-2′ in Fig. 11.3.

Both methods of hadronic recoil resolution correction are described in the following sections

11.2.1 Event activity correction

The distributions of event activity are shown in Fig. 11.4. A visible shift between the data and the MC distribution for both W boson channels is observed. The standard procedure of hadronic recoil resolution correction (used in the M_T^W measurement at 7 TeV [93]) uses a Smirnov transformation applied on the distributions of $\sum E_T$ and P_T^{bos} from simulated events. Distributions of the event activity in the Z-boson candidate events are shown in Fig. 11.5. The discrepancies between data and simulation are not visible using the χ^2-test, therefore this procedure cannot be adapted for the $\sqrt{s}$ = 2.76 TeV data. The W-boson candidate events are used to determine the event activity correction instead.

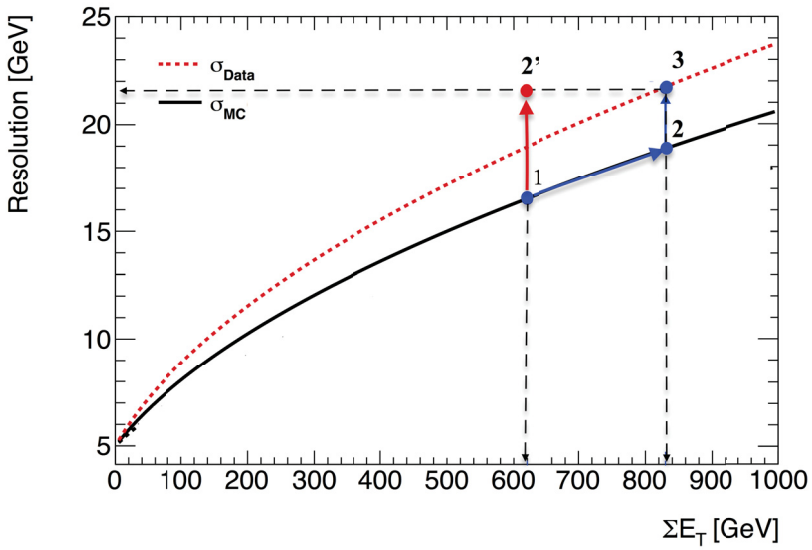

Fig. 11.3: Schematic view of hadronic recoil correction procedure: this figure illustrates the resolution of $u_\perp$ as a function of event activity $\sum E_T$. The dotted curve represents $u_\perp$ resolution in data(σ_{data}) and the solid black line a nominal $u_\perp$ resolution in simulation (σ_{MC}). Modified from [93].

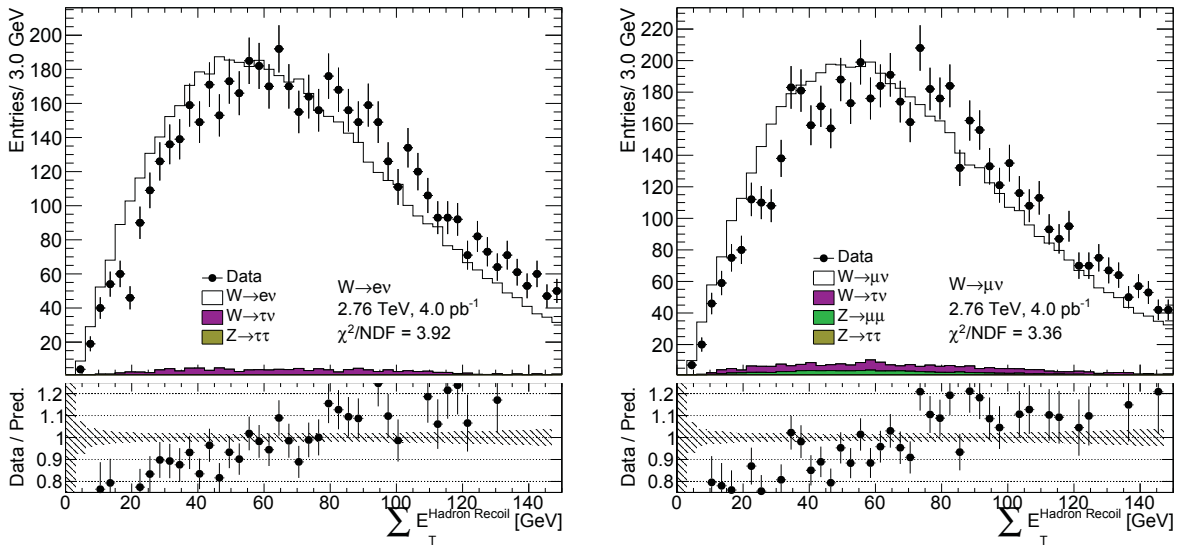

a) b)

Fig. 11.4: $\sum E_T$ distribution from a) the $W \to e\nu$ and b) the $W \to \mu\nu$ analysis selection.

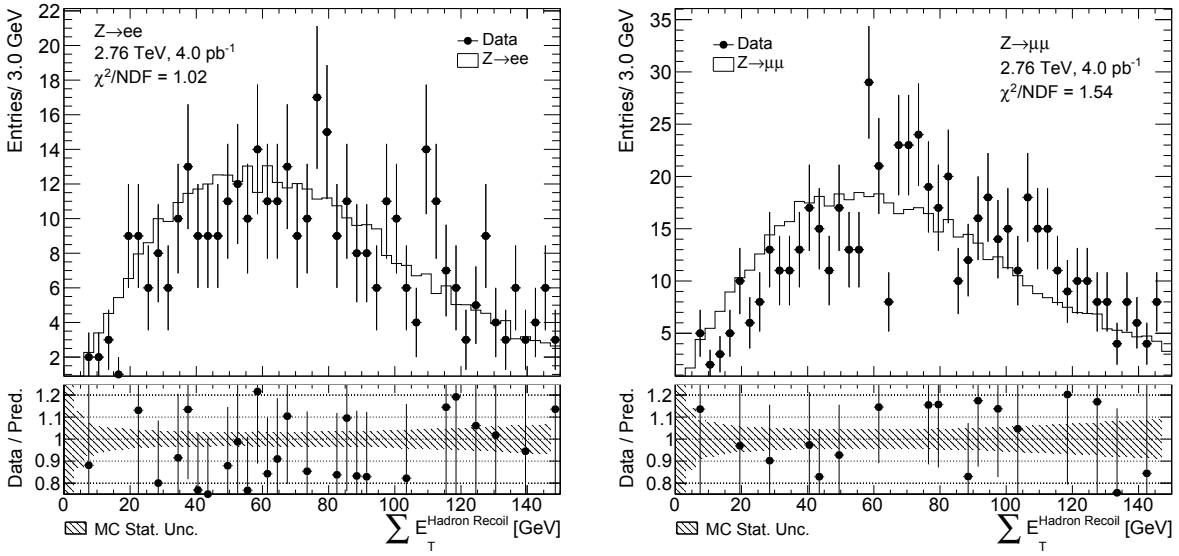

a) b)

Fig. 11.5: $\sum E_T$ distribution from a) the $Z \to ee$ and b) the $Z \to \mu\mu$ analysis selection.

The event activity $\sum E_T$ is correlated to the truth transverse momentum of the boson, as shown in Fig. 11.6. In order to avoid introducing a bias in the P_T^W spectrum by the reweighting, the reweighting constant are considered as a function of reconstructed W-boson transverse momentum $P_T^{W,rec}$. For each $P_T^{W,rec}$ bin the reweighting scale factors are calculated as:

$$SF^{channel} = \frac{\sum E_T^{data,\,selection}}{\sum E_T^{MC,\,no\,selection}}, \tag{11.3}$$

where $\sum E_T^{data,\,selection}$ is a $\sum E_T$ distribution inside a given $P_T^{W,rec}$ for events satisfying the full event selection. The second term, $\sum E_T^{MC,\,no\,selection}$, stands for $\sum E_T$ distribution in MC before applying event selection. The total number of $P_T^{W,rec}$ bins is 6. The scale factors are applied as a reconstructed weight on simulated events.

The distribution of $\sum E_T$ for two different $P_T^{W,rec}$ regions is shown in Fig.11.7. The scale factors determined for $W \to e\nu$ and $W \to \mu\nu$ MC samples are shown in Fig. 11.8. The $\sum E_T$ distribution after the correction is shown in Fig. 11.9. This correction has almost no effect on the reconstructed transverse momentum distribution and introduces only a small change in the truth boson spectrum, as shown in Fig. 11.10.

Method cross-check

The method can be cross-checked using the approximation of the correction constants by first or second degree polynomial using the χ^2-fit [94], in which the following quantity is minimized:

$$\chi^2(\mu) = \sum_{i=1}^{N} \frac{(y_i - y(x_i, \mu))^2}{\sigma_i^2}, \tag{11.4}$$

where index i runs over all of the data points (x_i, y_i), the σ_i is the error of the i-th measurement, $\mu \in \boldsymbol{R}^{n+1}$ is the fit parameters vector and $y(x_i, \mu) = \mu_0 + \mu_1 \cdot x_i + ... + \mu_n \cdot x_i^n$ in case of poly-

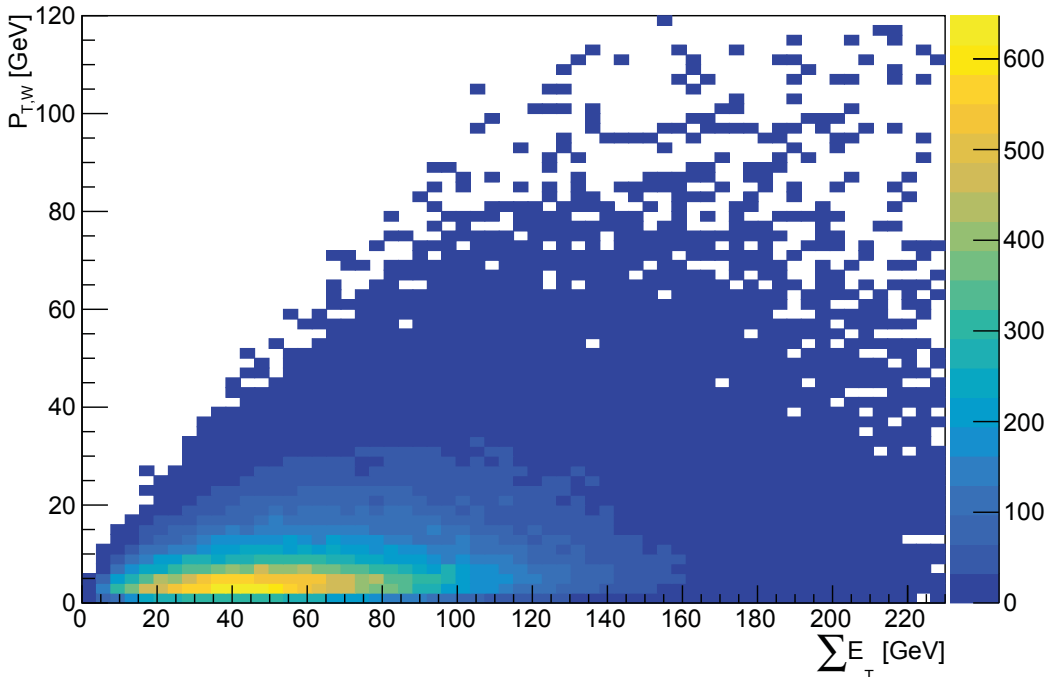

Fig. 11.6: Distribution of $\sum E_T$ vs true transverse momentum of the W boson ($P_T^{W\ truth}$) in the $W^+ \to e^+\nu$ MC sample.

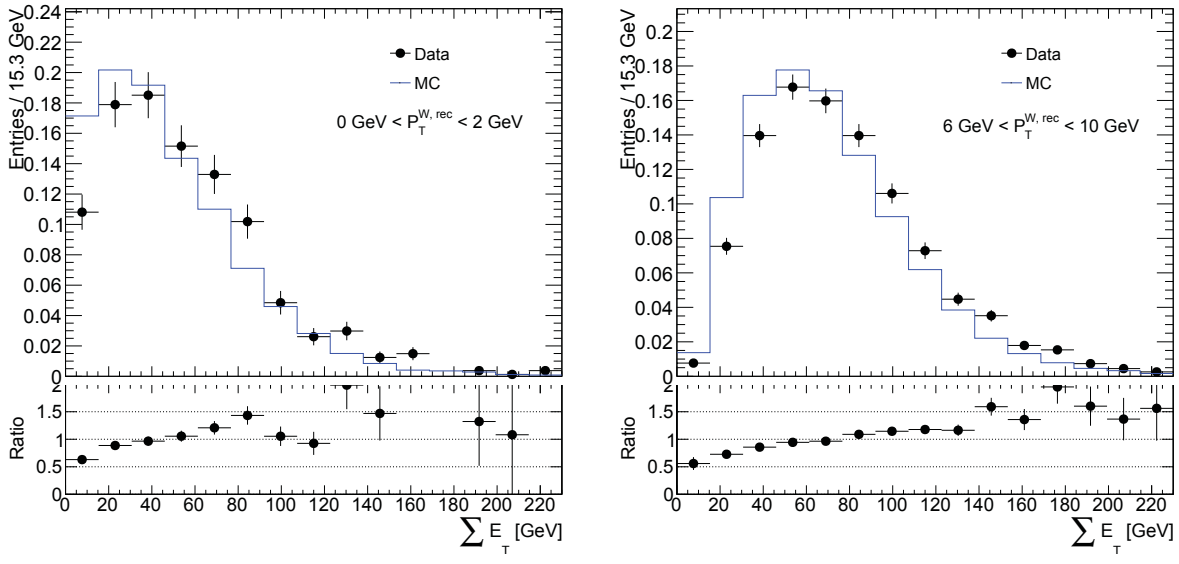

a) b)

Fig. 11.7: $\sum E_T$ distribution for the a) $P_T^{W,rec} < 2$ GeV b) 6 GeV $< P_T^{W,rec} < 10$ GeV .

nomial order n. The covariance matrix $\mathbf{C}$ for the obtained fit parameters is calculated from a

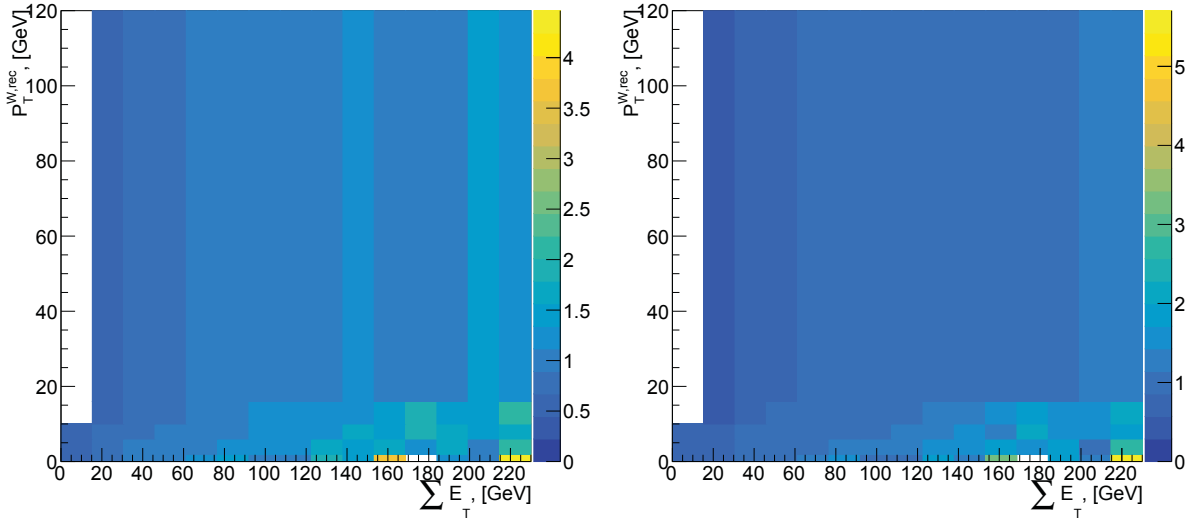

Fig. 11.8: $\sum E_T$ reweighting constants derived for a) $W^+ \to e\nu$ and b) $W^+ \to \mu\nu$ MC sample.

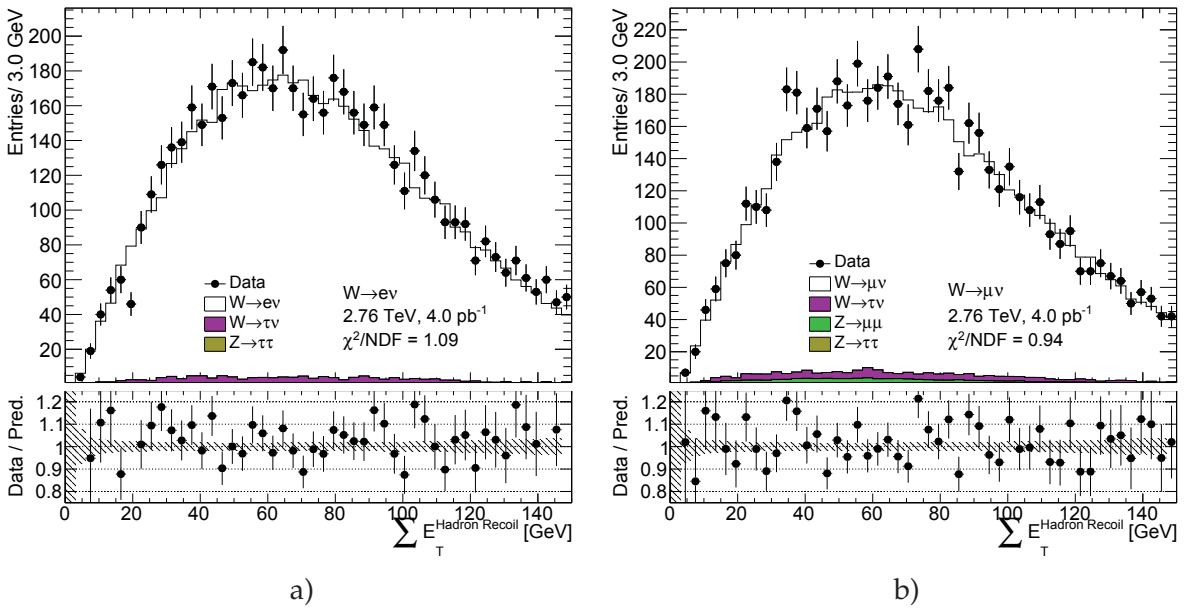

Fig. 11.9: $\sum E_T$ distribution from a) the $W \to e\nu$ and b) the $W \to \mu\nu$ analysis channels after applying $\sum E_T$ correction.

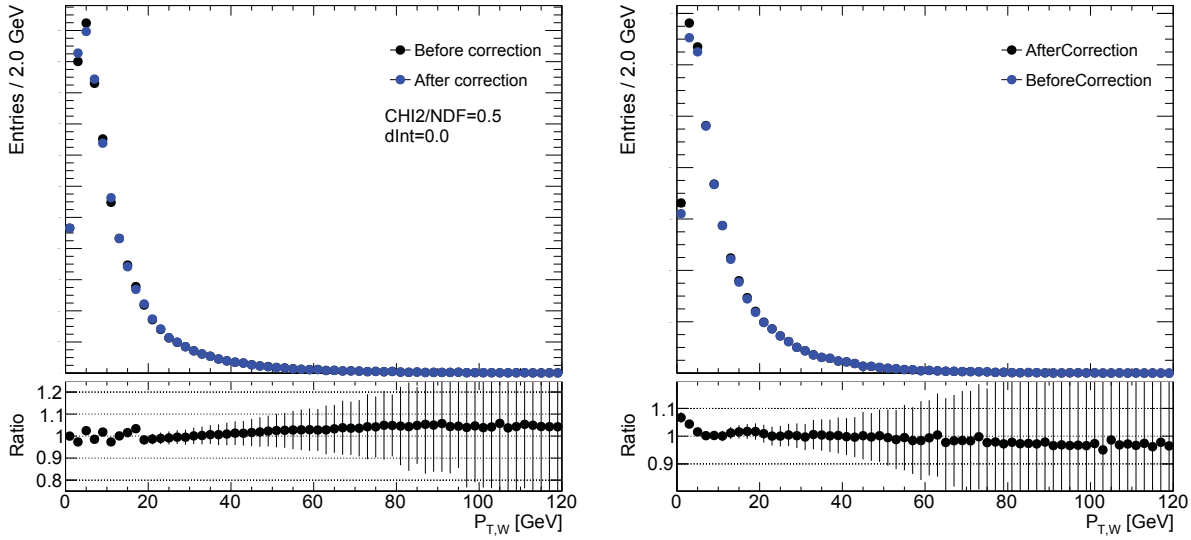

a) b)

Fig. 11.10: Effect of the $\sum E_T$ reweighting on a) reconstructed transverse momentum of the boson and b) truth transverse momentum of the W-boson.

derivative of the minimized χ^2 function as:

$$C_{ij} = 2\Big(\frac{\delta\chi^2}{\delta\mu_i\delta\mu_j}\Big)^{-1}. \tag{11.5}$$

This method allows removing effects related to statistical fluctuations in data, especially for the high $\sum E_T$ regions (with a low number of events). The reweighting constants after applying smoothing procedure are shown in Fig. 11.11.

Statistical error estimation

The statistical error related to the $\sum E_T$ reweighting procedure is estimated using pseudo-experiments (as described in Chap.13). The parameters of polynomial, obtained from the χ^2-fit are varied inside each $P_T^{W,rec}$ bin within their fit uncertainties using the Eq. 13.3.

Because of the possible correlations between the fit parameters, a multivariate Gaussian distribution is used. This distribution is calculated as:

$$p(x;\mu,\mathbf{C}) = \frac{1}{(2\pi)^{n/2}|\mathbf{C}|^{1/2}} exp\Big(-\frac{1}{2}(x-\mu)^T\mathbf{C}^{-1}(x-\mu)\Big), \tag{11.6}$$

where $x \in \boldsymbol{R}^n$ and $(x-\mu)^T$ is a transpose of the vector $(x-\mu)$. For the statistical error determination a total of 25 pseudo-experiments is used. The total error is calculated using Eq.13.4.

Effect of the $\sum E_T$ correction on the cross section measurement

The effect of the $\sum E_T$ correction on the measured cross section is estimated by applying different correction factors on simulated events. The related uncertainty is estimated by calculating

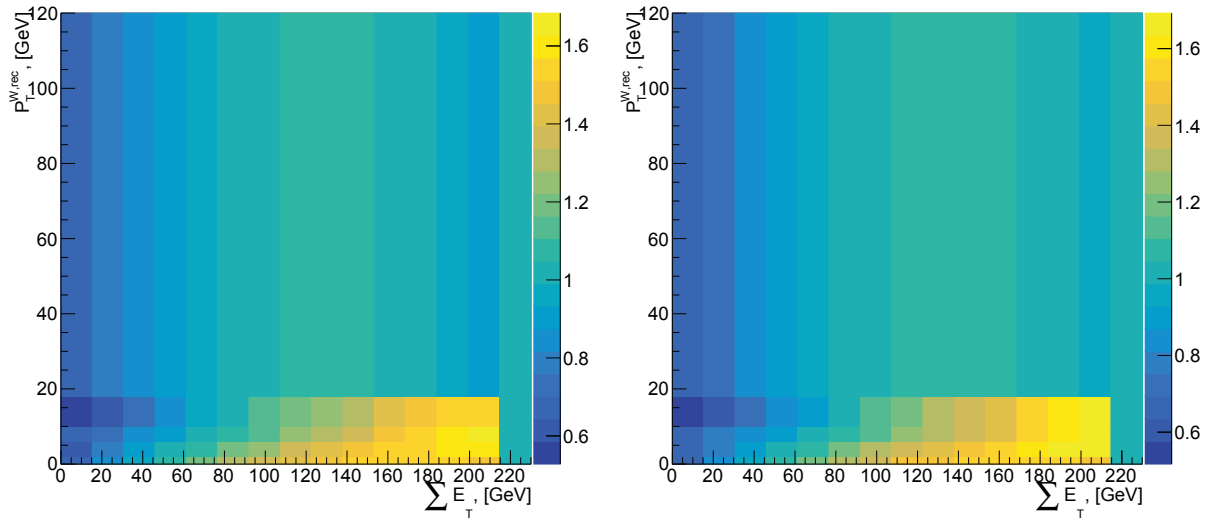

Fig. 11.11: $\sum E_T$ reweighting constants derived for a) $W^+ \to e\nu$ and b) $W^+ \to \mu\nu$ analysis channels after polynomial approximation.

Table 11.1: Effect of $\sum E_T$ correction on C_W for different analysis channels and $\sum E_T$ correction methods.

Channel	δC_W no approximation	δC_W polynomial order 2	δC_W polynomial order 1	δC_W Toy MC
$W^+ \to e^+\nu$	0.48%	0.39%	0.31%	0.03%
$W^- \to e^-\nu$	0.49%	0.33%	0.22%	0.03%
$W^+ \to \mu^+\nu$	-0.27%	-0.20%	-0.28%	0.03%
$W^- \to \mu^-\nu$	-0.29%	-0.21%	-0.27%	0.03%

a difference in correction factor C_W using the On/Off method (see Chap. 13). The overall effect of the $\sum E_T$ correction for different correction methods is summarized in Tab. 11.1. Statistical error, estimated using pseudo-experiments, is negligible. The systematic uncertainty is calculated as a difference between C_W for two methods and is observed to be small.

The behavior of the hadronic recoil should not depend on the flavor of the analysis. However, it is observed, that in the data correction of the hadronic recoil mismodelling introduces changes to C_W in the different directions. This discrepancies are considered to come from the introduced bias in the P_T^W distributions. The correction is not used in the final analysis.

11.2.2 Resolution correction using Z boson candidate events

A possible way to check the hadronic recoil resolution effects is to study $u_\perp$ and $u_\parallel - P_T^Z$ distributions in Z-boson candidate events. This procedure assumes that the hadronic recoil resolution has a significant effect on simulation, while the effect of $\sum E_T$ mismodelling is subleading.

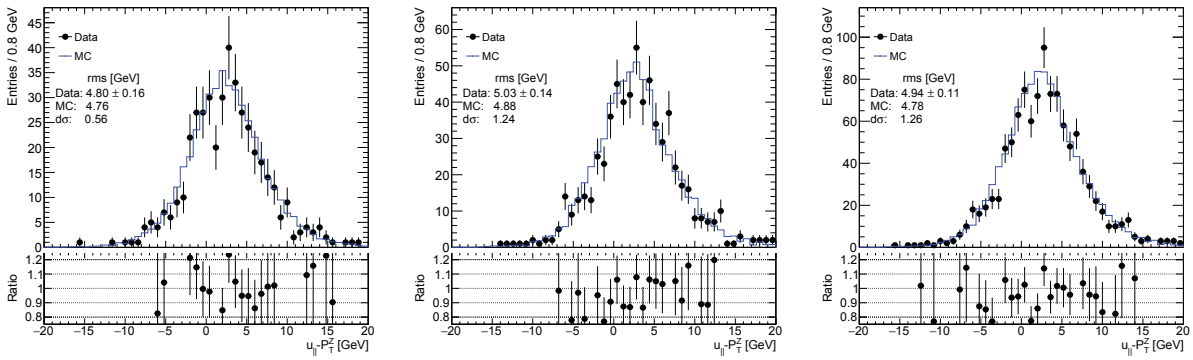

a) b) c)

Fig. 11.12: Difference between parallel hadronic recoil component ($u_{\parallel}$) and the transverse momentum of the Z-boson from a) the $Z \rightarrow ee$ b) $Z \rightarrow \mu\mu$ and c) combined analysis channels. The expected contribution from signal is estimated with Monte Carlo simulation, wherea any background sources are considered negligible.

A difference in hadronic recoil resolutions ($d\sigma$) between the data and the simulation can be obtained as:

$$d\sigma = \sqrt{\sigma^2_{data} - \sigma^2_{MC}}, \tag{11.7}$$

where σ_{data} and σ_{MC} are the RMS of some distribution in the data and simulation respectively. The statistical uncertainty of the RMS is calculated as [95]:

$$\delta(\sigma_{data}) = \frac{\sigma_{data}}{\sqrt{2N}}, \tag{11.8}$$

where N is the number of events. The distribution of $u_{\perp}$ and $u_{\parallel} - P^Z_T$ for $Z \rightarrow ll$ event selection are shown in Fig. 11.12-Fig. 11.13. A typical resolution uncertainty for data is around 0.1 GeV, while the difference in hadronic recoil resolution is around 1.0 GeV. The overall difference in resolutions is consistent between $u_{\perp}$ and $u_{\parallel} - P^Z_T$ distributions. For the resolution correction it was decided to use the resolution difference $d\sigma$, obtained from combined $Z \rightarrow ll$ analysis, where $d\sigma$ = 1.3 GeV.

The hadronic recoil resolution in simulation is corrected using the Gaussian smearing of perpendicular and parallel component of hadronic recoil using the equations:

$$u'_{\parallel} = u_{\parallel} + Gaus(0, d\sigma) \tag{11.9}$$

$$u'_{\perp} = u_{\perp} + Gaus(0, d\sigma), \tag{11.10}$$

Estimation of systematic uncertainty

The effect of hadronic recoil resolution smearing correction is estimated using the On/Off method (Chap. 13). The scan through the possible $d\sigma$ parameters shows a decrease in the correction factor C_W with the growth of the smearing parameter $d\sigma$ (Fig. 11.14).

The systematic uncertainty is estimated by repeating the correction procedure 25 times (Fig. 11.15). The mean of the obtained parameters C_W is treated as a systematic ucertainty

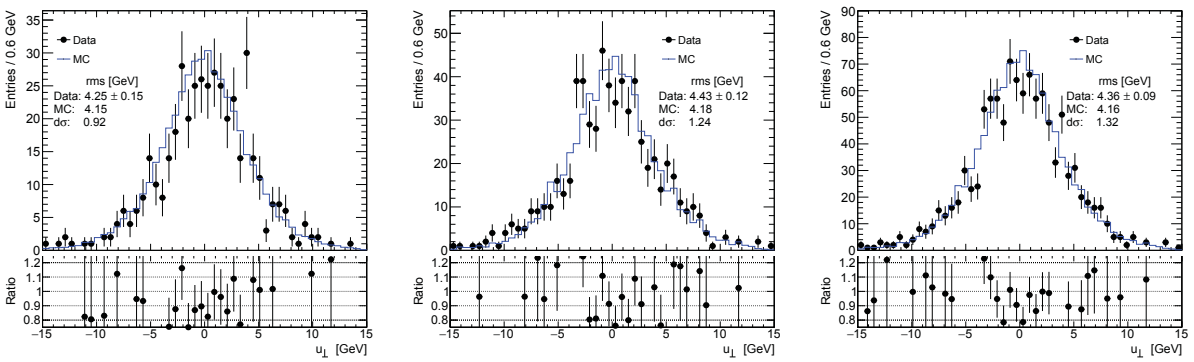

a) b) c)

Fig. 11.13: Perpendicular hadronic recoil component ($u_\perp$) from a) the $Z \to ee$ b) $Z \to \mu\mu$ and c) combined analysis channels. The expected contribution from signal is estimated with Monte Carlo simulation, whereas any background sources are considered negligible..

Table 11.2: The effect of hadronic recoil smearing correction on C_W for different channels. The statistical error (noted *stat.err.*) of the mean value is estimated using Eq. 11.11.

Channel	$\delta C_W \pm stat.err.$	rms
$W^+ \to e^+\nu$	-0.20±0.01%	0.04%
$W^- \to e^-\nu$	-0.11±0.01%	0.06%
$W^+ \to \mu^+\nu$	-0.16±0.01%	0.04%
$W^- \to \mu^-\nu$	-0.12±0.01%	0.07%

of the resolution correction. Tab. 11.2 presents the results of C_W systematic error measurement together with standard deviation and the error of the mean, calculated as:

$$\delta\Big(C_W\Big) = \frac{\sigma(C_W)}{\sqrt{N}}, \tag{11.11}$$

where $\sigma(C_w)$ is the standard deviation of the C_W distribution and $N = 25$ is the total number of repetitions used. The overall systematic effect is below 0.2% for each analysis channel, which is significantly lower than a statistical uncertainty for the W-boson analyses (Chap. 13).

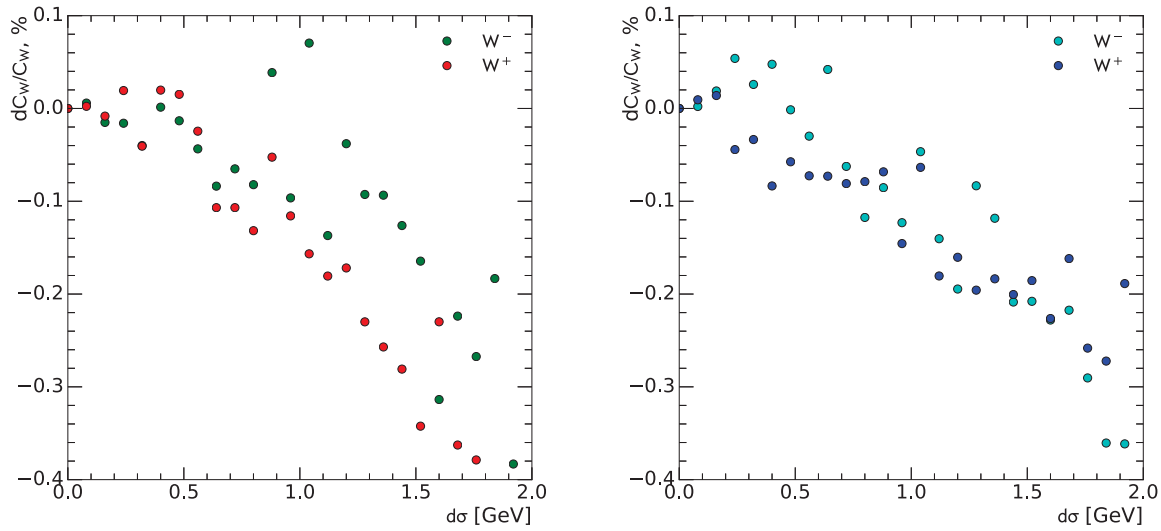

a) b)

Fig. 11.14: Shift in correction factor C_W from hadronic recoil resolution correction as a a function of smearing correction ($d\sigma$) for a) $W \to e\nu$ b) $W \to \mu\nu$ analysis channels.

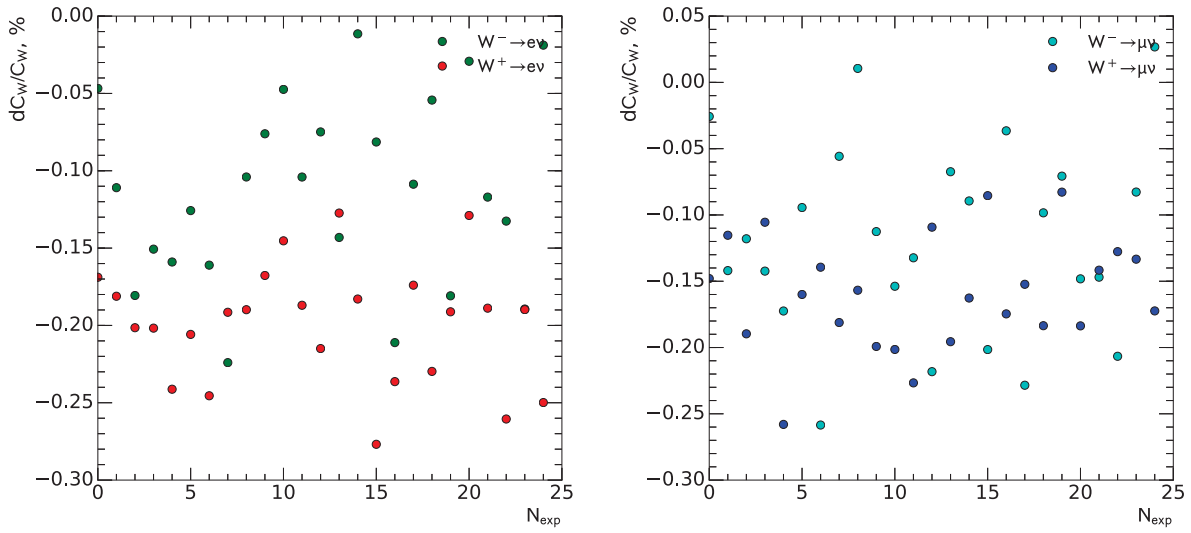

a) b)

Fig. 11.15: Shift in correction factor C_W from hadronic recoil resolution correction ($d\sigma$ = 1.3 GeV) for a) $W \to e\nu$ b) $W \to \mu\nu$ analysis channels as a function of number of repetitions.

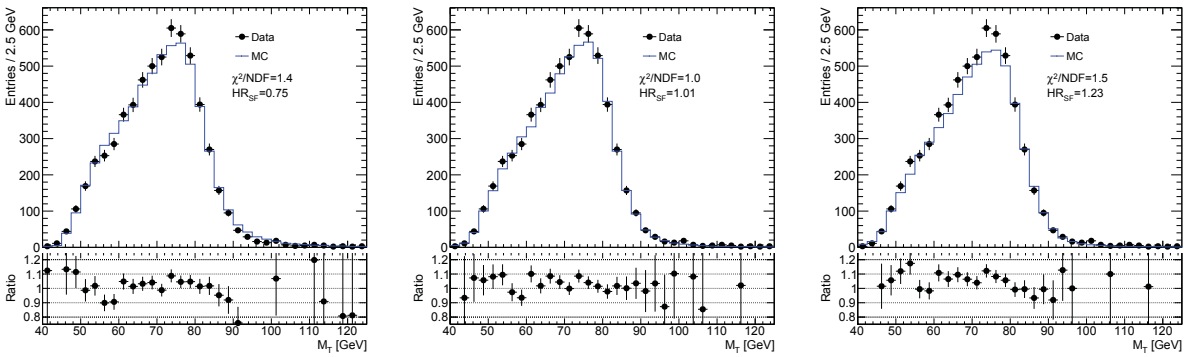

a) b) c)

Fig. 11.16: Transverse mass distribution for the $W \to e\nu$ event candidates for different choice of hadronic recoil correction factors: a) HR_{SF}=0.75 b) HR_{SF}= 1.1 c) HR_{SF}=1.23. The expected contributions from signal and background processes are estimated using Monte Carlo simulation.

11.3 Hadronic recoil bias correction

As discussed in Sec. 11.1, the hadronic recoil distribution in the simulation may be shifted with respect to the data due to the mismodelling of the underlying event and calorimeter cluster responses. The correction of the hadronic recoil bias is performed by applying the relevant correction factor HR_{SF} to the hadronic recoil in simulation:

$$u_{\parallel}^{cor} = u_{\parallel} \cdot HR_{SF}, \tag{11.12}$$

where $u_{\parallel}$ is the parallel component of the hadronic recoil measured with the respect to the W-boson direction.

The determination of the optimal parameter HR_{SF} is performed through the scan of correction factor values. It is assumed that the best value of the hadronic recoil bias corresponds to the best agreement between the data and simulation, tested using the χ^2-test, calculated as sum of the χ^2 over the all bins. The correction value is obtained through the χ^2 fit of χ^2-test results using the function:

$$\chi^2 = \frac{(HR_{SF} - sf_{best})^2}{\sigma_{sf}^2} + \chi_0^2, \tag{11.13}$$

where sf_{best} is the hadronic recoil correction scale factor, obtained from the χ^2 fit, σ_{sf} is the statistical error of correction factor and χ_0^2 is the value of χ^2 at its minimum.

In the following sections, methods of hadronic recoil bias determination using W and Z-boson candidate events are discussed.

11.3.1 Bias determination from the M_T^W distribution

The hadronic recoil bias determination is performed using distributions that are not sensitive to the true P_T^W spectrum, to exclude the effect of possible P_T^W mismodelling in the simulation. One of the optimal choices is the M_T^W distribution. Transverse mass distributions for different values of the correction factors HR_{SF} is shown in Fig. 11.16.

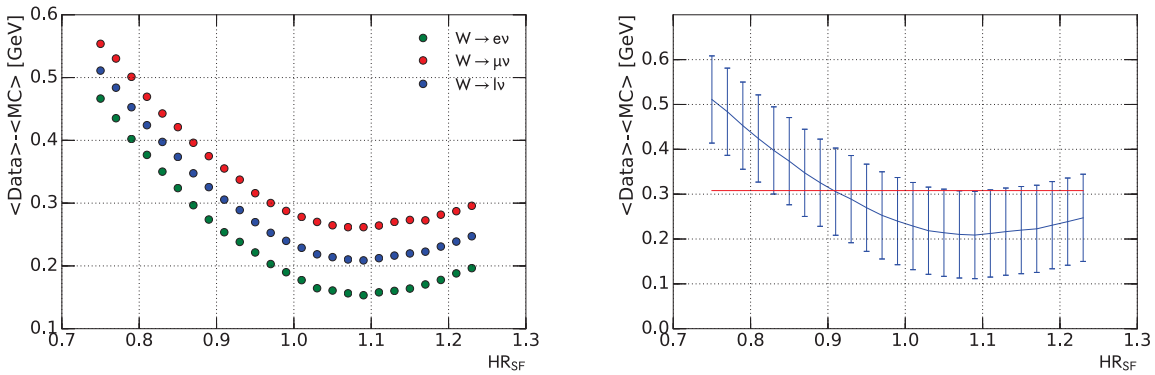

a) b)

Fig. 11.17: Distribution of the difference in the mean transverse mass $< M_T^W >$ between data and simulation as a function of the hadronic recoil correction factor HR_{SF} a) for various W-boson decay channels and b) for combined $W \to l\nu$ selection.

One of the possible methods to determine the correction factor is to use the difference in the mean of the transverse mass distributions in data and simulation (Fig. 11.17). The statistical uncertainty on HR_{SF} is considered to be the dominant source of uncertainty. It is estimated as the standard error of the mean $\delta(< M_T^W >)$, calculated as:

$$\delta\Big(< M_T^W > \Big) = \frac{\sigma(M_T^W)}{\sqrt{N}}, \tag{11.14}$$

where $\sigma(M_T^W)$ is the standard deviation of M_T^W distribution and N is the total number of events. The minimum difference is reached at $HR_{SF} = 1.1 \pm 0.2$. Due to the large statistical uncertainty of this method, it is used as a cross-check for other methods of hadronic recoil bias determination.

The distributions of χ^2-test values for different values of HR_{SF} for the W-boson selection are shown in Fig. 11.18 a). Because of a possible mismodelling of the tail of the M_T^W distribution, events with $M_T^W > 100$ GeV are not included in the χ^2-test. There is a small peak visible in the χ^2 distribution for $W \to e\nu$ events, that is assumed to come from the missing multijet background contribution. Hadronic recoil bias parameters are determined through the fit of χ^2-test distribution in the combined $W \to l\nu$ analysis using Eq. 11.13. The resulting correction factor is $HR_{SF} = 1.02$, with the statistical uncertainty of 0.06.

The range of the M_T^W distribution used in the χ^2-test introduces an additional source of systematic uncertainty. This uncertainty is estimated by repeating the χ^2-test and χ^2 fit procedure for different M_T^W ranges, as shown in Fig. 11.19. The resulting hadronic recoil correction factor is $HR_{SF} = 1.02 \pm 0.06(stat.) \pm 0.03(syst.) = 1.02 \pm 0.07$.

11.3.2 Bias determination from the $u_{\parallel}$ distribution

The correction factors can be determined from the Z sample using the $u_{\parallel}/P_T^Z$ distribution, as shown in Fig. 11.20. Results of the χ^2-test for different values of HR_{SF} for data and simulation for $Z \to ll$ selection are shown in Fig. 11.21. A χ^2 fit of the χ^2-test values distribution for

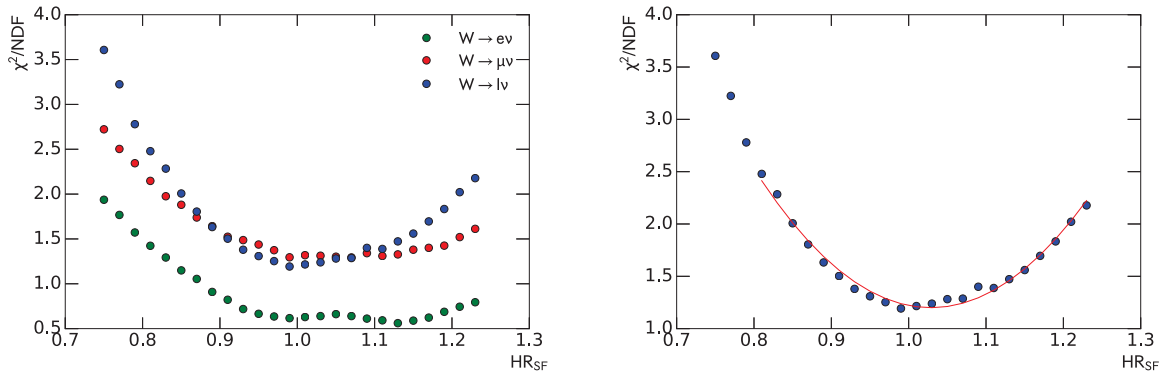

a) b)

Fig. 11.18: Distribution of χ^2-test results for and simulation for $< M_T^W >$ distribution as a function of hadronic recoil correction factor HR_{SF} a) for different W boson channels. b) for combined $W \to l\nu$ selection and the χ^2 fit results.

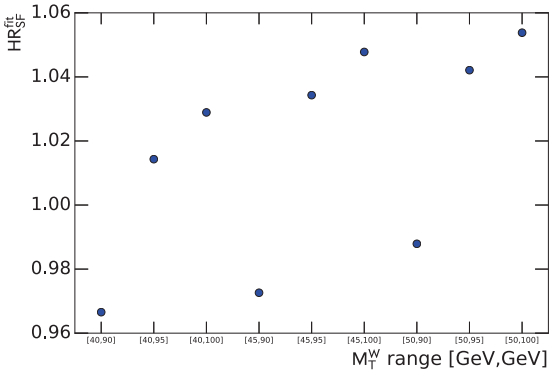

Fig. 11.19: Hadronic recoil scale correction factors as a function of M_T^W fit range.

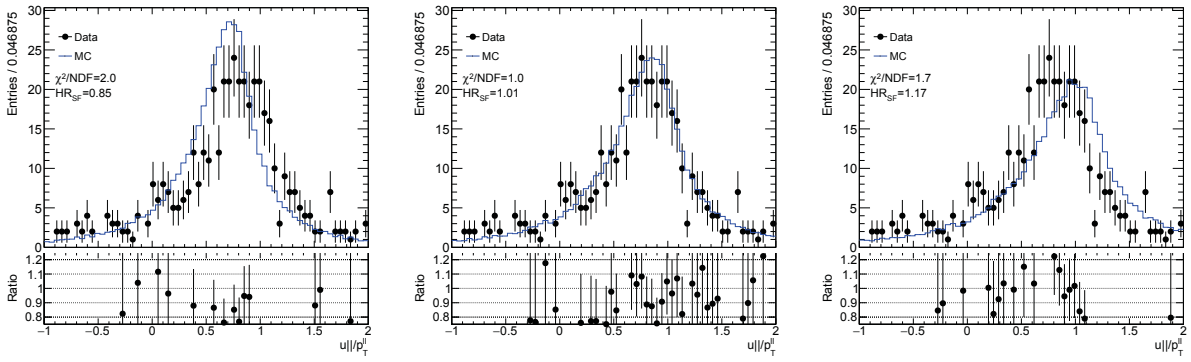

a) b) c)

Fig. 11.20: Hadronic recoil component $u_{\parallel}$ divided by the transverse momentum of the Z-boson for $Z \rightarrow ee$ event selection for different hadronic recoil correction factors: a) HR_{SF}=0.75, b) HR_{SF}= 1.1 and c) HR_{SF}=1.23.

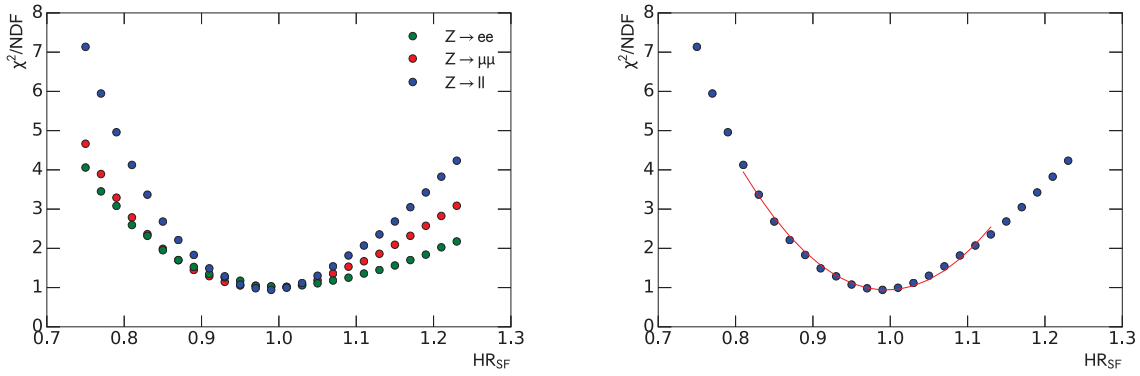

a) b)

Fig. 11.21: Distribution of χ^2-test values for data and simulation for $u_{\parallel}/P_T^{bos}$ distribution as a function of hadronic recoil scale correction factors HR_{SF} for a) different Z boson channels. b) for combined $Z \rightarrow ll$ selection with the χ^2 fit results.

combined channel gives the most precise estimation of the hadronic recoil bias, $HR_{SF} = 1.00 \pm 0.01$.

11.3.3 Systematic uncertainty estimation

A summary of the hadronic recoil correction factors is shown in Tab. 11.3. The results are consistent with each other within the uncertainty. In the final step, it was decided to choose HR_{SF} determined with the smallest uncertainty (from $Z \rightarrow ll$ analysis). Scale factors extracted using other methods are used as a cross-check.

The effect of the hadronic recoil bias correction for different bias correction factors are presented in Fig. 11.22. The systematic error, coming from the bias correction, is estimated using the Offset method (see Chap. 13).

Table 11.3: Hadronic recoil bias determination results and errors for different methods.

Method	SF	error
Mean M_T^W	1.10	0.2
M_T^W χ^2	1.01	0.07
$u_\parallel$ χ^2	1.00	0.014

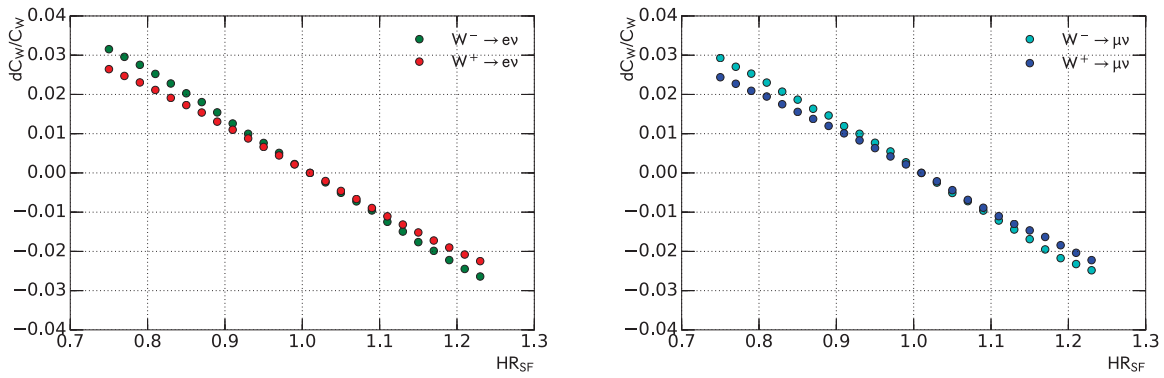

a) b)

Fig. 11.22: Shift in the C_W for a different hadronic recoil scale correction factors for a) $W \to e\nu$ b) $W \to \mu\nu$ event selection.

11.4 Summary of hadronic recoil calibration

Using the standard E_T^{miss} reconstruction algorithm the data is not described properly by the simulation, therefore it has decided to use a dedicated hadronic recoil algorithm for E_T^{miss} reconstruction. The methodology of hadronic recoil calibration was developed for the $\sqrt{s} = 2.76$ TeV data.

The hadronic recoil calibration procedure consists of two parts: the correction of resolution effects and the bias correction. The hadronic recoil resolution has been corrected using the following methods:

- Event activity correction through the reweighting of $\sum E_T$ distribution. Different methods of the data/MC ratio parameterization have been developed and showed a consistent result. However, this method gives a nonphysical difference between electron and muon channels, that cannot be accounted for the data uncertainty, so it was decided to drop this method;

- Smearing correction of the hadronic recoil. This method uses the Z sample to determine the difference in resolutions of the hadronic recoil components. The overall effect of these corrections was estimated by repeating the smearing 25 times and consistent between electron and muon channels.

The bias of hadronic recoil is estimated using W and Z-boson candidate with the following three methods:

Table 11.4: Systematic uncertainties from the hadronic recoil calibration for different W boson decay channels.

Systematic source	$W^+ \to e^+\nu$	$W^- \to e^-\nu$	$W^+ \to \mu^+\nu$	$W^- \to \mu^-\nu$
Hadronic recoil resolution	-0.2%	-0.11%	-0.16%	-0.12%
Hadronic recoil scale	0.21%	0.20%	0.23%	0.24%

- Comparison of the mean of the M_T^W distributions between data and simulation. This method gives the biggest uncertainty and is used as a cross-check for other results;
- From the χ^2 fit of the χ^2-test results for M_T^W distribution for different values of hadronic recoil corrections. Error on this method is dominated by the statistics;
- From the χ^2 fit of the χ^2-test results for $u_\parallel / P_T^Z$ distribution for different values of hadronic recoil corrections. Despite the limited statistics of the Z-boson sample, this method gives the best sensitivity to the hadronic recoil scale choice. It was decided to use this method as a baseline for the hadronic recoil bias.

The corresponding systematic uncertainties for the hadronic recoil calibration are summarized in Tab. 11.4. The overall uncertainty on E_T^{miss} is around 0.3 % for W-boson decay channels.

Chapter 12

Background estimation

Main backgrounds for W analysis are coming from:

- Processes with τ leptons, misidentified as an electron or muon;
- Leptonic Z-boson decays with one missreconstructed lepton;
- QCD (or multijet) processes. In the electron channel the background is mostly jets faking electrons, while in the muon channel it consists of real muons produced in decays of mesons.

Most of the background processes are estimated using the MC simulation. In order to estimate the expected number of events, the simulated events are normalized to the cross-section predictions. Full list of simulated background samples together with the corresponding cross section predictions is shown in Tab. 12.1. The multijet background is estimated using data driven method, as described below.

Table 12.1: Background processes with their associated cross sections and uncertainties (if given) for $W \to l\nu$ and $Z \to ll$ processes. The quoted cross sections are used to normalize expected number of events.

Process	$\sigma \cdot BR(\pm\text{unc.})$ [pb]	Order
$W^+ \to l\nu$	2116($\pm$41)	NNLO
$W^- \to l\nu$	1267($\pm$24)	NNLO
$Z \to ll$	303($\pm$6)	NNLO
$t\bar{t}$	7.41	LO
WW	0.6	LO
ZZ	0.7	LO
WZ	0.2	LO

12.1 Multijet background estimation

The jet can fake the W-boson signature with single isolated lepton and large E_T^{miss} in the event. Due to a large large theoretical uncertainties and high statistics needed, generation of MC simulation events for multijet background estimation becomes impractical. Instead data driven technique for multijet background estimation is used in $W \to e\nu$ and $W \to \mu\nu$ analysis channels. In case of $\sqrt{s}$ = 2.76 TeV data the expected contribution from the multijet background in the Z sample is below 1% [96], what is negligible compared to the statistical uncertainty (Fig. 14.15).

The template selection used in data driven method is applied to produce the multijet enriched and signal supressed region. The template selection uses the reversed identification or isolation criteria. It is assumed, that template selection does not introduce differences in multijet backgound shape compared to the signal region. The normalization constants are derived in the control region through the template fit. This section describes method of multijet background determination, that have been used in 2.76 TeV data.

12.1.1 Template selection

Because of the origin of the multijet background, relaxing the E_T^{miss} requirement allows to obtain higher statistics for a multijet template. Another possibility is to relax the transverse mass M_T^W requirement. Most of the multijet background events should contribute to the lower M_T^W values. A template can contain also contributions from other backgrounds (mostly coming from $W \to l\nu$).

In electron channel, template selection requires that the electron candidate fails medium identification criteria, but passes loose selection criteria. Control distributions for different template selection criteria in electron channel analysis are shown in Fig. 12.1. Relaxing E_T^{miss} criteria gives higher template statistics.

In the muon channel a template is build by inverting isolation criteria ($P_T^{cone,20} > 0.1$). Then, for the multijet background template the higher data statistics is achieved by relaxing transverse mass requirement $M_T^W > 40$ GeV (Fig. 12.2).

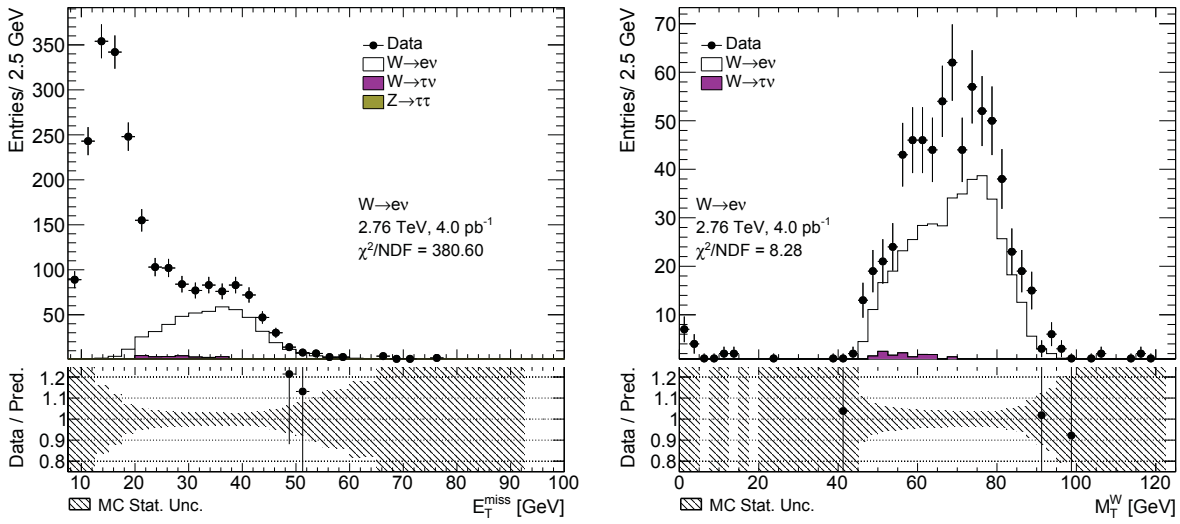

a) b)

Fig. 12.1: Distribution of a) missing transverse energy (E_T^{miss}) and b) transverse mass (M_T^W) from the multijet template selection for $W \to e\nu$ candidate events.

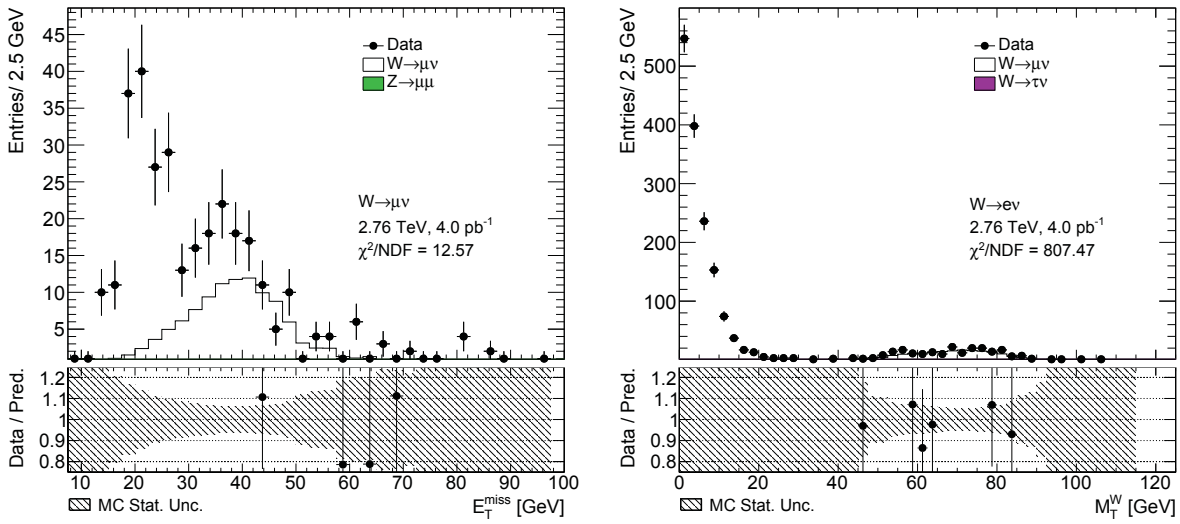

a) b)

Fig. 12.2: Distribution of a) missing transverse energy (E_T^{miss}) and b) transverse mass (M_T^W) from the multijet template selection for $W \to \mu\nu$ candidate events.

The electroweak processes (signal and other backgrounds) are subtracted from a template distribution. The total number of events in the template can be defined as:

$$N_{template} = N_{data}^{bkg\,enriched} - \sum_{j}^{MC} N_{MC_j}^{bkg\,enriched}, \tag{12.1}$$

where $N_{data}^{bkg\,enriched}$ and $N_{MC_j}^{bkg\,enriched}$ are numbers of the events in data and MC simulation respectively. The resulting template contains 1348 and 1509 events for $W \to e\nu$ and $W \to \mu\nu$ channels respectively.

12.1.2 Template normalization

The normalization constant for the template is obtained through the χ^2 fit to the data. The following model is used for the multijet background estimation:

$$M(x) = \sum_{i=1}^{N-1} f_i F_i(x) + (1 - \sum_{i=1}^{N-1} f_i) \cdot F_{QCD}(x), \tag{12.2}$$

where the index i goes over signal and electroweak background MC samples, x is a fit variable (E_T^{miss} or M_T^W), $F_i(x)$ and $F_{QCD}(x)$ are the probability density functions associated with signal and EWK background and multijet background template respectively. The fit parameters f_i, that represent the fraction of events in the fit region, are allowed to be varied within 5% uncertainty, in order to take into account luminosity and cross-section uncertainties.

The normalization constant of the multijet events is calculated from the obtained fit parameters as:

$$scale = \frac{(1 - \sum_i f_i) \cdot N_{Data}^{fit}}{N_{template}}, \tag{12.3}$$

where $\sum_i f_i$ is a sum signal and background fractions in the fit region, N_{Data}^{fit} is a number of data events and $N_{template}$ is a number of events in a multijet template. The χ^2 fit is performed separately for W^+, W^- and W analysis channels. The distributions before the inclusion of multijet background are shown in Fig. 12.3. The results of the fitting procedure are shown in Fig. 12.4 .

12.1.3 Systematic uncertainty

The uncertainty of the multijet background estimation method can be divided into four main components:

$$\delta_{QCD} = \sqrt{\delta_{fit\,unc}^2 + \delta_{MC}^2 + \delta_{fit\,bias}^2 + \delta_{template}^2}, \tag{12.4}$$

where $\delta_{fit\,unc}$ is the uncertainty of the normalization constant coming from the χ^2-fit uncertainty.

The second component (δ_{MC}) comes from a possible shape mismodelling in the simulated sample. It is estimated by comparing fit results for W, W^+ and W^- analysis channels. Number of multijet background events is expected to be equal for W^+ and W^- selection as:

$$N_{QCD}^{W^+} = N_{QCD}^{W^-} = 0.5 \times N_{QCD}^{W}. \tag{12.5}$$

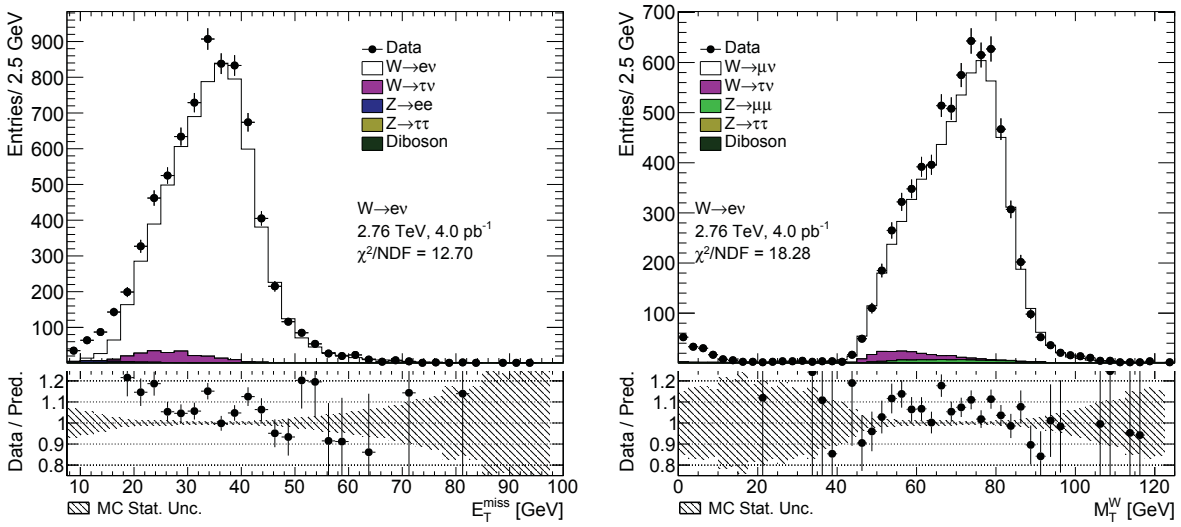

a) b)

Fig. 12.3: Distribution of a) missing transverse energy (E_T^{miss}) and b) transverse mass (M_T^W) used for the multijet background estimation.

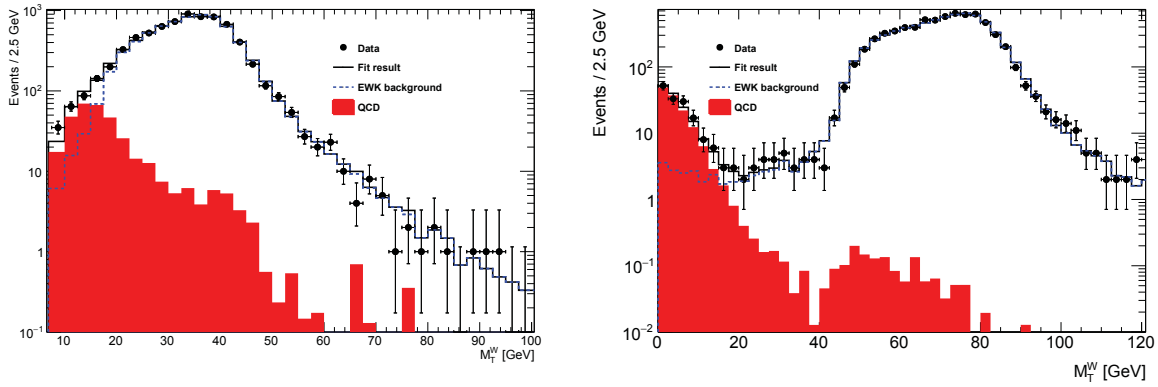

a) b)

Fig. 12.4: Control distribution in the multijet background estimation for a) events satisfying reversed ID criteria and released E_T^{miss} criteria and b) events satisfying released M_T^W criteria.

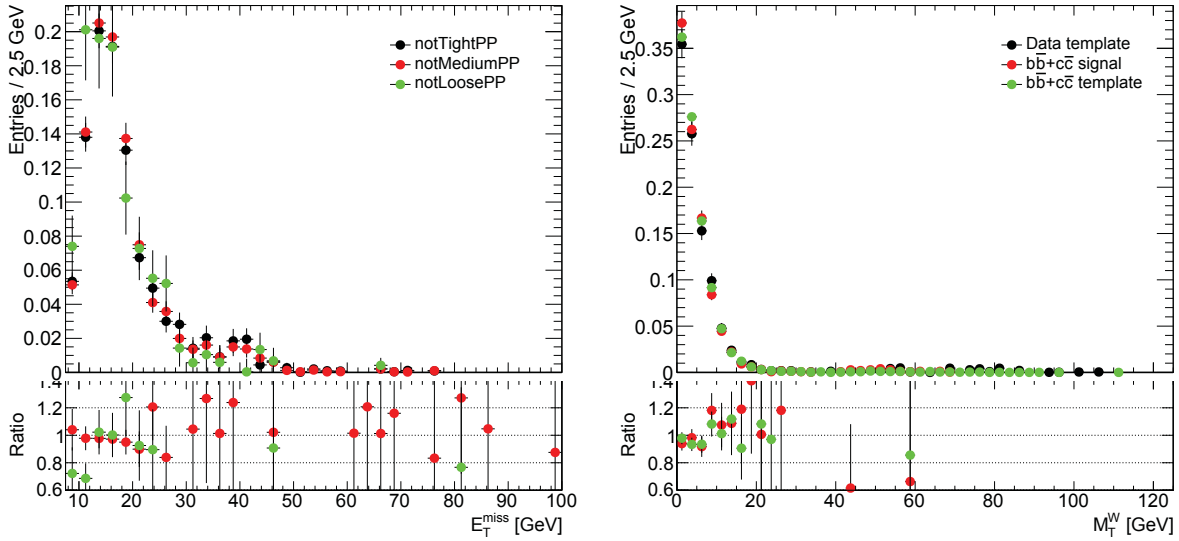

a) b)

Fig. 12.5: The different QCD template comparison for a) $W \to e\nu$ and b) $W \to \mu\nu$ analyses.

Table 12.2: Results of the multijet background estimation for $W \to e\nu$ analysis channels and its systematical uncertainties. Last row (total per channel) shows the final result for $W^+ \to \mu\nu$ and $W^- \to \mu\nu$ after averaging.

Charge	N_{QCD}	$\delta N_{fit\,unc}$	δN_{MC}	$\delta N_{fit\,bias}$
W^+	38.3	7.0	7.0	5.0
W^-	21.5	0.7	9.4	4.0
W	66.1	21.2	4.2	10.
Total per channel	31.0	6.1	8.6	4.7

The standard deviation of the obtained number of events is taken as a systematic uncertainty. Since in $W \to \mu\nu$ channel the multijet template normalization is derived from the fit at the low M_T^W region (where electroweak contributions are negligible) this systematic source is not considered in the calculation.

The third component ($\delta_{fit\,bias}$) comes from the arbitrary choice of the bin width . This uncertainty is estimated by repeating the fit procedure for different bin widths. This component is assumed negligible for the $W \to \mu\nu$ analysis channel.

The uncertainty ($\delta_{template}$) is due to a potential bias in the template, as a result of the template selection and statistical uncertainty. For estimation of this uncertainty, several different template selections are used. For $W \to e\nu$ channel, different reversed isolation criteria are tested (Fig. 12.5 a). For $W \to \mu\nu$ channel template variations are estimated comparing the fit results for data template and $b\bar{b} + c\bar{c}$ MC simulated samples as a multijet template. Fig. 12.5 b) compares multijet template obtained from the data and $b\bar{b} + c\bar{c}$ template obtained using the signal and template selection. Results for a different choice of template fits are presented in Tab. 12.3

Summary of the multijet background uncertainty estimation is shown in Tab. 12.2 and

Table 12.3: Results of the multijet background estimation for $W \to \mu\nu$ analysis channels.

Analysis	N_{QCD} data template	N_{QCD} $b\bar{b} + c\bar{c}$ template selection	N_{QCD} $b\bar{b} + c\bar{c}$ signal selection
W^+	2.48	0.73	1.34
W^-	2.48	0.73	1.35
W	4.97	1.47	2.70
Mean number	2.48	0.73	1.35
Fit error	0.60	0.73	0.19

Tab. 12.3. The overall number of multijet background events is estimated as 31.00 ± 13.0 for $W \to e\nu$ channels and 2.48 ± 0.9, for $W \to \mu\nu$ channels. The overall fraction of the multijet events is lower, than in 7 TeV [96] and 13 TeV [34] analysis, what is in agreement with expectations.

12.2 Background-subtracted W and Z boson candidate events

Tab. 12.4 summarizes the number of background events for W and Z selections. The main sources of background uncertainties for the backgrounds estimated using the simulated events are: statistical uncertainty, cross section uncertainty (if given) and 3.1% of luminosity determination uncertainty.The multijet background estimation uncertainty is esimtated in Sec. 12.1.3. For the background-subtracted events the statistical uncertainty is quoted first, followed by the total systematic uncertainty, derived from the EWK+top and multijet backgrounds ones, considering the sources as uncorrelated. The main background contribution comes from $W \to \tau\tau$ background process for W-boson selection and diboson production for Z-boson selection.

Table 12.4: Number of observed candidate events for the $W \to l\nu$ channel, electroweak (EWK) and top, and data-driven multijet background events, and background-subtracted signal events and their corresponding uncertainties.

l	Observed candidates $N_{data} \pm \delta_{data.stat}$	Background (EWK + top) $N_{EWK+top} \pm \delta_{EWK+top}$	Background (Multijet) $N_{QCD} \pm \delta_{QCD}$	Background-subtracted candidates $N_W^{sig} \pm \delta_{data.stat} \pm \delta_{EWK+top} \pm \delta_{QCD}$
	W-boson selection			
e^+	3914±62.6	108.1 ± 5.7	31.00 ± 13.0	$3774.9 \pm 62.6 \pm 5.7 \pm 13.0$
e^-	2209±47.0	74.2 ± 3.3	31.00 ± 13.0	$2103.8 \pm 47.0 \pm 3.3 \pm 13.0$
μ^+	4365±66.1	152.4 ± 6.7	1.50 ± 0.9	$4211.1 \pm 66.1 \pm 6.7 \pm 0.9$
μ^-	2460±49.6	107.5 ± 4.2	1.50 ± 0.9	$2351.0 \pm 49.6 \pm 4.2 \pm 0.9$
	Z-boson selection			
e	430±20.7	1.3 ± 0.0	-	$428.7 \pm 20.7 \pm 0.0$
μ	646±25.4	1.6 ± 0.1	-	$644.4 \pm 25.4 \pm 0.1$

Chapter 13

Uncertainties in the cross section measurement

The cross section measurement relies on theoretical models and corrections, used in the Monte Carlo, therefore the corresponding uncertainties should be propagated to a final result. The methods of uncertainties propagation are discussed in Sec. 13.1. The sources of systematic uncertainties on $C_{W/Z}$ are discussed in Sec. 13.3, the statistical uncertainty is described in Sec. 13.2. Sec. 13.4 discussed the theoretical uncertainties of the extrapolation factors $A_{W/Z}$ and $E_{W/Z}$. In Sec. 13.5 treatment of correlation between uncertainties for different analyses is demonstrated.

Tab. 13.1 summarizes main sources of uncertainties and their effect on the cross section errors. Systematic errors coming from the hadronic recoil calculation are discussed in Sec. 11.

Table 13.1: Summary of different terms contributing to the uncertainty on fiducial cross section measurement.

Analysis channel		$W^+ \to e\nu$	$W^- \to e\nu$	$W^+ \to \mu\nu$	$W^- \to \mu\nu$	$Z \to ee$	$Z \to \mu\mu$
Value C		0.6801	0.6799	0.7458	0.7491	0.5575	0.8020
Source of uncertainty	Evaluation method	$\delta C_W/C_W(\%)$	$\delta C_W/C_W(\%)$	$\delta C_W/C_W(\%)$	$\delta C_W/C_W(\%)$	$\delta C_Z/C_Z(\%)$	$\delta C_Z/C_Z(\%)$
Electron reconstruction	Toy MC	0.11	0.09	-	-	0.12	-
Electron identification	Toy MC	0.32	0.30	-	-	0.54	-
Electron trigger efficiency	Toy MC	0.14	0.13	-	-	0.001	-
Muon reco + id	Toy MC	-	-	0.03	0.02	-	0.03
Muon trigger	Offset	-	-	1.07	1.07	-	0.03
Electron energy scale	Offset	0.44	0.43	-	-	0.34	-
- Statistical error	Offset	0.05	0.04	-	-	0.04	-
- Bias in method	Offset	0.41	0.40	-	-	0.31	-
- Scale uncertainty	Offset	0.00	0.00	-	-	0.00	-
- Presampler energy scale	Offset	0.04	0.03	-	-	0.04	-
- Material knowledge	Offset	0.14	0.13	-	-	0.14	-
Electron energy resolution	Offset	0.05	0.03	-	-	0.03	-
Muon energy scale	Offset	-	-	0.05	0.05	-	0.03
Muon energy resolution total	Offset	-	-	0.02	0.01	-	0.02
- Muon ID energy scale	Offset	-	-	0.02	0.01	-	0.01
- Muon MS energy scale	Offset	-	-	0.01	0.00	-	0.01
Hadronic recoil scale	Offset	0.15	0.17	0.15	0.19	-	-
Hadronic recoil resolution	On/Off	0.20	0.11	0.16	0.12	-	-
MC statistics		0.24	0.31	0.24	0.34	0.30	0.43
Theory		0.31	0.23	0.13	0.26	0.11	0.06
Total		0.69	0.76	1.12	1.15	0.72	0.43
		Backgrounds					
EWK + $t\bar{t}$ background	Offset	0.15	0.16	0.16	0.18	0.01	0.01
QCD	Offset	0.34	0.62	0.02	0.04	-	-
		Data statistics					
		1.60	2.13	1.51	2.02	4.82	3.93

13.1 Methods of uncertainties propagation

There are three main methods of uncertainties propagation used in this thesis. The Offset method shiftes the correction factor used by its systematic uncertainty ($\pm 1\sigma$) . The contribution of each correction's uncertainty on the observable (e.g. $C_{W/Z}$, $A_{W/Z}$ or a cross section) is taken as a symmetric approximation:

$$\delta_i^{Offset} = \frac{\sigma_i^{up} - \sigma_i^{down}}{2}, \tag{13.1}$$

where $\sigma_i^{up(down)}$ is the change in an observable due to the shift of the correction by $+\sigma$ (up) or $-\sigma$ (down).

For the On/Off method the contribution of each correction is estimated with (σ^{On}) and without(σ^{Off}) correction applied. A systematic error can be then estimated as:

$$\delta^{On/Off} = \sigma^{On} - \sigma^{Off}. \tag{13.2}$$

The Toy MC method [97] uses pseudo experiments with modified input corrections. For electron and muon scale factors binned in P_T and η, the uncertainties within each bin can be divided to correlated and uncorrelated components and statistical uncertainty. For each pseudo-experiment new scale factors are produced, where for each bin a scale factor is randomly varied:

$$SF_i^{Toy_n} = SF_i + Gauss(0, \Delta SF_i^{uncorr+stat}) + \sum \Delta SF_i^{corr} \cdot Gauss(0,1), \tag{13.3}$$

where $SF_i^{Toy_n}$ is a new scale factor in i-th bin, $\Delta SF_i^{uncorr+stat}$ - is the quadratic sum of uncorrelated and statistical errors and ΔSF_i^{corr} is a correlated uncertainty.

The overall effect on a given observable is calculated as a standard deviation in pseudo-experiments:

$$\delta^{Toy} = \sqrt{\frac{\sum_{n=1}^{N} \sigma_i^2}{N} - \left(\frac{\sum_{n=1}^{N} \sigma_i}{N}\right)^2}, \tag{13.4}$$

where n runs over the number of pseudo-experiments. The total number (N) of Toy MC scale factors should be sufficiently large (typically above 20) to avoid possible bias in the uncertainty estimation.

13.2 Statistical uncertainty

The statistical uncertainty comes from the limited data and MC statistics. It is calculated separately for each analysis using the total number of events N satisfying event selection:

$$\delta N = \sqrt{N}. \tag{13.5}$$

13.3 Systematic uncertainties on $C_{W/Z}$ factor

13.3.1 Electron energy scale and resolution

Electron energy scale correction, described in Sec. 10.2 has its associated uncertainty that comes from various sources [98]:

- Statistical component of the electron energy scale uncertainty;
- Uncertainty from the possible bias of the electron energy calibration method;
- Scale uncertainty from the choice of the generator;
- Uncertainty from the EM calorimeter presampler energy scale;
- Imperfect knowledge of the material in front of EM calorimeter.

The uncertainty contribution to the energy scale from each component is estimated using the Offset method.

13.3.2 Muon energy scale and resolution

Systematic uncertainties coming from muon momentum corrections (described in Sec. 10.3) can be divided into three categories:

- variations of the smearing constants for the MS track;
- variation of the smearing constants for the ID track;
- overall muon correction scale uncertainty.

The uncertainty contribution on the muon momentum from each component is estimated using Offset method.

13.3.3 Muon and electron efficiency

The systematic uncertainty coming from lepton efficiency scale factors is estimated using the Toy MC method for electron reconstruction, identification and trigger scale factors and muon reconstruction and identification. Since the muon trigger scale factors are not η and p_{T} dependent for $\sqrt{s}$ = 2.76 TeV data, the Offset method for corresponding uncertainty estimation is used.

For the electron scale factors the correlated and uncorrelated uncertainties are considered to be negligible compared to the statistical uncertainty. The total number of 30 pseudo-experiments is used.

13.3.4 Theoretical uncertainty

The impact of theoretical uncertainty is considered to originate from imperfect knowledge of parton density functions. It is calculated as:

Table 13.2: Acceptance corrections $A_{W/Z}$ together with their relative uncertainties. Various components of the uncertainties are defined in the text. The total uncertainties (δA_{tot}) are obtained as a quadratic sum.

	A	δA^{pdf}_{err} (%)	δA^{pdf}_{sets} (%)	δA_{hs+ps} (%)	δA_{tot} (%)
W^+	0.62	0.20	0.95	0.9	1.3
W^-	0.57	0.64	1.04	0.9	1.5
Z	0.63	0.40	1.37	0.9	1.68

- Uncertainty coming from the choice of PDF set is estimated using the PDF reweighting procedure [99] the original MC generated using CT10 to the following PDF sets: ATLAS-epWZ12 [100], abkm09 [101] and NNPDF23 [102]. The error is calculated as a maximum deviation between the $C_{W/Z}$ calculated using CT10 and $C_{W/Z}$ from the different PDF set;

- Systematic uncertainty within one PDF is evaluated using CT10 NLO set. This set contains 52 associated error sets, corresponding to 90% C.L. limits along 26 eigenvectors. The total uncertainty within one PDF set is estimated as:

$$\delta_X = \frac{1}{2} \cdot \sqrt{\sum_{i=1}^{N} (X^+ - X^-)^2}, \tag{13.6}$$

  where the sum goes over N=26 eigenvectors. The X^+ and X^- are the up and down variations along one eigenvector.

13.4 Uncertainty on $A_{W/Z}$ and $E_{W/Z}$

The effect of theoretical uncertainties is estimated for extrapolated cross sections, through their effect on extrapolation factors $A_{W/Z}$ and $E_{W/Z}$. The main sources of theoretical uncertainties for $A_{W/Z}$ are summarized in Tab. 13.2. The main sources of uncertainties are:

- Uncertainty coming from an arbitrary choice of PDF set (δA^{pdf}_{sets}(%)) and systematic error within one PDF set (δA^{pdf}_{err}(%)). These uncertainties are estimated in the same way, as for $C_{W/Z}$ (see Sec. 13.3.4). These sources are considered to be uncorrelated and are added in quadrature;

- The uncertainties arising from the choice of the generator and the parton shower model (δA_{hs+ps}). They are calculated as a difference in the acceptance factors for events, generated using the same PDF set, but different models for showering and matrix element modeling, namely Powheg + Pythia and Sherpa.

  Due to the lack of additional Z-boson simulation samples, the uncertainty for Z-boson analyses is estimated using the assumption of uncertainty equality for W and Z-boson selection. The corresponding uncertainties are in agreement within the uncertainty with uncertainties in measurements of W and Z bosons at $\sqrt{s}$ = 7 TeV and $\sqrt{s}$ = 13 TeV.

The values of $E_{W/Z}$ factors, used for extrapolation to the 13 TeV fiducial phase space, are 1.09, 1.07, 1.11 for W^+, W^- and Z bosons respectively. The corresponding theoretical uncertainties are considered to be negligible.

13.5 Correlation between uncertainties

The correlation between different uncertainties sources is taken into account in combination and averaging steps. In this section correlation between the uncertainties are discussed.

Systematic uncertainties related with electroweak background modeling are treated as uncorrelated between W and Z-analysis channels. However, this sources are fully correlated for different decay channels of W and Z-bosons . In addition the following systematic sources are considered to be fully correlated between $W^+ \to e\nu$, $W^- \to e\nu$, $W^+ \to \mu\nu$ and $W^- \to \mu\nu$ channels:

- Multijet background estimation;
- Hadronic recoil scale;
- Hadronic recoil resolution.

In addition to the above mentioned systematic uncertainties, the following uncertainties are considered fully correlated in the electron channel analyses:

- Electron energy scale;
- Electron resolution

and in muon analyses:

- Muon energy scale;
- Muon resolution;
- Muon trigger efficiency.

The PDF uncertainties are considered to be fully correlated in all analyses. The statistical uncertainty of MC sample is considered to be fully uncorrelated for all analyses.

The following sources of uncertainties are considered to be partially correlated between Z, W^+ and W^- analyses:

- Electron trigger efficiency;
- Electron resolution efficiency;
- Electron identification efficiency;
- Muon reconstruction and identification efficiency.

For each source of uncertainty, correlation coefficient between analysis X and Y is estimated as:

$$\rho_{XY} = \frac{1}{\sigma(o_X)\sigma(o_Y)} \cdot \frac{1}{N}\sum_{i=1}^{N}(o_X^i - \bar{o}_X)(o_Y^i - \bar{o}_Y) = \frac{C_{XY}}{\sigma(o_X)\sigma(o_Y)}, \tag{13.7}$$

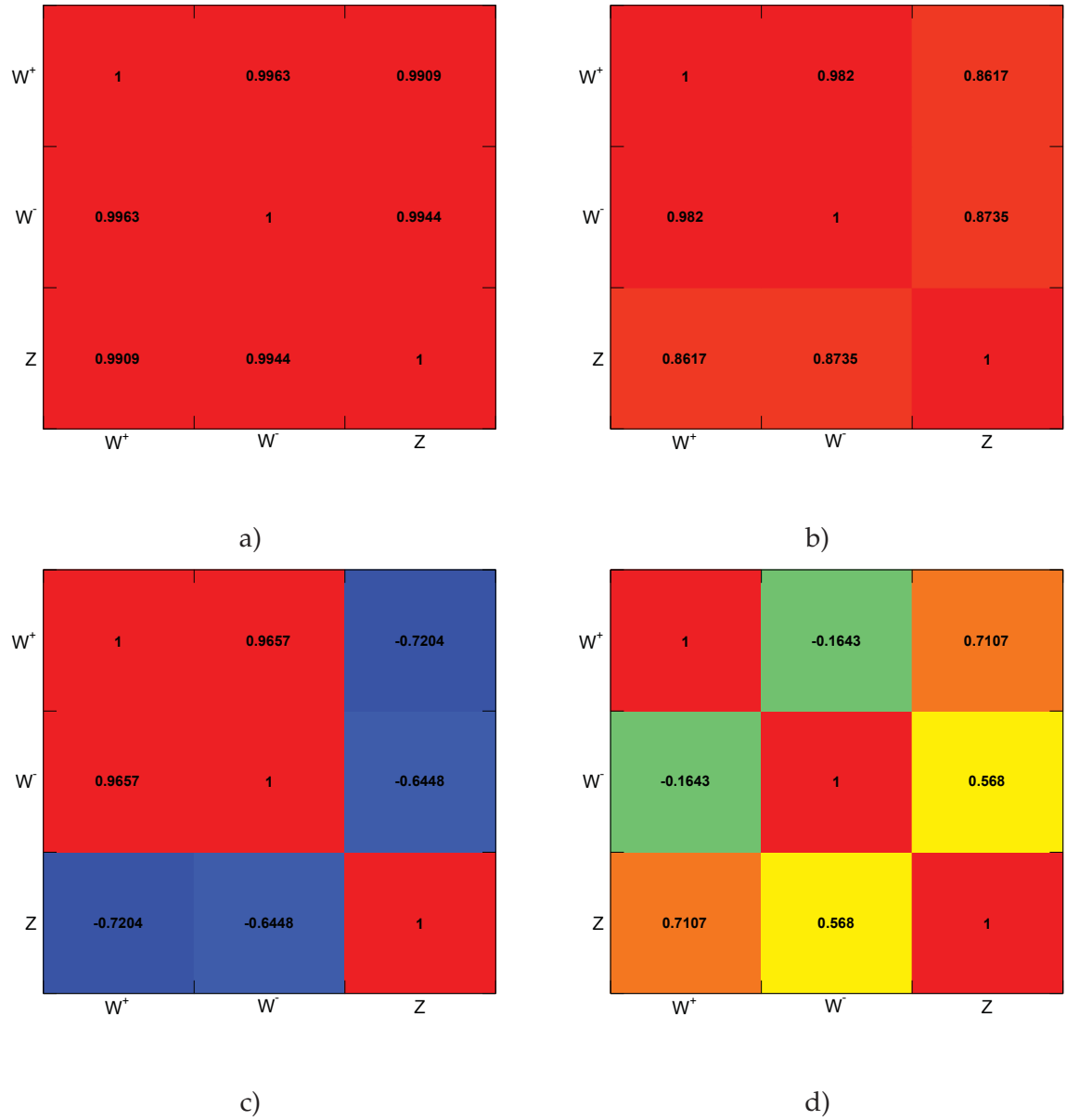

Fig. 13.1: Correlation coefficients ρ_{XY} between C_Z , C_{W^+} and C_{W^-} factors for a) electron reconstruction, b) electron identification, c) electron trigger and d) muon trigger uncertainties.

where $\bar{o}_X$ and $\bar{o}_Y$ are the mean values of the observables o_X and o_Y respectively. The $\sigma(o_X)$ and $\sigma(o_Y)$ are the standard deviations of the observables. The index i runs over the experiments. C_{XY} denotes elements of the covariance matrix. Resulting correlation matrices for each Toy MC systematic source are shown in Fig. 13.1.

The Cholesky decomposition method [103] allows to decompose the corresponding correlation matrices to three sources of uncorrelated uncertainties. In this method the covariance matrix C is re-written as:

$$C = L \cdot L^T, \tag{13.8}$$

where L is a lower triangular matrix, and L^T is a transpose of this matirx.

Rows of the matrix L correspond to the three systematic error vectors, that are fully correlated between W^+, W^- and Z analyses. The quadratic sum of each row corresponds to a total systematic uncertainty:

$$\sigma_X^{tot} = \sum_i^3 L_{iX}^2. \tag{13.9}$$

The results of the Cholesky decomposition can be found in Appendix A. The correlation coefficients matrices for different analyses are provided in Appendix B.

Chapter 14

Control distributions

Kinematic distributions for events satisfying all selection criteria (Chap. 9) are presented in this chapter. Data are compared to MC predictions, corrected following the prescription from Chap. 10. Distributions for $W \to l\nu$ analyses are presented separately for positively and negatively charged leptons and are shown in Figs. 14.1- 14.12. Distributions for $Z \to l^+l^-$ analysis are shown in Figs. 14.13-14.17.

For each plot the expected statistical uncertainty of MC is shown as a shaded band. The expected background contributions are estimated using techniques described in Chap. 12.

Good overall agreement between data and expectations is observed.

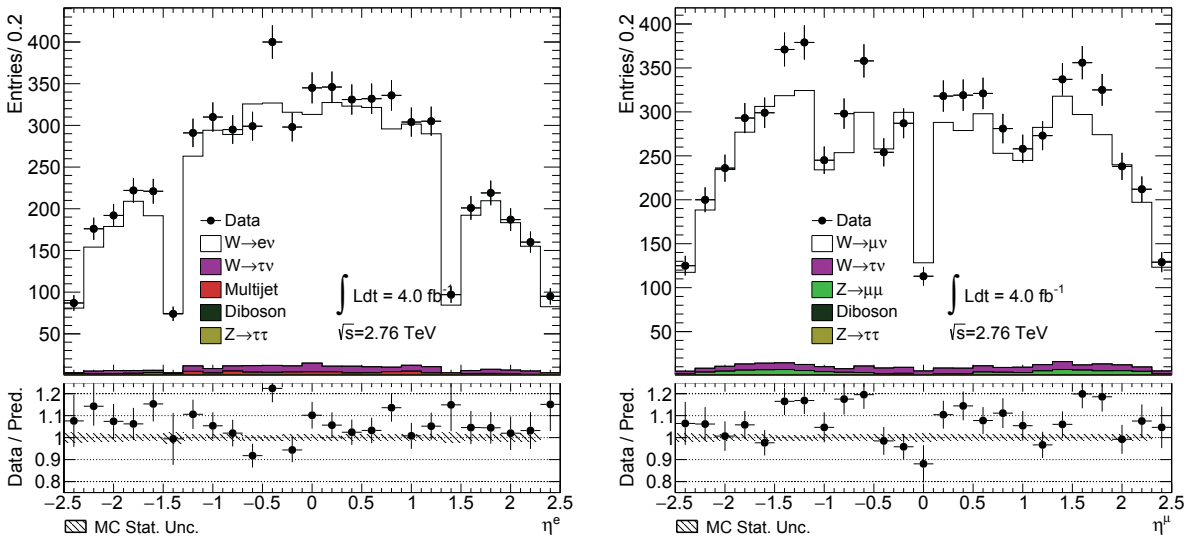

a) b)

Fig. 14.1: Lepton pseudorapidity distribution for a) $W \to e\nu$ and b) $W \to \mu\nu$ candidate events.

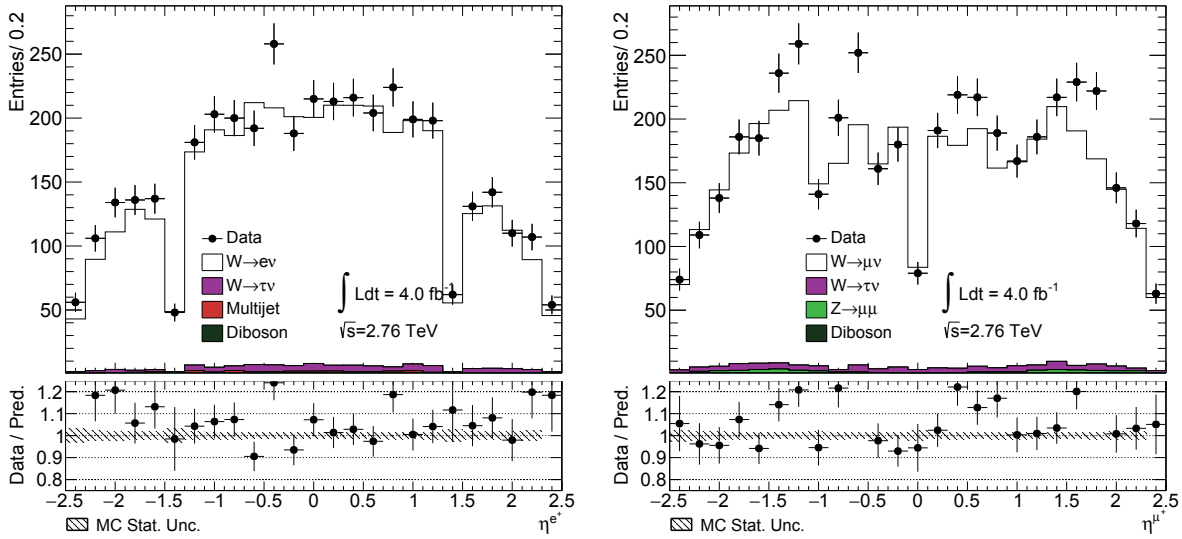

a) b)

Fig. 14.2: Lepton pseudorapidity distribution for a) $W^+ \to e^+\nu$ and b) $W^+ \to \mu^+\nu$ candidate events.

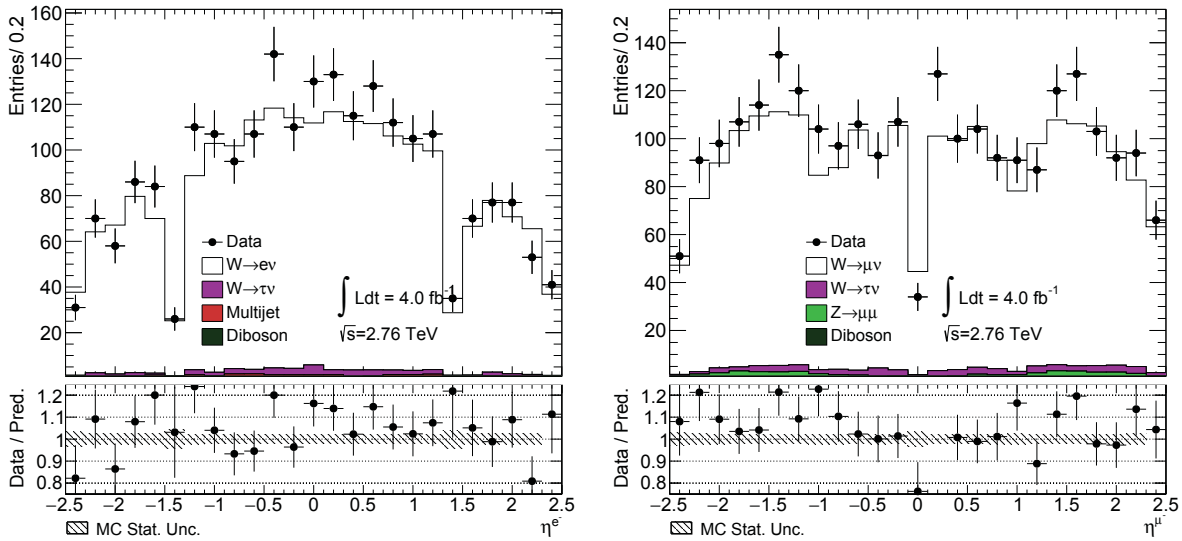

a) b)

Fig. 14.3: Lepton pseudorapidity distribution for a) $W^- \to e^-\nu$ and b) $W^- \to \mu^-\nu$ candidate events.

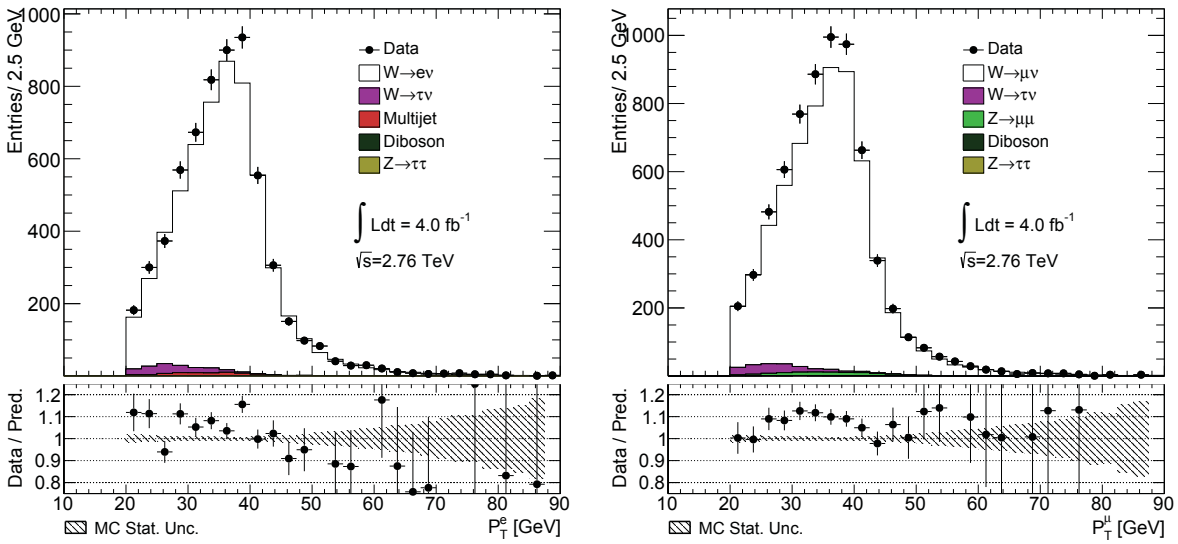

a) b)

Fig. 14.4: Lepton transverse momentum distribution for a) $W \to e\nu$ and b) $W \to \mu\nu$ candidate events.

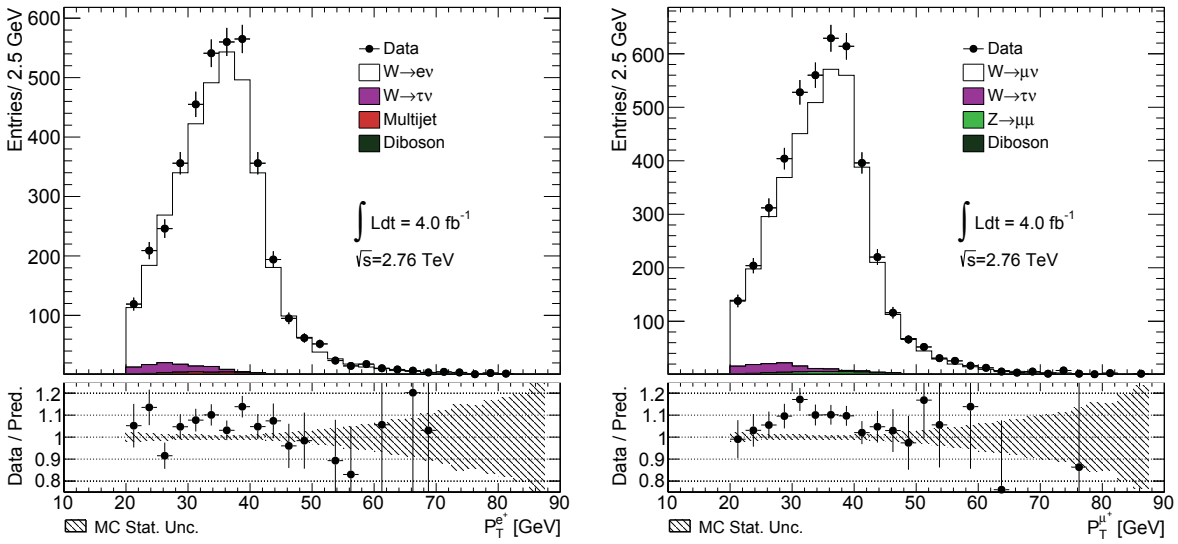

a) b)

Fig. 14.5: Lepton transverse momentum distribution for a) $W^+ \to e^+\nu$ and b) $W^+ \to \mu^+\nu$ candidate events.

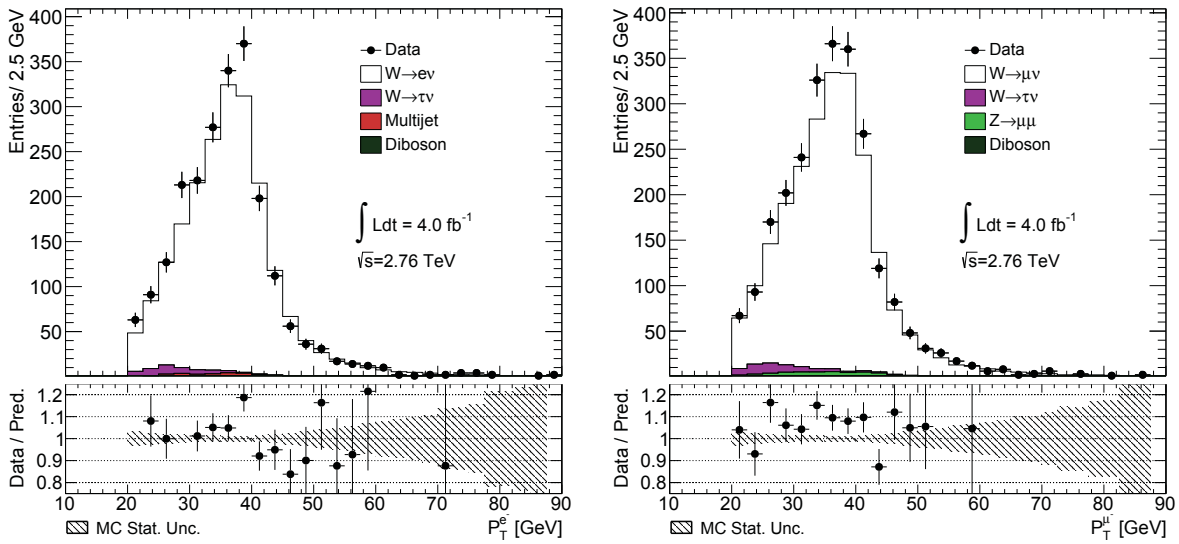

a) b)

Fig. 14.6: Lepton transverse momentum distribution for a) $W^- \rightarrow e^-\nu$ and b) $W^- \rightarrow \mu^-\nu$ candidate events.

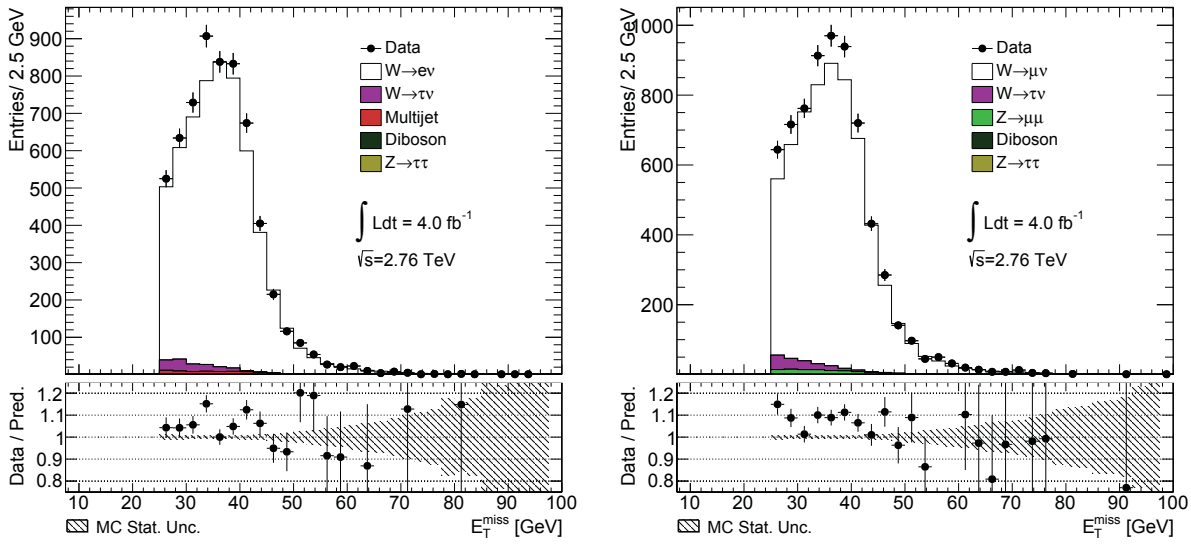

a) b)

Fig. 14.7: Missing transverse energy distribution for a) $W \rightarrow e\nu$ and b) $W \rightarrow \mu\nu$ candidate events.

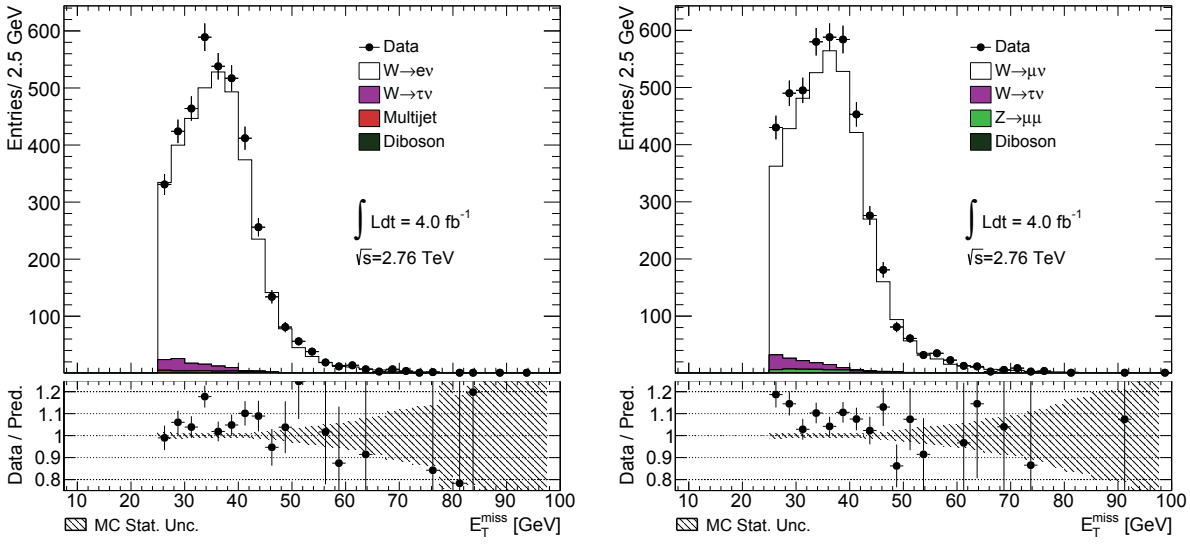

a) b)

Fig. 14.8: Missing transverse energy distribution for a) $W^+ \to e^+\nu$ and b) $W^+ \to \mu^+\nu$ candidate events.

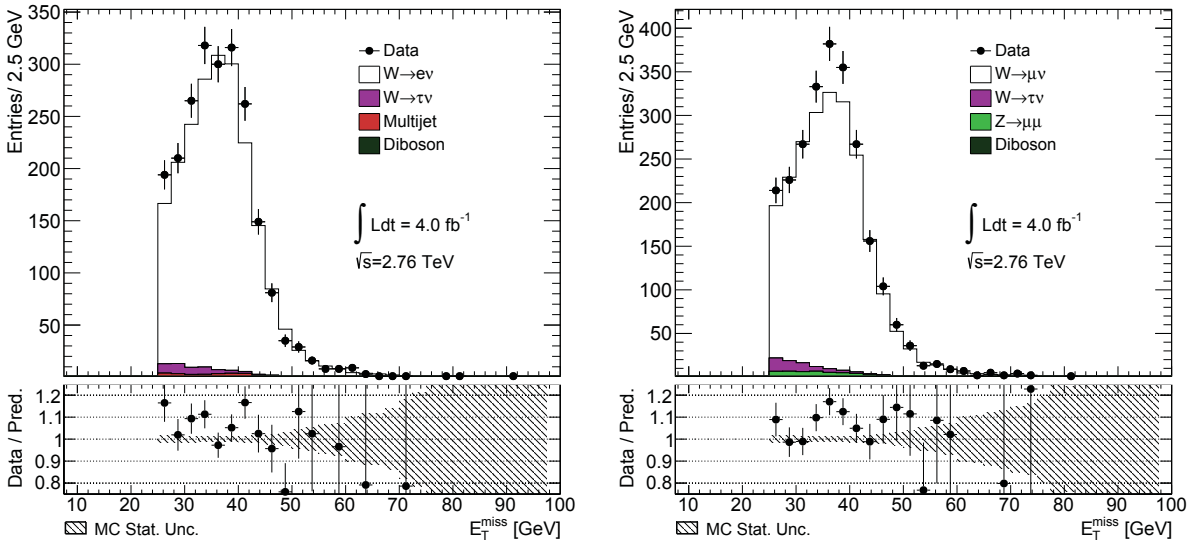

a) b)

Fig. 14.9: Missing transverse energy distribution for a) $W^- \to e^-\nu$ and b) $W^- \to \mu^-\nu$ candidate events.

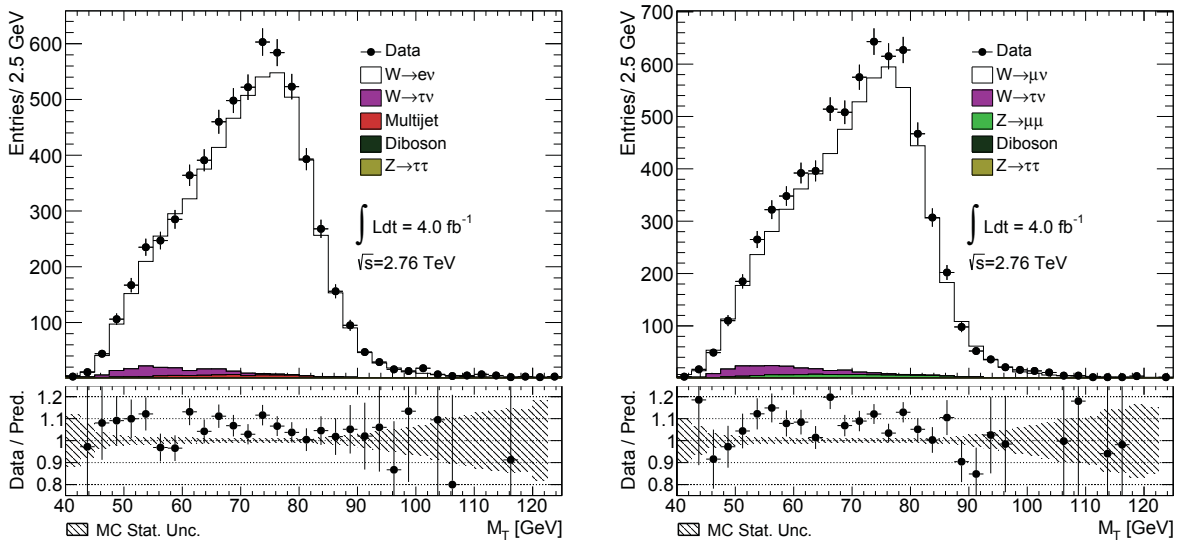

a) b)

Fig. 14.10: Transverse mass distribution distribution for a) $W \to e\nu$ and b) $W \to \mu\nu$ candidate events.

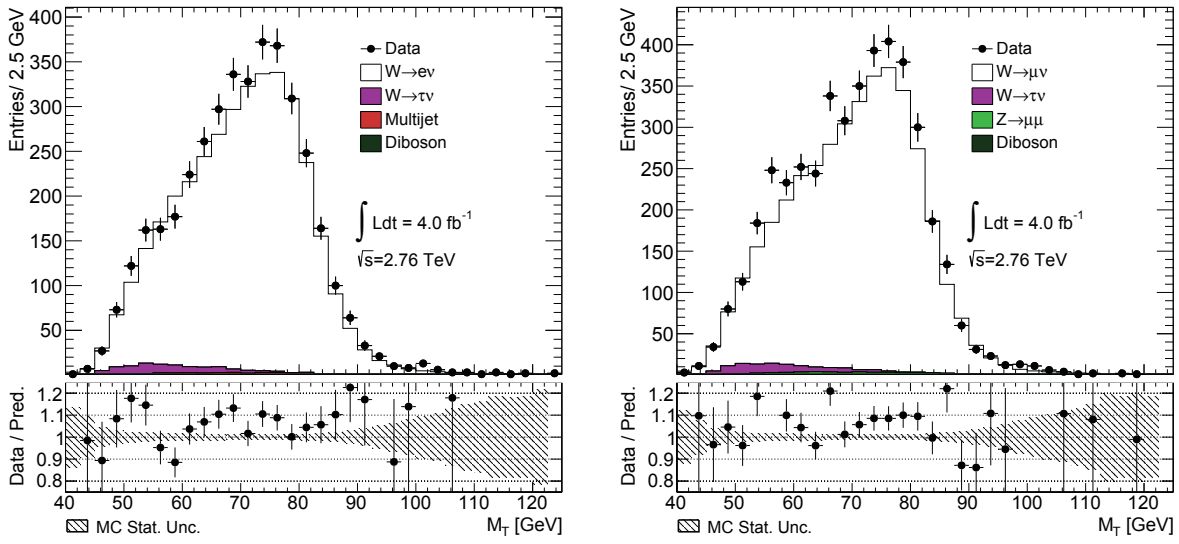

a) b)

Fig. 14.11: Transverse mass distribution distribution for a) $W^+ \to e^+\nu$ and b) $W^+ \to \mu^+\nu$ candidate events.

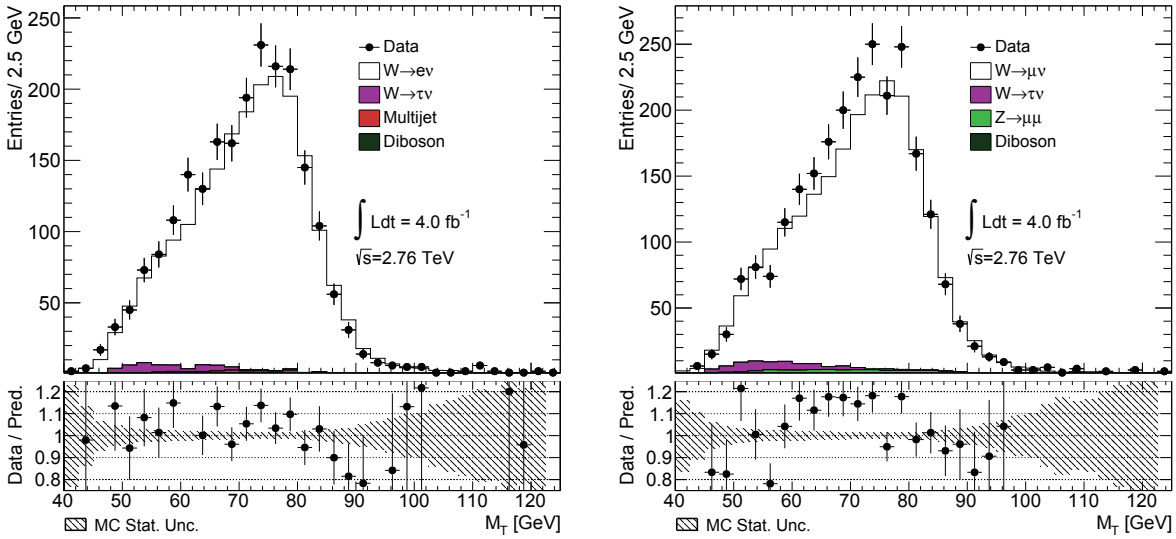

a) b)

Fig. 14.12: Transverse mass distribution distribution for a) $W^- \to e^-\nu$ and b) $W^- \to \mu^-\nu$ candidate events.

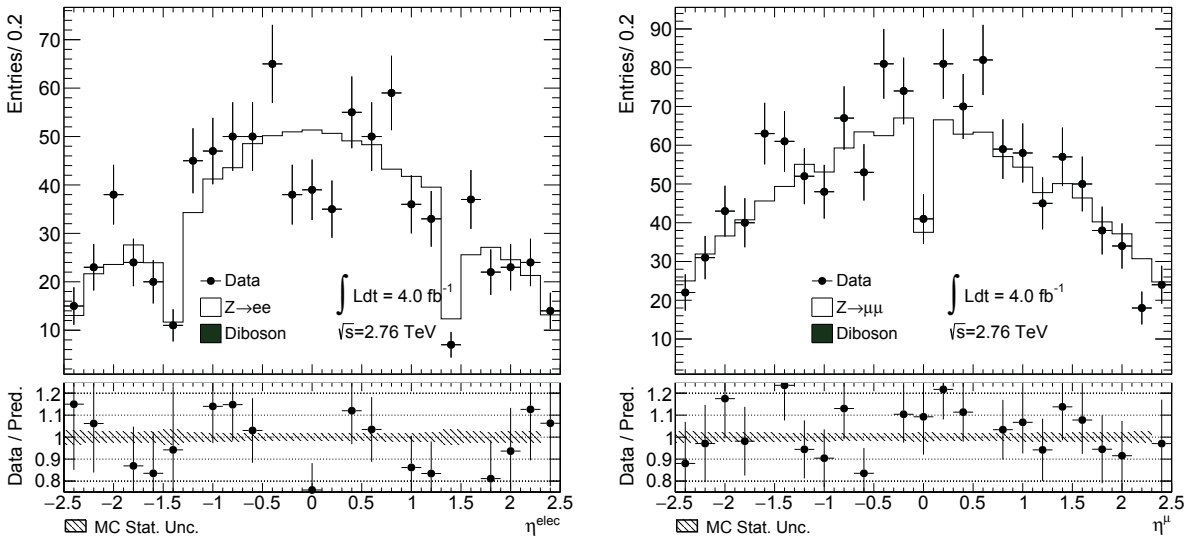

a) b)

Fig. 14.13: Lepton pseudorapidity distribution for a) $Z \to e^+e^-$ and b) $Z \to \mu^+\mu^-$ candidate events.

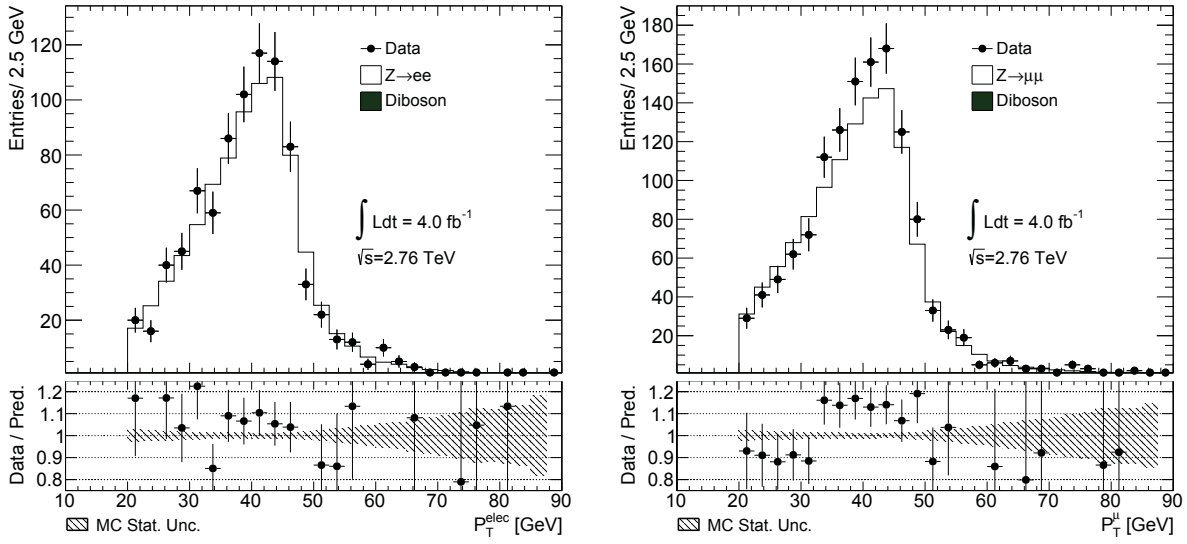

a) a)

Fig. 14.14: Lepton transverse momentum distributions for a) $Z \rightarrow e^+e^-$ and b) $Z \rightarrow \mu^+\mu^-$ candidate events.

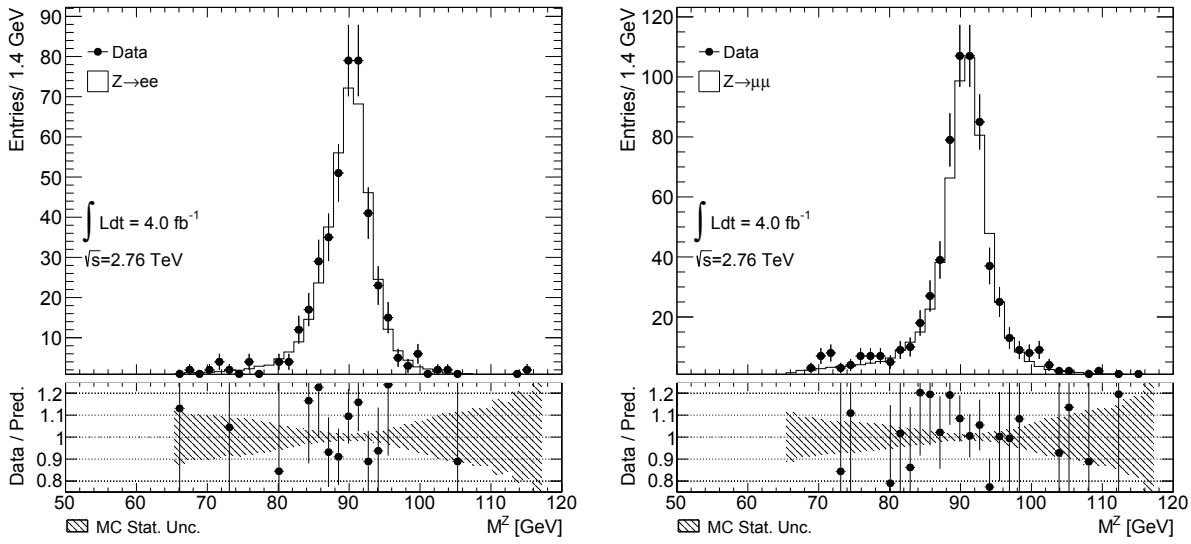

a) a)

Fig. 14.15: Dilepton mass distribution distributions for a) $Z \rightarrow e^+e^-$ and b) $Z \rightarrow \mu^+\mu^-$ candidate events.

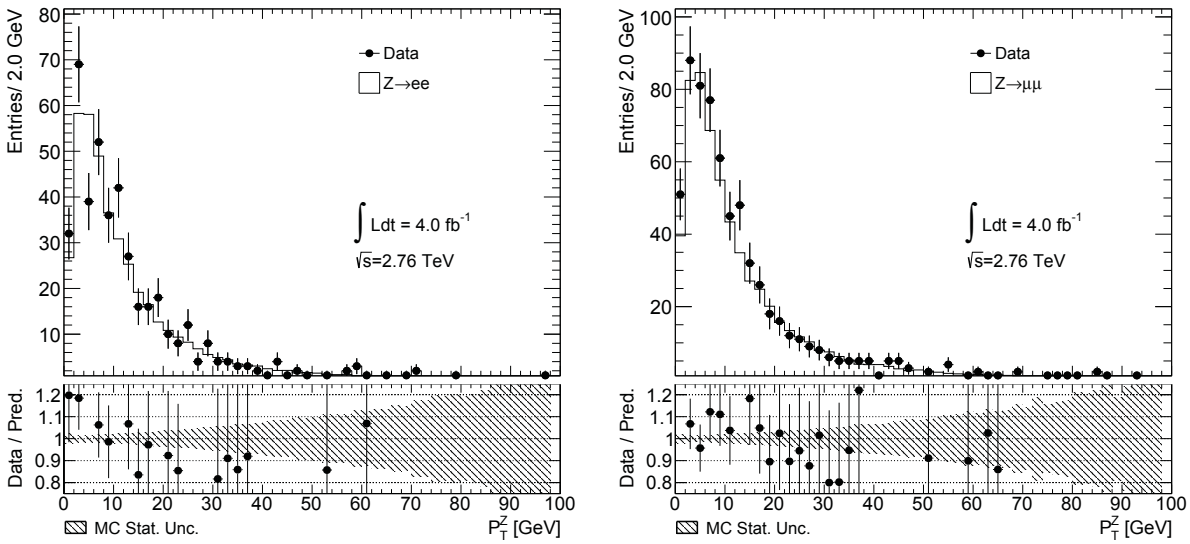

a) a)

Fig. 14.16: Z boson transverse momentum distributions for a) $Z \rightarrow e^+e^-$ and b) $Z \rightarrow \mu^+\mu^-$ candidate events.

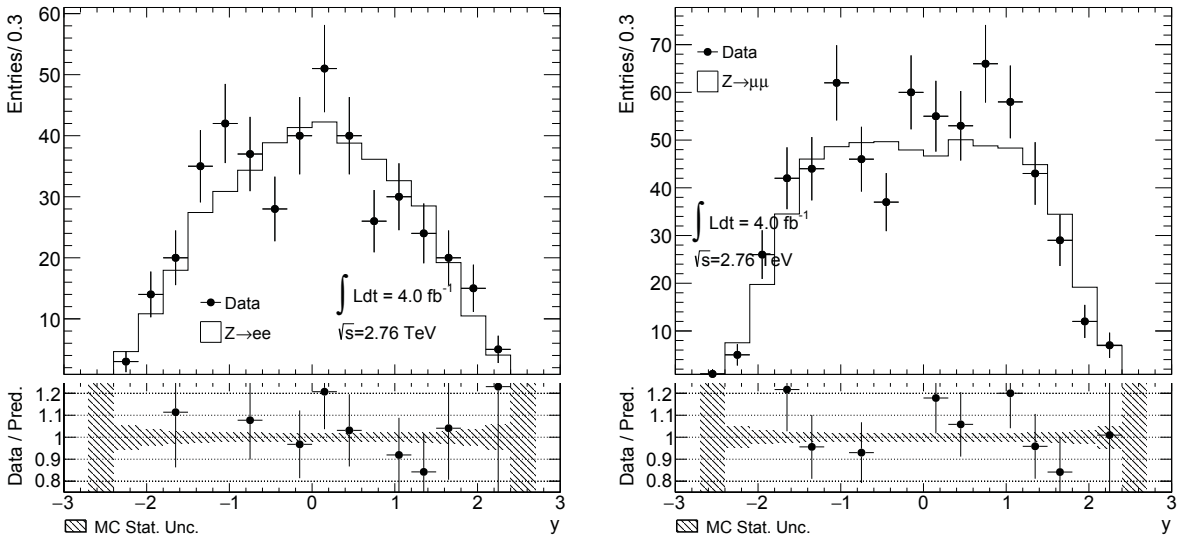

a) a)

Fig. 14.17: Z boson rapidity distribution for a) $Z \rightarrow e^+e^-$ and b) $Z \rightarrow \mu^+\mu^-$ candidate events.

Chapter 15

Results

In this chapter results for the W/Z cross section measurements at $\sqrt{s}$ = 2.76 TeV and their interpretation are discussed. In Sec. 15.1 the cross sections measured for both lepton flavors are presented. These results are used to test lepton universality. Sec. 15.3 describes the results obtained for combined lepton channels. Finally, in Sec. 15.4, the interpretation in terms of parton density functions (PDFs) is presented.

15.1 Cross section measurement results

The cross sections are calculated separately for W and Z-bosons and lepton flavor, as described in Chap. 3. The cross-sections are measured in the fiducial region ($\sigma^{fid}_{W/Z}$) corresponding to the detector acceptance and are extrapolated to the full phase space ($\sigma^{tot}_{W/Z}$) and fiducial region of W and Z-boson measurements at $\sqrt{s}$ = 13 TeV ($\sigma^{13}_{W/Z}$), following the methodology from Chap. 3. The obtained cross sections are summarized in Tab. 15.1.

The main source of uncertainty for the cross section measurement is a luminosity uncertainty. The statisitcal uncertainty of the data is a second dominant uncertainty. For the measurement of *W*-boson cross section decaying to electron and neutrino, total systematic uncertainty is around 1%, which is significantly lower, than statistical uncertainty. For the W-boson decays in muon channel, total systematic uncertainty is higher (around 1.2%) because of the high uncertainty of the trigger scale factors. The systematic uncertainty of Z-boson cross sections is negligible. The obtained results are consistent within the uncertainties between different lepton flavors.

Table 15.1: Results on a fiducial σ^{fid} and total cross section measurement for W^+, W^- and Z bosons in electron and muon channels. The cross sections are shown with their statistical (stat), systematical (syst) and luminosity (lumi) uncertainties (and extrapolation uncertainty (ext) for total cross section) quoted in that order.

	central value ± stat ± syst ± lumi (± ext)	central value ± stat ± syst ± lumi (± ext)
	W^+	
	$W^+ \to e\nu$	$W^+ \to \mu\nu$
σ_W^{fid} [pb]	$1406.0 \pm 23.3 \pm 8.9 \pm 43.6$	$1430.0 \pm 22.4 \pm 18.3 \pm 44.3$
σ_W^{tot} [pb]	$2253.2 \pm 37.3 \pm 14.2 \pm 69.8 \pm 20.3$	$2291.7 \pm 36.0 \pm 29.3 \pm 71.0 \pm 20.6$
σ_W^{13} [pb]	$1293.9 \pm 21.4 \pm 8.9 \pm 40.1$	$1316.7 \pm 20.7 \pm 14.9 \pm 40.8$
	W^-	
	$W^- \to e\nu$	$W^- \to \mu\nu$
σ_W^{fid} [pb]	$784.0 \pm 17.5 \pm 6.9 \pm 24.3$	$795.0 \pm 16.8 \pm 10.9 \pm 24.6$
σ_W^{tot} [pb]	$1373.0 \pm 30.7 \pm 12.1 \pm 42.6 \pm 12.4$	$1392.3 \pm 29.4 \pm 19.1 \pm 43.2 \pm 12.5$
σ_W^{13} [pb]	$733.8 \pm 16.4 \pm 5.0 \pm 22.7$	$743.7 \pm 15.7 \pm 8.6 \pm 23.1$
	Z	
	$Z \to ee$	$Z \to \mu\mu$
σ_Z^{fid} [pb]	$194.8 \pm 9.4 \pm 1.4 \pm 6.0$	$203.5 \pm 8.0 \pm 0.9 \pm 6.3$
σ_Z^{tot} [pb]	$310.5 \pm 15.0 \pm 1.6 \pm 9.6 \pm 2.8$	$324.8 \pm 12.8 \pm 0.6 \pm 10.1 \pm 2.9$
σ_Z^{13} [pb]	$176.1 \pm 8.5 \pm 1.3 \pm 5.5$	$183.2 \pm 7.2 \pm 0.8 \pm 5.7$

15.2 Lepton universality test

Because of the lepton universality in the Standard Model (SM), the equal cross sections for different lepton decay channels are expected. The measured W cross sections are calculated in the fiducial region (following the prescription from Sec. 3.1.3) are:

$$\sigma_W^{fid}(W \to e\nu) = 2190.0 \pm 29.1(stat.) \pm 14.5(sys.) \pm 67.9(lumi.)\ [pb],$$
$$\sigma_W^{fid}(W \to \mu\nu) = 2225.0 \pm 28.0(stat.) \pm 28.2(sys.) \pm 69.0(lumi.)\ [pb],$$

which gives following ratio:

$$R_W = \frac{\sigma_W^{\mu}}{\sigma_W^{e}} = \frac{BR(W\to\mu\nu)}{BR(W\to e\nu)} = 1.015 \pm 0.026(sys.) \pm 0.019(stat.),$$

which is in agreement with the SM prediction of its unity and the world average $R_W^{world} = 0.991 \pm 0.018$ [31].

Similarly, such ratio can be defined in a Z boson decays:

$$R_Z = \frac{\sigma_Z^{\mu}}{\sigma_Z^{e}} = \frac{BR(Z\to\mu\mu)}{BR(Z\to ee)} = 1.046 \pm 0.004(sys.) \pm 0.065(stat.),$$

which is also in agreement with the SM prediction and the world average $R_Z^{world} = 1.0009 \pm 0.0028$ [31].

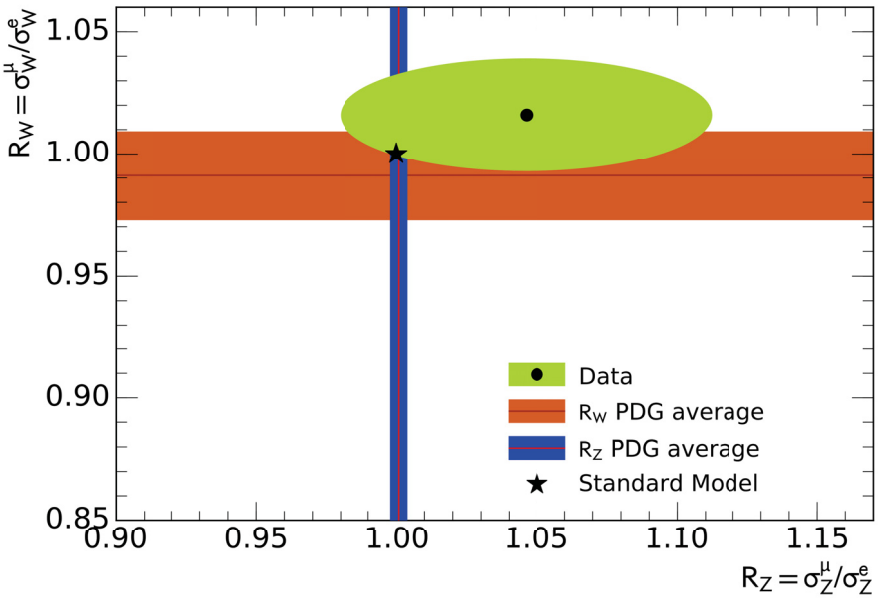

Fig. 15.1: The correlated measurement of the muon-to-electron fiducial cross section ratios in the W and the Z channels. The vertical (horizontal) band represents the uncertainty of the corresponding Z (W) branching fractions based on the current world average data. The green ellipse illustrates the 1 σ for the correlated measurement of R_W and R_Z.

A comparison of R_W and R_Z, taking into account the correlated systematic uncertainties, with world average and SM predictions is shown in Fig. 15.1. The correlation matrix for R_W and R_Z can be found in Appendix B. The ellipse angle is obtained from the correlation matrix using the eigenvector decomposition and corresponds to the angle between x axis and the one of the 2 eigenvectors. The obtained values agree, within the 68% confidence level, with the Standard Model expectations and the world average.

15.3 Combined results

Since the results for different analysis are agree withing the uncertainty, it is possible to perform averaging procedure as described in Sec. 3.2. The combination is done in the fiducial region. The combined cross sections are extrapolated afterwards to the full phase space and fiducial region of $\sqrt{s} = 13$ TeV. The common luminosity uncertainty is excluded from the combination process.

The resulting combined cross sections are summarized in Tab. 15.2. The combination procedure allows to significantly reduce statistical uncertainty of the measurement compared to individual lepton flavor cross sections. The systematic uncertainty is also reduced, because most of the sources are uncorrelated for different lepton flavors of the analysis. The combination yields good $\chi^2/NDF \approx 1/3$, indicating a good agreement between the measurements. The W cross section is calculated from the combined W^+ and W^- cross sections.

Table 15.2: Results on a fiducial σ^{fid} and total cross section measurement for W^+, W^- and Z bosons in electron and muon channels. The cross sections are shown with their statistical (stat), systematical (syst) and luminosity (lumi) uncertainties (and extrapolation uncertainty (ext) for total cross section) quoted in that order.

	value ± stat ± syst ± lumi (± ext)	value ± stat ± syst ± lumi (± ext)
	$W^{+/-}$	
	$W^+ \to l\nu$	$W^- \to l\nu$
σ_W^{fid} [pb]	$1417.2 \pm 16.2 \pm 6.7 \pm 43.9$	$789.1 \pm 12.1 \pm 4.5 \pm 24.5$
σ_W^{tot} [pb]	$2271.2 \pm 25.9 \pm 10.7 \pm 70.4 \pm 20.4$	$1382.0 \pm 21.2 \pm 7.8 \pm 42.8 \pm 12.4$
σ_W^{13} [pb]	$1303.8 \pm 14.9 \pm 6.1 \pm 40.4$	$738.9 \pm 11.3 \pm 4.2 \pm 22.9$
	$W \to l\nu$	
σ_W^{fid} [pb]	$2206.3 \pm 20.2 \pm 10.6 \pm 68.4$	
σ_W^{tot} [pb]	$3653.2 \pm 33.5 \pm 17.5 \pm 113.2 \pm 32.9$	
σ_W^{13} [pb]	$2042.6 \pm 18.7 \pm 9.8 \pm 63.3$	
	$Z \to ll$	
σ_Z^{fid} [pb]	$200.4 \pm 6.1 \pm 0.3 \pm 6.2$	
σ_Z^{tot} [pb]	$319.1 \pm 9.8 \pm 0.5 \pm 9.9 \pm 2.9$	
σ_Z^{13} [pb]	$181.2 \pm 5.5 \pm 0.3 \pm 5.6$	

15.3.1 Comparison with theoretical predictions

Theoretical predictions are obtained at NLO and NNLO level of precision. The NLO calculations are performed using the MCFM generator [104], interfaced with APPLGRID [105], that provides an x vs Q^2 grid for a calculation and convolution with a given PDF set. The NNLO predictions, provided to the author, are calculated using the FEWZ program [32].

The comparison between NLO and NNLO predictions for CT14nnlo [33] PDF set and the obtained cross sections in the fiducial region for W^+, W^-, $W^\pm$ and Z-bosons decaying in electron, muon and combined channels are shown in Fig. 15.2 and Fig. 15.3. The NLO and NNLO cross sections are in agreement with each other and with experimental data withing the PDF uncertainty. The values of NLO cross section predictions are smaller, than the obtained experimental results and have a higher uncertainty. The NNLO predictions have better agreement with data.

Additionally, the obtained W^+, W^- and Z cross sections in a combined channel are compared to the NNLO predictions for various PDF sets: ABM12nlo [106], CT14nnlo [33], MMHTnnlo [20], ATLASepWZ12 [100], NNPDF3.0 [102] and HERApdf2.0nnlo [107] in Fig. 15.4-15.6. The best overall agreement is achieved with NNPDF3.0 PDF set. Additional plots theoretical comparison plots can be found in the Appendix C.

Fig 15.7 shows the LHC, Tevatron and other pp and p$\bar{p}$ results on measuring W and Z-boson cross sections. It the same plot that has shown earlier in Chap. 2 (Fig. 2.7), however the cross sections measured in this analysis are added. The cross sections measured at $\sqrt{s}$ = 2.76 TeV are fully consistent with earlier LHC results and CT14 NNLO theoretical predictions. The good overall agreement is achieved on the whole center-of-mass energies range accessible at LHC.

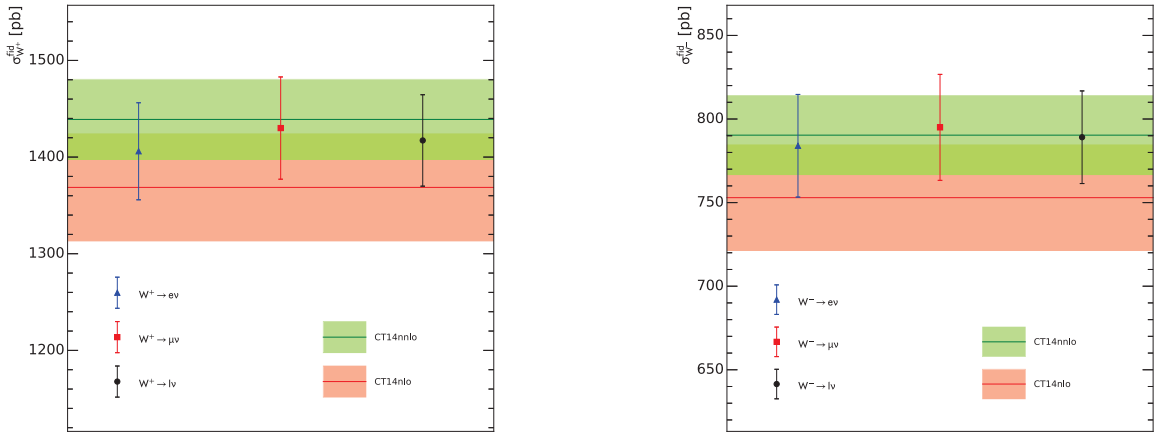

a) b)

Fig. 15.2: The NLO and NNLO theoretical predictions calculated using the CT14nnlo PDF set compared to the measured fiducial cross sections as given in Tab. 15.1 and Tab. 15.2 for a) $\sigma^{fid}_{W^+}$ and b) $\sigma^{fid}_{W^-}$. The blue and red dots correspond to the electron and muon channels respectively, while black dots represent the combined channel. The NLO and NNLO predictions are presented by the red and green lines with error-bands respectively.

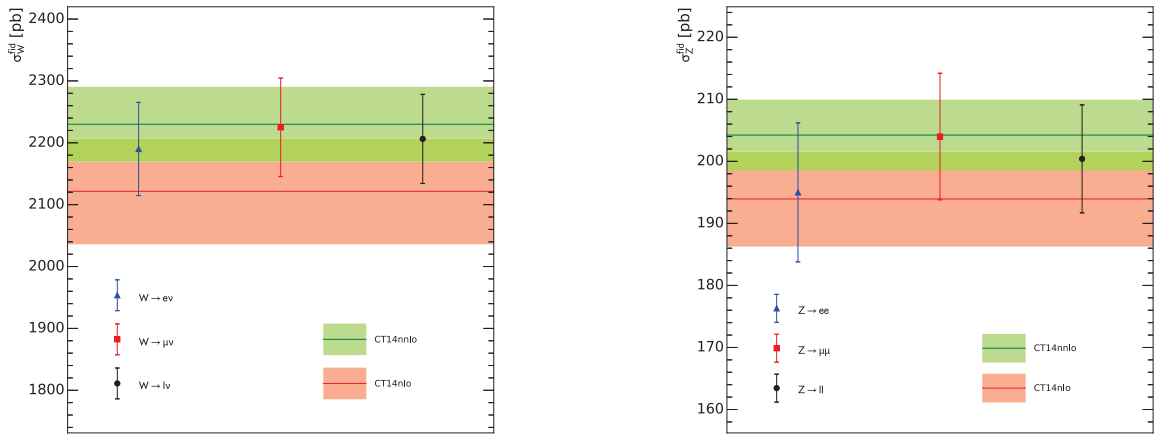

a) b)

Fig. 15.3: The NLO and NNLO theoretical predictions calculated using the CT14nnlo PDF set compared to the measured fiducial cross sections as given in Tab. 15.1 and Tab. 15.2 for a) σ^{fid}_{W} and b) σ^{fid}_{Z}. he blue and red dots correspond to the electron and muon channels respectively, while black dots represent the combined channel. The NLO and NNLO predictions are presented by the red and green lines with error-bands respectively.

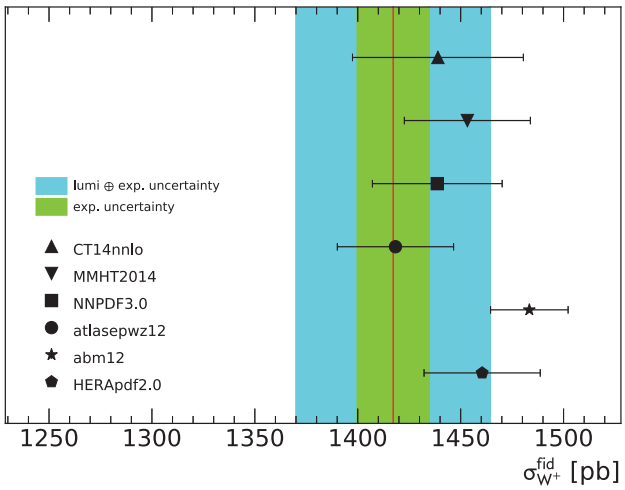

Fig. 15.4: NNLO predictions for the fiducial cross section $\sigma^{fid}_{W^+}$ in pb for the six PDFs CT14nnlo, MMHT2014, NNPDF3.0, ATLASepWZ12, abm12, HERApdf2.0 compared to the measured fiducial cross section as given in Tab. 15.2. The green (cyan) band corresponds to the experimental uncertainty without (with) the luminosity uncertainty. The theory predictions are given with the corresponding PDF uncertainties shown as error bands.

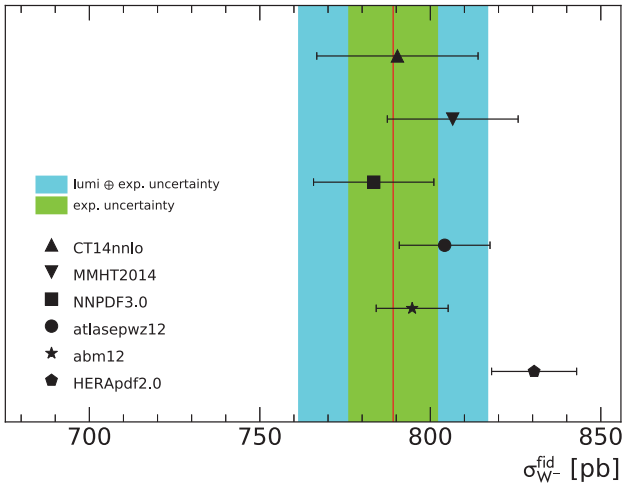

Fig. 15.5: NNLO predictions for the fiducial cross section $\sigma^{fid}_{W^-}$ in pb for the six PDFs CT14nnlo, MMHT2014, NNPDF3.0, ATLASepWZ12, abm12, HERApdf2.0 compared to the measured fiducial cross section as given in Tab. 15.2. The green (cyan) band corresponds to the experimental uncertainty without (with) the luminosity uncertainty. The theory predictions are given with the corresponding PDF uncertainties shown as error bands.

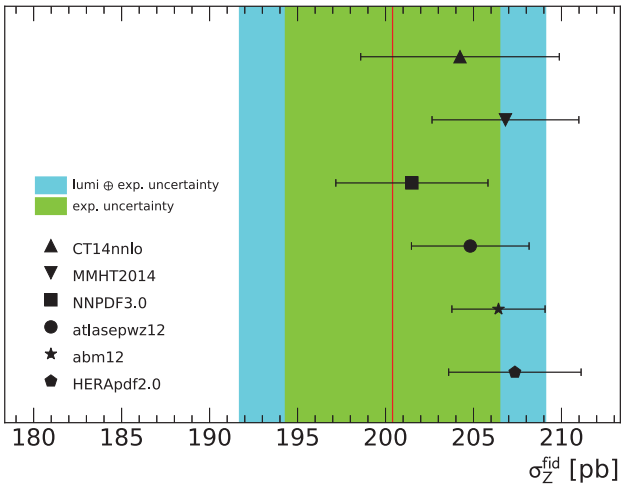

Fig. 15.6: Predictions for the fiducial cross section σ_Z^{fid} in pb for the six PDFs CT14nnlo, MMHT2014, NNPDF3.0, ATLASepWZ12, abm12, HERApdf2.0 compared to the measured fiducial cross section as given in Tab. 15.2. The green (cyan) band corresponds to the experimental uncertainty without (with) the luminosity uncertainty. The theory predictions are given with the corresponding PDF uncertainties shown as error bands.

15.3.2 Cross section ratios

Measurement of cross section ratios is a powerful tool to test PDF predictions, because of the cancellation of luminosity uncertainty and partial cancellation of other sources of systematic uncertainties. The ratios of W and Z-boson production cross sections have been measured at $\sqrt{s}$ = 7 TeV [96] and $\sqrt{s}$ = 13 TeV [34]. The measurement of the ratio R_{W^+/W^-} is potentially sensitive to the u_v, d_v valence quarks distributions, while the ratio $R_{W/Z}$ can put a constrains on the strange quark distributions. The ratios of W and Z-boson production cross sections are calculated in a fiducial region, following the procedure from Sec. 3.3. For the electron channel, the ratios are:

$$\begin{aligned}
R^e_{W/Z} &= 11.231 \pm 0.563\,(stat.) \pm 0.058\,(sys.);\\
R^e_{W^+/Z} &= 7.210 \pm 0.369\,(stat.) \pm 0.034\,(sys.);\\
R^e_{W^-/Z} &= 4.021 \pm 0.214\,(stat.) \pm 0.030\,(sys.);\\
R^e_{W^+/W^-} &= 1.793 \pm 0.050\,(stat.) \pm 0.004\,(sys.)
\end{aligned}$$

and for the muon channel:

$$\begin{aligned}
R^\mu_{W/Z} &= 10.907 \pm 0.452\,(stat.) \pm 0.150\,(sys.);\\
R^\mu_{W^+/Z} &= 7.010 \pm 0.298\,(stat.) \pm 0.097\,(sys.);\\
R^\mu_{W^-/Z} &= 3.897 \pm 0.174\,(stat.) \pm 0.057\,(sys.);\\
R^\mu_{W^+/W^-} &= 1.799 \pm 0.047\,(stat.) \pm 0.003\,(sys.).
\end{aligned}$$

The ratios in combined channel are benefiting from the reduced cross section uncertainties.

$$R_{W/Z} = 11.010 \pm 0.351\,(stat.) \pm 0.052\,(sys.);$$
$$R_{W^+/Z} = 7.072 \pm 0.231\,(stat.) \pm 0.033\,(sys.);$$
$$R_{W^-/Z} = 3.938 \pm 0.135\,(stat.) \pm 0.022\,(sys.);$$
$$R_{W^+/W^-} = 1.796 \pm 0.034\,(stat.) \pm 0.002\,(sys.).$$

The uncertainties on ratios are dominated by the statistical uncertainty. The ratios are in agreement between electron, muon and combined channel. The ratios for combined cross analysis are used to compare with NLO predictions (Fig. 15.8 and Fig. 15.9) for the six PDFs CT14nnlo, MMHT2014, NNPDF3.0, ATLASepWZ12, abm12, HERApdf2.0. Thanks to the higher statistics in the combined W-boson analysis the ratio R_{W^+/W^-} has the lowest statistical uncertainty, that is compatible with the uncertainty within one PDF set. The ratios to the Z-boson production cross section ($R_{W/Z}$, $R_{W^+/Z}$ and $R_{W^-/Z}$) are significantly less accurate because of the large statistical uncertainty of the Z-boson cross section measurement. The best agreement with the data is provided by the MMHT PDF set.

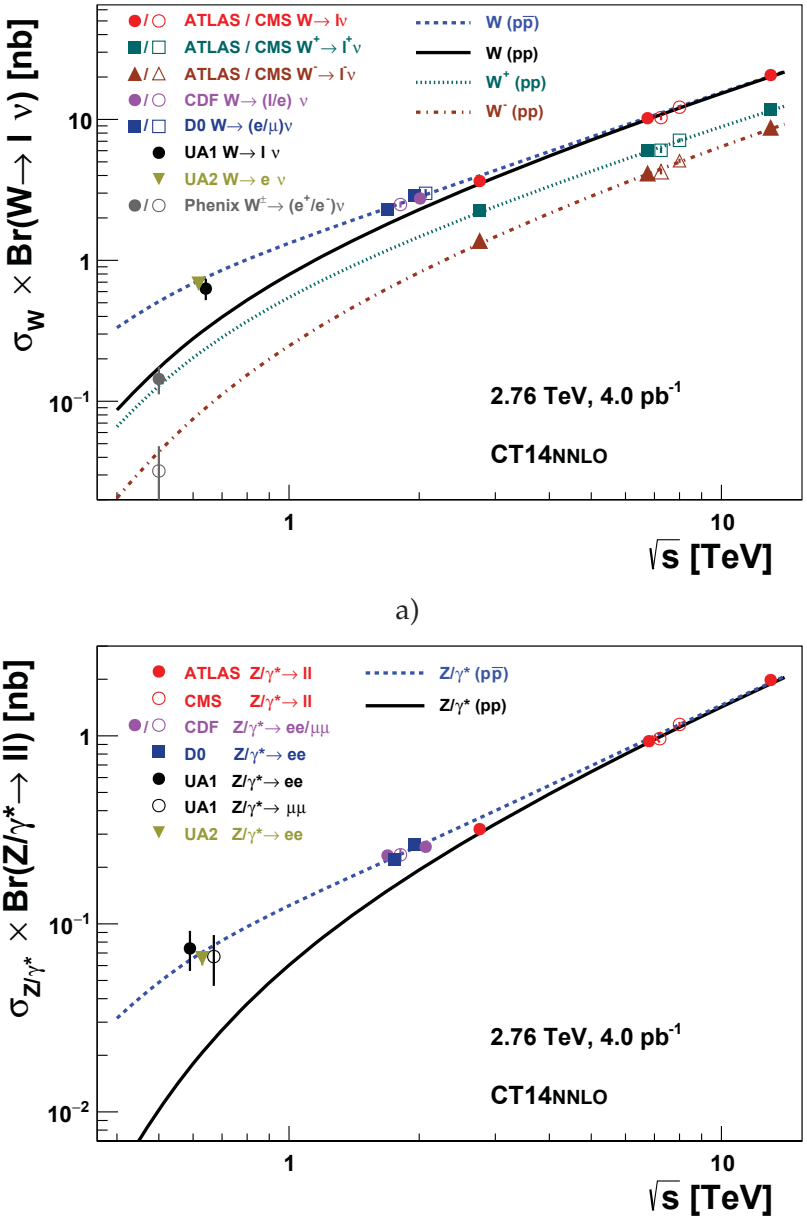

Fig. 15.7: The measured values of a) $\sigma_{W\to l\nu}$ for W^+, W^- and their sum and b) $\sigma_{Z\to ll}$ for Z-boson compared to the theoretical predictions based on NNLO QCD calculations. The ATLAS official results with addition of the 2.76 TeV measurement are shown for the combined electron-muon channel only . The predictions and previous measurements are shown for both proton-proton and proton-antiproton colliders as a function of $\sqrt{s}$. The data points at the various energies are staggered to improve readability. All data points are displayed with their total uncertainty. The calculations were performed with the program FEWZ using the CT14nnlo parton density function parameterization. The theoretical uncertainties on the cross section predictions are not shown.

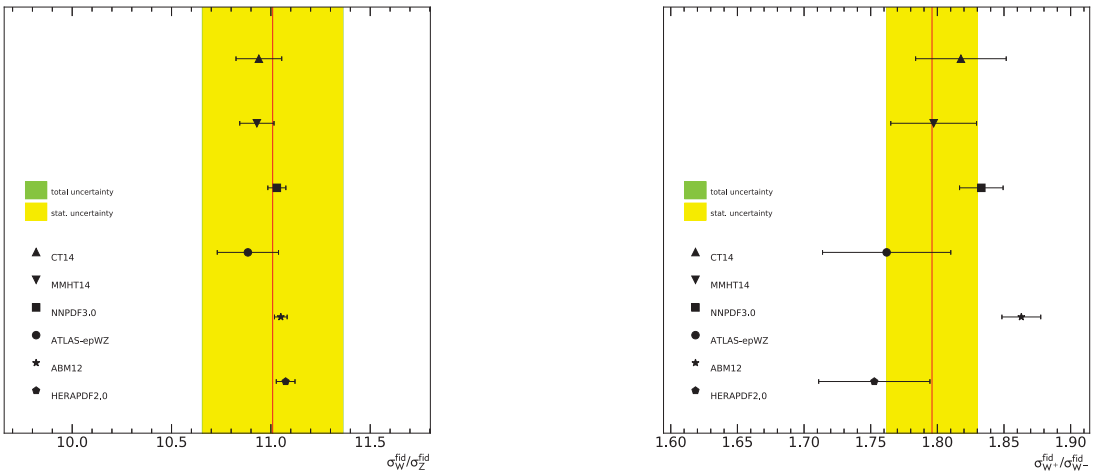

a) b)

Fig. 15.8: Ratio of a) W to Z and b) W^+ to W^- fiducial cross sections compared to predictions based on the six PDF sets: CT14nnlo, MMHT2014, NNPDF3.0, ATLASepWZ12, abm12, HERApdf2.0. The yellow band corresponds to the statistical uncertainty, while the systematic uncertainty is considered to be negligible. Theory predictions are given with the corresponding PDF uncertainties, denoted as error bars.

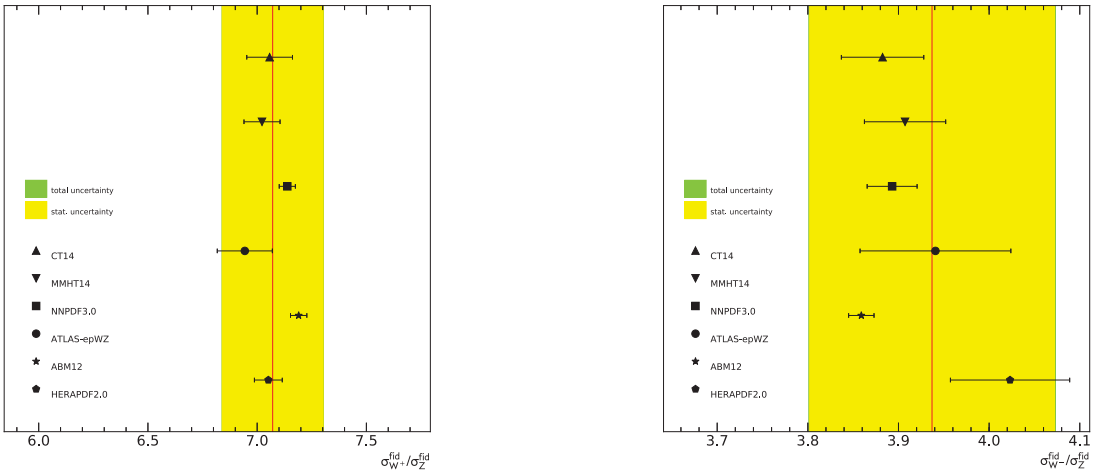

a) b)

Fig. 15.9: Ratio of a) W^+ to Z and b) W^- to Z fiducial cross sections compared to NLO predictions based on the six PDF sets: CT14nnlo, MMHT2014, NNPDF3.0, ATLASepWZ12, abm12, HERApdf2.0. The yellow band corresponds to the statistical uncertainty, while the systematic uncertainty is considered negligible. Theory predictions are given with the corresponding PDF uncertainties, denoted as error bars.

15.4 Impact on parton density functions

The effect of addition of obtained cross sections in the global PDF analysis are estimated using the profiling method, as described in Sec. 3.4. As a reference predictions, it is decided to use CT14 PDF set, because of its relatively good agreement with the data for both NLO and NNLO calculation. The studies are performed at NLO.

As mentioned in Chap. 2 the measurement at $\sqrt{s}$ = 2.76 TeV is mostly sensitive to the valence (u_v and d_v), light-sea ($\bar{d}$ and $\bar{u}$) quark distributions. The addition of cross sections at $\sqrt{s}$ = 2.76 TeV in the PDF set can introduce both the reduction of the uncertainties and shift in the distributions.

A sensitivity of this measurement to the PDF uncertainties is studied with adding into the PDF set the W and Z cross sections scaled to match the theoretical predictions. The resulting distributions are shown in Fig. 15.10 for the initial scale $Q^2 = 1.9$ GeV^2. There is a reduction of the uncertainties on $\bar{u}$ and $\bar{d}$ distributions and in low-x region for the valence quarks. Because of the statistical uncertainty, the addition of the cross sections measured at $\sqrt{s}$ = 2.76 TeV can not reduce the uncertainties on the strange quark distributions. As expected, the W and Z cross sections are not sensitive to the gluon density. It is also possible to reduce the uncertainties on PDF distribution with inclusion of 5, 7 and 13 TeV W and Z cross sections in the analysis, because of the large number of correlated uncertainties for a different energy measurements (especially luminosity).

The full PDF analysis results are shown in Fig. 15.11- 15.12. The starting value of χ^2/NDF = 1.2/3 for a CT14 set shows a good agreement with theoretical predictions, however the profiling procedure allows get better agreement with theory predictions (χ^2/NDF=0.8/3). This method introduces a shift in u_v, d_v, $\bar{u}$, $\bar{v}$, s quark distributions. The gluon distribution is left unchanged. The additional figures for PDF analysis can be found in Appendix D.

The comparison between predictions from the original and profiled CT14 PDF set are shown in Fig. 15.13- 15.14. The best agreement with data is achived by the profiled PDF set.

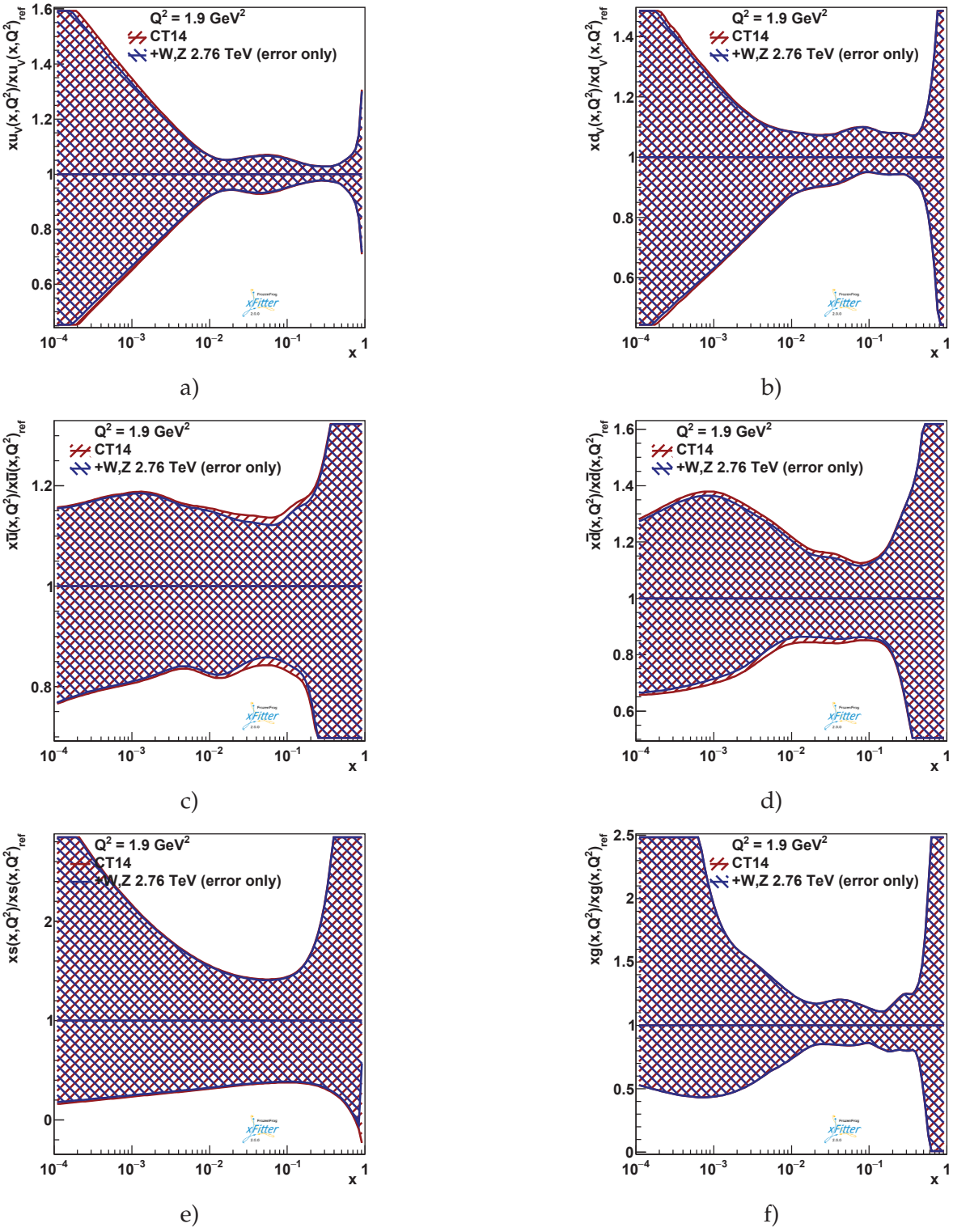

Fig. 15.10: Relative experimental uncertainties for the a) u_v b) d_v c) $\bar{u}$ d) $\bar{d}$ e) s quark and f) gluon densities as a function of x at scale $Q^2 = 1.9$ GeV^2. The red band denotes the reference NLO PDF distributions from CT14 pdf set. The impact of the addition of the new W,Z cross sections at 2.76 TeV on the PDF set uncertainties is shown by the blue boundaries.

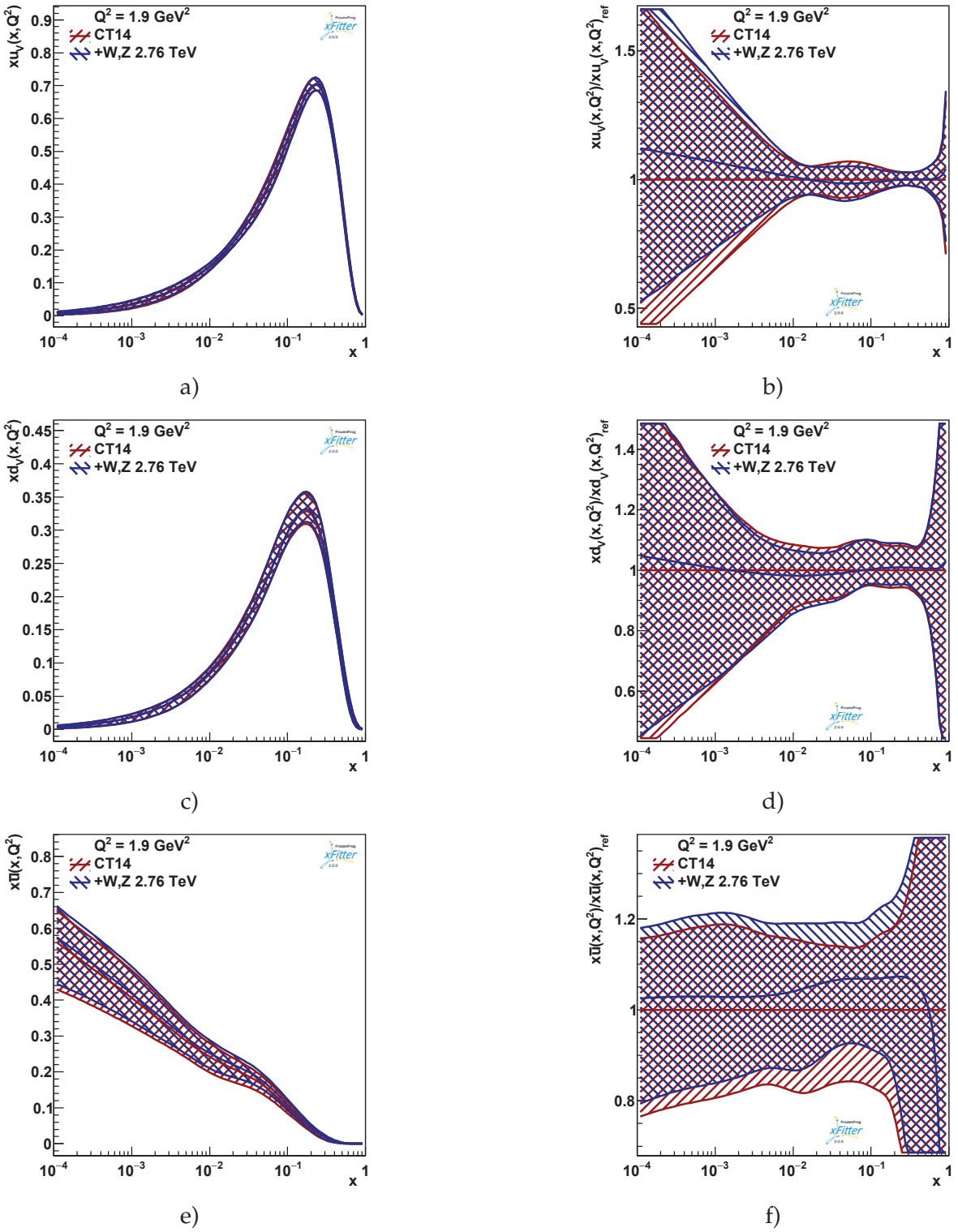

Fig. 15.11: Absolute (for a) u_v, c) d_v, e) $\bar{u}$ quarks) and relative (for b) u_v, d) d_v, f) $\bar{u}$ quarks) parton densities distributions as a function of x at scale $Q^2 = 1.9\,\mathrm{GeV}^2$ with the experimental uncertainties. The red band denotes the reference NLO PDF distributions from CT14 pdf set. The impact of the addition of the new W,Z cross sections at 2.76 TeV on the PDF set is shown by the blue boundaries.

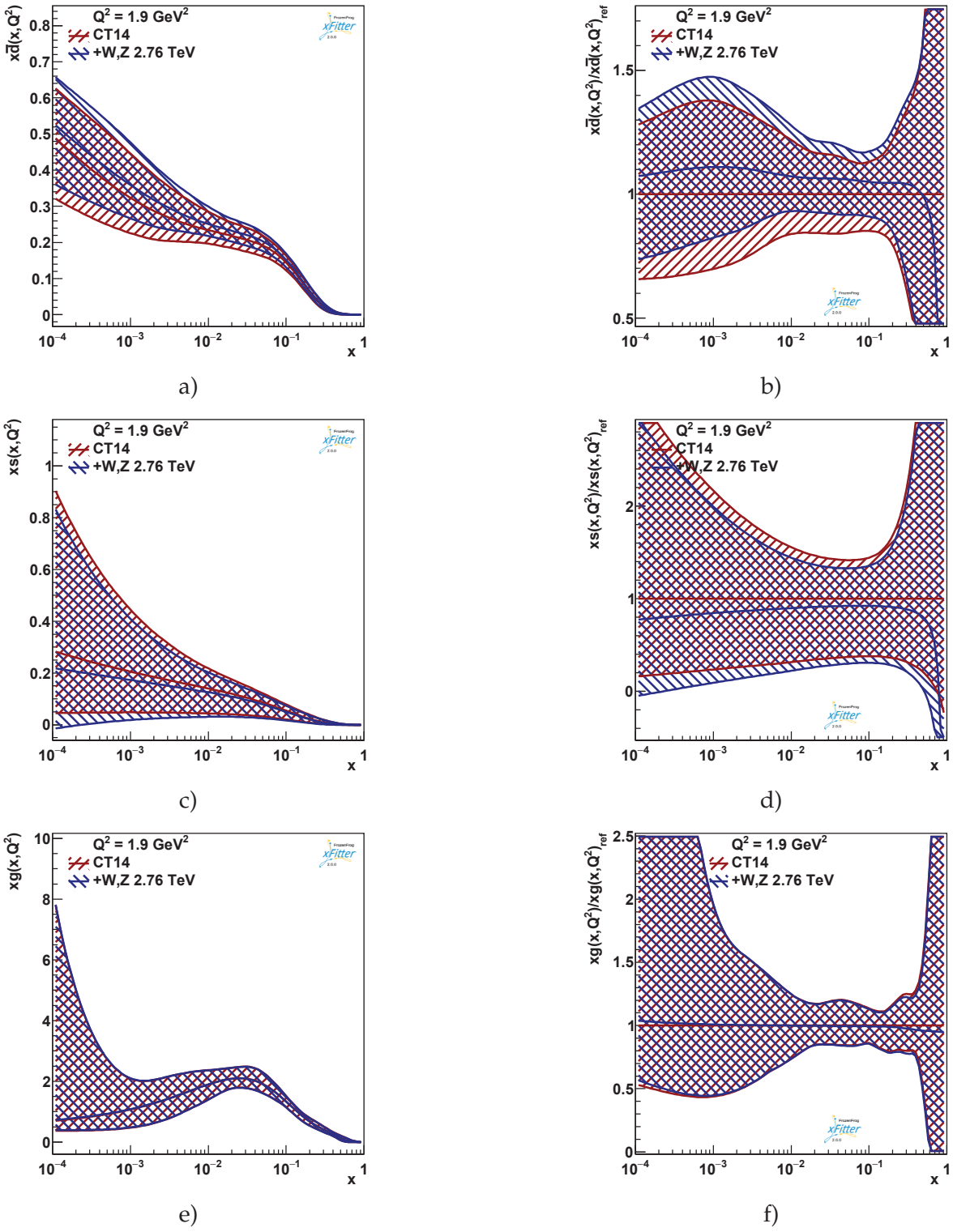

Fig. 15.12: Absolute (for a) $\bar{d}$ c) s quarks and e) gluon) and relative (for b) $\bar{d}$ d) s quarks and f) gluon) distributions for parton densities as a function of x at scale $Q^2 = 1.9$ GeV^2 with the experimental uncertainties. The red band denotes the reference NLO PDF distributions from CT14 pdf set. The impact of the addition of the new W,Z cross sections at 2.76 TeV on the PDF set is shown by the blue boundaries.

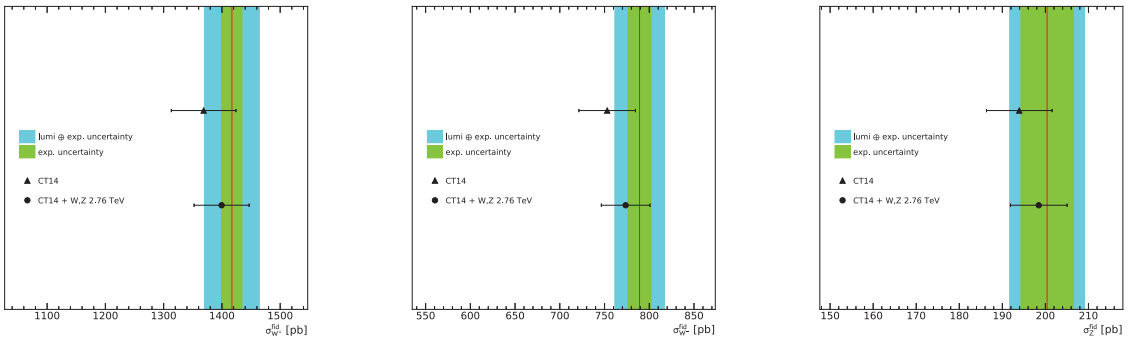

a) b) c)

Fig. 15.13: The measured a) W^+, b) W^- and c) Z production fiducial cross sections in combined channel compared to NLO predictions based on the original and profiled CT14 PDF set.

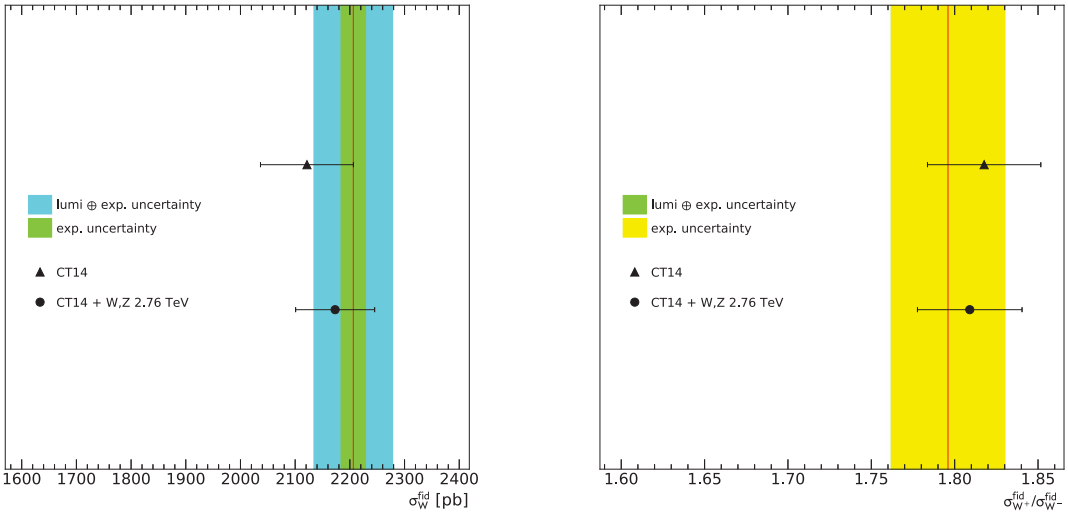

c) b)

Fig. 15.14: The measured a) W and b) ratio of W^+ to W^- fiducial cross sections in combined channel compared to NLO predictions based on the original and profiled CT14 PDF set.

Chapter 16

Summary

This thesis presents the measurement of the $W \rightarrow l\nu$ and $Z \rightarrow ll$ cross sections, where l represents electrons or muons and ν stands for neutrino. These leptonic decay channels offer a clear experimental signature and thus allows performing a high-precision measurement. Theoretical predictions are available up to next-to-next-to leading order accuracy in quantum chromodynamics (QCD) and include electroweak (EW) corrections at next-to leading order accuracy. The cross section predictions depend on the parton distribution functions (PDFs) of protons and therefore the measurement of the W and Z-boson cross sections allows testing models of parton dynamics and offers input for a more precise determination of the parton distribution functions of the proton.

In this analysis, a sample of pp collisions collected at the ATLAS experiment at the center-of-mass energy 2.76 TeV is used. The data corresponds to an integrated luminosity of $4pb^{-1}$. In total about 5500 (500) W-boson (Z-boson) candidates were found per lepton channel.

Due to the very limited size of the sample used, the statistical uncertainty is one of the main uncertainties of this measurement. Several sources of the systematic uncertainties were studied as well. The uncertainty of the luminosity measurement is the dominant one. Studies of the hadronic recoil calibration for the missing transverse energy reconstruction have been performed. The corresponding uncertainties have a small, but not negligible, contribution to the systematic uncertainties of the W analyses. The contribution of the main background process has been estimated using Monte Carlo simulation, except for the multijet background for which a data-driven method was used.

The measured $W \rightarrow e\nu$ and $Z \rightarrow ee$ fiducial cross sections are:

$$\sigma_W^{fid}(W \rightarrow e\nu) = 2190.0 \pm 29.1(stat.) \pm 7.8(sys.) \pm 65.7(lumi.)\,[pb],$$
$$\sigma_Z^{fid}(Z \rightarrow ee) = 195.0 \pm 9.4(stat.) \pm 1.0(sys.) \pm 6.0(lumi.)\,[pb],$$

and the cross section for $W \rightarrow \mu\nu$ and $Z \rightarrow \mu\mu$ are:

$$\sigma_W^{fid}(W \rightarrow \mu\nu) = 2217.0 \pm 27.9(stat.) \pm 50.6(sys.) \pm 66.5(lumi.)\,[pb],$$
$$\sigma_Z^{fid}(Z \rightarrow ee) = 204.0 \pm 8.0(stat.) \pm 0.4(sys.) \pm 6.3(lumi.)\,[pb].$$

The measured values of cross sections agree with each other within the uncertainties and as well agree with theoretical predictions in different orders of QCD accuracy.

The measurement of the cross-section ratios benefits from the partial cancellation of correlated experimental uncertainties and full cancellation of the luminosity uncertainty, which makes them a powerful tool to test SM predictions. The measured cross section ratios in the muon to electron channels in the fiducial region are:

$$R_W = \frac{\sigma_W^\mu}{\sigma_W^e} = \frac{BR(W\to\mu\nu)}{BR(W\to e\nu)} = 1.012 \pm 0.026(sys.) \pm 0.019(stat.),$$
$$R_Z = \frac{\sigma_Z^\mu}{\sigma_Z^e} = \frac{BR(Z\to\mu\mu)}{BR(Z\to ee)} = 1.046 \pm 0.004(sys.) \pm 0.065(stat.)$$

which is in agreement, within the uncertainty, with SM predictions and the world average.

The combination of the electron and muon channel cross section results allows to further reduce the statistical uncertainties of the measurements:

$$\sigma_W^{fid}(W \to l\nu) = 2206.3 \pm 20.2(stat.) \pm 10.6(sys.) \pm 68.4(lumi.)\,[pb],$$
$$\sigma_Z^{fid}(Z \to ll) = 200.4 \pm 6.1(stat.) \pm 0.3(sys.) \pm 6.2(lumi.)\,[pb].$$

These results are used to measure the W to Z-boson cross section ratios:

$$R_{W/Z} = 11.010 \pm 0.351\,(stat.)\ \pm 0.052\,(sys.),$$

which has an uncertainty comparable with the uncertainty of the next-to leading order predictions.

The obtained cross sections have been used to constrain the proton PDF distributions and have shown a slight reduction of uncertainties for the u, d and $\bar{u}$, $\bar{d}$ distribution functions. The analysis dedicated to constraining the PDF distributions would certainly benefit from a bigger data sample collected at a similar center-of-mass energy and a combination with measurements of the W and Z-boson cross sections at other center-of-mass energies.

Appendix A

Cholesky transformation results

In this Appenndix results of Cholesky decomposition for partially correlated uncertainties (see Sec. 13.5) are presented. The resulting uncorrelated systematic sources are shown in Fig. A.1 in source vs the analysis plane. The content of the cell corresponds to the value of $\delta C/C(\%)$. The resulted systematic uncertainties are included in averaging process and PDF profiling.

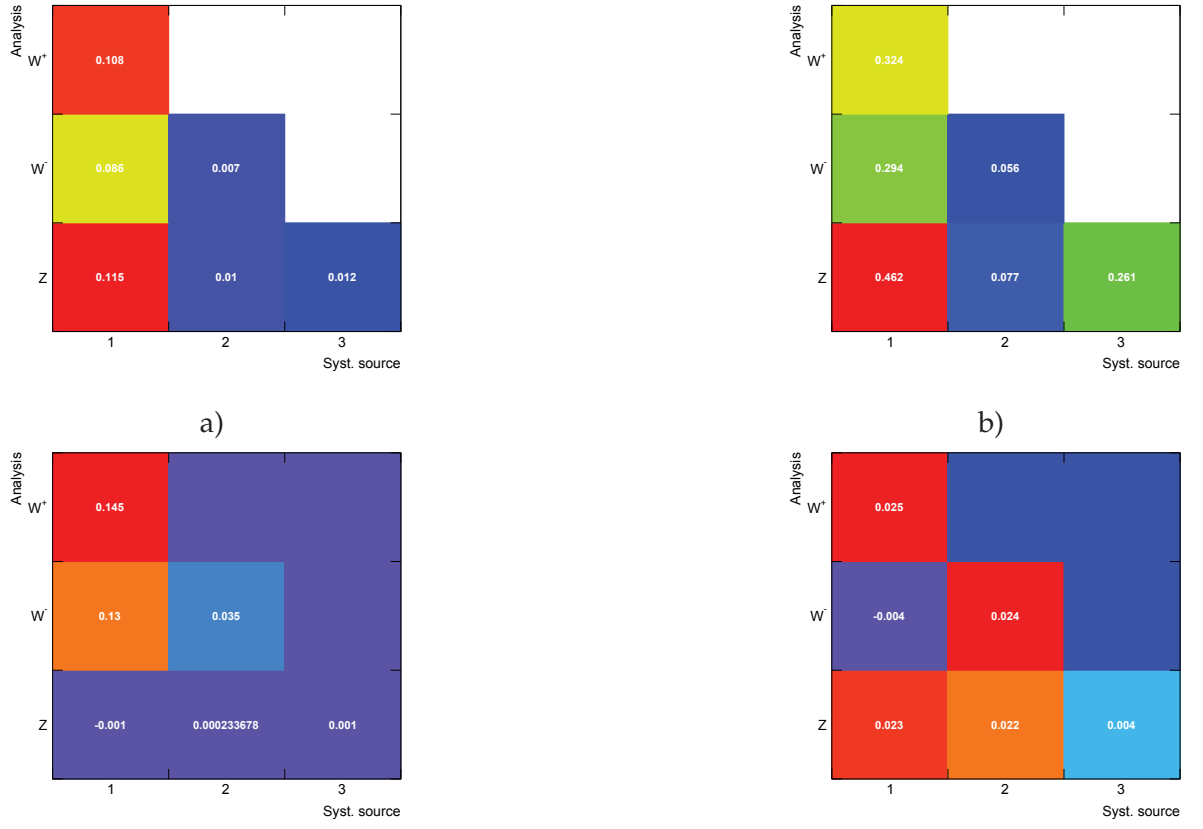

Fig. A.1: Results of Cholesky decomposition for correlated uncertainties for a) electron reconstruction, b) electron identification, c) electron trigger and d) muon trigger scale factor uncertainties estimated using the Toy MC method.

Appendix B

Covariance matrixes

The covariance matrix of cross sections measurements is calculated as:

$$C_{XY} = \sum_k \sigma_X^k \sigma_Y^k \rho_{XY}^k, \tag{B.1}$$

where index k runs over all independent sources of uncertainties, σ_X^k and σ_Y^k are the k-th uncertainties of the measurement X and Y respectively. The coefficient ρ_{XY}^k - is a correlation coefficient between two estimates from the correlation matrix. Each element of the diagonal matrix is equal to 1. The off-diagonal elements are equal to 0 for non correlated sources of uncertainty, to 1 for totally correlated and -1 for totally uncorrelated. The uncertainties sources and their correlations are explained in Chap. 13.

The covariance matrix for the cross-section measurements in electron and muon channels are shown in Fig. B.1- B.2. The correlation matrix for the combined measurement is shown in Fig. B.3. The correlation matrix of the ratios R_W and R_Z used in Sec. 15.2 is shown in Fig. B.4.

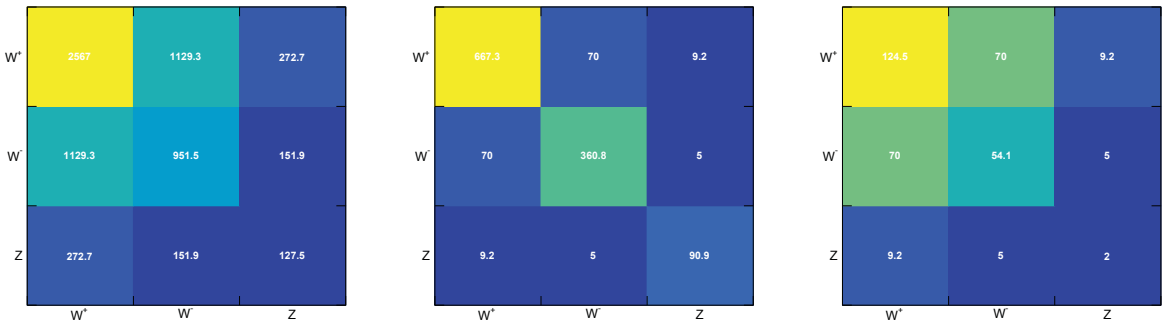

c) b) c)

Fig. B.1: Covariance matrix for the measurements of Z, W^+ and W^- cross sections for electron channel in fiducial region a) for all uncertainty b) for all but luminosity uncertainty c) for all but luminosity and statistical uncertainty.

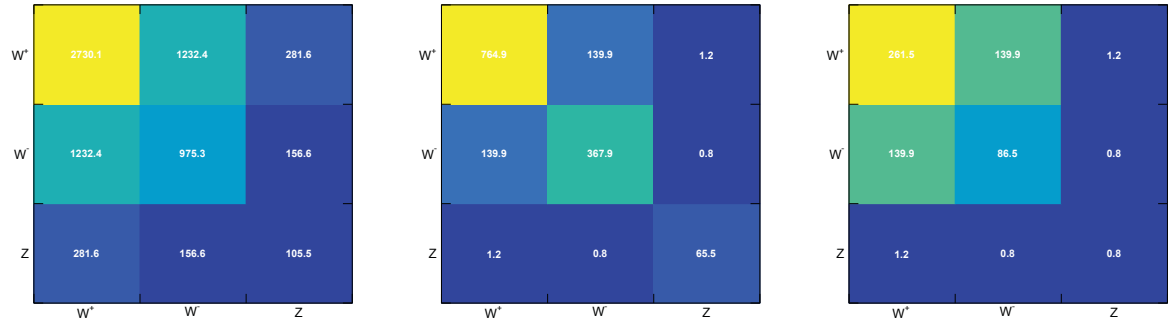

c) b) c)

Fig. B.2: Covariance matrix for the measurements of Z, W^+ and W^- cross sections for muon channel in fiducial region a) for all uncertainty b) for all but luminosity uncertainty c) for all but luminosity and statistical uncertainty.

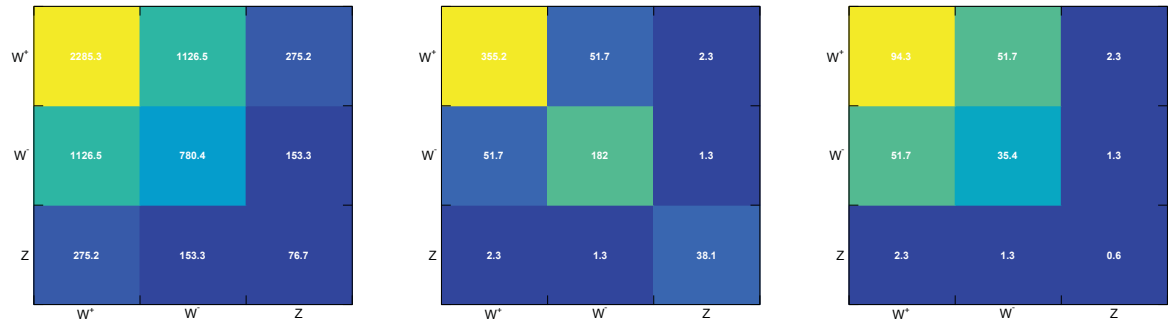

c) b) c)

Fig. B.3: Covariance matrix for the measurements of Z, W^+ and W^- cross sections for combined channel in fiducial region a) for all uncertainty b) for all but luminosity uncertainty c) for all but luminosity and statistical uncertainty.

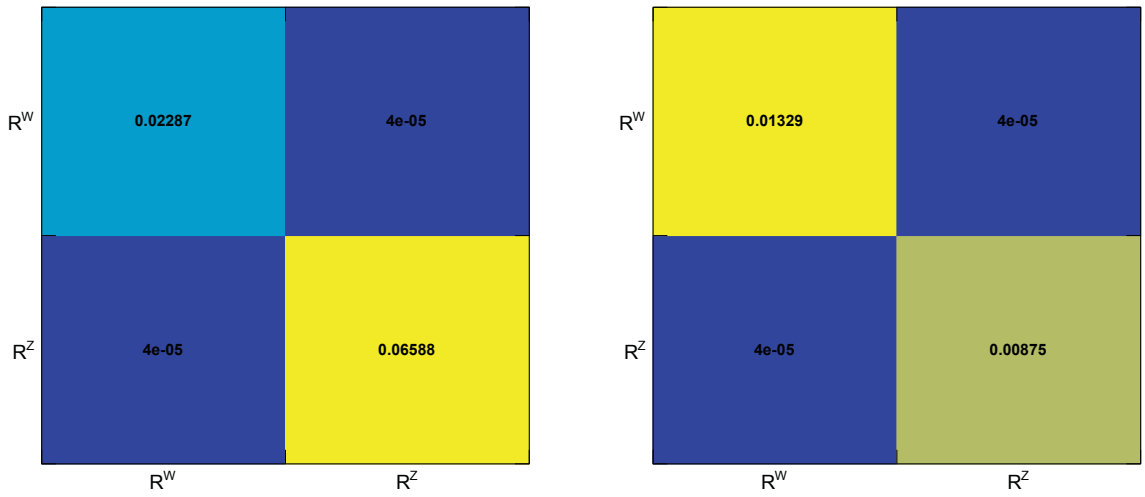

c) b)

Fig. B.4: Covariance matrix for the measurements of R_W and R_Z ratios from Sec. 15.2 for electron channel in fiducial region a) for all uncertainty b)for all but statistical uncertainty.

Appendix C

Additional comparisons with theoretical predictions

The cross section results for combined channel in fiducial regions have been compared to NNLO predictions for different PDF sets in Sec. 15.3. This appendix presents the comparison of cross section in full and extrapolated to 13 TeV regions with NNLO predictions (Fig. C.1-Fig. C.3). The agreement between predictions and results in full region is worse, than for fiducial and extrapolated regions, however it is still within 2σ of uncertainty.

Additionally, the comparison for NLO predictions in fiducial region is presented in Fig. C.4-C.5.

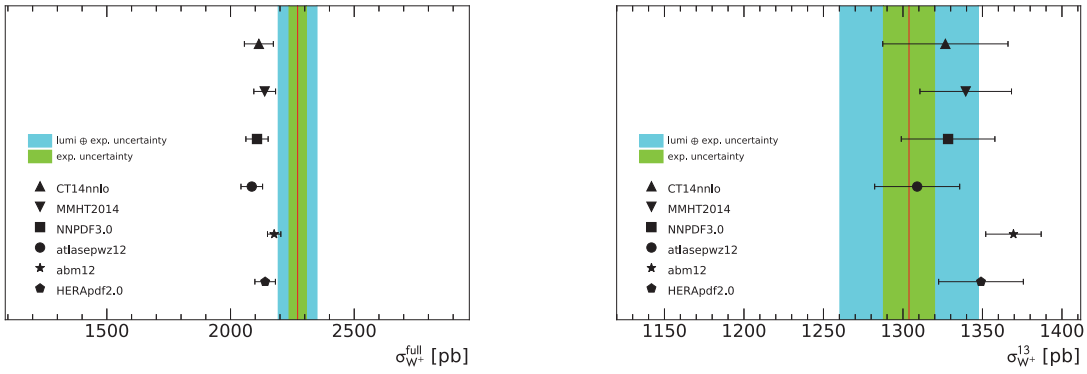

a) b)

Fig. C.1: The NNLO predictions for the W^+ cross section in a) full phase space and b) new 13 TeV phase space in pb for the six PDFs CT14nnlo, MMHT2014, NNPDF3.0, ATLASepWZ12, abm12, HERApdf2.0 compared to the measured cross section as given in Tab. 15.2. The green (cyan) band corresponds to the experimental uncertainty without (with) the luminosity uncertainty. The theory predictions are given with the corresponding PDF uncertainties shown as error bands.

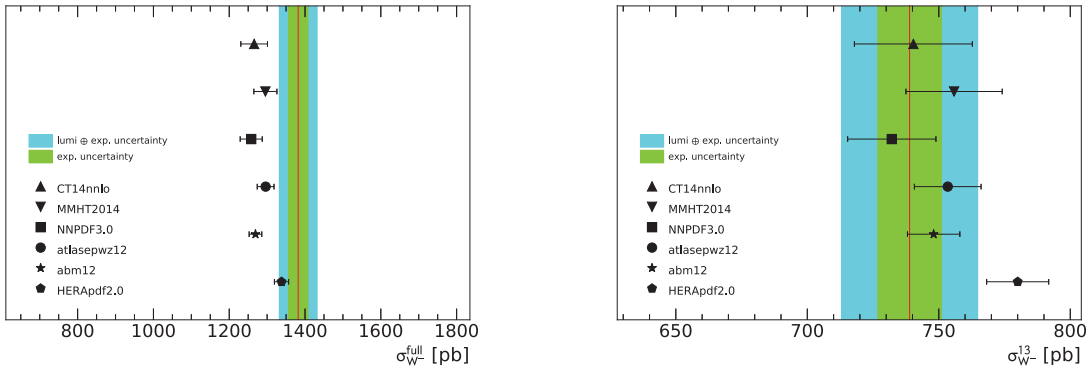

a) b)

Fig. C.2: The NNLO predictions for the W^- cross section in a) full phase space and b) new 13 TeV phase space in pb for the six PDFs CT14nnlo, MMHT2014, NNPDF3.0, ATLASepWZ12, abm12, HERApdf2.0 compared to the measured cross section as given in Tab. 15.2. The green (cyan) band corresponds to the experimental uncertainty without (with) the luminosity uncertainty. The theory predictions are given with the corresponding PDF uncertainties shown as error bands.

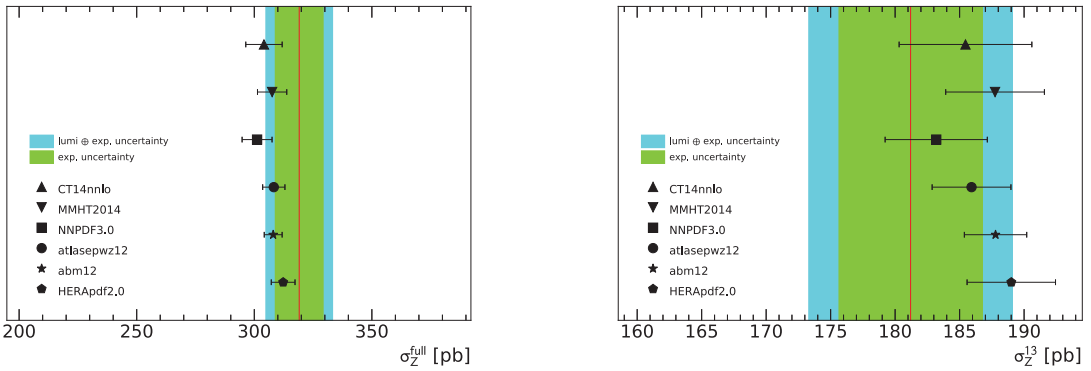

a) b)

Fig. C.3: The NNLO predictions for the Z cross section in a) full phase space and b) new 13 TeV phase space in pb for the six PDFs CT14nnlo, MMHT2014, NNPDF3.0, ATLASepWZ12, abm12, HERApdf2.0 compared to the measured cross section as given in Tab. 15.2. The green (cyan) band corresponds to the experimental uncertainty without (with) the luminosity uncertainty. The theory predictions are given with the corresponding PDF uncertainties shown as error bands.

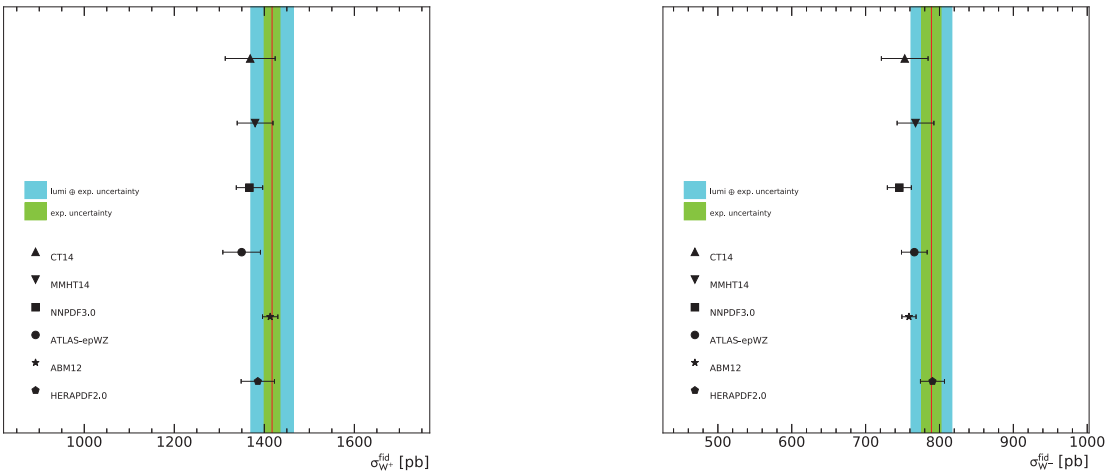

a) b)

Fig. C.4: The NLO predictions for the fiducial cross section a) σ^{fid}_{W+} b) σ^{fid}_{W-} in pb for the six PDFs CT14nnlo, MMHT2014, NNPDF3.0, ATLASepWZ12, abm12, HERApdf2.0 compared to the measured fiducial cross section as given in Tab. 15.2. The green (cyan) band corresponds to the experimental uncertainty without (with) the luminosity uncertainty. The theory predictions are given with the corresponding PDF uncertainties shown as error bands.

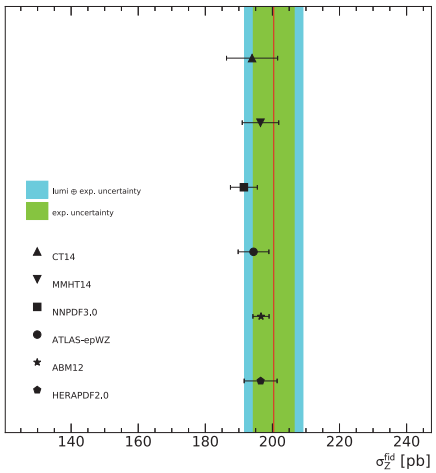

Fig. C.5: The NLO predictions for the fiducial cross section σ^{fid}_{Z} in pb for the six PDFs CT14nnlo, MMHT2014, NNPDF3.0, ATLASepWZ12, abm12, HERApdf2.0 compared to the measured fiducial cross section as given in Tab. 15.2. The green (cyan) band corresponds to the experimental uncertainty without (with) the luminosity uncertainty. The theory predictions are given with the corresponding PDF uncertainties shown as error bands.

Appendix D

Additional PDF profiling plots

The results of PDF profiling have been showed in Sec. 15.4. In this Appendix the effect on valence quarks ratio d_v/u_v (Fig. D.1) and difference in sea u and d quarks $\bar{d} - \bar{u}$ (Fig. D.2) is shown. The effect of inclusion of the new data at the scale of the measurement $Q^2 \approx M_W^2$ is shown in Fig. D.3- D.5.

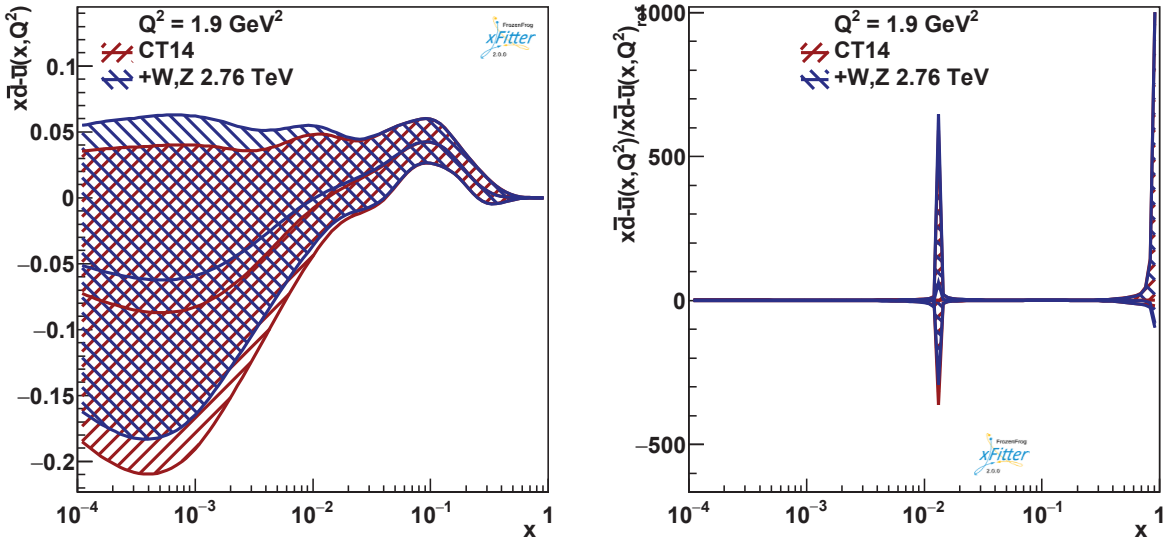

a) b)

Fig. D.1: The a) absolute and b) relative distributions for the $\bar{d} - \bar{u}$ quark densities as a function of x at scale $Q^2 = 1.9$ GeV^2 with the experimental uncertainties. The red band denotes the reference NLO PDF distributions from CT14 pdf set. The impact of addition of the new W,Z cross sections at 2.76 TeV on the PDF set is shown by the blue boundaries.

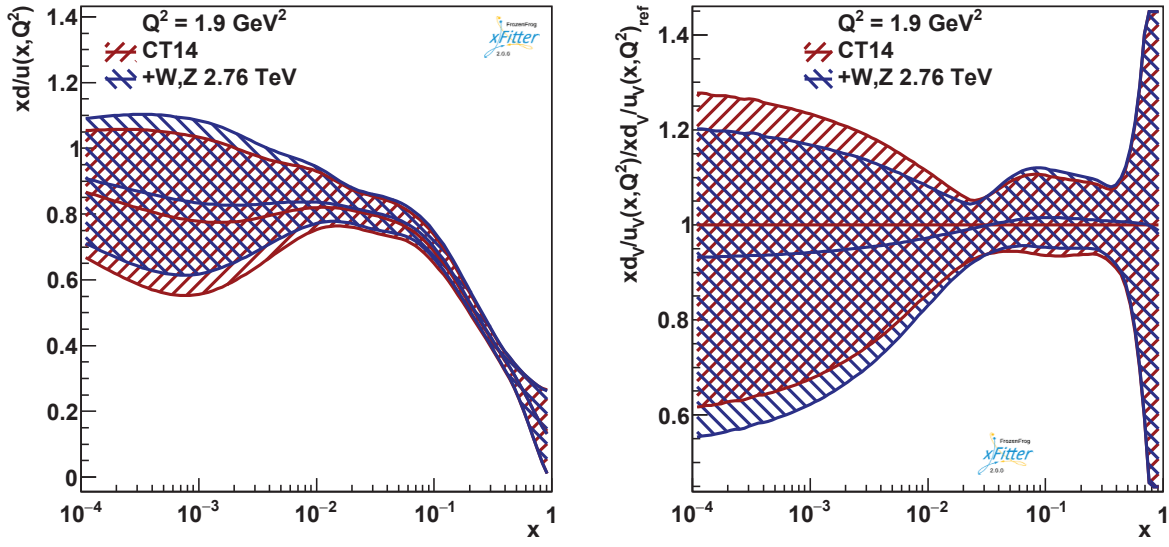

a) b)

Fig. D.2: The a) absolute and b) relative distributions for the u_v/d_v quark densities as a function of x at scale $Q^2 = 1.9$ GeV^2 with the experimental uncertainties. The red band denotes the reference NLO PDF distributions from CT14 pdf set. The impact of addition of the new W,Z cross sections at 2.76 TeV on the PDF set is shown by the blue boundaries

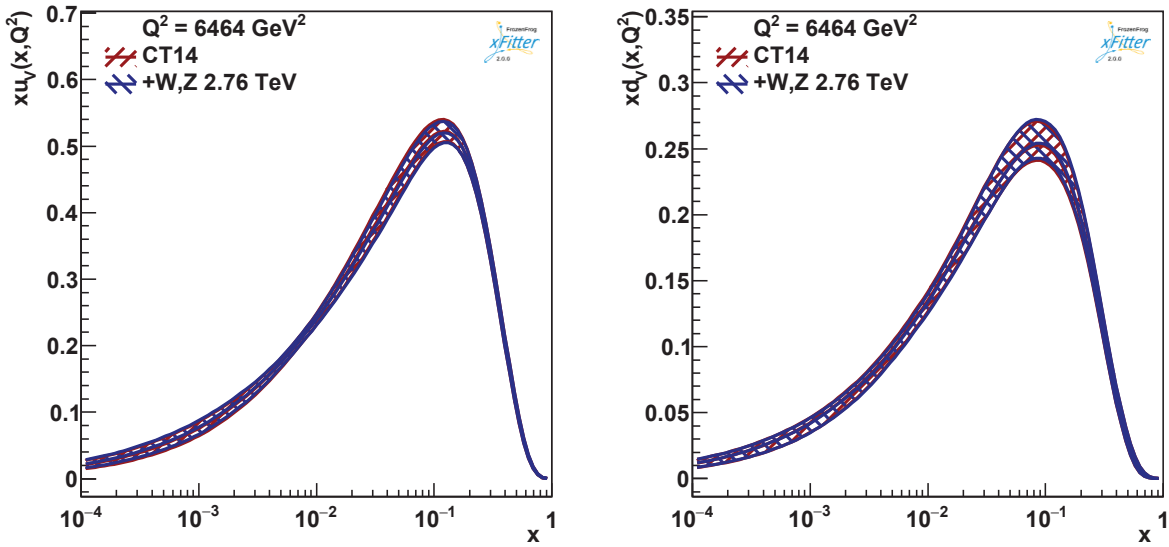

a) b)

Fig. D.3: The absolute for the a) u_v and b) d_v quark densities as a function of x at scale $Q^2 = M_W^2$ with the experimental uncertainties. The red band denotes the reference NLO PDF distributions from CT14 pdf set. The impact of addition of the new W,Z cross sections at 2.76 TeV on the PDF set is shown by the blue boundaries.

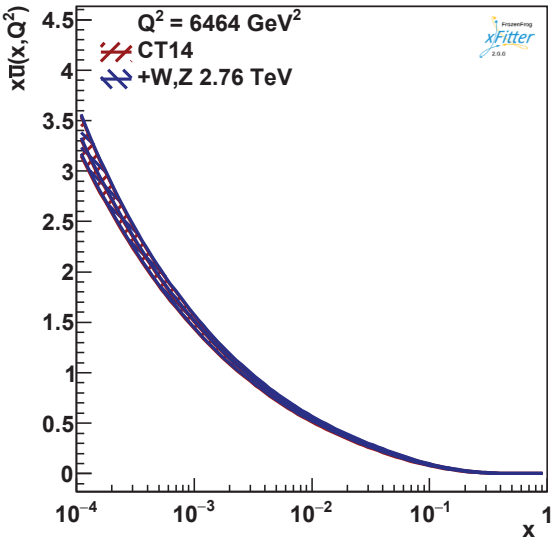

c)

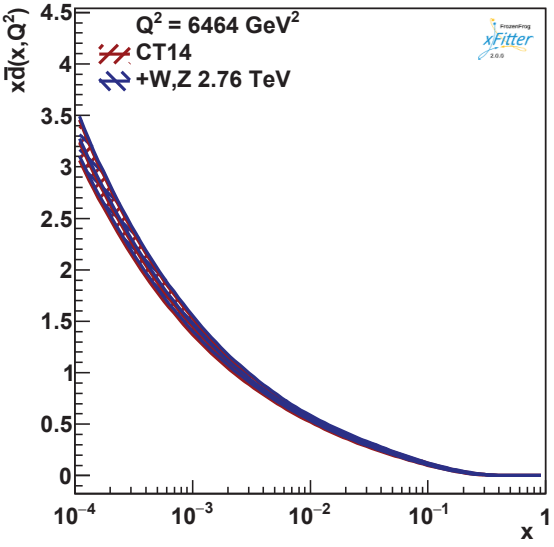

d)

Fig. D.4: The absolute for the a) $\bar{u}$ and b) $\bar{d}$ quark densities as a function of x at scale $Q^2 = M_W^2$ with the experimental uncertainties. The red band denotes the reference NLO PDF distributions from CT14 pdf set. The impact of addition of the new W,Z cross sections at 2.76 TeV on the PDF set is shown by the blue boundaries.

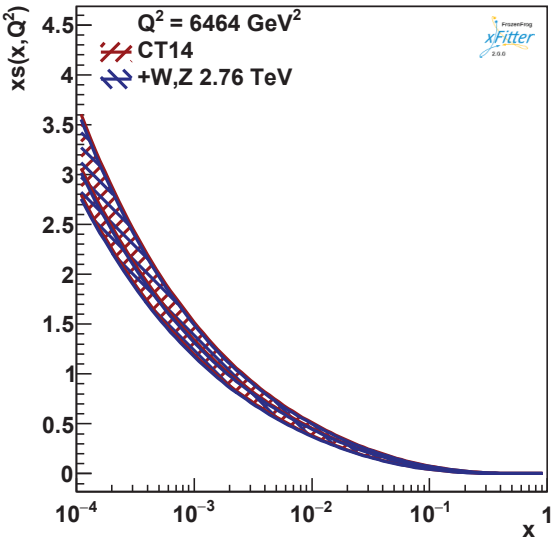

e)

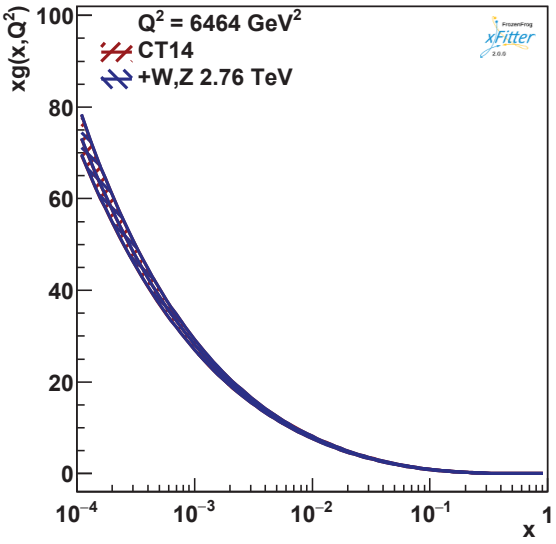

f)

Fig. D.5: The absolute for the a) s quark and b) gluon densities as a function of x at scale $Q^2 = M_W^2$ with the experimental uncertainties. The red band denotes the reference NLO PDF distributions from CT14 pdf set. The impact of addition of the new W,Z cross sections at 2.76 TeV on the PDF set is shown by the blue boundaries.

Bibliography

[1] J. M. Campbell, J. W. Huston, and W. J. Stirling, "Hard Interactions of Quarks and Gluons: a Primer for LHC Physics", doi:10.1088/0034-4885/70/1/R02, arXiv:hep-ph/0611148.

[2] L. Okun, "Leptons and Quarks". North-Holland Personal Library. Elsevier Science, 2013.

[3] S. L. Glashow, "Partial-symmetries of weak interactions", *Nucl. Phys.* **22** (feb, 1961) 579–588, doi:10.1016/0029-5582(61)90469-2.

[4] S. Weinberg, "A Model of Leptons", *Phys. Rev. Lett.* **19** (nov, 1967) 1264–1266, doi:10.1103/physrevlett.19.1264.

[5] A. Salam, "Renormalizability of Gauge Theories", *Phys. Rev.* **127** (jul, 1962) 331–334, doi:10.1103/physrev.127.331.

[6] Planck Collaboration, "Planck 2015 results. XIII. Cosmological parameters", arXiv:1502.01589.

[7] ATLAS Collaboration, "Standard Model public results". https://twiki.cern.ch/twiki/bin/view/AtlasPublic/StandardModelPublicResults.

[8] ATLAS Collaboration, "Observation of a new particle in the search for the Standard Model Higgs boson with the ATLAS detector at the LHC", *Phys. Lett.* **B716** (2012) 1–29, doi:10.1016/j.physletb.2012.08.020, arXiv:1207.7214.

[9] CMS Collaboration, "Observation of a new boson at a mass of 125 GeV with the CMS experiment at the LHC", *Phys. Lett.* **B716** (2012) 30–61, doi:10.1016/j.physletb.2012.08.021, arXiv:1207.7235.

[10] Wikimedia, "Standard Model of Elementary Particles". http://en.wikipedia.org/wiki/Standard_Model.

[11] E. Noether, "Invarianten beliebiger Differentialausdrücke.", *Nachr. Ges. Wiss. Göttingen, Math.-Phys. Kl.* **1918** (1918) 37–44.

[12] E. Noether, "Invariante Variationsprobleme.", *Nachr. Ges. Wiss. Göttingen, Math.-Phys. Kl.* **1918** (1918) 235–257.

[13] H. Fritzsch, M. Gell-Mann, and H. Leutwyler, "Advantages of the Color Octet Gluon Picture", *Phys. Lett.* **B47** (1973) 365–368, doi:10.1016/0370-2693(73)90625-4.

[14] D. J. Gross and F. Wilczek, "Ultraviolet Behavior of Non-Abelian Gauge Theories", *Phys. Rev. Lett.* **30** (jun, 1973) 1343–1346, doi:10.1103/physrevlett.30.1343.

[15] H. D. Politzer, "Reliable Perturbative Results for Strong Interactions?", *Phys. Rev. Lett.* **30** (jun, 1973) 1346–1349, doi:10.1103/physrevlett.30.1346.

[16] J. C. Collins, "Renormalization: general theory", arXiv:hep-th/0602121.

[17] S. Bethke, "The 2009 World Average of α_s", *Eur. Phys. J.* **C64** (2009) 689–703, doi:10.1140/epjc/s10052-009-1173-1, arXiv:0908.1135.

[18] R. P. Feynman, "Very High-Energy Collisions of Hadrons", *Phys. Rev. Lett.* **23** (dec, 1969) 1415–1417, doi:10.1103/physrevlett.23.1415.

[19] J. C. Collins, D. E. Soper, and G. Sterman, "Factorization of Hard Processes in QCD", arXiv:hep-ph/0409313.

[20] L. A. Harland-Lang, A. D. Martin, P. Motylinski, and R. S. Thorne, "Parton distributions in the LHC era: MMHT 2014 PDFs", doi:10.1140/epjc/s10052-015-3397-6, arXiv:1412.3989.

[21] V. N. Gribov and L. N. Lipatov, "Deep inelastic e p scattering in perturbation theory", *Sov. J. Nucl. Phys.* **15** (1972) 438–450. [Yad. Fiz.15,781(1972)].

[22] L. N. Lipatov *Sov. J. Nucl. Phys.* **20** (1975).

[23] G. P. G. Altarelli, "Asymptotic Freedom in Parton Language", *Nucl. Phys.* **B126** (1977) 298.

[24] Y. L. Dokshitzer, "Deep inelastic e p scattering in perturbation theory", *Sov. Phys. JETP* **46** (1977) 641.

[25] UA1 Collaboration, "Experimental observation of isolated large transverse energy electrons with associated missing energy at $\sqrt{s}$ = 540 GeV", *Phys. Lett. B* **122** (Jan, 1983) 103–116. 31 p.

[26] UA2 Collaboration, "Observation of Single Isolated Electrons of High Transverse Momentum in Events with Missing Transverse Energy at the CERN anti-p p Collider", *Phys. Lett.* **122B** (1983) 476–485, doi:10.1016/0370-2693(83)91605-2.

[27] UA1 Collaboration, "Observation of Muonic Z0 Decay at the anti-p p Collider", *Phys. Lett.* **B147** (1984) 241–248, doi:10.1016/0370-2693(84)90628-2.

[28] UA2 Collaboration, "Evidence for Z0 —> e+ e- at the CERN anti-p p Collider", *Phys. Lett.* **B129** (1983) 130–140, doi:10.1016/0370-2693(83)90744-X.

[29] K. Lohwasser. personal communication.

[30] R. K. Ellis, W. J. Stirling, and B. R. Webber, "QCD and Collider Physics". Cambridge monographs on particle physics, nuclear physics, and cosmology. Cambridge Univ. Press, Cambridge, 2003. Photography by S. Vascotto.

[31] Particle Data Group Collaboration, "Review of Particle Physics", *Chin. Phys.* **C40** (2016) 100001, doi:10.1088/1674-1137/40/10/100001.

[32] R. Gavin, Y. Li, F. Petriello, and S. Quackenbush, "FEWZ 2.0: A code for hadronic Z production at next-to-next-to-leading order", *Comput. Phys. Commun.* **182** (2011) 2388–2403, doi:10.1016/j.cpc.2011.06.008, arXiv:1011.3540.

[33] S. Dulat et al., "New parton distribution functions from a global analysis of quantum chromodynamics", *Phys. Rev.* **D93** (2016), no. 3, 033006, doi:10.1103/PhysRevD.93.033006, arXiv:1506.07443.

[34] ATLAS Collaboration, "Measurement of W^+, W^- and Z/γ^* production cross sections in pp collisions at $\sqrt{s}$ = 13 TeV with the ATLAS detector", *Phys. Lett. B* **759** (aug, 2016) 601–621.

[35] A. Glazov, "Averaging of DIS cross section data", *AIP Conf. Proc.* **792** (2005) 237–240, doi:10.1063/1.2122026. [,237(2005)].

[36] S. Alekhin et al., "HERAFitter, Open Source QCD Fit Project", arXiv:1410.4412.

[37] xFitter Collaboration, "xFitter PDF Fitting package". https://www.xfitter.org/xFitter/xFitter/DownloadPage?action=AttachFile&do=view&target=manual.pdf, 2017.

[38] H. Paukkunen and P. Zurita, "PDF reweighting in the Hessian matrix approach", *J. High Energy Phys.* **12** (2014) 100, doi:10.1007/JHEP12(2014)100, arXiv:1402.6623.

[39] P. Giubellino, "Heavy Ion Physics at the LHC", arXiv:0809.1062.

[40] L. Evans and P. Bryant, "LHC Machine", *JINST* **3** (2008) S08001, doi:10.1088/1748-0221/3/08/S08001.

[41] ALICE Collaboration, "The ALICE experiment at the CERN LHC", *JINST* **3** (2008) S08002, doi:10.1088/1748-0221/3/08/S08002.

[42] ATLAS Collaboration, J. T. Shank, "The ATLAS Detector: Status and Results from Cosmic Rays", in *Particles and fields. Proceedings, Meeting of the Division of the American Physical Society, DPF 2009, Detroit, USA, July 26-31, 2009*. 2009. arXiv:0910.3081.

[43] CMS Collaboration, "The CMS Experiment at the CERN LHC", *JINST* **3** (2008) S08004, doi:10.1088/1748-0221/3/08/S08004.

[44] LHCb Collaboration, "The LHCb Detector at the LHC", *JINST* **3** (2008) S08005, doi:10.1088/1748-0221/3/08/S08005.

[45] J. Goodson, "Search for Supersymmetry in States with Large Missing Transverse Momentum and Three Leptons including a Z-Boson". PhD thesis, Stony Brook University, May, 2012. Presented 17 Apr 2012.

[46] ATLAS Collaboration, "The ATLAS experiment at the CERN Large Hadron Collider", *JINST* **3** (2008) doi:10.1088/1748-0221/3/08/S08003.

[47] S. van der Meer, "Calibration of the Effective Beam Height in the ISR", *Cern Internal Report ISR-PO* **68-31** (1968).

[48] ATLAS Collaboration, "Concepts, Design and Implementation of the ATLAS New Tracking (NEWT)", Technical Report ATL-SOFT-PUB-2007-007. ATL-COM-SOFT-2007-002, CERN, Geneva, Mar, 2007.

[49] R. Fruhwirth, "Application of Kalman filtering to track and vertex fitting", *Nucl. Instrum. Meth.* **A262** (1987) 444–450, doi:10.1016/0168-9002(87)90887-4.

[50] W. Lampl et al., "Calorimeter clustering algorithms: Description and performance", *ATL-LARG-PUB-2008-002, ATL-COM-LARG-2008-003* (2008).

[51] ATLAS Collaboration, "Electron reconstruction and identification efficiency measurements with the ATLAS detector using the 2011 LHC proton-proton collision data", doi:10.1140/epjc/s10052-014-2941-0, arXiv:1404.2240.

[52] ATLAS Collaboration, "Expected Performance of the ATLAS Experiment - Detector, Trigger and Physics", arXiv:0901.0512.

[53] ATLAS Collaboration, "A Muon Identification and Combined Reconstruction Procedure for the ATLAS Detector at the LHC at CERN", *IEEE Trans. Nucl. Sci.* **51** (2004) 3030–3033, doi:10.1109/TNS.2004.839102.

[54] ATLAS Collaboration, "A muon identification and combined reconstruction procedure for the ATLAS detector at the LHC using the (MUONBOY, STACO, MuTag) reconstruction packages", *Nucl. Instrum. Meth.* **A572** (2007) 77–79, doi:10.1016/j.nima.2006.10.340.

[55] ATLAS Collaboration, "Performance of missing transverse momentum reconstruction in proton-proton collisions at $\sqrt{s}$ = 7 TeV with ATLAS", *Eur. Phys. J. C* **72** (jan, 2012) doi:10.1140/epjc/s10052-011-1844-6.

[56] ATLAS Collaboration, "Pile-up Suppression in Missing Transverse Momentum Reconstruction in the ATLAS Experiment in Proton-Proton Collisions at $\sqrt{s}$ = 8 TeV", Technical Report ATLAS-CONF-2014-019, CERN, Geneva, May, 2014.

[57] T. H. V. Nguyen, N. Besson, and M. Boonekamp, "ETmiss from the reconstruction and calibration of the hadronic recoil", Technical Report ATL-PHYS-INT-2010-039, CERN, Geneva, Apr, 2010.

[58] M. Schott, G. Siragusa, J. Cuth, and T.-h. Lin, "Measurement of m_W at 7 TeV: Reconstruction of the hadronic recoil", Technical Report ATL-COM-PHYS-2014-1435, CERN, Geneva, Nov, 2014.

[59] P. Calafiura et al., "The Athena control framework in production, new developments and lessons learned", in *Computing in high energy physics and nuclear physics. Proceedings, Conference, CHEP'04, Interlaken, Switzerland, September 27-October 1, 2004*, pp. 456–458. 2005.

[60] "MonteCarloGenerators – Sherpa – Hepforge". https://sherpa.hepforge.org/trac/wiki/MonteCarloGenerators.

[61] S. Drell and T.-M. Yan, "Massive Lepton Pair Production in Hadron-Hadron Collisions at High-Energies", *Phys.Rev.Lett.* **25** (1970) 316–320, doi:10.1103/PhysRevLett.25.316.

[62] B. R. Webber, "Fragmentation and Hadronization", arXiv:hep-ph/9912292.

[63] P. Nason, "A New method for combining NLO QCD with shower Monte Carlo algorithms", *J. High Energy Phys.* **0411** (2004) 040, doi:10.1088/1126-6708/2004/11/040, arXiv:hep-ph/0409146.

[64] S. Alioli, P. Nason, C. Oleari, and E. Re, "NLO vector-boson production matched with shower in POWHEG", *J. High Energy Phys.* **0807** (2008) 060, doi:10.1088/1126-6708/2008/07/060, arXiv:0805.4802.

[65] T. Sjostrand, S. Mrenna, and P. Z. Skands, "PYTHIA 6.4 Physics and Manual", *J. High Energy Phys.* **0605** (2006) 026, doi:10.1088/1126-6708/2006/05/026, arXiv:hep-ph/0603175.

[66] B. Andersson, G. Gustafson, G. Ingelman, and T. Sjostrand, "Parton Fragmentation and String Dynamics", *Phys.Rept.* **97** (1983) 31–145, doi:10.1016/0370-1573(83)90080-7.

[67] G. Corcella et al., "HERWIG 6.5: an event generator for Hadron Emission Reactions With Interfering Gluons (including supersymmetric processes)", *J. High Energy Phys.* **01** (2001) 010, arXiv:hep-ph/0011363.

[68] A. Banfi, G. Corcella, and M. Dasgupta, "Angular ordering and parton showers for non-global QCD observables", *J. High Energy Phys.* (2006) doi:10.1088/1126-6708/2007/03/050, arXiv:hep-ph/0612282.

[69] A. Kupco, "Cluster Hadronization in HERWIG 5.9", arXiv:hep-ph/9906412.

[70] T. Gleisberg et al., "Event generation with SHERPA 1.1", *J. High Energy Phys. 0902:007,2009* (2008) doi:10.1088/1126-6708/2009/02/007, arXiv:0811.4622.

[71] E. Barberio and Z. Was, "PHOTOS - a universal Monte Carlo for QED radiative corrections: version 2.0", *Comput. Phys. Commun.* **79** (1994), no. 2, 291 – 308, doi:http://dx.doi.org/10.1016/0010-4655(94)90074-4.

[72] Z. Was, "TAUOLA for simulation of tau decay and production: perspectives for precision low energy and LHC applications", *Nucl.Phys.Proc.Suppl.* **218** (2011) 249–255, doi:10.1016/j.nuclphysbps.2011.06.040, arXiv:1101.1652.

[73] GEANT4 Collaboration, "GEANT4: A Simulation toolkit", *Nucl.Instrum.Meth.* **A506** (2003) 250–303, doi:10.1016/S0168-9002(03)01368-8.

[74] W. Lukas, "Fast Simulation for ATLAS: Atlfast-II and ISF", Technical Report ATL-SOFT-PROC-2012-065, CERN, Geneva, Jun, 2012.

[75] ATLAS Collaboration, "Fast simulation of electromagnetic showers in the ATLAS calorimeter: Frozen showers", *J. Phys. Conf. Ser.* **160** (2009) 012082, doi:10.1088/1742-6596/160/1/012082.

[76] A. Vovenko et al., "Energy resolution and structure of a calorimeter", *Nucl. Instr. Meth. Phys. Res.* **212** (jul, 1983) 155–162, doi:10.1016/0167-5087(83)90686-5.

[77] T. M. Mitchell, "Machine Learning". McGraw-Hill Education, 1997.

[78] F. Pedregosa et al., "Scikit-learn: Machine Learning in Python", *J. Mach. Learn. Res.* **12** (2011) 2825–2830.

[79] L. Breiman, J. H. Friedman, R. A. Olshen, and C. J. Stone, "Classification and Regression Trees". Statistics/Probability Series. Wadsworth Publishing Company, Belmont, California, U.S.A., 1984.

[80] S. Vajapeyam, "Understanding Shannon's Entropy metric for Information", arXiv:1405.2061.

[81] V. Vapnik and A. Lerner, "Pattern Recognition using Generalized Portrait Method", *Autom. Remote Control* **24** (1963).

[82] "Validation of the frozen showers libraries on forward electrons results". http://atlas-computing.web.cern.ch/atlas-computing/links/PhysValDir/Egamma/electrons/10_02_2017/task1/.

[83] "Validation of the frozen showers libraries on Zee sample with 1 electron in a forward region". http://atlas-computing.web.cern.ch/atlas-computing/links/PhysValDir/SMZee/01-12-2016/task1_norm/Zee/FWDZee/index.html.

[84] "Validation of the frozen showers libraries on jets sample". https://atlas-computing.web.cern.ch/atlas-computing/links/PhysValDir/JetEtMiss/jet_17-02-10_task1/JetsETmiss/Jets/AntiKt10LCTopoJets/index.html.

[85] ATLAS Collaboration, "Measurements of the Nuclear Modification Factor for Jets in Pb+Pb Collisions at $\sqrt{s_{\mathrm{NN}}}$ = 2.76 TeV with the ATLAS Detector", doi:10.1103/PhysRevLett.114.072302, arXiv:1411.2357.

[86] H.-L. Lai et al., "New parton distributions for collider physics", *Phys. Rev. D* **82** (Oct, 2010) 074024, doi:10.1103/PhysRevD.82.074024.

[87] ATLAS Collaboration, "Summary of ATLAS Pythia 8 tunes", Technical Report ATL-PHYS-PUB-2012-003, CERN, Geneva, Aug, 2012.

[88] J. Pumplin et al., "New Generation of Parton Distributions with Uncertainties from Global QCD Analysis", *J. High Energy Phys.* **2002** (jul, 2002) 012–012, doi:10.1088/1126-6708/2002/07/012.

[89] ATLAS Collaboration, "First tuning of HERWIG/JIMMY to ATLAS data", Technical Report ATL-PHYS-PUB-2010-014, CERN, Geneva, Oct, 2010.

[90] S. Heim and K. Lohwasser, "Status of electron ID and other Recommendations for Run-2". https://indico.cern.ch/event/363200/session/6/contribution/46/material/slides/0.pdf.

[91] ATLAS Collaboration, "Electron and photon energy calibration with the ATLAS detector using LHC Run 1 data", doi:10.1140/epjc/s10052-014-3071-4, arXiv:1407.5063.

[92] ATLAS Collaboration, "Measurement of the muon reconstruction performance of the ATLAS detector using 2011 and 2012 LHC proton-proton collision data", doi:10.1140/epjc/s10052-014-3130-x, arXiv:1407.3935.

[93] A. Dimitrievska, N. Vranjes, M. Schott, and M. Boonekamp, "Measurement of m_W at 7 TeV: Hadronic recoil corrections", Technical Report ATL-COM-PHYS-2015-344, CERN, Geneva, Apr, 2015.

[94] G. S. Watson, "Linear Least Squares Regression", *Ann. Math. Stat.* **38** (dec, 1967) 1679–1699, doi:10.1214/aoms/1177698603.

[95] Kendall, Maurice, and Alan Stuart, "The advanced theory of statistics". London: Griffin, 1969.

[96] ATLAS Collaboration, "Measurement of the $W \to l\nu$ and $Z/\gamma^* \to ll$ production cross sections in proton-proton collisions at $\sqrt{s} = 7$ TeV with the ATLAS detector", *J. High Energy Phys.* **2010** (dec, 2010) doi:10.1007/jhep12(2010)060.

[97] P. Saracco, M. G. Pia, and M. Batic, "Theoretical grounds for the propagation of uncertainties in Monte Carlo particle transport", doi:10.1109/TNS.2014.2300112, arXiv:1401.4045.

[98] ATLAS Collaboration, "Electron performance measurements with the ATLAS detector using the 2010 LHC proton-proton collision data", *Eur. Phys. J. C72 (2012) 1909* (2011) doi:10.1140/epjc/s10052-012-1909-1, arXiv:1110.3174.

[99] M. R. Whalley, D. Bourilkov, and R. C. Group, "The Les Houches Accord PDFs (LHAPDF) and Lhaglue", arXiv:hep-ph/0508110.

[100] ATLAS Collaboration, "Determination of the Strange-Quark Density of the Proton from ATLAS Measurements of the $W \to e\nu$ and $W \to ee$ Cross Sections", *Phys. Rev. Lett.* **109** (jul, 2012) doi:10.1103/physrevlett.109.012001.

[101] S. Alekhin, J. Blümlein, S. Klein, and S. Moch, "The 3-, 4-, and 5-flavor NNLO Parton from Deep-Inelastic-Scattering Data and at Hadron Colliders", *Phys.Rev.D* **81** (2009) doi:10.1103/PhysRevD.81.014032, arXiv:0908.2766.

[102] R. D. Ball et al., "Parton distributions with LHC data", *J. Nucl. Phys. B* (2012) doi:10.1016/j.nuclphysb.2012.10.003, arXiv:1207.1303.

[103] B. Dickinson, "Estimation of partial correlation matrices using cholesky decomposition", in *1978 IEEE CDC*. IEEE, jan, 1978. doi:10.1109/cdc.1978.267934.

[104] J. M. Campbell and R. Ellis, "MCFM for the Tevatron and the LHC", *Nucl.Phys.Proc.Suppl.* **205-206** (2010) 10–15, doi:10.1016/j.nuclphysbps.2010.08.011, arXiv:1007.3492.

[105] T. Carli et al., "A posteriori inclusion of parton density functions in NLO QCD final-state calculations at hadron colliders: The APPLGRID Project", doi:10.1140/epjc/s10052-010-1255-0, arXiv:0911.2985.

[106] S. Alekhin, J. Bluemlein, and S. Moch, "The ABM parton distributions tuned to LHC data", doi:10.1103/PhysRevD.89.054028, arXiv:1310.3059.

[107] H1 and ZEUS Collaboration, "Combination of Measurements of Inclusive Deep Inelastic $e^{\pm}p$ Scattering Cross Sections and QCD Analysis of HERA Data", arXiv:1506.06042.